ANL-6938

325
2/24/65

ANL-6938

Argonne National Laboratory

RADIOLOGICAL PHYSICS DIVISION

ANNUAL REPORT

July 1963 through June 1964

DISCLAIMER

LEGAL NOTICE

This report was prepared as an account of Government sponsored work. Neither the United States, nor the Commission, nor any person acting on behalf of the Commission:

A. Makes any warranty or representation, expressed or implied, with respect to the accuracy, completeness, or usefulness of the information contained in this report, or that the use of any information, apparatus, method, or process disclosed in this report may not infringe privately owned rights; or

B. Assumes any liabilities with respect to the use of, or for damages resulting from the use of any information, apparatus, method, or process disclosed in this report.

As used in the above, "person acting on behalf of the Commission" includes any employee or contractor of the Commission, or employee of such contractor, to the extent that such employee or contractor of the Commission, or employee of such contractor prepares, disseminates, or provides access to, any information pursuant to his employment or contract with the Commission, or his employment with such contractor.

Printed in USA. Price $6.00. Available from the Clearinghouse for Federal Scientific and Technical Information, National Bureau of Standards, U. S. Department of Commerce, Springfield, Virginia

ANL-6938
Biology and Medicine
(TID-4500, 37th Ed.)
AEC Research and
Development Report

ARGONNE NATIONAL LABORATORY
9700 South Cass Avenue
Argonne, Illinois 60440

RADIOLOGICAL PHYSICS DIVISION ANNUAL REPORT

July 1963 through June 1964

L. D. Marinelli, Division Director

Preceding Report:
ANL-6769 - July 1962 through June 1963

Operated by The University of Chicago
under
Contract W-31-109-eng-38
with the
U. S. Atomic Energy Commission

THIS PAGE INTENTIONALLY
WAS INTENTIONALLY
LEFT BLANK

TABLE OF CONTENTS

TABLE OF CONTENTS

TABLE OF CONTENTS

THIS PAGE
WAS INTENTIONALLY
LEFT BLANK

FLUORESCENCE DECAY-TIME MEASUREMENTS OF SEVERAL DEUTERATED COMPOUNDS*

I. B. Berlman and O. J. Steingraber

Abstract

Fluorescence decay times of several completely deuterated organic compounds and of similar but nondeuterated fluors have been measured. Each solute was dissolved in a common solvent, cyclohexane, and was excited directly by monochromatic pulsed uv radiation. The technique of making fluorescence decay-time measurements in the nanosecond region has been published.(1) The apparatus has been improved by replacing many components with equipment of more advanced design; and a deuterium-filled flash tube has been tested. Preliminary values** for completely deuterated p-terphenyl, naphthalene, and anthracene are 0.9 nsec, 96 nsec, and 4.8 nsec, respectively, and for similar nondeuterated compounds 0.9 nsec, 95 nsec, and 4.9 nsec, respectively. These values are believed to be correct to within ±10%. Thus the fluorescence decay time of ordinary and completely deuterated compounds are essentially equal within the experimental error. In sharp contrast to this result for fluorescence decay, the published value(2) of the phosphorescence decay time of completely deuterated naphthalene is 16.9 sec, whereas that of ordinary naphthalene is 2.1 sec.

References

1. O. J. Steingraber and I. B. Berlman, Rev. Sci. Instr. 34, 524 (1963).

2. C. A. Hutchinson, Jr. and B. W. Mangum, J. Chem. Phys. 32, 1261 (1960).

---

*Published in Bull. Am. Phys. Soc. 9 (1), 76 (1964).

**Several of these values have been corrected and are, therefore, different from those appearing in Radiological Physics Division Summary Report ANL-6769, p. 4 (1963). These changes were brought about, not by any electronic malfunction, but by an improvement in the technique of evaluating the final curves.

NANOSECOND FLUORESCENCE DECAY-TIME MEASUREMENTS*

I. B. Berlman

Abstract

A new versatile apparatus has been used to measure the fluorescence decay times of four series of related compounds, each dissolved in an appropriate solvent. The solutes were excited directly by pulsed monochromatic radiation, and the pulse contour of the emitted radiation was recorded. Molecular types were 1) simple polynuclear compounds, such as diphenyl, p-terphenyl, etc.; 2) compounds with condensed benzene rings, e.g., naphthalene, anthracene, etc.; 3) oxadiazole compounds; and 4) oxazole compounds. All the solute molecules chosen have a high fluorescence quantum yield. The oxadiazole compounds as a class have very fast decay times with 2,5 di-(4-biphenylyl)-1,3,4-oxadiazole (BBD) having the fastest decay time of all the compounds tested, 0.9 nsec. In fact, this decay time is the shortest reported to date. Generally, the longer the molecule the shorter the fluorescence decay time.

*Published in Bull. Am. Phys. Soc. 8 (3), 238 (1963).

Ar-N

SCINTILLATIONS IN ARGON-NITROGEN MIXTURES: EFFECT OF CONCENTRATION AND PRESSURE

H. A. Schultz

Introduction

In a mixture of gases, the rate of transfer of energy directly from one type of particle (ion, molecule, or electron) to another is porportional to the frequency of impacts between the two types of particles. Accordingly, this rate depends upon the total pressure of the gas as well as the partial pressures or relative concentrations.

This report covers a pulse height study of scintillations produced by alpha particles in argon-nitrogen mixtures with concentrations ranging from 100% argon to 100% nitrogen and total pressures from 3 to 6 atmospheres.

Description of Apparatus

The gas cell cross section is shown in Figure 1. The cell, and in fact the whole gas-handling system, was designed to be as free as possible from any type of organic material to reduce quenching of the scintillations by organic vapors. The quartz window was sealed by a lead ring pressed into place by a steel clamping ring. The cavity was a truncated cone, a simple approximation to a parabolic reflector; and its surfaces were aluminized. No solid wavelength shifter was used. The source was Cm^{244} (5.8 MeV alpha) on a stainless steel surface 0.32 cm in diameter, projecting 0.16 cm from the plane surface of the cell.

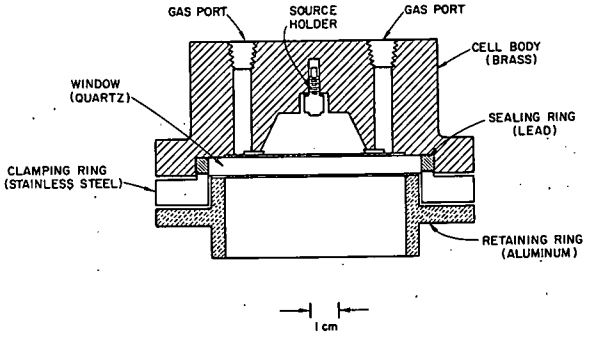

Figure 1

Cross section of cell. The cavity in the form of a truncated cone has a diameter of 3.97 cm at the lower base and is 1.43 cm deep. The half angle of the apex is 30°. The retaining and clamping rings are secured by six machine screws (not shown).

A quartz-windowed photomultiplier tube, RCA 6903, was coupled to the window with glycerin, which transmits visible light and ultraviolet above 2300A. To avoid changes in the detected pulse height, the optical coupling was not changed during the entire series reported here. The ten-stage tube has a 3.8-cm diameter photocathode with a S-13 response (Figure 2). The tube voltage was 770 volts with photocathode grounded. The load resistor

was 2 x 10^5 ohms, and the capacitance of the photomultiplier and associated wiring was estimated to be 10 pF; the calculated time constant of the resistance-capacitance combination (RC) was, therefore, 2 μsec. A transistorized preamplifier and a TMC model 404 analyzer were used. The analyzer was designed for pulses of approximately 0.25 μsec rise time and 2.5 μsec decay time. The noise level was negligible relative to all the pulse height spectra. The counting rate was 2.77 x 10^4 counts per minute, and the majority of the runs were of 40 minutes' duration.

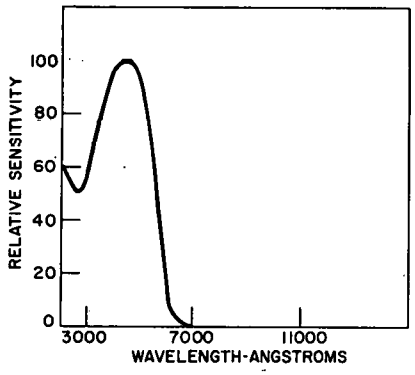

Figure 2

Spectral sensitivity of a 6903 photomultiplier tube (S-13 response).

The gas-handling system was fabricated of glass and metal. The mercury vapor diffusion pump was isolated from the filling system and cell by two liquid nitrogen traps in series. Whenever the system was shut down, the mercury was removed at once from the trap nearest the pump. There has been no evidence of mercury inside the re-entrant tube of this trap or anywhere in the second trap. In an argon purifier (Figure 3), the gas was recirculated over barium. The barium metal was received from the supplier* in a vacuum can, free of the protective film of oil commonly used. The effectiveness of the purifier was checked by adding nitrogen to the argon and then obtaining pulse height spectra as the nitrogen was being removed. The argon as received was specified as 99.996% pure,** and the

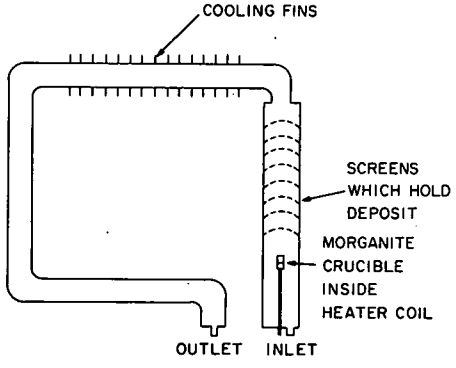

Figure 3

Sketch of Argon Purifier. Morganite crucible 1.0 cm inside diameter x 2.5 cm deep filled with barium chips is heated in argon at approximately 6 atmospheres by 70 watts to activate, or by 19 watts to maintain the gas circulation. Height is approximately 38 cm.

*Kemet Department, Linde Company, Division of Union Carbide Corporation, Cleveland, Ohio.

**Argon from Airco. Typical analysis, 99.9989% argon, 3 ppm oxygen, 6 ppm nitrogen, less than 1 ppm carbon dioxide, less than 1 ppm hydrocarbons, and -90°F dew point.

nitrogen 99.996% pure.* The nitrogen was passed through a solid carbon dioxide-alcohol trap before being used.

Experimental Results

The pulse height spectra are symmetrical, bell-shaped distribution curves, provided the particles are stopped within the gas and do not strike the walls (Figure 4). A small number of noise pulses from the photomultiplier are accumulated in the lowest channels of the analyzer, and a number of pulses are recorded in channels between the noise pulses and the toe of the main peak. It is thought that these pulses may be due to particles which originate at the edge of the source and strike the upper surface of the cell. In the spectra of 100% argon, 1.6% of the total counts fall in the valley between the noise and the spectral peak (Figure 4).

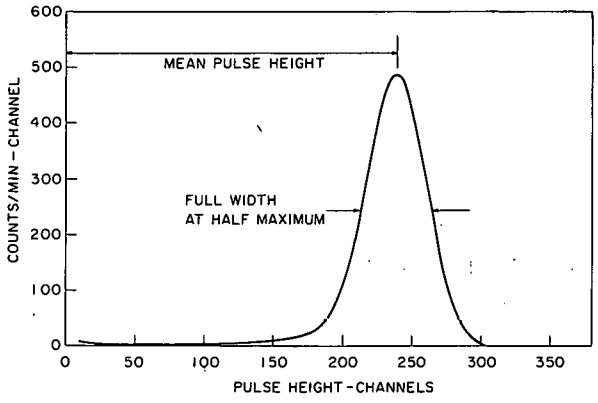

Figure 4

Example of a pulse height spectrum, 100% argon at 6.00 atmospheres

The effect of concentration upon pulse height at pressures of 4.00 and 5.00 atmospheres is summarized in Figure 5 and Table 1. Corrections have been made for nonlinearities in the preamplifier and anlyzer which affect the data at the lower pulse heights. A small correction for change in pulse height with time was made in the 34.2% and 67.1% nitrogen data, which were obtained two months later than the other data. Two standards were used to detect drift: 1) Pulses from a pulse generator were used to calibrate the analyzer and also the preamplifier-analyzer combination once or twice a day; 2) pure argon spectra were obtained occasionally. The argon pulse height was found to decrease at a rate of 2.1% per 100 days. Approximately one-third of this was due to the observed drift in the high voltage supply; the remainder was attributed to changes in the properties of the photomultiplier and in the reflectance and transmittance of the optical components. To determine whether this drift rate was also applicable to mixtures, observations upon a 16.5% nitrogen mixture were compared with data obtained 17 weeks earlier, and the same drift was found.

*Nitrogen from the Matheson Company, Inc., prepurified grade, 99.996% minimum purity, typical oxygen content 8 ppm, typical dew point -90°F.

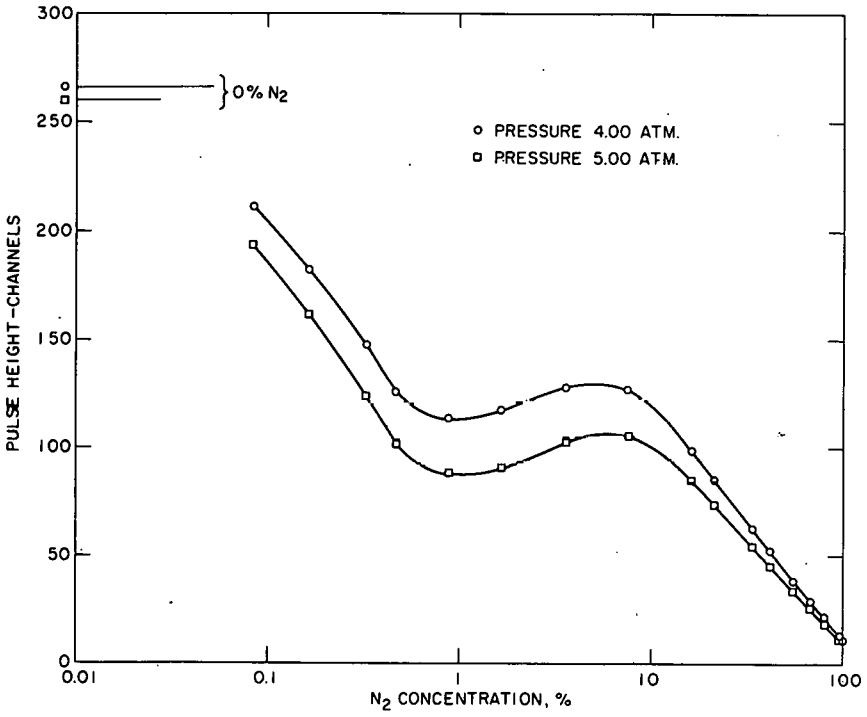

Figure 5

Pulse height vs. nitrogen concentration in argon-nitrogen mixtures at 4.00 and 5.00 atmospheres

Table 1

Pulse height as a function of nitrogen concentration

% Nitrogen	Pulse height, channels			Decrease in Pulse height, %
	At 4.00 atm	At 5.00 atm	Decrease	
0	265.5	260.0	5.5	2.07
0.085	210.6	193.4	17.2	8.15
0.164	181.8	161.0	20.8	11.4
0.33	148.5	123.9	24.6	16.6
0.47	125.4	100.8	24.6	19.6
0.88	114.1	87.8	26.3	23.0
1.68	116.9	90.0	26.9	23.0
3.59	127.8	102.5	25.3	19.8
7.65	126.3	105.4	20.9	16.5
16.4	99.1	85.4	13.7	13.8
16.5	98.9	85.3	13.4	13.6
21.5	85.4	74.0	11.4	13.3
34.2	62.1	54.4	7.7	12.4
41.4	51.5	44.9	6.6	12.8
54.8	38.3	33.3	5.0	13.1
67.1	29.3	25.8	3.5	11.9
79.6	22.0	18.6	3.4	15.5
94.2	13.3	11.4	1.9	14.3
100.0	11.0	-	-	-

The pulse-height-concentration relations in Figure 5 show very definite maxima and minima. A similar relation for helium-xenon combinations has been reported by Northrup, Gorsky, and Johnsrud.[1] An essentially continuous curve of the same shape was obtained from a diffusion experiment designed to confirm the effectiveness of the purifier. Starting with an argon-16.7% nitrogen mixture, at 5.68 atm pressure in the cell, pulse height spectra were taken serially while the composition of the sample was changing continuously because of diffusion into the purifier system, where the nitrogen was removed. The diffusion rate was determined by comparison of pulse height data with those for known mixtures, and this rate was used to estimate smaller nitrogen concentrations. At the time the test was terminated the calculated nitrogen concentration in the cell was 29 ppm. The separation of the two pulse height-concentration curves (Figure 5) is greatest in the range 1% to 10% nitrogen; the ratio of the separation to the pulse height at 4.00 atmospheres is greatest near 1% (Table 1).

The mean pulse heights obtained from individual spectra are tabulated in Table 2 and plotted vs. pressure at constant concentration in Figures 6, 7, and 8. All pressures are given in equivalent standard atmospheres at 0°C. The room temperatures were near 25°C. Spectra were also obtained at somewhat lower pressures, but were excluded since there was experimental evidence that these spectra were distorted by particles striking the walls of the enclosure. The first evidence of this as the pressure is lowered is a slight elevation at the toe of the distribution curve on the lower pulse-height side, the beginning of a second peak. Table 3 lists pressures at which this elevation was and was not observed. The 3.09-atm limit for 67.1% nitrogen was assumed to be valid for higher concentrations, since at 79.6% nitrogen and above, the toe of the curve was below the threshold of the analyzer. Calculations based on the published range data[2,3] give somewhat higher values for the limits, provided it is assumed that the active material is distributed over the entire face of the source. These calculations indicate that particles will strike the nearest wall of the cell below 3.84 atm in 100% nitrogen and 4.02 atm in 100% argon; and the quartz window below 3.31 atm in nitrogen and 3.46 atm in argon. Tests run under vacuum conditions do not show any pulses that may be attributed to emission at the walls or the window.

The pulse height vs. pressure curves of Figures 6, 7, and 8 are all concave upward except those for 100% argon and 100% nitrogen which are approximately linear.

The "resolution widths" of the above set of spectra are tabulated in Table 2 and plotted in Figure 9. "Resolution width" is defined as the relative full width of the spectral peak at half maximum, that is, as the ratio

$$\frac{\text{Full width at half maximum}}{\text{Mean pulse height}}.$$

At nitrogen concentrations of 7.65% and above, the resolution width increases

with pressure, as might be expected from the fact that the pulse heights decrease with pressure. However, at nitrogen concentrations below 7.65% the resolution width does not change very much with pressure (Figure 9), even though the pulse height varies by a factor of about 3 to 1. This effect will be examined in the next section.

Table 2

Relative pulse height and resolution width (%) as a function of pressure in argon-nitrogen mixtures

% Nitrogen											
0	Press., atm				4.03	4.37	4.65	4.99	5.28	5.58	6.00
	Pulse height				265.1	263.6	262.1	259.7	258.5	256.5	255.1
	Res. width, %				24.6	22.7	21.6	20.5	20.4		
0.085	Press., atm			3.71	4.03	4.32	4.67	5.01	5.33		
	Pulse height			216.2	(210.6, 210.0)	204.0	198.4	193.1	189.2		
	Res. width, %			27.4	25.4	23.9	23.1	22.6	22.4		
0.164	Press., atm			3.70	4.02	4.36	4.64	4.98	5.25	5.59	
	Pulse height			189.0	181.0	173.2	167.2	161.5	156.5	151.9	
	Res. width, %			26.7	25.7	24.9	24.6	24.4	24.5	24.5	
0.33	Press., atm		3.41	3.74	4.04	4.35	4.65	4.96	5.26	5.54	5.88
	Pulse height		168.0	155.9	147.3	138.9	131.6	124.5	118.6	113.9	109.7
	Res. width, %		31.0	28.7	27.2	27.6	27.0	27.2	27.9	28.1	28.2
0.47	Press., atm		3.36	3.66	3.99	4.26	4.54	4.82	5.16		
	Pulse height		149.1	136.5	125.8	117.6	110.8	104.6	98.0		
	Res. width, %		31.4	29.5	28.4	28.6	28.3	28.9	29.4		
0.88	Press., atm		3.41	3.72	4.01	4.37	4.71	5.01	5.38		
	Pulse height		137.2	124.8	113.4	102.4	94.0	88.0	80.2		
	Res. width, %		31.0	29.6	29.1	29.2	29.8	30.3	31.4		
1.68	Press., atm		3.41	3.74	4.03	4.35	4.69	5.00	5.30	5.64	
	Pulse height		139.6	126.6	115.4	104.8	97.1	90.0	84.5	79.4	
	Res. width, %		29.6	28.0	27.9	28.5	29.0	29.9	29.9	31.5	
3.59	Press., atm		3.42	3.71	4.00	4.30	4.66	5.00	5.25	5.58	5.93
	Pulse height		150.9	138.4	127.4	118.0	109.6	102.5	97.8	93.0	88.3
	Res. width, %		28.4	27.2	26.5	26.4	27.4	27.2	27.6	27.8	28.2
7.65	Press., atm		3.32	3.72	4.02	4.34	4.65	4.97	5.35		
	Pulse height		149.2	(133.5, 134.0)	126.0	117.8	111.4	105.8	100.0		
	Res. width, %		29.1	26.4	27.0	26.9	27.2	27.5	27.6		
16.4	Press., atm		3.42	3.67	3.98	4.28	4.57	5.02		5.62	
	Pulse height		112.2	(105.2, 106.0)	99.4	94.2	89.4	85.0		80.7	
	Res. width, %		31.2	(30.3, 30.2)	29.4	29.8	30.1	30.0		31.7	
21.5	Press., atm		3.38	3.68	4.01	4.34	4.65	4.98	5.32		
	Pulse height		96.4	89.8	85.3	81.2	77.2	74.2	71.2		
	Res. width, %		32.7	31.8	31.1	31.6	31.8	32.8	32.6		
34.2	Press., atm		3.40	3.66	3.99	4.30	4.62	4.97	5.35		
	Pulse height		69.3	65.4	62.5	59.5	56.7	54.4	52.4		
	Res. width, %		37.1	36.2	36.4	36.6	37.0	37.4	38.2		
41.4	Press., atm		3.38	3.71	4.01	4.29	4.62	4.94	5.24	5.60	
	Pulse height		57.6	54.2	51.4	48.8	46.8	45.6	43.4	42.4	
	Res. width, %		39.9	39.1	39.0	39.4	40.7	40.1	41.8	42.2	
54.8	Press., atm		3.38	3.72	4.00	4.35	4.63	4.91	5.16	5.42	
	Pulse height		42.6	40.2	38.2	35.9	34.5	33.6	32.7	32.0	
	Res. width, %		44.8	44.3	45.3	46.2	47.2	47.3	49.0	49.4	
67.1	Press., atm		3.38	3.70	3.99	4.29	4.62	4.98	5.22	5.64	
	Pulse height		32.9	30.8	29.3	28.3	26.9	25.7	25.2	24.1	
	Res. width, %		50.0	51.1	51.4	51.7	53.8	55.0	55.3	58.4	
79.6	Press., atm		3.38	3.72	3.98	4.28	4.59	4.90	5.20	5.43	
	Pulse height		24.6	23.2	22.0	21.0	19.6	18.8	18.1	17.5	
	Res. width, %		57.4	59.4	5.95	61.4	66.3	68.1	69.0	72.6	
94.2	Press., atm		3.38	3.71	4.01	4.34	4.70	5.01	5.29		
	Pulse height		15.6	14.2	13.3	12.5	11.9	11.3	(10.8, 11.0)		
	Res. width, %		78	80	-	-	-	-	-		
100.0	Press., atm	3.09	3.39	3.70	4.00	-	-	-	-		
	Pulse height	13.5	12.6	11.8	11.0	-	-	-	-		

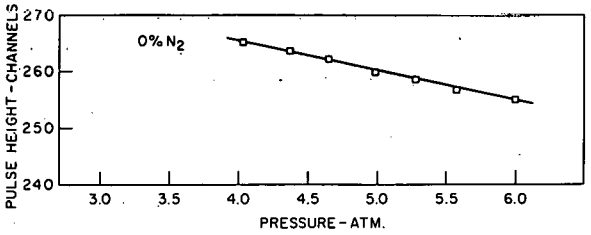

Figure 6

Pulse height vs. pressure,
100% argon

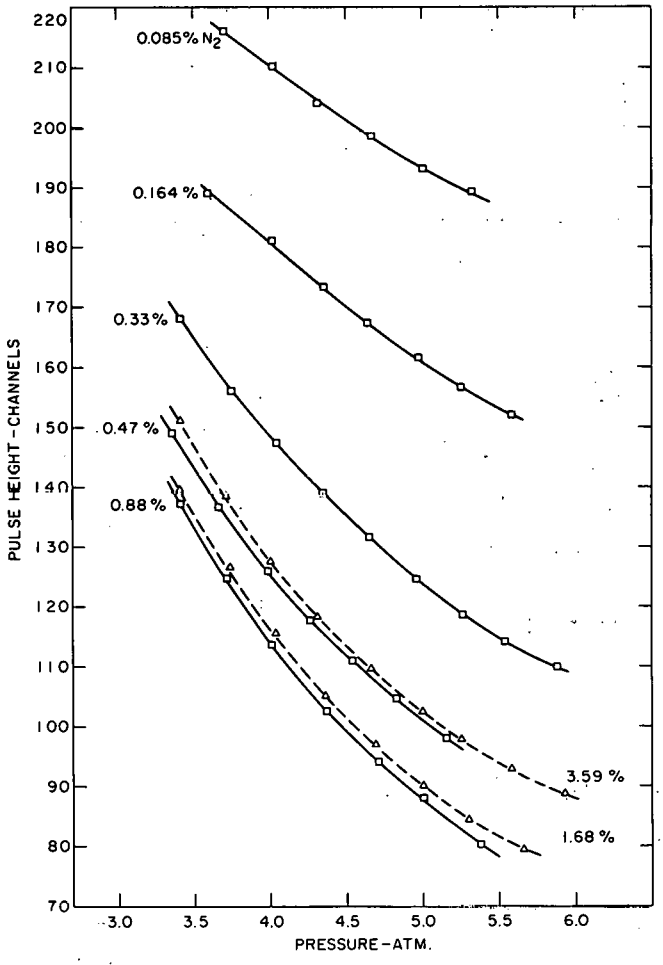

Figure 7

Pulse height vs. pressure,
0.085 to 3.59% nitrogen

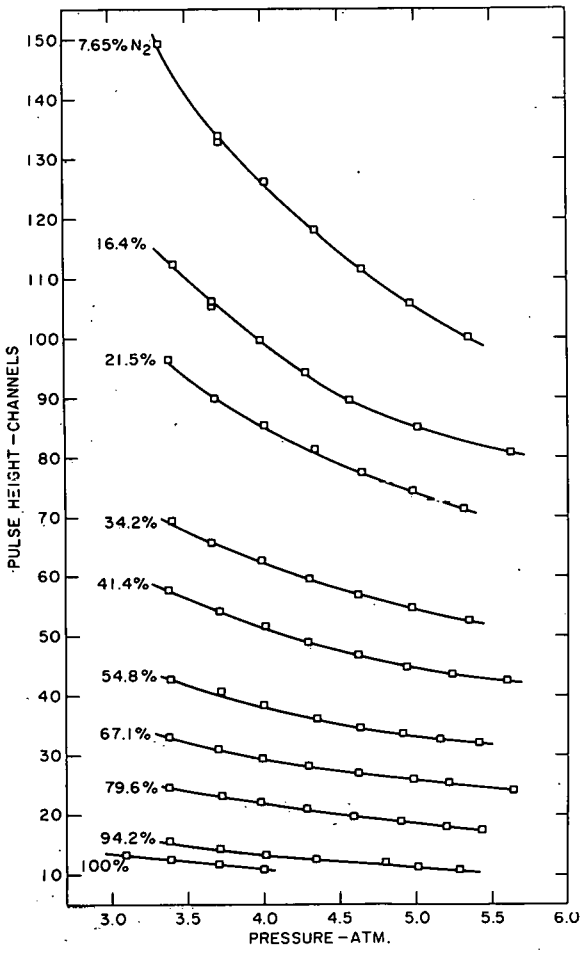

Figure 8

Pulse height vs. pressure,
7.65 to 100% nitrogen

Table 3

Pressure at which an elevation of the toe of the spectrum first appears

N_2 concentration, %	Pressures, atm		N_2 concentration, %	Pressures, atm	
	No evidence of elevation at toe of spectrum	Evidence of elevation at toe of spectrum		No evidence of elevation at toe of spectrum	Evidence of elevation at toe of spectrum
0	4.03	3.75	7.65	3.32	3.04
0.085	3.71	3.41	16.4	3.42	3.08
0.164	3.70	3.41	16.5	3.40	3.10
0.33	3.41	3.10	21.5	3.38	3.12
0.47	3.36	3.08	34.2	3.40	3.10
0.88	3.41	3.10	41.4	3.38	3.10
1.68	3.41	3.12	54.8	3.39	3.10
3.59	3.42	3.11	67.1	3.09	2.73

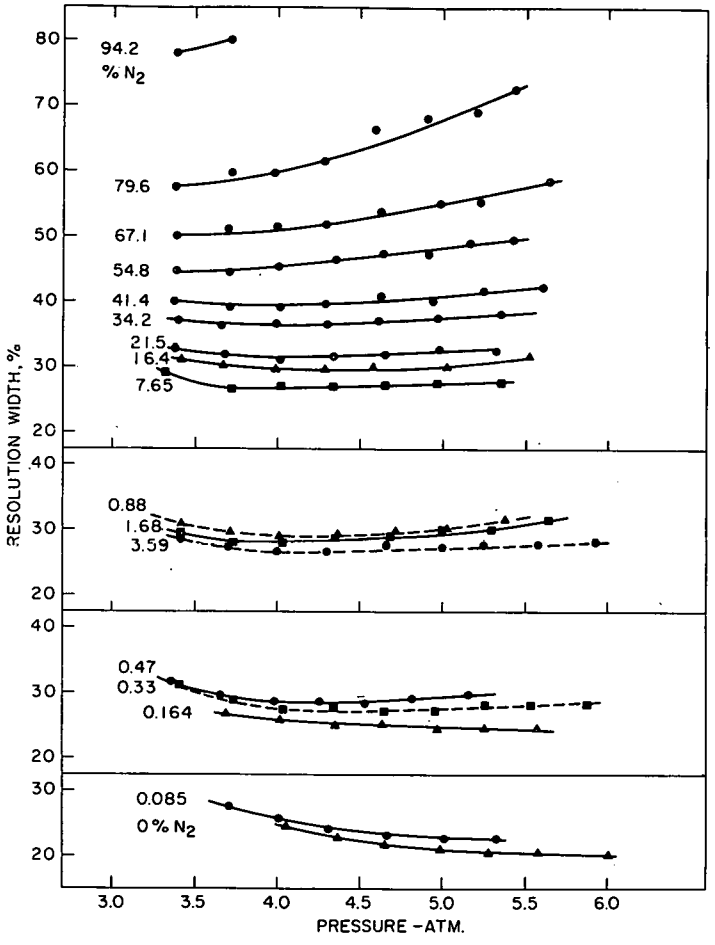

Figure 9

Resolution width vs. pressure in argon-nitrogen mixtures at indicated % nitrogen

Discussion

According to estimates of the experimental errors in the data (Table 4) the largest relative errors were associated with the lowest values of the nitrogen concentrations. This is because the errors accumulated as the samples were prepared by successive dilutions.

Table 4

Estimated standard deviations of experimental variables

Nitrogen concentration, %	
0.085 ± 0.006	1.68 ± 0.05
0.164 ± 0.011	3.59 ± 0.09
0.33 ± 0.02	7.65 ± 0.14
0.47 ± 0.02	16.4 ± 0.2
0.88 ± 0.03	21.5 ± 0.3
	over 21.5 ± 0.3

Pressure, ±0.01 atm

Pulse height, ±0.5 channel

From the shape of the pulse height vs. concentration relation (Figure 5), it is suggested that at least two separate emission processes made a contribution to the spectral peaks obtained with the lower nitrogen concentrations. Data on the resolution of the spectra make this suggestion appear to be even more reasonable.

If the distribution of pulse heights depended only upon the statistical nature of processes in the gas and in the photomultiplier, the absolute width of the spectral peak would be proportional to the square root of the mean pulse height. However, the spectral peaks may have been broadened as a result of geometrical effects.

It has been shown[4] that the statistics of a given scintillator may be treated by use of the equation

$$V_Q = V_T + \frac{1 + V_M}{\overline{X}\,\overline{T}}$$

in which V_Q is the relative variance of the over-all process and is equal to 0.1803 times the square of the resolution width of the spectral peak; V_T is the relative variance of the transfer efficiency (of light from the point of origin to the photocathode), V_M is the relative variance of the multiplication process in the photomultiplier; $\overline{X}$ is the average number of photons emitted per pulse, $\overline{T}$ the average transfer efficiency; therefore, $\overline{XT}$ is proportional

to the mean pulse height. Accordingly, if the square of the resolution width is plotted against the reciprocal of the pulse height, the points are expected to fall along a straight line with intercept proportional to V_T, the relative variance of the transfer efficiency.

In the case of the gas cell, the pulse height is varied by changing the composition and pressure of the gas, while the size and shape of the cell and the energy of the particles remain constant. In Figure 10 resolution data for nitrogen concentration from 3.59% to 79.6% are plotted as suggested above. (At higher concentrations the resolution data are not very reliable because the pulse heights are small.) The straight line was drawn by visual averaging to represent the 5-atm data. The intercept is obviously small; it represents a contribution of only 0.2% to the 27.5% resolution width at 3.59% nitrogen concentration, an even smaller contribution at the higher nitrogen concentrations. The 4.00-atm data appear to be consistently higher than the others; in this case the variance in transfer efficiency might contribute 2.3% to the 26.8% resolution width at 3.59% nitrogen concentration.

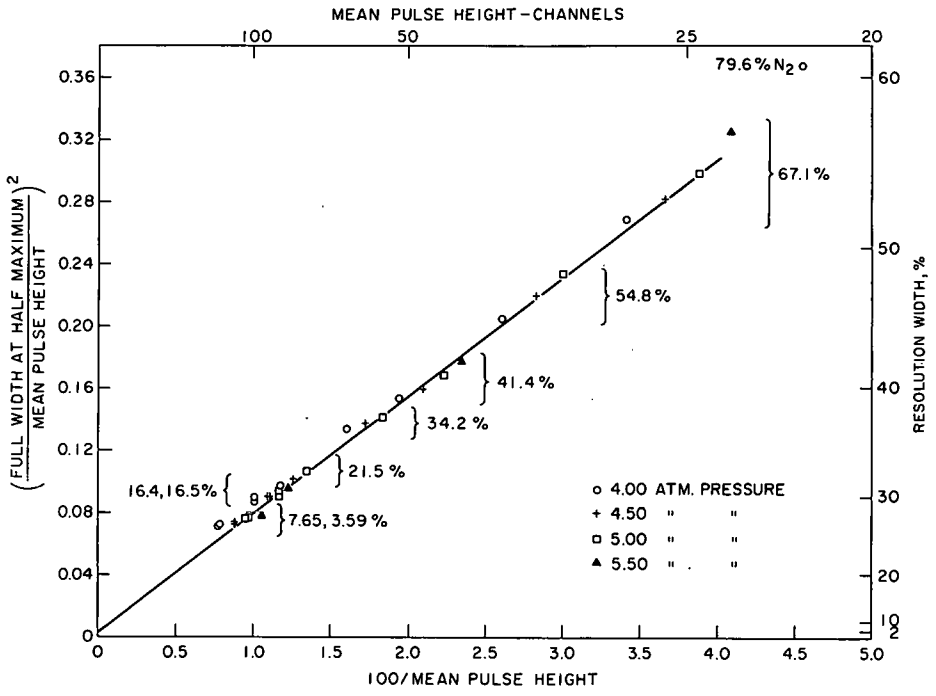

Figure 10

Square of the resolution width vs. the reciprocal of the mean pulse height for nitrogen concentrations of 7.65% to 79.6%. The line was drawn to represent 5.00 atm. data.

Resolution data for nitrogen concentration of 21.5% and less have been plotted in the same manner on larger scale graphs in Figures 11 and

12, and the diagonal line from Figure 10 has been dotted in for comparison. Referring to the 5.00-atm data (Figure 11), it is noted that the curve doubles back upon itself between 7.65% nitrogen and 1.68% nitrogen, as the slope of the pulse height-concentration relation changes sign (Figure 5). At still lower nitrogen concentrations, an entirely new curve of "hook" shape is formed. Similar curves result at other pressures, but the 4.00-atm curve (Figure 12), appears to have a somewhat different shape from the others.

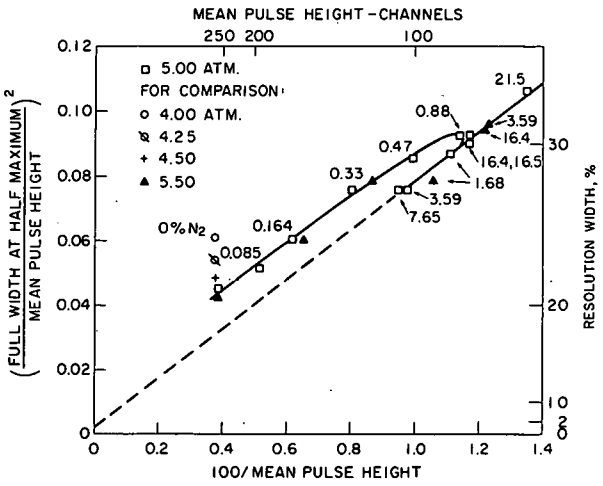

Figure 11

Square of the resolution width vs. the reciprocal of the mean pulse height on a larger scale than in Figure 10 for nitrogen concentrations of 0 to 21.5% and a pressure of 5.00 atm. The dotted line represents the line in Figure 10.

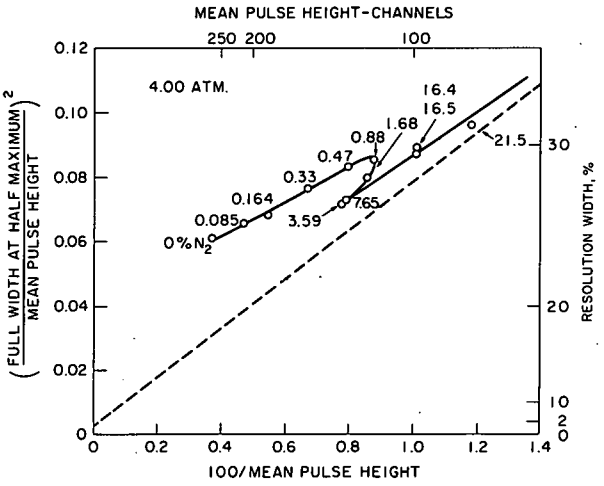

Figure 12

Square of the resolution width vs. the reciprocal of the mean pulse height on a larger scale than in Figure 10 for nitrogen concentrations of 0 to 21.5% and a pressure of 4.00 atm. The dotted line represents the line in Figure 10.

A plausible explanation of the loss of expected resolution may be based on the assumption that the spectral distribution of the emitted light, and not just its intensity, changed with composition at nitrogen concentrations of 1% and less. This would be equivalent to changing the scintillator from one experiment to another. Since the photocathode varies in sensitivity with wavelength, and the optical components of the system vary in reflectance and transmittance to some extent, a change in the emission spectrum might be accompanied by a change in the variability of the light-transfer process and the photoelectron-emission process.

The relatively large pulse height at low nitrogen concentrations was unexpected, in view of the results of previous workers who have found that the pulse height increased with low nitrogen concentrations to a maximum at 8 to 10%, and then decreased.[5,6,7] Continuous circulation of the argon (as supplied) over barium surfaces in the purifier changed pulse height very little; there appeared to be an increase of about 0.5 channel in 260 or 0.2%.

The intensities are low in all cases. From the properties of the photomultiplier and analyzer, it is estimated that the maximum (100% argon) pulse heights represent a total of approximately 65 photoelectrons. If the light losses near the source and around the photomultiplier were as large as 50% and the photocathode efficiency were 1 photoelectron per 15 photons, this would represent only 10^{-2} photons per ion pair. Throughout the entire pressure and concentration range reported, the pulse height from the quartz-windowed 6903 photomultiplier diminished with increase in pressure; that is, with increase in the frequency of collisions between molecules. The relative rate of decrease was least in the case of 100% argon (Table 1).

References

1. J. A. Northrup, J. M. Gorsky, and A. E. Johnsrud. IRE Trans. NS-5 (3), 81-87 (1958).

2. K. Schmieder. Ann. Physik 35, 445-64 (1939).

3. M. Stanley Livingstone and H. A. Bethe. Rev. Mod. Phys. 9, 245-390 (1937).

4. E. Breitenberger. Progress in Nuclear Physics. Pergamon Press, New York, 1955. Vol. 4, pp. 56-94.

5. C. Eggler and C. M. Huddleston. Nucleonics 14 (4), 34-36 (1956).

6. C. Eggler and C. M. Huddleston. IRE Trans. NS-3 (4), 36-38 (1956).

7. L. Koch. Thesis, University of Paris No. 620 (1959); K. Bergheim and K. Scarsvag. Nuclear Electronics 1, 111-114 (1962).

AN APPARATUS FOR MEASURING PHOTOIONIZATION EFFICIENCIES AS A FUNCTION OF ENERGY

James C. Person

The photoionization efficiency at any photon energy is the ratio of the photoionization cross section to the absorption cross section. The absorption cross section σ and the photoionization cross section σ_i are given by

$$\sigma = \frac{\ln(I_0/I)}{nl}$$

and

$$\sigma_i = \frac{i\sigma}{e(I_0-I)}$$

where I_0 is the light intensity in photons/sec when there is no sample in the light path, I is the light intensity after passing through a length l of a sample of n molecules/cm^3, and (i/e) is the number of ions/sec produced in the sample. (i is the saturated ion current and e is the electronic charge.)

The experimental apparatus consists of a) a lamp and monochromator to provide a source of monochromatic light, b) a means of measuring I_0/I and I_0, and c) an ionization chamber and a vacuum system for sample manipulation and for measuring i and n.

The present light source is a Hinteregger-type source[1] powered by an ac power supply (60 ma at 15 kV). Hydrogen gas is being used to provide a many-lined spectrum from 900 A to 1650 A. We have just received a more powerful dc power supply (200 ma at 20 kV), and experiments are planned using argon gas in the source to provide a continuum from 1050 A to 1500 A.[2] The McPherson Model 225 vacuum monochromator has a dispersion of 17 A/mm which gives a resolution of about 1 A when using 50-μ slit widths.

The detection system uses a split-beam technique to correct for fluctuations in I_0 during the experiment.[3] The light beam from the monochromator passes first through a sodium salicylate-coated grid and then through the sample chamber, and finally it strikes a sodium salicylate-coated EMI 9514S photomultiplier. The grid is at a 45-degree angle with the light beam so that the sodium salicylate fluorescence is in view of a second photomultiplier, mounted at right angles to the light beam. This 90-degree photomultiplier is used to monitor changes in I_0. At present, the absolute value of I_0 is determined by using NO in the sample chamber and assuming that Watanabe's values[4] for the photoionization efficiency of NO are correct. However, we are planning to measure the light intensity more directly with a calibrated thermopile.

The sample chamber is 51 mm long and has a thin LiF window on each end. The chamber has two electrodes which are parallel plates, except that they are bent towards each other along the front edge, so that the field strength is higher near the front window. The cell is now being tested to determine how well the ion current saturates as the voltage is increased and to determine the pressure range for which the saturated ion current is independent of pressure when corrections are made for light not absorbed.

The vacuum system has valves with Teflon or Kel-F seats so that no stopcock grease is in contact with the sample gas. Pressure measurements may be made with a McLeod gauge or with an MKS Baratron pressure meter. The latter may be used with nonideal gases, such as organic vapors, with a stated accuracy of ±0.4% or better in the pressure range of 0.25 to 11 mm Hg.

Experiments are now being done with gases of well-known cross section to test the apparatus. Experiments planned for the near future will search for an isotope effect in the photoionization of various organic vapors and their deuterated analogues (such as C_6H_6 and C_6D_6). From the results of these experiments we shall be able to make deductions about the importance of "superexcited" states in photoionization.[5] The apparatus can be modified for use with light in the 600- to 1050-A region by constructing a windowless sample chamber and using helium in the light source. Experiments in this region are planned for the coming year.

References

1. R. G. Newburgh, L. Heroux, and H. E. Hinteregger. Appl. Opt. 1, 733 (1962).

2. R. E. Huffman, Y. Tanaka, and J. C. Larrabee. Proc. Sixth Intern. Conf. on Ionization Phenomena in Gases. Serma, Paris, 1963. Vol. I, p. 145.

3. R. W. Ditchburn. J. Quant. Spectry. Radiative Transfer 2, 361 (1962).

4. K. Watanabe, Advances in Geophysics, ed. H. E. Landsberg and J. Van Mieghem. Academic Press, New York, 1958. Vol. V, p. 153.

5. R. L. Platzman. J. Chem. Phys. 38, 2775 (1963); Vortex 23, 372 (1962).

EFFECT OF IMPURITY ON EXCITATION MIGRATION IN A LINEAR CHAIN OF MOLECULES*

Mitio Inokuti and Michio Matsuzawa**

Abstract

The effect of an impurity on the second moment of an exciton wave packet is studied in the case of a simple one-dimensional model of molecular crystal with nearest-neighbor coupling. An expression is derived for the first-order correction, in the sense of perturbation theory, to the second moment and numerical evaluation is made.

*Published in J. Chem. Phys. 41, 732 (1964).

**Department of Applied Physics, Faculty of Engineering, University of Tokyo, Tokyo, Japan.

EXCITON IMPURITY LEVEL AND ITS IMPLICATIONS TO RADIATION CHEMISTRY

Kanji Katsuura** and Mitio Inokuti

Abstract

Dipole matrix elements corresponding to transitions to exciton states and other associated quantities are calculated for a simple one-dimensional model of a molecular crystal containing an impurity. Emphasis is placed on transitions to certain exciton levels, characteristic of the presence of an impurity. Absorption of radiation energy by molecular aggregates containing an impurity is discussed in view of the results of the calculation.

*Published in J. Chem. Phys. 41, 989 (1964).

**Department of Chemistry, Northwestern University, Evanston, Illinois.

ENERGY TRANSFER AND QUENCHING IN PLASTIC SCINTILLATORS. I. FLUORESCENCE OF POLYSTYRENE. II. EFFECTS OF ADDED CHLORO- AND BROMO-SUBSTITUTED ORGANIC COMPOUNDS ON LUMINESCENCE PROPERTIES OF PLASTIC SCINTILLATORS*

Fumio Hirayama

Abstract

The purpose of this study is to obtain a better understanding of intermolecular energy transfer and luminescence quenching occurring in plastic scintillators.

In Part I, the fluorescence spectrum of polystyrene, commonly used as the bulk medium for plastic scintillators, was investigated both in solid phase and in liquid solution. Also measured were fluorescence spectra of related compounds - ethylbenzene, 1,3-diphenylpropane, 1,3,5-triphenylpentane; polyvinyltoluene, poly-(p-chlorostyrene); poly-(styrene/methyl methacrylate), poly-(styrene/p-chlorostyrene).

Fluorescence of bulk thermally polymerized polystyrene is almost entirely that emitted from residual styrene monomer. The fluorescence spectrum of pure polystyrene, free of residual monomer, is a structureless band with maximum at 328 mμ and half-width 50 mμ. The spectrum of polystyrene in solution consists of two bands - a smaller band at about 280 mμ (S band), and a larger structureless band with maximum at 333 mμ (P band). Relative intensities of S band and P band are found to be independent of molecular weight of polystyrene (10,500-570,000) and concentration (0.3-30 g/l.), and dependent on the kind of solvent (cyclohexane, p-dioxane and 1,2-dichloroethane). P band is more effectively quenched by dissolved oxygen than S band.

From these results, together with those obtained on related compounds, it is concluded than an electronically excited segment of polystyrene interacts with an unexcited segment to form an excited associate, or an "excimer," and that the emission from these excimers is responsible for fluorescence of solid polystyrene and P band fluorescence of the solution, S band fluorescence being the emission from unassociated segments. In solution, it appears that the excited segment forms an excimer with its first- or second-neighbor segment, depending on local segmental configuration. In solid polystyrene, however, excimer formation appears to occur regardless of whether the interacting segments belong to the same or different molecules.

---

*To be published in Dissertation Abstracts 25 (3) (1964).

In Part II, luminescence quenching in plastic scintillators was studied on two plastic systems: 1) polystyrene + 9,10-diphenylanthracene + quencher, and 2) polystyrene + quencher. In the latter system, residual styrene monomer was treated as the fluorescent solute. The quenchers used were: p-dichlorobenzene, p-dibromobenzene, hexachlorobenzene, 1,2,3,4,5,6-hexachlorocyclohexane, 2-chloronaphthalene and 2-bromonaphthalene. For these samples, absorption and fluorescence spectra, light output under ultraviolet and beta ray excitation, and fluorescence decay times under pulsed electron excitation, were measured.

The solvent and solute quenching constants, α and β, respectively, are determined from the experimental data. Also, these constants are calculated theoretically from the optical data of individual components of the samples, making use of Förster's theory of electric dipole-dipole energy transfer. Calculations of α are made for two cases: "Case S" - energy transfer occurs directly from the excited segment to fluor or to quencher; "Case P" - energy transfer occurs from the excimer to fluor or to quencher.

Experimental values of α for uv excitation agree well with theoretical values calculated for Case S, supporting Case S transfer by dipole-dipole interaction as a means of energy transfer. This is further interpreted as an indication of efficient energy migration through the polystyrene medium.

Luminescence quenching under beta-ray excitation was generally greater than under uv excitation. In particular, in sample series containing hexachlorocyclohexane, no quenching was observed under uv excitation, while under beta-ray excitation the decrease in luminescence output was as large as 50%. It is suggested that this phenomenon may result from occurrence of energy transfer at higher excited states of polystyrene.

Observed solute quenching in some series of polystyrene + 9,10-diphenylanthracene + quencher is not accounted for by usual mechanisms of quenching. Such quenching can be explained qualitatively by assuming the energy transfer from the singlet excited state of 9,10-diphenylanthracene to the triplet state of the quencher.

INTRAMOLECULAR EXCIMER-FORMATION IN DIPHENYL- AND TRIPHENYL-ALKANES

Fumio Hirayama

Introduction

Fluorescence from a transient dimer, or an "excimer," formed by the association of an electronically excited molecule and an unexcited molecule has been observed for a number of polycyclic hydrocarbons, e.g., pyrene, 1,2-benzanthracene, naphthalene, in liquid solution.(1-6) Typical characteristics of the excimer emission are as follows: 1) its spectrum is a broad structureless band appearing about 6000 cm^{-1} to the red of the emission band of monomolecular species; 2) the half-width of the excimer band is 15-20% of the frequency of the intensity maximum; 3) on going from dilute to concentrated solutions, the intensity of the excimer band increases, whereas that of the monomer band decreases; 4) the monomer and excimer bands are quenched to a different degree by dissolved oxygen; 5) the appearance of the excimer band is not accompanied by any change in the absorption spectrum.

In Reference 7, the author reported that the fluorescence spectrum of polystyrene in solution consists of two bands which exhibit the characteristics of monomer and excimer bands as stated above, except that relative intensities of the two bands are independent of the polystyrene concentration. This fact led the author to conclude that excimer formation in polystyrene occurs intramolecularly by the association of excited and unexcited phenyl groups. The present investigation is aimed at obtaining more insight into the mechanism of intramolecular excimer formation by studying the fluorescence spectra of a variety of diphenyl- and triphenyl-alkanes in liquid solution. The results indicate that intramolecular excimers can be formed in these compounds only when some favorable steric condition is satisfied.

Experimental Procedures

Diphenyl- and triphenyl-alkanes used in the present study are listed in Table 5. Fluorescence spectra were recorded on a Beckman DK-2 spectrophotometer under front surface excitation by uv radiation. The 2537 A radiation from a high-pressure mercury lamp (Hanovia S-100) was isolated by means of a Bausch and Lomb grating monochromator and was focused onto the surface of the sample solution at nearly normal incidence. The fluorescence emitted from the exciting side of the sample was viewed by a condensing mirror, and was reflected into the entrance slit of the spectrophotometer. The recorded spectral curves were corrected for the spectral response of the spectrophotometer so that the corrected spectra give the relative number of photons emitted as a function of wave number.

Table 5

Fluorescence characteristics of diphenyl- and triphenyl-alkanes in 0.01Mϕ solutions

	Compound*	Excimer emission	λ_{max}, mμ	Relative fluorescence yield, F**	
				In cyclohexane $N_2\left(\frac{Air}{N_2}, \frac{O_2}{N_2}\right)$	In p-dioxane $N_2\left(\frac{Air}{N_2}, \frac{O_2}{N_2}\right)$
I-1	Toluene	No	282	100(.3, .1)	80(.6, .2)
I-2	Ethylbenzene	No	282	100(.4, .1)	80(.6, .2)
		Diphenylalkanes			
II-1	ϕ-C-ϕ	No	284	105(.4, .1)	
II-2	ϕ-C-C-ϕ	No	282	105(.4, .1)	
II-3	ϕ-C-C-C-ϕ	Yes	S 282 D 333	4.0(.8, .5) 9.8(.4, .1)	5.9(.9, .5) 9.0(.6, .2)
II-4	ϕ-C-C-C-C-ϕ	No	284	100(.4, .1)	
II-5	ϕ-C-C-C-C-C-ϕ	No	282	110(.4, .1)	
II-6	ϕ-C-C-C-C-C-C-ϕ	No	282	110(.4, .1)	
II-3a	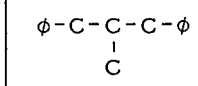	Yes	S 282 D 334	4.7(.8, .5) 10.0(.4, .1)	
II-3b	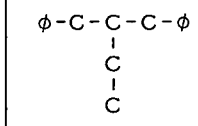	Yes	S 282 D 334	3.9(.7, .4) 11.8(.4, .1)	
II-3c	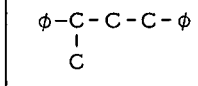	Yes	S 282 D 331	5.4(.7, .4) 9.8(.3, .1)	
II-3d	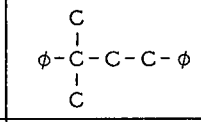	Yes	S 282 D 333	1.9(.8, .5) 8.4(.4, .1)	
		Triphenylalkanes			
III-1	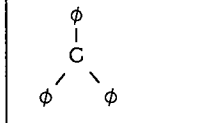	No	282	~100(.4, -)†	
III-2	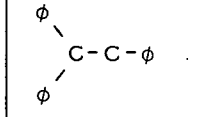	No	282	-†	
III-3	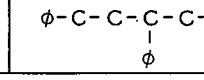	Yes	S 282 D 333	2.7(.8, .5) 10.0(.4, .1)	4.4(.8, .4) 8.7(.6, .2)

*ϕ indicates a phenyl group.

**The relative yield of ethylbenzene in cyclohexane is taken as 100 for convenience.

†Intensities of III-1 and III-2 decrease rapidly with time during the measurement due to some photochemical reaction. In the case of III-2, a structured band appears in 370 mμ region which increases with time.

The sample solutions in cyclohexane or in p-dioxane were contained in a cylindrical quartz cell, 2.2 cm in diameter and 1 cm long, and were measured under aerated, nitrogenated, and oxygenated conditions, the latter two achieved by bubbling a fine flow of the gas through the solution.

Results

Figure 13 shows the fluorescence spectra of nitrogenated solutions of toluene, ethylbenzene, diphenylalkanes II-1 through II-6, and 1,3,5-triphenylpentane (III-3) at a 0.01M concentration of the benzene ring unit (hereafter called 0.01Mϕ). One readily observes that while the spectral distribution and intensities of the diphenylalkanes, except for II-3, are essentially the same as those of toluene or ethylbenzene, the spectrum of II-3 is entirely different. The fluorescence intensity of II-3 is smaller by one order of magnitude than that of ethylbenzene, and the spectrum consists of two bands appearing in 280 mμ and 330 mμ regions. We shall call the two bands an S band (segmer band) and a D band (dimer band), respectively. The spectrum of III-3 is very similar to that of II-3, except for the smaller intensity of the S band.

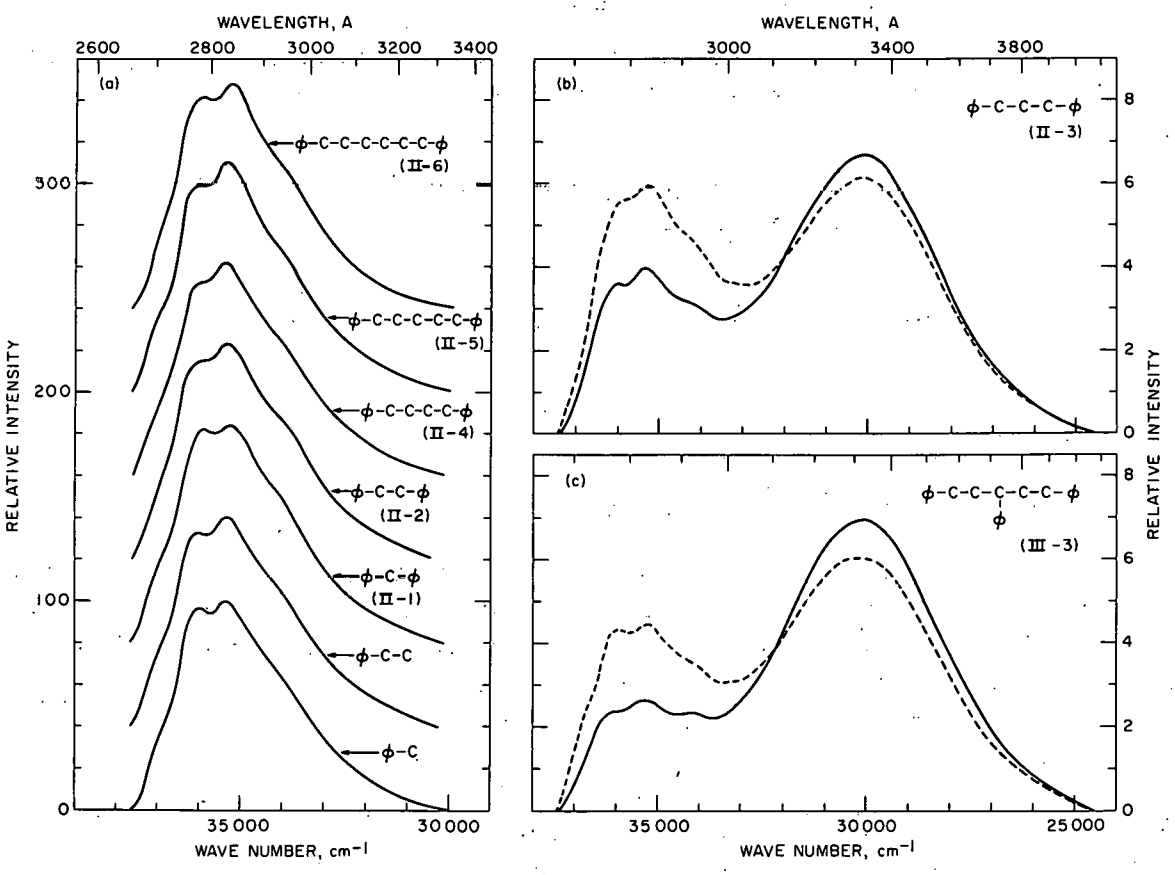

Figure 13

Fluorescence spectra of toluene, ethylbenzene, diphenylalkanes II-1 through II-6, and 1,3,5-triphenylpentane in 0.01Mϕ nitrogenated solutions: (——) in cyclohexane; (– – –) in p-dioxane. The curves in Figure 13a have been displaced upward on the ordinate axis by 40 unit increments from the curve immediately below.

Fluorescence characteristics of all the compounds studied are summarized in Table 5, in which are given the band maxima λ_{max}, the relative intensities F of nitrogenated solutions, and the factors by which the intensity decreases by aeration and by oxygenation. From Table 5 and Figure 13, and from the results of measurements for the concentration range 0.001Mϕ-1Mϕ, the following characteristics are found:

(A) The D bands appear in the spectra of only those compounds in which two phenyl groups are separated by the main chain consisting of three carbon atoms.

(B) No D bands are observed, even in 1Mϕ solutions, for the remainder of the compounds which do not satisfy the condition in (A).

(C) If the D band is assumed to have a symmetrical shape on the wave number scale, then the S band has the same spectral distribution as that of ethylbenzene fluorescence. The D band is a structureless band which appears about 5,500 cm^{-1} to the red of the S band, its half-width being about 15% of the frequency of the intensity maximum.

(D) On going from dilute to concentrated solutions, the intensity ratio of the S and D bands decreases somewhat but does not change drastically.

(E) The dissolved oxygen quenches the D band much more effectively than the S band.

(F) The absorption spectra of compounds II-3, II-3a through II-3d, and III-3 are almost exactly the same as that of ethylbenzene.

Interpretation

Intramolecular Excimer Formation

Characteristics (C) and (F) cited above immediately suggest that the D band is indeed an emission from the excimer formed by excited and unexcited phenyl groups. Moreover, from characteristics (B) and (D), one may reasonably assume that these excimers are formed intramolecularly by two phenyl groups belonging to the same molecule.

We shall first be concerned with the fact that intramolecular excimer formation in diphenyl end-substituted alkanes $\phi(CH_2)_n\phi$ occurs only when n = 3 (hereafter called "n = 3 rule") and shall seek the explanation for this on the basis of the spatial configuration of these molecules. Let us assume a sandwich-type configuration of excimer, the two benzene rings lying parallel face to face.[8-11] Without deformation of tetrahedral bond angles of

the alkane chains, such a parallel arrangement is impossible for n = 1 and 2. For n = 3, the parallel configuration can be obtained with a trans form of the propane chain, if the two benzene rings can approach the mutual distance R = 2.54 A. Since the thickness of the π-orbital of a benzene ring is 3.2 A, the two electron clouds must overlap in this case. For n = 4,5, and 6, it can be seen by examination of a scale model that the minimum values of R for the parallel arrangement are approximately 3.7 A, 3.4 A, and 3.7 A, respectively. In these configurations, the alkane chains are in eclipsed form for n = 5, and halfway between eclipsed and staggered forms for n = 4 and 6; in all cases some of nonbonded hydrogen atoms are in contact with, or very close to, each other. As far as the alkane chains themselves are concerned, these configurations are quite unstable ones.[12]

Postponing any inquiry into the stable configurations of these diphenylalkanes, the simplest explanation for the "n = 3 rule" would be to assume the excimer configuration to be a parallel sandwich type with a certain degree of overlapping of the two π-orbitals; formation of such a type of excimer is possible only when n = 3.

Assuming the above model of intramolecular excimer to be correct, a question immediately arises whether excimer formation in II-3 occurs as a result of this molecule being in such a parallel arrangement in its electronic ground state. That such is not the case can be shown by the following considerations: First, Cram, Allinger and Steinberg[13] found that paracyclophanes, in which two benzene rings are bridged by $(CH_2)_m$ and $(CH_2)_n$ groups, show an abnormal, long wavelength absorption when $m \leq 3$ and $n \leq 4$. This absorption has been interpreted as being due mainly to the transannular resonance effect between the two benzene rings which are held face to face. The absorption spectrum of II-3 does not show such an abnormal band. Second, the fluorescence spectrum of EPA* solution of II-3 measured at liquid nitrogen temperature is found to be almost exactly the same as that of ethylbenzene, both in spectral distribution and in intensity, indicating that no excimers are formed in the rigid matrix of the EPA solvent. These two facts conflict with the idea of the ground state association of the two phenyl groups. It, therefore, seems reasonable to assume that the stable configuration of II-3 is such that the two phenyl groups are located rather far from each other, and that, due to the freedom of motion of the two phenyl groups, they approach the range of interaction during the lifetime of the excited one to form an excimer.

Kinetic Considerations

The kinetic sequence of intramolecular excimer formation may be represented by the following reaction scheme:

*5,5,2 parts by volume of ethyl ether, isopentane, and ethanol.

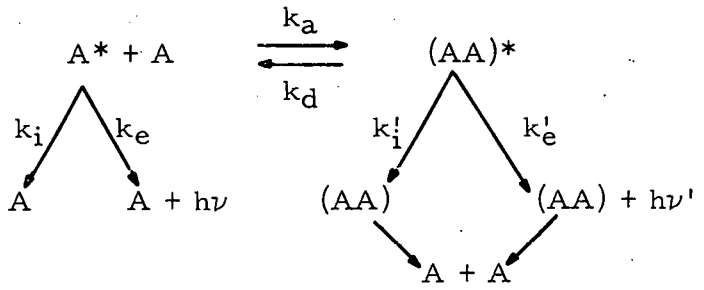

Here A* and (AA)* represent the excited phenyl segment and the excimer, and k_a, etc., are the respective rate constants. ν and ν' are the frequencies of the S band and the D band, respectively. We shall assume, for the time being, that regeneration of A* from dissociation of (AA)* is negligible at room temperature. Then the intensities of the S and D bands, F_S and F_D, are expressed by:

$$F_S = C(1 - \Phi)\eta, \tag{1}$$

$$F_D = C\,\Phi\eta', \tag{2}$$

where

$$\eta = k_e/(k_e + k_i), \tag{3}$$

$$\eta' = k_e'/(k_e' + k_i'), \tag{4}$$

$$\Phi = k_a/(k_e + k_i + k_a). \tag{5}$$

η and η' are fluorescence quantum yields of A* and (AA)*, respectively, and Φ is the quantum efficiency of excimer formation. C is a constant determined by experimental conditions.

Let us evaluate the parameters in the above equations, for example those for 0.01Mϕ solutions of II-3. From the fact that the fluorescence yields of compounds II-1 through II-6, except for II-3, are approximately the same as that of ethylbenzene (see Figure 13), one may reasonably assume that the quantum yield η of A* in the absence of the excimer-formation process is about the same as that of ethylbenzene in the same solvent. Then, employing the intensity unit given in Table 5, values of $C\eta$ in Equation 1 are 100 in cyclohexane and 80 in p-dioxane. The observed values of F_S are 4 in cyclohexane and 6 in p-dioxane, giving the values Φ = 0.96 and 0.93, respectively. If one assumes that the quantum yield η' of (AA)* is about the same in the two solvents, Equation 2 predicts nearly the same values of F_D in the two solvents; in agreement with the observed results.

The values of k_e as determined from the extinction coefficient integrated over the first absorption band of ethylbenzene is 6.9×10^6 sec^{-1}.(7)

The measured decay time of ethylbenzene fluorescence, which should be the reciprocal of $(k_e + k_i)$, is 27 nsec in cyclohexane.[7] Thus, $k_e + k_i = 3.7 \times 10^7$ sec^{-1} and $\eta = 0.19$ in cyclohexane. In p-dioxane, $\eta = 0.15$ and thus $k_e + k_i = 4.6 \times 10^7$ sec^{-1}. Putting the above values of parameters into Equation 5, we obtain the values: $k_a \sim 9 \times 10^8$ sec^{-1} in cyclohexane; $k_a \sim 6 \times 10^8$ sec^{-1} in p-dioxane.

According to the above kinetics, the rate constant for excimer formation in II-3 is one and a half times larger in cyclohexane than in p-dioxane. This may be qualitatively explained by the following considerations. Cyclohexane is a poor solvent for polystyrene, while p-dioxane is a good solvent.[14,15] This means that the frequency of contact between a pair of phenyl groups in a polystyrene molecule is larger in cyclohexane than in p-dioxane because of the difference in the segment-solvent interaction force.[14] Since compound II-3 can be regarded as two consecutive segment units in a polystyrene chain, we may suppose that the frequency of contact between the two phenyl groups in II-3 is also influenced by the same solvent effect.* This will result in the higher rate of excimer formation in cyclohexane than in p-dioxane.

Next, we shall consider the fact that F_S of III-3 is about 30% smaller than that of II-3, while the values of F_D of the two compounds are almost the same, both in cyclohexane and in p-dioxane (Table 5). These results are compatible with the higher value of k_a for III-3 than for II-3, and can be explained by the assumption that because of the presence of the extra phenyl group, the equilibrium positions and the motion of neighboring phenyl groups in III-3 are different enough from those in II-3 to result in more frequent contact of phenyl groups in III-3. The different values of F_S and the almost identical values of F_D among the group of compounds II-3a through II-3d (Table 5) can also be explained in a similar manner. That is, the attachment of a methyl or ethyl group to a different carbon atom in the main propane chain causes the difference in the equilibrium positions of the two phenyl groups in these compounds, which leads to a different rate constant for excimer formation.

Discussion thus far has been based on the kinetics in which we assumed that dissociation of (AA)* to produce A* is a negligible process and that the S band is the emission from an originally excited A* which is left unassociated. (This will be called Kinetics I.) A quite different kinetics, which we shall call Kinetics II, may also be proposed for the explanation of the observed results. In Kinetics II, we assume that 1) intramolecular excimer formation occurs with an efficiency very close to 100% so that the

*According to the theory of polymer configuration in solution,[14] it is generally accepted that this kind of solvent effect is operative mostly for two segments which are far apart along the polymer chain but happen to approach each other owing to polymer coiling. However, there is no reason to believe that the phenyl groups neighboring along the polystyrene chain would not be influenced by the same solvent effect.

emission from the originally excited A* becomes negligibly small, and 2) the observed S band is due entirely to the emission from A* which is regenerated by dissociation of (AA)*.

It would be reasonable to assume that the rate constant k_d for such a dissociation process is dependent on, among other things, the torsional force which tends to pull apart the associated phenyl groups. The strength of this force will depend on the relative spatial positions of the phenyl groups in the equilibrium configurations of the diphenyl- and triphenylalkanes. Thus, the above-mentioned variation in the S band intensities may be attributed to the difference in this torsional force which may depend on the kind of compound and also on the kind of solvent. Since dissociation of only 2-6% of excimers is needed to produce the observed intensities of the S band, Kinetics II is consistent with the result that the D band intensity remains nearly constant, although the S band intensity varies.

However, there is one objection to Kinetics II. This is that the S band is quenched by dissolved oxygen to a much smaller degree than the D band is (see Table 5). By Kinetics II, we would expect the degree of the S band quenching to be greater than that of the D band. If collision between an excimer and an oxygen molecule leads to the enhancement of excimer dissociation in some manner, this small quenching might be expected. However, there has been no experimental evidence supporting such an idea. On the other hand, the small oxygen quenching of the S band is expected by Kinetics I, since the lifetime of the originally excited A* will become quite short because of efficient excimer formation so that collisional deactivation of A* by oxygen will not be very effective. Thus, Kinetics I appears more plausible than Kinetics II in this respect. A more direct way of choosing between Kinetics I and II would be to measure the decay time of the S band emission. From Kinetics I it is predicted that the decay time will be of the order 10^{-10}-10^{-9} sec, while from Kinetics II it is expected to be about 2×10^{-8} sec. (This latter value is the decay time of polystyrene fluorescence in solution.[7]) This phase of the investigation is left for some future study.

The author wishes to thank Dr. I. B. Berlman and Dr. M. Inokuti for stimulating discussions. He is indebted to Professor H. Pines of Northwestern University for furnishing compounds II-3, II-4, II-3a through II-3d, and III-3, and to Mr. A. J. Streiff of the Carnegie Institute of Technology for supplying compounds II-5 and II-6.

References

1. Th. Förster and K. Kasper. Z. Elektrochem. 59, 976 (1955).

2. I. B. Berlman. J. Chem. Phys. 34, 1083 (1961).

3. I. B. Berlman and A. Weinreb. Mol. Phys. 5, 313 (1962).

4. E. Döller and Th. Förster. Z. Physik. Chem. (Frankfurt) 31, 274 (1962).

5. J. B. Birks and L. G. Christophorou. Nature 194, 442 (1962); 196, 33 (1962); 197, 1064 (1963); Spectrochimica Acta 19, 401 (1963).

6. T. V. Ivanova, G. A. Mokeeva, and B. Ya. Sveshnikov. Opt. Spectry. (USSR) (English Transl.) 12, 325 (1962).

7. F. Hirayama. Thesis, Energy Transfer and Quenching in Plastic Scintillators. University of Michigan, 1963.

8. G. J. Hoijtink. Z. Elektrochem. 64, 156 (1960).

9. Th. Förster. Molecular Spectroscopy. Butterworths, London, 1962. p. 121.

10. J. N. Murrell and J. Tanaka. Mol. Phys. 7, 363 (1963-64).

11. T. Azumi and S. P. McGlynn. J. Chem. Phys. 41, 3131 (1964).

12. S. Mizushima. Structure of Molecules and Internal Rotation. Academic Press, Inc., New York, 1954.

13. D. J. Cram, N. L. Allinger, and H. Steinberg. J. Am. Chem. Soc. 76, 6132 (1954).

14. P. J. Flory. Principles of Polymer Chemistry. Cornell University Press, Ithaca, New York, 1953. Ch. XIV.

15. L. H. Cragg, T. E. Dumitru, and J. E. Simkins. J. Am. Chem. Soc. 74, 1977 (1952).

he Ar

INELASTIC COLLISION CROSS SECTIONS OF NEON AND ARGON FROM MEASUREMENTS OF ELECTRON DRIFT VELOCITY*

Joseph C. Bowe

Abstract

The cross section of excitation of neon and argon by electron impact is assumed to be given by $Q_1(u) = h(u - u_1)^{\gamma}$, where u_1 is the excitation energy. Formulas for drift velocity and overshoot, derived in a previous paper, are used with the experimental mobility data to evaluate the constant h for each gas for values of $\gamma = 0$, $1/2$, and $3/2$. For argon at 12 eV, the cross sections found by this procedure lie in the range 0.6 to 7.6 x 10^{-17} cm^2 compared to Maier-Leibnitz's value of 0.9 x 10^{-17} cm^2 and in neon at 16.9 eV the values are in the range from 1.0 to 1.6 x 10^{-19} cm^2 compared to Maier-Leibnitz's value of 5.6 x 10^{-18} cm^2. These values are, however, tentative and preliminary pending the outcome of further work.

Introduction

If the cross sections for all the interactions between electrons and molecules of a gas were known as functions of energy, it would then be possible to state in detail precisely how the energy of a primary electron is dissipated when it passes through a gas. That is, it would be possible to specify the number of ions produced, the charge states of the ions, the number of excited molecules and identification of their states, the prompt radiation induced by the primary electron, etc. In addition, it would also be possible, at least in principle, to compute various properties of a swarm of electrons that drift through a gas. That is, such quantities as the electron drift velocity, diffusion, average energy of the swarm, etc., could be computed. All the cross sections, however, are not known. Hence, the immediate goal of this work is to solve the inverse problem, namely, the evaluation of cross sections from measurements on swarms. In essence the problem consists of solving appropriate integral equations, wherein the numerical values of the integrals are experimentally determined and the unknown cross sections are contained under the integral sign.

---

*A brief report of this work was presented at the Sixteenth Annual Gaseous Electronics Conference, Pittsburgh, Pennsylvania, October 16-18, 1963.

Ultimately, the cross sections should be derived from beam experiments which detect single collisions between monoenergetic electrons and molecules. It is anticipated that these experiments will in the future yield the differential scattering cross section for all energies and angles of scattering. At the present time, however, absolute values for the cross sections are obtained from beam experiments that are performed with energies of the order of electron volts. The energy range below a few tenths eV is outside the reach of beam experiments. The energy region below 1 eV is of interest, not only in regard to knowing the cross sections for elastic collisions, but also because rotational and vibrational excitations are significant energy-loss processes for slow electrons. The threshold energies for the lowest of each of these excited states are usually less than 0.1 eV and 1.0 eV, respectively. The extremely low-energy region is currently being explored by means of electron swarm experiments at Westinghouse Laboratories.

Swarm measurements, in addition to extending the information about cross sections derived from beam measurements to lower energy, have also revealed inelastic processes that were not previously observed. Of no less importance is the fact that analysis of swarm experiments yields absolute values for the cross sections.

The sensitivity of beam measurements in many instances is also vanishingly small immediately above the threshold energy of an inelastic process, even though the energy itself is not low. A case in point is the excitation near threshold of the first excited states of the noble gas atoms. The only measurement of these cross sections for helium, neon, and argon was obtained by the remarkable experiment and analysis of Maier-Leibnitz[1] who measured the energy distribution of a swarm of electrons that diffused through a gas at low pressure. From the kinks in the retarding-potential curves, he was able not only to resolve the excitation functions for helium and neon, but also to deduce an absolute value for the cross sections for these transitions. He estimates that the total cross sections are in error by not more than 50%. To the resolved cross sections, he assigns an uncertainty factor of two. It is desirable that these measurements be checked in a different, independent experiment.

Schulz,[2] by means of a beam experiment, measured the excitation function for the lowest levels in helium but was unable to calibrate his instrument to assign an unambiguous value to the cross section.

Engelhardt and Phelps,[3] in a recent study of swarm data of argon, used Maier-Leibnitz's curves for the inelastic cross section and adjusted the values of the cross section for elastic scattering to obtain agreement between the measured and computed transport coefficients.

This report presents the preliminary results of an attempt to make an independent determination of the cross section for inelastic collisions near the threshold energies for neon and argon from the author's measurements of electron drift velocity in these gases.[4] The value of the inelastic cross section for neon at a few tenths eV above threshold is found by this work to be 35 to 55 times smaller than Maier-Leibnitz's value. For argon at 12 eV, the values reported here range from 0.6 to 7.6×10^{-17} cm^2. These can be compared with Maier-Leibnitz's value which is 10^{-17} cm^2.

This report also illustrates the method by which these cross sections are determined. More precise measurements of drift velocity over a larger range of values of E/p and a more refined analysis of the data are currently being undertaken to determine if, by this method, a better evaluation of the cross section can be made.

Method

Each of the drift velocity curves shown in Figure 14 has a sharp break which is ascribed to inelastic collisions. The sudden change in the slope of these curves can be understood if it is assumed that inelastic collisions effectively cut off the energy distribution function at an energy u_0 that is greater than the excitation energy u_1. That is, the effect of inelastic collisions can be interpreted in terms of an energy barrier at u_0 which is not penetrated by electrons in the swarm. This cut-off energy u_0 is intuitively expected to increase as the applied field-to-pressure ratio, E/p, is increased.

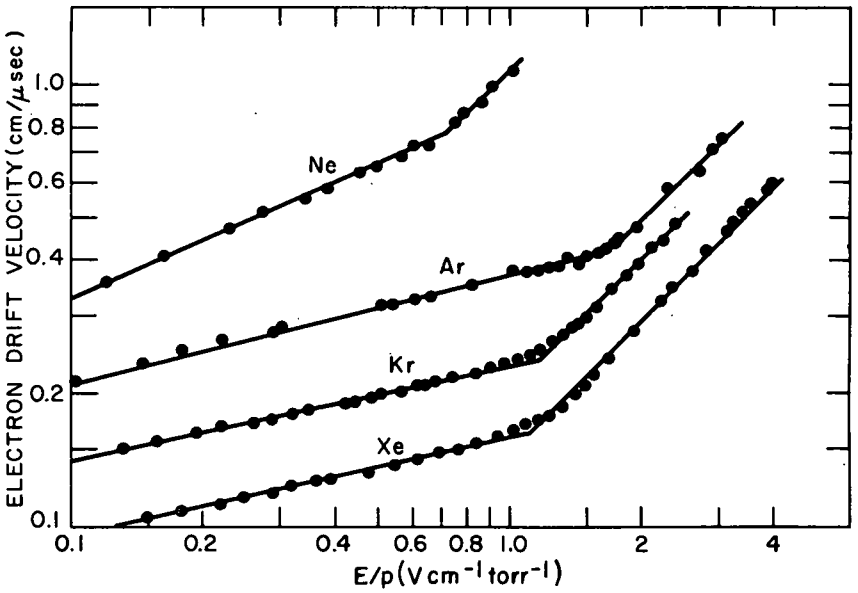

Figure 14

Experimental drift-velocity curves plotted on a log-log graph

A formula[5] for drift velocity, which takes inelastic collisions into account, is derived in closed form by following the procedures used by Allis and Brown[6] in which integrations are performed only over the low-energy ($u < u_1$) distribution function. Omission of integrations over the high-energy ($u > u_1$) distribution is accounted for by setting the low-energy function equal to zero at an appropriate energy u_0 that is greater than the excitation energy u_1. The drift velocity v_d is expressed in terms of E/p and the collision frequency, and depends implicitly upon w_0, which is the exponent of the generalized Druyvesteyn function evaluated at the cut-off energy u_0 for each value of E/p. The formula, which applies for values of E/p greater than the critical value $(E/p)^*$ at which the drift-velocity curve breaks, is given by

$$v_d(E/p, w_0) = \frac{1}{6} \frac{e}{300\ m} \frac{1}{\nu_m(v_0)} \frac{S_j(w_0)}{S_{j+1}(w_0)} \frac{E}{p}, \tag{1}$$

where $\nu_m(v_0)$, the collision frequency of electrons having the cut-off energy u_0, and E/p (in $V\ cm^{-1}\ torr^{-1}$) are referred to 0°C. The S_j are infinite series, e/m is the ratio of electron change to mass, and

$$w(E/p, u) = \frac{3M}{2m(j+1)} \left[\frac{2mu}{M} \frac{p}{eE} N_0 Q_m(u) \right]^2 \tag{2}$$

where M is the mass of the gas atom and N_0 is the number of atoms per cm^3. Values for j are determined by the effective cross section for momentum transfer, which is represented by the power function $N_0 Q_m(v) = a v^{j-1}$ (in cm^{-1}).

Notice that the quantity in the bracket of Equation 2 is the ratio of the energy that an electron loses in elastic recoil to the energy that it gains from the electric field between elastic collisions. Thus, the value of w is unity for those electrons of energy u for which the energy gain is $[3M/2m(j+1)]^{1/2}$ times the energy loss.

Equation 2 also shows that at a <u>fixed</u> value of E/p, the low energy electrons (i.e., those that have small values of w) gain much more energy from the field than they lose by elastic collisions. Allis and Brown[6] show that w has a simple interpretation when the collision frequency is independent of energy; i.e., when $j = 0$, w is 3/2 the ratio of the elastic-recoil energy loss $(2m/M)u$ to the <u>average</u> energy $(eE)^2/2m\nu^2$ that an electron gains from the field between collisions.

The values of w extend from zero to infinity when inelastic collisions do not occur [i.e., when $E/p < (E/p)^*$] and the <u>average</u> value, which is readily computed for this case, is $3/(2j+2)$. Comparison of this <u>average</u> value with the magnitudes obtained for the <u>maximum</u> values of w at each E/p (Figure 15) gives an indication of the extent of inelastic

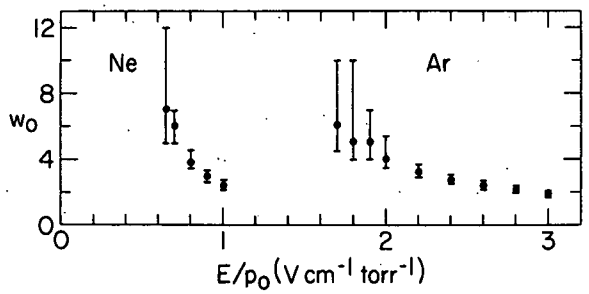

Figure 15

Evaluation of the dimensionless variable w_0 for neon and argon. The limits on each point correspond to an uncertainty of ±5% in the slope of the drift-velocity curve.

collisions. Thus, for the relatively small magnitudes of $w_0 = w(E/p, u_0)$, it is evident that energy balance can be maintained only if the elastic collisions are supplemented by another energy-loss mechanism, namely inelastic collisions.

The cut-off energy u_0 is calculated by the following procedure. First insert the experimental values of pv_d/E into Equation 1 and solve for $\nu_m^{-1} S_j/S_{j+1}$. Next, for each value of E/p, find that value of w_0 for which the computed value of $[\nu_m(E/p, w_0)]^{-1}[S_j(w_0)/S_{j\pm1}(w_0)]$ agrees with the value in the first step. Then, by using these values of w_0 (see Figure 15), compute u_0 from Equation 2 in which $N_0Q_m(u)$ is evaluated at u_0. The values of overshoot $(u_0 - u_1)$ obtained by this procedure are plotted in Figure 16. For the larger values of E/p an extrapolation, in which the mobility is assumed to remain constant is used. The values of the series S_j and S_{j+1} are given in Table 6, and the ratio is plotted in Figure 17; the appropriate value of the collision frequency, defined as $\nu_m = v_0N_0Q_m(u_0)$, is derived from curves (not shown) in which $\nu_m(E/p, w_0)$ is plotted against w_0 on log-log graph paper for a number of pertinent values of E/p.

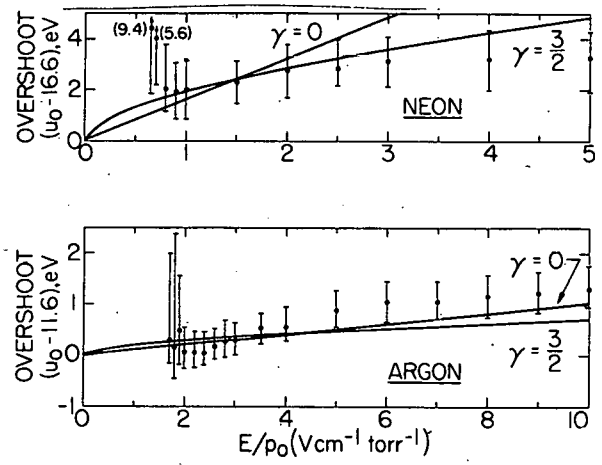

Figure 16

The cut-off energy u_0 is obtained for each value of E/p by inserting the experimental value of $v_d(E/p)^{-1}$ into Equation 1 which then determines $w_0(u_0, E/p)$. The curves represent the best fit of $(u_0 - u_1) = \beta(E/p)^{2/(\gamma+2)}$ to the points contained in the intervals $0.8 \leq E/p \leq 2.0$ V cm^{-1} torr^{-1} for neon, and $2 \leq E/p \leq 5$ V cm^{-1} torr^{-1} for argon.

Table 6

Values of the infinite series contained in Equation 1*

Neon			Argon		
w_0	$(S_1 - 1)$	$(S_2 - 1/9)$	w_0	S_3	S_4
0.2	4.66680×10^{-2}	5.70423×10^{-3}	0.1	1.02057×10^{0}	6.85811×10^{-2}
0.4	9.81704×10^{-2}	1.19762×10^{-2}	0.2	1.04233×10^{0}	7.05993×10^{-2}
0.6	1.55151×10^{-1}	1.88883×10^{-2}	0.3	1.06537×10^{0}	7.27283×10^{-2}
0.8	2.18357×10^{-1}	2.65236×10^{-2}	0.4	1.08978×10^{0}	7.49754×10^{-2}
1	2.88642×10^{-1}	3.49772×10^{-2}	0.5	1.11566×10^{0}	7.73488×10^{-2}
2	7.86915×10^{-1}	9.39792×10^{-2}	0.6	1.14312×10^{0}	7.98572×10^{-2}
3	1.70065×10^{0}	1.99267×10^{-1}	0.7	1.17228×10^{0}	8.25098×10^{-2}
4	3.46998×10^{0}	3.97207×10^{-1}	0.8	1.20327×10^{0}	8.53168×10^{-2}
5	7.06048×10^{0}	7.86939×10^{-1}	0.9	1.23622×10^{0}	8.82890×10^{-2}
6	1.46368×10^{1}	1.58537×10^{0}	1	1.27129×10^{0}	9.14379×10^{-2}
7	3.11433×10^{1}	3.27662×10^{0}	2	1.78137×10^{0}	1.35968×10^{-1}
8	6.80530×10^{1}	6.95982×10^{0}	3	2.80349×10^{0}	2.20779×10^{-1}
9	1.52354×10^{2}	1.51680×10^{1}	4	4.96200×10^{0}	3.90699×10^{-1}
10	3.48272×10^{2}	3.38140×10^{1}	5	9.71369×10^{0}	7.45985×10^{-1}
12	1.91262×10^{3}	1.77581×10^{2}	6	2.05170×10^{1}	1.51539×10^{0}
14	1.10364×10^{4}	9.86147×10^{2}	7	4.57003×10^{1}	3.22977×10^{0}
16	6.59992×10^{4}	5.70392×10^{3}	8	1.05560×10^{2}	7.13898×10^{0}
18	4.05838×10^{5}	3.42229×10^{4}	9	2.50050×10^{2}	1.62221×10^{1}
20	2.59070×10^{6}	2.18789×10^{5}	10	6.03168×10^{2}	3.76553×10^{1}
25	9.24923×10^{8}	9.37498×10^{7}	15	5.76067×10^{4}	3.09167×10^{3}

*The integrals contained in Equations 17 and 19 of Reference 5 can be evaluated by using the following relations:

$$\int_0^{w_0} w^{-1/2} e^{-w} \int_0^{w_0} t^{-1} e^{t}\, dt dw = 4 w_0^{1/2}\, S_1(w_0)$$

$$\int_0^{w_0} w^{-1/4} e^{-w} \int_0^{w_0} t^{-1} e^{t}\, dt dw = 16 w_0^{3/4}\, S_2(w_0)$$

$$\int_0^{w_0} w^{-3/4} e^{w}\, dw = 4 w_0^{1/4}\, S_3(w_0)$$

$$\int_0^{w_0} w^{-5/8} e^{-w} \int_0^{w_0} t^{-3/4} e^{t}\, dt dw = 64 w_0^{5/8}\, S_4(w_0)$$

The infinite series were evaluated by an IBM-704 computer. Convergence was assumed when the value of the $(n+1)$ term was less than 10^{-5} of the sum of the preceding n terms.

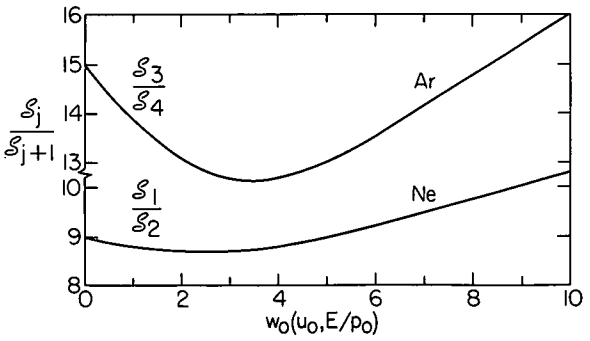

Figure 17

The ratio of series that appear in Equation 1 for drift velocity is plotted against the dimensionless variable w_0 which is the exponent of the generalized Druyvesteyn function evaluated at the cut-off energy

Figure 16 shows that the overshoot increases very slowly with E/p. It is, therefore, possible in a first approximation to assign to each gas, as Allen[7] did, a constant value of u_0 that is consistent with the drift-velocity curves. On the other hand, however, it is more appropriate to fit the points in Figure 16 to the theoretical expression for overshoot[5] that is given by

$$(u_0 - u_1) = \frac{1}{(\gamma+2)^{\gamma/(\gamma+2)}} \frac{\Gamma[1/(\gamma+2)]}{\Gamma[(\gamma+1)/(\gamma+2)]} \left[\frac{e^2E^2}{3N_0^2p^2hQ_m(u_1)}\right]^{1/(\gamma+2)} = \beta\left(\frac{E}{p}\right)^{2/(\gamma+2)} \quad (3)$$

when the cross section for inelastic collisions is $Q_1(u) = h(u - u_1)^\gamma$. In this way, harmony is achieved not only with the drift-velocity data, but also with Equation 3 which does not allow the overshoot to be independent of E/p. The curves in Figure 16 are least-square fits of Equation 3 to those points that lie only in the interval $0.8 \leq E/p \leq 2$ for neon, and $2 \leq E/p \leq 5$ for argon. The values of overshoot immediately above $(E/p)^*$ have a large uncertainty and, therefore, were not used for the curve-fitting computations.

The overshoot in Figure 16 is substantially constant for large values of E/p. This result can be understood as follows: the series S_j and S_{j+1} in Equation 1 approach a constant value as the magnitude of w_0 is decreased (i.e., for large values of E/p), and, therefore, the collision frequency must be clamped at a fixed value if v_d is to continue to increase linearly with E/p as it was assumed to do. A constant collision frequency could imply a constant cut-off speed v_0. Alternatively, if it is assumed that the cut-off energy cannot be rigidly clamped, it then follows that the drift-velocity curve must depart from linearity at higher values of E/p unless, of course, the collision frequency is energy independent; in that case, the linearity is preserved. To observe the departure from linearity when it is expected to occur might require extremely precise measurements of the drift velocity because the overshoot increases so slowly with E/p.

The small values for the overshoot in argon are consistent with the computations of Barbiere.[8] His computations show that there is little variation in the drift velocity when the distribution function is cut off at u_1 in contrast to when the inelastic cross section is assumed to have a constant value comparable to the one that we find (see computations, this paper).

Finally, the experimental value of $(E/p)^*$ offers additional information that can be used to evaluate the cross section for momentum transfer in an elastic collision. This cross section can be solved for if the formula for v_d at high values of E/p and the formula for low values of E/p are equated at the value $(E/p)^*$ at which the curve breaks.

Computations

For neon, the experimental value of the product of pressure and mobility is $v_d(E/p)^{-1} = 1.08 \pm 0.03$ cm^2 V^{-1} μsec^{-1}, where the assigned error is the maximum deviation obtained by drawing the various possible lines through the points of Figure 14. Inserting this value into Equation 1 leads to $[\nu_m(v_0)]^{-1}(S_3/S_4) = (3.7 \pm 0.1) \times 10^{-9}$ sec. When the drift-velocity formulas for high and low values of E/p are equated at $(E/p)^* = 0.65 \pm 0.02$ V cm^{-1} torr^{-1}, the cross section for momentum transfer is found to be $N_0Q_m = 9.86 \pm 0.22$ cm^{-1}. Previous analysis[9] of the drift-velocity data for neon at low E/p yielded $N_0Q_m(u) = 6.05\ u^{0.157}$ which when evaluated at 16.6 eV gives $N_0Q_m(u_1) = 9.4$ cm^{-1}. For the computations made in this paper, the cross section for neon is assumed to have a constant value of 9.6 cm^{-1}.

The quantity β is evaluated by fitting Equation 3 to the points that are contained in the interval $0.8 \leq E/p \leq 2$ in Figure 16. Once β is found, h follows directly. These constants are given in Table 7 and the cross sections are given in Figure 18.

Table 7

Values of the constants contained in the expressions for overshoot $(u_0 - u_1) = \beta(E/p)^{2/(\gamma+2)}$ and the inelastic cross section $Q_1(u) = h(u - u_1)^\gamma$. The value of β is in (torr^2 cm^2 eV$^\gamma$)$^{1/(\gamma+2)}$ and h is in cm^2 eV$^\gamma$

	Neon		Argon	
γ	β	h	β	h
0	1.71	1.67×10^{-19}	0.104	5.93×10^{-18}
1/2	1.76	2.60×10^{-19}	0.148	1.62×10^{-17}
1	1.87	1.87×10^{-19}	0.170	6.72×10^{-17}
3/2	1.94	1.94×10^{-19}	0.188	3.00×10^{-16}

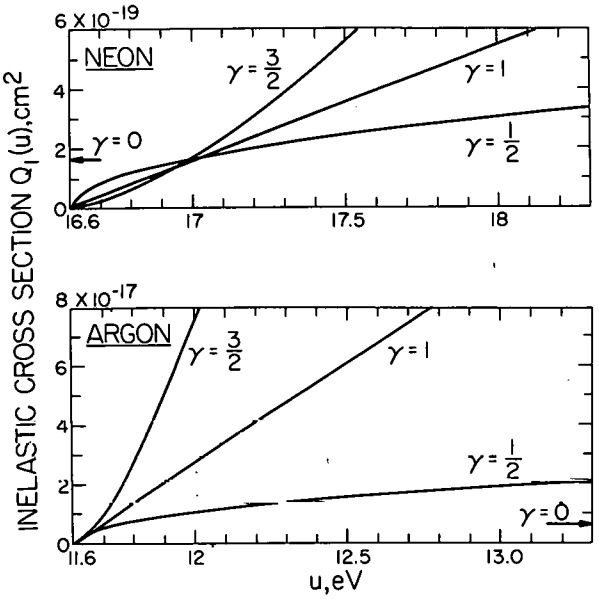

Figure 18

The cross section $Q_1(u) = h(u - u_1)^{\gamma}$ for inelastic collisions deduced from measurements of electron drift velocity

For argon, the experimental value of mobility is $v_d(E/p)^{-1} = 0.247 \pm 0.012$ cm^2 V^{-1} μsec^{-1}. From this it follows that $[\nu(v_0)]^{-1}(S_1/S_2) = (8.4 \pm 0.4) \times 10^{-10}$ sec. For $(E/p)^* = 1.7 \pm 0.1$ V cm^{-1} torr^{-1}, $\alpha = 6.4 \pm 0.1$ cm^{-1} eV^{-1}, where $N_0 Q_m(u) = \alpha u$. Previous analysis[9] of the drift-velocity data for low E/p yielded $\alpha = 6.3 \pm 0.6$ cm^{-1} eV^{-1}, which is in good agreement. The value 6.4 cm^{-1} eV^{-1} is used in the present computations.

Discussion

It is highly desirable to check the cross sections obtained by Maier-Leibnitz[1] by another method of measurement. The striking effect that inelastic collisions have upon the drift velocity of electrons in the noble gases appears to offer an opportunity to do this, especially since it is evidently easier to measure absolute values of the drift velocity than to measure the absolute value of the cross section near threshold by scattering monoenergetic electrons from a beam.

The inelastic cross sections reported here, however, must be considered tentative and preliminary, inasmuch as they represent the first attempt to determine these quantities from drift-velocity data. The fact that the drift-velocity curves break at a value of E/p that is consistent with elastic cross sections derived from the data for values of $E/p < (E/p)^*$ gives confidence that the drift velocity formulas and measurements are essentially correct. Nevertheless, further refinements in the computations and in the measurements of drift velocity should be attempted. In particular, it is hoped that the two arbitrary constants h and γ can be determined independently.

Finally, the approach used here differs from that used by Barbiere[8] and by Engelhardt and Phelps.[3] Whereas these authors compute the drift velocity for various assumed values of the cross sections, the present study computes the cross sections from the measured values of drift velocity. Thus, when they find that the computed values of drift velocity are insensitive to the value of the inelastic cross section, it does not necessarily follow that the cross sections are insensitive to the value of drift velocity. Evidently more precise measurement of the electron drift velocity is desirable.

I wish to thank Mr. B. S. Garbow of the Applied Mathematics Division, who evaluated the infinite series on the IBM-704 computer, and Messrs. R. K. Langs and A. F. Rodde, Jr.,* who carried out many of the desk-computations.

References

1. H. Maier-Leibnitz. Z. Physik 95, 499 (1936).

2. G. J. Schulz. Phys. Rev. 116, 1141 (1959).

3. A. G. Engelhardt and A. V. Phelps. Phys. Rev. 133, A 375 (1964).

4. J. C. Bowe. Phys. Rev. 117, 1411 (1960).

5. J. C. Bowe. Phys. Rev. 134, A 355 (1964).

6. W. P. Allis and S. C. Brown. Phys, Rev. 87, 419 (1952).

7. H. W. Allen. Phys. Rev. 52, 707 (1937).

8. D. Barbiere. Phys. Rev. 84, 653 (1951).

9. J. C. Bowe. Phys. Rev. 117, 1416 (1960).

*Summer Student Aide from St. Procopius College, 1963.

EFFECT OF INELASTIC COLLISIONS ON THE DRIFT VELOCITY OF ELECTRONS IN NOBLE GASES.*

Joseph C. Bowe

Abstract

The experimental curves for drift velocity v_d are linear functions of E/p when inelastic collisions occur. These data can be understood on the basis of a formula derived in the Allis-Brown[1] approximation: $v_d = (1/6)(e/m)[\nu_m(v_0)]^{-1}[S_j(w_0)/S_{j+1}(w_0)](E/p)$, where $w_0(E/p, u_0)$ is a dimensionless variable, u_0 is the cutoff energy that is greater than the excitation energy u_1, $\nu_m(v_0)$ is the collision frequency for momentum transfer, and (S_j/S_{j+1}) is a ratio of infinite series where j denotes the power law of the elastic cross section, i.e., $Q_m(v) \propto v^{j-1}$. An expression is also derived for the overshoot from which the cross section for inelastic collisions $Q_1(u) = h(u - u_1)^\gamma$ can be deduced, i.e., $(u_0 - u_1) = \{\Gamma[1/(\gamma+2)]/\Gamma[(\gamma+1)/(\gamma+2)]\}\{3(\gamma+2)^\gamma N_0^2 Q_m(u_1)h(eE/p)^{-2}\}^{-1/(\gamma+2)}$. Note that the correct overshoot of 0 and ∞ is obtained in the limiting cases where Q_1 (i.e., h) is ∞ and 0, respectively.

Reference

1. W. P. Allis and S. C. Brown. Phys. Rev. 87, 419 (1952).

*This abstract appeared in Bull. Am. Phys. Soc. 9, 186 (1964).

MOBILITY OF ELECTRONS IN THE NOBLE GASES*

Joseph C. Bowe

Abstract

This paper presents a theoretical study which leads to formulas that relate the cross section for inelastic collisions near the threshold energy to the drift velocity v_d of electrons in noble gases. Derivation of general formulas for v_d follows a qualitative interpretation of the main features of the experimental drift-velocity curves. The formulas for v_d are derived for the case in which the elastic cross section for momentum transfer is given by $N_0Q_m(v) = av^{j-1}$. Closed-form expressions for v_d are obtained by integrating only over the distribution function for electrons that have energy less than the excitation energy u_1. By this procedure, integration over the high-energy ($u > u_1$) distribution function is avoided and the use of analytical methods is made possible. A partial correction to this approximation is obtained by extending the low-energy ($u < u_1$) distribution function to pass through zero at an energy u_0 that is greater than u_1. From the drift-velocity formula and the experimental values of v_d, the cutoff energy u_0 can, in principle, be evaluated as a function of E/p. The high-energy distribution function is used to derive an expression for the overshoot $(u_0 - u_1)$ which is shown to be proportional to $(E/p)^{2/(\gamma+2)}$ and to depend upon the constants h and γ when the inelastic-collision cross section has the form $Q_1(u) = h(u - u_1)^{\gamma}$. Possible applications of these theoretical results to drift-velocity data for gas mixtures are also briefly discussed.

*Published in Phys. Rev. 134, A355 (1964).

ELECTRON VELOCITY DISTRIBUTION IN GASES*

Joseph C. Bowe

Abstract

An analytical expression for the velocity-distribution function for the low-energy region ($u < u_1$) is obtained from the Maxwell-Boltzman transport equation on the assumption that inelastic collisions occur at $u = u_1$. The exact linear differential equation that defines the distribution function in the high-energy ($u > u_1$) region is also derived. The mathematical difficulties and the usual approximations that are associated with this equation are briefly examined. An approximate analytical solution is given in terms of Hankel functions of the first kind when the cross section for inelastic collisions is assumed to be proportional to $(u - u_1)^{\gamma}$. The theory, which is developed in an elementary formalism, applies to electrons that are in a uniform dc electric field. Physical interpretations and the effects of inelastic collisions are emphasized.

*Published in Am. J. Phys. 31, 905 (1963).

RECOVERY FROM DIVISION DELAY IN IRRADIATED GAMETES OF ARBACIA PUNCTULATA*

Patricia McClement Failla

One of the effects of exposure to ionizing radiation of either the egg or sperm of the sea urchin is a delay in the time of first division of the fertilized egg. The remarkably synchronous first cleavage of the Arbacia punctulata zygote makes this excellent material for quantitative studies. In early experiments Henshaw[1,2] showed that the magnitude of the radiation-induced cleavage delay decreased with the length of time eggs remained in sea water after irradiation but before fertilization. No such "recovery" was exhibited by irradiated sperm. Recently, however, a post-fertilization recovery process has been demonstrated for both irradiated eggs and sperm.[3] This process involves a prolongation of the first division cycle by anoxia during which time the radiation effect is reduced. Observations on this process have now been extended and are described below.

Materials and Methods

Many of the experimental procedures have been described previously[3,4] and will only be outlined here. The sea urchins, Arbacia punctulata, were segregated according to sex and kept in running sea water in aquaria. Eggs and sperm were procured by electrical stimulation of the animals with an alternating potential of about 10 Volts. The criterion of radiation effect was the increase in the time between fertilization and first cleavage of the irradiated compared to the unirradiated gamete combination. The determination of the time of first cleavage was by microscopic observation of the fertilized eggs, usually in a fingerbowl containing about 200 cc of filtered sea water.

To characterize better the postfertilization recovery process, it was decided to prolong the first cell division not only by removal of oxygen but by exposure to cold and to deuterated sea water. The effect of puromycin on the recovery mechanism was also tested. Some of the techniques involved are described below.

In those experiments involving puromycin, where volumes were minimal for economic reasons, a suitably smaller number of eggs was observed in small plastic petri dishes containing about 5 cc of liquid. The visual method of estimating the time at which 50% of the eggs have cleaved, because of the synchrony of division mentioned above, is considered good to within ±1 minute. Cleavage delay times are, therefore, reliable to within about ±2 minutes.

*Work performed at the Marine Biological Laboratory, Woods Hole, Mass.

For the stoppage of cell division by removal of oxygen, the fertilized egg suspensions were put into test tubes containing about 25 cc sea water, through which purified nitrogen was continually bubbled. After cessation of the nitrogen treatment the tubes were emptied into fingerbowls of fresh sea water. All manipulations, unless specifically noted, were carried out at room temperature.

The deuterated sea water used was very kindly provided by Dr. D. Marsland. This medium was prepared by mixing salts in the proportions found in sea water in the Woods Hole area[5] in D_2O of over 98% purity.[6] The control medium in the deuterium experiments was artifical sea water of the same formula prepared with glass distilled water. The stock puromycin solution was made up in filtered natural sea water to a 10^{-3} molar concentration.

A gamma-ray unit consisting of two 2500-Curie cesium-137 sources with variable spacing between them was used for all irradiations. The samples were placed in plastic petri dishes, which were positioned halfway between the two sources. A source-sample distance was used which exposed the specimens to a dose rate of 5,000 r/min. A single dose of 10,000 r was delivered unless otherwise specified.

Results

It has been established that the postfertilization recovery process is somewhat more efficient than that operative in the irradiated egg before fertilization.[3] It was decided to compare certain other properties of the two processes such as dose response and temperature sensitivity. The results are described below.

Henshaw[2] demonstrated that the rate of recovery from cleavage delay occurring in irradiated eggs when insemination is delayed is independent of the dose of radiation and, thus, of the magnitude of radiation effect. Similar results were found for both irradiated eggs and sperm when division after fertilization was delayed by removal of oxygen. A typical set of data is shown in Figure 19. The prolongations of the cell division cycle by anoxia are plotted on the abscissa as "recovery" periods. It may be seen that the recovery curves for the three doses indicated are roughly parallel on a semilogarithmic plot indicating that, regardless of absolute amount, a certain proportion of the damage is repaired in a given time.

Similar parallel recovery curves were obtained for sperm irradiated in air or in nitrogen. The initial effect for the same dose, however, was about 15% less for sperm anoxic at the time of exposure. This recovery, therefore, may be independent not only of magnitude but perhaps of kind of damage as well. It should be recognized, however, that the oxygen effect

for this criterion of radiation injury is very small. On the other hand, although the proportion of oxygen-dependent damage is minor, it is not only from this type of damage that recovery can occur.

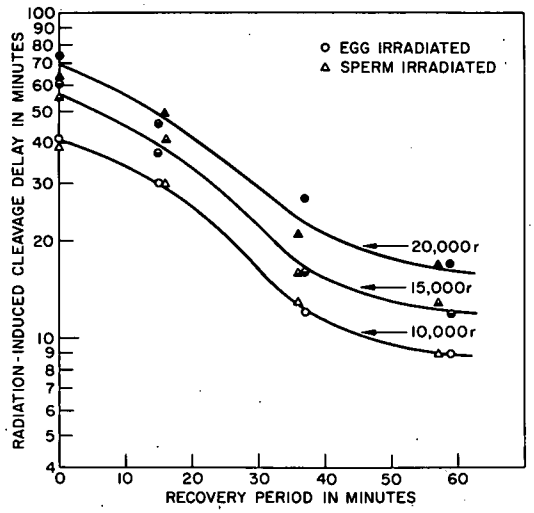

Figure 19

Effect of prolongation of cell division cycle by anoxia on radiation-induced cleavage delay

The data in Figure 19 show also that the zygote recovers at the same rate whether it is the egg or the sperm which is irradiated. As will be discussed below, this is additional evidence for the predominant role of the egg in this recovery process.

In order to elucidate the prefertilization recovery mechanism, Henshaw[1] compared the reduction in cleavage delay when irradiated eggs were kept before insemination at 0°C and at room temperature for various periods of time. He found a greatly reduced recovery rate at the lower temperature. To characterize similarly the postfertilization recovery process, eggs inseminated with irradiated sperm were kept at 0°C for periods up to an hour. This exposure to cold five minutes after fertilization, like exposure to nitrogen, effectively stopped the cell division process and afforded the cells time to recover from the radiation insult. However, with cold treatment recovery was minimal or undetectable. Figure 20 illustrates this result.

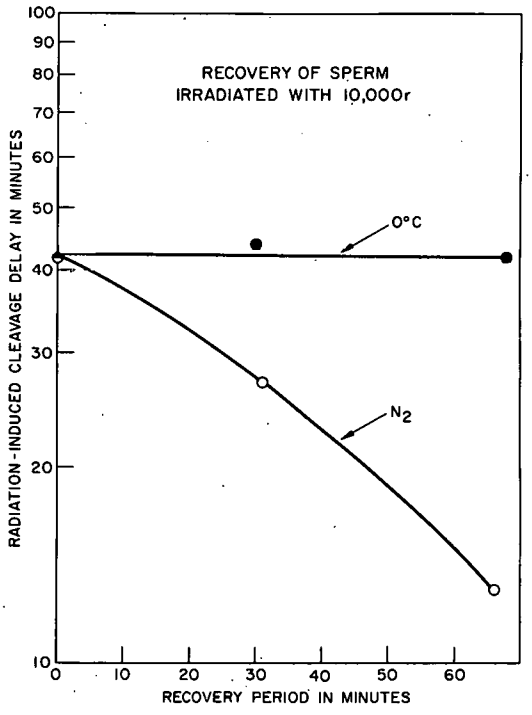

Figure 20

Intra-egg recovery of irradiated sperm as a function of postfertilization prolongation of division cycle by exposure to 0°C or N_2

That is, the effect of cold on recovery is similar for both irradiated unfertilized eggs and eggs fertilized with irradiated sperm.

In view of the parallelism in properties of the two recovery processes, it was of interest to investigate their additivity. Irradiated eggs were permitted to "recover" for various periods up to an hour, inseminated with normal sperm, and then tested for further recovery under nitrogen treatment. Typical additivity results are shown in Figure 21 where it is evident that prefertilization recovery does not abrogate or impair the recovery of the zygote. These data also illustrate the greater efficiency of the postfertilization recovery process previously noted.

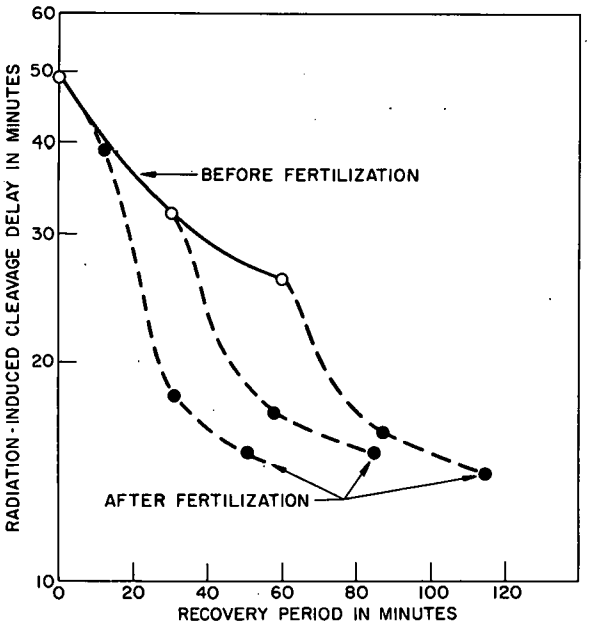

Figure 21

Additivity of pre- and postfertilization recovery processes

During a study of the recovery of eggs irradiated *in vivo* it was found that eggs remaining inside the animal for about 4 hours or more lost the capacity to recover *in vitro* before fertilization.(4). Accordingly, it was decided to test the ability of such eggs to recover after fertilization. Eggs were removed from an irradiated female urchin at various postexposure times, fertilized with sperm from an unirradiated male, and tested for recovery when cell division was delayed by anoxia. As shown in Figure 22, the recovery power under these conditions was unchanged for eggs remaining in the irradiated female up to at least 28 hours. The pre- and postfertilization recovery processes then differ in this respect. The decrease in initial

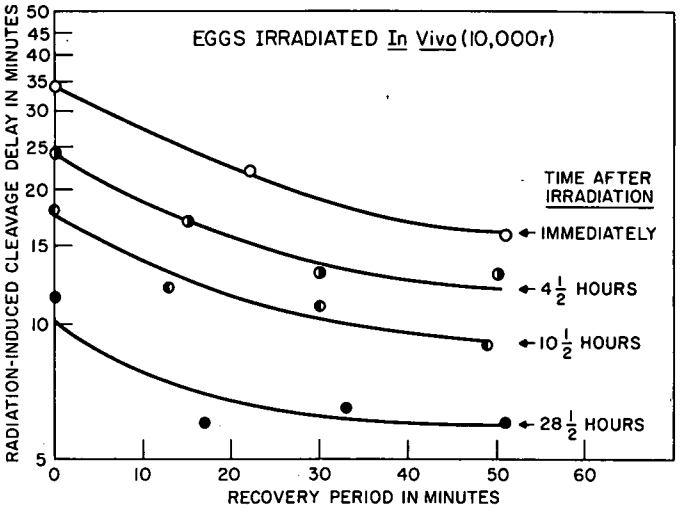

Figure 22

In vitro postfertilization recovery of eggs irradiated *in vivo* as a function of the length of time after irradiation the eggs remained in the animal

cleavage delay with time of removal of eggs apparent in Figure 22 exemplifies the slow in vivo recovery process described in a previous publication.(4)

Since the postfertilization recovery process is more efficient and persistent than that operative in the unfertilized egg, some experiments were designed in an attempt to elucidate the underlying mechanism. It was decided first to provide time for recovery by postponing cell division by a means other than removal of oxygen or exposure to cold. Immersion of Arbacia eggs in deuterated sea water has been shown to halt cell division reversibly through a rigidification of the cytoplasm and mitotic apparatus.(6,7,8) Accordingly, a drop of concentrated suspension of eggs fertilized with irradiated sperm was added to 4 cc of D_2O-sea water (95+%) ten minutes after insemination. After 30 or 60 minutes the deuterated medium was diluted out in about 200 cc of natural sea water and division permitted to progress. For comparison, a sample of the same egg suspension was also delayed in division by exposure in the usual way to nitrogen. One set of results is shown in Figure 23 (bottom two curves). In three such experiments, the recovery during treatment in D_2O was more rapid than that in N_2 although the absolute rates and rate ratios varied with each gamete combination. "Freezing" of the various gel structures in the egg, thus, did not block the activity necessary for repair of the radiation damage causing cleavage delay, but, in fact, was less inhibitory than interference with oxidative metabolism. It was then decided to assess the effect on the recovery mechanism of interfering specifically with protein metabolism.

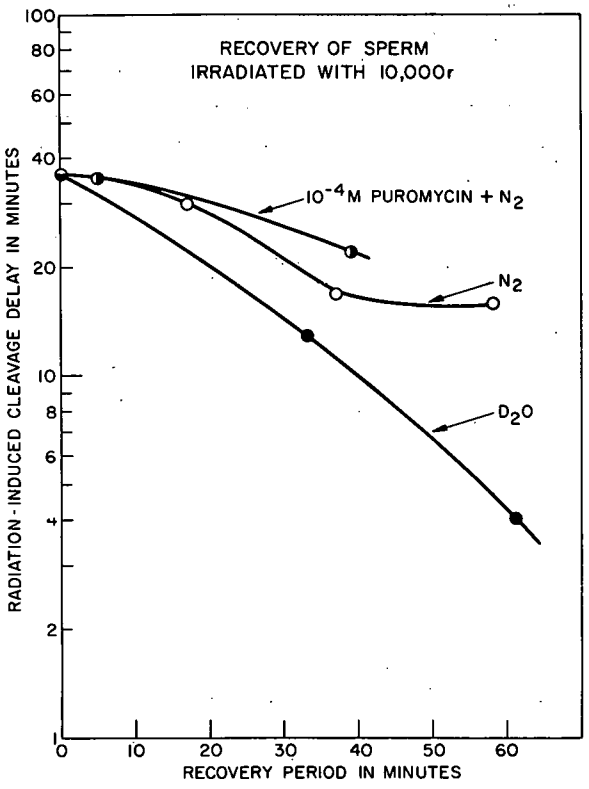

Figure 23

Intra-egg recovery of sperm as a function of postfertilization prolongation of division cycle by exposure to D_2O, nitrogen or nitrogen in the presence of puromycin

Puromycin is known to inhibit protein synthesis at the ribosome level and has been shown to prolong the cell division cycle in Arbacia eggs.(9,10) Pretreatment of eggs in a 10^{-4} M sea water solution of puromycin dihydrochloride for 20 minutes before fertilization delayed the first cleavage by only about 5 minutes, affording too short a time in which to observe recovery.

(At this concentration, development of the zygote was halted in the 4- or 8-cell stage; at higher concentrations, 100% first cleavage was not assured.) Puromycin incubation of eggs beginning 20 minutes before insemination with irradiated sperm was, therefore, combined with postfertilization exposure to nitrogen. The effect, compared with that elicited solely by nitrogen or D_2O treatment of the same gametes, is shown in Figure 23. In five similar experiments the rate of recovery under nitrogen in the presence of puromycin was either virtually the same or somewhat less than that under nitrogen treatment alone.

The results of these experiments also demonstrated in varying degrees a synergistic action of radiation and puromycin, i.e., treatment with both agents produced a cleavage delay larger than expected from the sum of effects of either agent acting alone. In this regard it should be noted that the sperm only were irradiated and did not come in contact with puromycin until time of fertilization. The deleterious effect of combined treatment might have been more pronounced if radiation exposure of either or both gametes had taken place in the presence of puromycin. It is obvious, however, that the puromycin treatment influenced the development of the cell but was relatively ineffective in modifying the recovery of the cell from radiation damage. This implies, therefore, that protein synthesis is not very importantly involved in repairing the damage responsible for radiation-induced cleavage delay.

Discussion

Radiation-induced cleavage delay has been interpreted as the time required for the zygote to repair or replace some component essential for division which has been damaged or destroyed.[11] A recent exhaustive study with sea urchin eggs by Rao[12] implicates a radiation-induced delay in the visible condensation of the chromosomes as being responsible for the mitotic inhibition. DNA synthesis did not appear to be influenced by the doses used to effect division delay nor did the radiation action appear to be on the DNA molecules themselves. Unfortunately the mechanism of chromosome condensation is not well enough understood to make possible identification or definition of the radiosensitive process which is subject to repair during the recovery period.

Studies of the recovery process, however, may shed some indirect light on the nature of the radiation-induced lesion. First of all, although the ultimate damage may be primarily to nuclear components, it is the cytoplasm of the egg which is required for recovery. The sperm, consisting of almost pure nuclear material, cannot repair its own damage. The egg, on the other hand, before fertilization can partially eliminate some of its selfsustained radiation damage and after fertilization can undo that borne by the sperm as well. Time appears to be the principal requirement. This

may be afforded by delaying insemination or prolonging the first division cycle. In this regard, this recovery process resembles that described by Baldwin for the insect Rhodnius[13] where delaying the onset of cell division after irradiation partially reverses the latent mitotic delay damage.

The cytoplasmic mechanism responsible for the repair of radiation damage in the sea urchin egg is so far best characterized by its lack of response to various agents. As seen from the experiments with nitrogen, D_2O, and puromycin, this mechanism requires neither oxygen, DNA synthesis, nor protein synthesis to function. The fact that recovery occurs in the metabolically dormant unfertilized egg, albeit more slowly than after fertilization, further points up the nonspecific nature of the process. From the much reduced in vivo recovery rate, however, it appears that the mechanism can be inhibited by prolonged contact with irradiated tissue. Yet this result might also be explained by continued environmental aggravation of the radiation lesion under these conditions. The recovery mechanism is strongly inhibited at 0°C but there is no information about its activity at intermediate temperatures. All in all, it is difficult to visualize a process as "passive" as these results imply. The restitution of chromosome breaks in Tradescantia requires aerobic metabolism and protein synthesis.[14] Would less be expected in the case of invertebrate eggs?

The nature of the postfertilization recovery process, thus, has been better characterized but is still far from definition. The results, however, should provide a valuable background for the future identification of not only the recovery mechanism but the radiation lesion itself.

Summary

The recovery from radiation-induced cleavage delay that occurs when the first cell division cycle is prolonged in the zygote of Arbacia punctulata has been studied. The following characteristics of this recovery process have been established:

1. The recovery rate is independent of radiation dose and, thus, magnitude of effect.
2. The recovery rate is approximately the same when either the egg or sperm is irradiated; it is also the same for anoxically and aerobically irradiated sperm.
3. The pre- and postfertilization recovery processes are additive. The postfertilization process is still operative in eggs irradiated in vivo and removed from the animal up to at least 28 hours after irradiation.
4. The recovery rate is very reduced at 0°C, but is insensitive to treatment of the zygote with D_2O or puromycin.

References

1. P. S. Henshaw. Further studies on the action of roentgen rays on the gametes of Arbacia punctulata. Am. J. Roentgenol. 43, 899-933 (1940).
2. P. S. Henshaw. Studies of the effect of roentgen rays on the time of first cleavage is some marine invertebrate eggs. I. Recovery from roentgen-ray effects in Arbacia eggs. Am. J. Roentgenol. 27, 890-898 (1932).
3. Patricia Failla. Recovery from radiation-induced delay of cleavage in gametes of Arbacia punctulata. Science 138, 1341-1342 (1962).
4. Patricia Failla. In vivo and in vitro recovery of irradiated gametes of Arbacia punctulata. Radiation Res. 17, 767-773 (1962).
5. G. M. Cavanaugh. Formulae and Methods IV of the Marine Biological Laboratory, Woods Hole, Mass. (1956).
6. D. Marsland and A. M. Zimmerman. Cell division: differential effects of heavy water upon the mechanisms of cytokinesis and karyokinesis in the eggs of Arbacia punctulata. Expl. Cell Res. 30, 23-25 (1963).
7. P. R. Gross and W. Spindel. The inhibition of mitosis by deuterium. Ann. N.Y. Acad. Sci. 84, 745-754 (1960).
8. P. R. Gross and W. Spindel. Heavy water inhibition of cell division: an approach to mechanism. Ann. N.Y. Acad. Sci. 90, 500-522 (1960).
9. T. Hultin. The effect of puromycin on protein metabolism and cell division in fertilized sea urchin eggs. Experientia 17, 410-411 (1961).
10. R. C. Rustad and B. R. Burchill. Protein synthesis and radiation-induced mitotic delay. Radiation Res. 22, 229 (1964).
11. D. E. Lea. Actions of Radiations on Living Cells. The Macmillan Co., New York, 1947.
12. Bhashine Rao. Analysis of x-ray-induced mitotic delay in sea urchin eggs. U. S. Atomic Energy Commission Report UCRL-10979 (1963).
13. W. F. Baldwin. Latent radiation damage and synchronous cell division in the epidermis of an insect. III. Spontaneous reversal of effects leading to delay during mitosis. Radiation Res. 14, 426-431 (1961).
14. Sheldon Wolff. Some post irradiation phenomena that affect the induction of chromosome aberrations. J. Cellular Comp. Physiol. 58 (Suppl. 1), 151-162 (1961).

ABSTRACT NO.: JOURNAL CATEGORY: SERIAL NO.:

Health Phys., 11: 50-2(Jan. 1965) C 1-28-65

ANL-6936(p.57-60) Unel.

THE RADIUM GAMMA-RAY RESPONSE OF MUSCLE-EQUIVALENT IONIZATION CHAMBERS. Jacob Kastner and Ramesh K. Rukkoo (Argonne National Lab., Ill.).
To be published in Health Physics.

C-48 P USA

☐ OTI ABSTRACT
☐ AUTHOR ABSTRACT

S-4

SHORT TITLE: Radium γ-ray response of muscle-equivalent ionization chambers

CORPORATE AUTHOR(S) 062,7000 3-5-65sec

OTI-70 (SDI) (4-64)

8. MICROCARD - MS.

8

THE RADIUM GAMMA-RAY RESPONSE OF MUSCLE-EQUIVALENT IONIZATION CHAMBERS*

Jacob Kastner and Ramesh K. Hukkoo**

Terrestrial background gamma radiation has been measured recently with relatively large ion chambers constructed of muscle-equivalent conducting plastic and filled with a muscle-equivalent (M.E.) gas mixture.[1-3] That such large chambers are essentially standard instruments for the measurement of the absorbed dose can be shown by comparing the ionization engendered therein by exposure to the gamma rays from a known source of radium to that expected from the internationally accepted specific gamma-ray emission of 8.25 R mg^{-1} h^{-1} at 1 cm.[4] To do this it was necessary to carry out an extrapolation to zero-wall thickness of the response of the chamber; this was done by adding M.E. shells of known thicknesses to a 2-mm M.E. wall, 8-inch diameter, sealed chamber filled with M.E. gas. Additional data were obtained from a similar unsealed chamber with a 1-mm wall through which N_2 and M.E. gases were passed successively and continuously at atmospheric pressure. Figure 24 is a graph of the

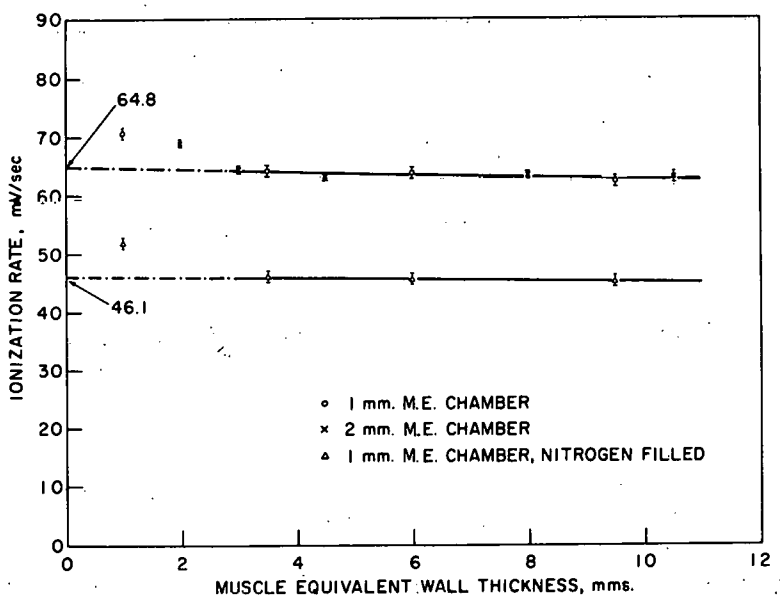

Figure 24

Ionization response for a sealed and an unsealed chamber

*To be published in Health Physics.

**On leave from the Atomic Energy Establishment, Trombay, Bombay, India, and supported by the U. S. Agency for International Development.

ionization response for the two chambers at one meter from a 1.11-mg radium standard enclosed in 0.5 mm platinum (certified by the National Research Council of Canada). Each point on the curve is the result of several measurements at each of several distances. Deviations from the inverse square law were negligible, especially when corrections were made for the small effects of floor and wall scattering (less than 0.5%) and air absorption (0.3%/meter).

The ionization observed at small wall thickness (1 to 2 mm) was rather high compared with that reported in the literature.[5,6] This may be the result of electrons produced in and scattered by air which penetrate the chamber.[7] However, as one would expect, the slopes of the curves beyond 3 mm correspond very well to an absorption coefficient σ_a of 0.035 cm^{-1} for radium gamma rays in muscle.

The volume and capacitance of the chambers were measured to better than 0.5%. An extremely precise and accurate determination was made for us by W. P. Jesse* of the energy required by β rays to create an ion pair in muscle gas, namely, W = 26.2 eV.**

The ionization rate from the 1.11-mg radium standard in air (N.T.P.) at one meter is

$$A = 530 \pm 11 \text{ ion pairs } cc^{-1} \text{ sec}^{-1} \quad (1)$$

The expected ionization in the muscle gas can be calculated as follows:

$$B = \frac{\text{Dose (muscle)}}{\text{Dose (air)}} \times \frac{W \text{ (air)}}{W \text{ (gas)}} \times \frac{\text{Experimental density (gas)}}{\text{Density at N.T.P. (air)}} \times A \quad (2)$$

Using Jesse's values of W for air[8] and the M.E. gas and the relative absorbed doses in air and muscle,[9] one obtains

$$B = \frac{0.959}{0.872} \times \frac{33.78}{26.20} \times \frac{1.069}{1.293} \times 530 = 620 \pm 12 \text{ ion pr } cc^{-1} \text{ sec}^{-1} \quad (3)$$

The ionization produced in the chamber with no attentuation (Figure 24) for M.E. gas is

---

*St. Procopius College, Lisle, Illinois.

**It should be emphasized that this value applies exclusively to the specific gas mixture given in Reference 2.

$$C = \frac{\text{charge rate}}{\text{volume} \times \text{charge per ion pair}}$$

$$= \frac{64.8 \times 10^{-3} \text{V sec}^{-1} \times 4.80 \times 10^{-12} \text{F}}{3170 \text{ cc} \times 1.6 \times 10^{-19} \text{ C ion pr}^{-1}} = 614 \pm 9 \text{ ion pr cc}^{-1} \text{ sec}^{-1} \qquad (4)$$

in agreement with Equation 3.

The expected ionization in nitrogen is

$$D = \frac{0.959}{0.872} \times \frac{33.78}{35.0} \times \frac{1.12}{1.293} \times \frac{1}{1.14}* \times 530 = 427 \pm 9 \text{ ion pr cc}^{-1} \text{ sec}^{-1} \qquad (5)$$

Experimentally, for N_2, the ionization was found to be:

$$E = 436 \pm 9 \text{ ion pr cc}^{-1} \text{ sec}^{-1} \qquad (6)$$

also in agreement with Equation 5.

Another chamber (13-inch diameter M.E. chamber with a 6-mm wall) used in our environmental radiation measurements[2] was also tested. The ionization produced in this chamber, corrected by a factor of 1.021 for the attenuation of the wall is

$$F = \frac{289 \times 10^{-3} \times 5.54 \times 10^{-12}}{16500 \times 1.6 \times 10^{-19}} \times 1.021 = 619 \pm 9 \text{ ion pr cc}^{-1} \text{ sec}^{-1} \qquad (7)$$

From this agreement with the expected quantities and the internal consistency of the experimental data, one can conclude that such large muscle-equivalent chambers may be used with confidence to provide absolute measures of the absorbed dose.

We are grateful to Dr. Francis R. Shonka of the Physical Sciences Laboratory, St. Procopius College, for providing the muscle-equivalent chambers and gas, and to Dr. John E. Rose of our Division for suggesting the experiment and for consultation. We are also most appreciative of the assistance rendered by Mr. William Prepejchal.

*The quantity 1.14 is the ratio of the effective mass stopping power in the wall to that in nitrogen,[10] which is applicable where the ionization is produced by electrons generated only in the wall.

References

1. F. R. Shonka, J. E. Rose, G. Failla. Progr. Nucl. Energy, Sec. XII, 1, 753 (1958).

2. J. Kastner, J. E. Rose and F. R. Shonka. Science 140, 1100 (1963).

3. P. Gustafson, J. Kastner and J. Luetzelschwab. Science 145, 44, (1964).

4. C. Garrett. Can. J. Phys. 36, 149 (1958).

5. W. V. Mayneord and J. E. Roberts. Brit. J. Radiol. 10, 365 (1937).

6. A. Ghosh, J. Kastner and G. N. Whyte. Nucleonics 11 (6), 70 (1953).

7. G. Failla and L. D Marinelli. Am. J. Roentgenol. 38, 334 (1937).

8. W. P. Jesse. Phys. Rev. 122, 1195 (1961).

9. U. S. Dept. of Commerce, National Bureau of Standards, Handbook 78, Government Printing Office, Washington, D. C., 1961, Report of ICRU, 1959, p. 30.

10. Ibid, p. 37, Table 5a.

ENVIRONMENTAL RADIATION: MEASUREMENTS OF DOSE RATES*

Philip F. Gustafson,** Jacob Kastner, and John Luetzelschwab†

Abstract

The exposure dose from environmental sources of radiation was determined by means of an ionization chamber, by gamma-ray spectrometry in the field, and by measurements of radioactivity in soil cores. The exposure dose from cosmic radiation was found to be 4.4 ± 0.2 μR/hr, that from natural radioactivity 8.0 ± 0.3 μR/hr, and the contribution from fission products varied from 2.0 to 7.5 μR/hr during the interval in question.

*Paper published in Science 145, 44 (1964).

**Division of Biological and Medical Research.

†Resident Student Associate from Washington University, St. Louis.

13

INTERNAL Sr^{90} BETA RAY DOSIMETRY WITH FLUORODS

Jacob Kastner, Donald R. Roberts,* and William Prepejchal

Introduction

Schulman-Etzel[1] fluorod dosimeters have been employed for the measurement of Sr^{90}-Y^{90}, beta-ray doses *in vivo* and *in vitro*.

The following is a description of the dosimetric problems associated with these fluorods.

Measurement System

Fluorods made from silver phosphate glass are now commercially available in the form of cylindrical rods one mm in diameter and six mm long. The Bausch and Lomb (B and L) Optical Company manufactures both high- and low-Z** (lithium phosphate) glass rods whose output was determined with their "Microdosimeter Reader."[2]

Very early in our work it was determined that the high-Z rods gave nonreproducible data and also faded quickly. The low-Z rods, however, are relatively permanent, and some institutions routinely locate these fluorods in personnel film badge holders as additional monitors.[3] Measurements were also made with Toshiba[4] low-Z fluorods which were read using the B and L instrument. The chuck (rod-holder) of this instrument was modified to provide a firmer grip and, thus, more reproducible data, even though the sensitivity was somewhat reduced in the process. (See Appendix A.)

The rods must be carefully cleaned before reading. For example, we use a succession of rinses in acetone, distilled water, and alcohol, or, alternatively, an ultrasonic bath in soap solution followed by rinsing in water and alcohol. After the rod is placed in the chuck it must be dusted by a puff of dry air.

Prior to reading the fluorod, the open chuck background was determined for each range. This value was subtracted from the mean of replicate fluorod readings to determine the photoluminescent output. In this work the pre-dose luminescence for each rod was subtracted from the final reading, but in most cases of biological interest the use of a pre-dose value which is the mean for a batch seems sufficiently precise.

---

*Resident Research Associate, summer 1963.

**Bausch and Lomb Microdosimeter, Catalogue No. 33-66-00.

A two-hour wait after exposure was sufficient to provide essential stability. The "reader" was on for about an hour before measurements were made, and its stability was checked periodically by means of the photoluminescence from manganese-doped glass standards.[5]

Co^{60} Gamma-Ray Calibration

Fluorods, in cylindrical Lucite holders with 4-mm thick walls, were exposed to various doses in the high intensity Co^{60} gamma facility of the Division of Biological and Medical Research. Figure 25 displays the relationship of instrument fluorescent units to the Co^{60} gamma-ray absorbed dose in rads. Over the region of interest the mean ratio of fluorescent units (F.U.) to Co^{60} dose in rads is: F.U./γ rad = 0.67. It should be noted, of course, that the specific ratio obtained is peculiar to the system used, and, furthermore, that the fluorescence is not really proportional to the dose over more than three decades.

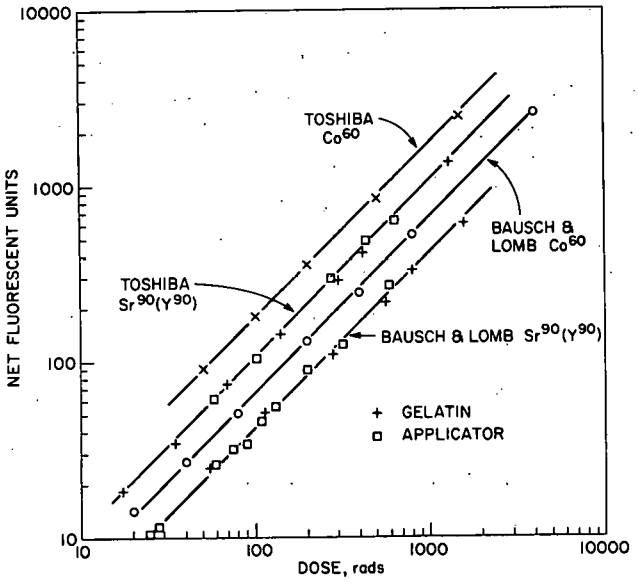

Figure 25

Fluorod dosimeter fluorescence vs absorbed dose

Beta-Ray Calibration

The beta flux varies through the internal volume of the dosimeter which cannot, therefore, be considered a point detector. For this reason, response of the dosimeter system per unit of dose received must be determined with the particular beta emitter being studied.

To provide isotropic 4π sources of Sr^{90}-Y^{90}, we first employed aqueous solutions of $SrCl_2$ with approximately one and ten microcuries per ml. The fluorods, in plastic tubing, were suspended so that the thickness of the surrounding solution exceeded the maximum range (~1 cm) of the Y^{90} beta rays. The results with these solutions were somewhat erratic, and recourse was made to the use of gelatin molds containing a known concentration of Sr^{90}. These molded gelatin cylinders were about 1 inch in diameter and 1 inch high and provided easily reproducible and very useful sources for delivering beta-ray doses in an isotropic manner. The open gelatin surfaces were covered by a 1/4-mil Mylar film, and the complete molds were sprayed with a light acrylic coat. The molds were kept in glass sealers with some water on the bottom to provide 100% humidity. Exposures and storage were carried out in a refrigerator at +7°C. The gels have been stable and have provided reproducible data for more than a year and show no signs of deterioration. The use of thin plastic sleeves* to protect and hold the fluorods proved to be convenient and efficient and yet lowered the net fluorescence by less than 10%. It is recommended that such sleeving be used in all tissue implants.

To verify the isotropic character of the gelatin system, the fluorescence of fluorods sandwiched between two beta-ray gelatin molds was compared with the fluorescent output when one of the molds was blank, i.e., contained no activity. This was done for times varying from two hours to as much as a week. In all cases the fluorescent output for 4π irradiation was almost exactly twice that in the 2π case. Furthermore, as can be seen in Figure 25, proportionality held over the complete range of measurements. The Sr^{90}-Y^{90} dose rate was computed using the well-known relation[6]

$$R_\beta = 51.2\ \overline{E}_\beta\ C \text{ rad/day}$$

where C is the concentration in $\mu C/g$ and $\overline{E}_\beta$ is the average beta-ray energy, 1.1 MeV.

A check measurement of Sr^{90} concentration in the gelatin was made upon completion of the fluorod calibration.

There is available in our laboratory a Sr^{90}-Y^{90} beta-ray applicator on which depth dose measurements in Lucite have been made by Amrik S. Chhabra using a Failla extrapolation ion chamber.[7] In contrast to the radiation from the gel, only the beta rays from Y^{90} emerge from the sealed source. We decided to use the applicator to check the beta-ray response of the fluorods and, in particular, to simulate the nonuniform source distribution which obtains in therapeutic practice. A Lucite holder was constructed to position the rods under the applicator with provision for various

*Intramedic Polyethylene tubing, No. PE160, Clay-Adams, Inc., New York.

Lucite absorbers. In this way, dose rates as well as exposure times could be varied over wide limits. As Figure 25 shows, the fluorescent response to the absorbed dose in rads was identical with that observed for the uniform irradiation supplied by the gelatin source. Furthermore, the response was proportional to the dose and independent of the dose rate over a range of at least two decades.

A summary of the responses of the fluorods to various sources is given in Table 8.

Table 8

Responses of fluorods to various sources

Source	Fluorescent units per rad		
	Bausch and Lomb	Toshiba	Toshiba/B and L
Co^{60}	0.67	1.78	2.7
Sr^{90}-Y^{90}	0.42	1.10	2.7
Sr^{90}/Co^{60}	0.62	0.62	

The two kinds give essentially the same beta-ray to gamma-ray response ratio, even though the Toshiba fluorods are 2.7 times as sensitive as the B and L dosimeters and despite the difference in their glass compositions. The density variation for the two glasses was less than 10%.

The beta-gamma ratio of fluorescent response is in good agreement with the results of other workers[8,9] provided their data are corrected for the small extra dose contributed by the Sr^{90} in their solution sources.

The two glasses also behaved similarly with regard to relative fluorescent output vs depth in Lucite. Figure 26 shows the excellent fit with Chhabra's extrapolation chamber data. Thus, even though the fluorods are not point detectors, they may give surprisingly useful information about beta-ray dose distributions. Incidentally, using the gelatin mold as a source of beta rays one obtains the same depth-dose curve in Lucite as for the applicator. This observation, together with the identity of response for the two sources, implies similarity in their beta-ray spectra.

Reader Geometry

The possible effect of the geometry of excitation of luminescent centers by the B and L reader was checked by using another reading system which has been described by N. F. Barr, et al.[10,11] We were fortunate to be able to borrow this apparatus from the Division of Biophysics of the

Sloan-Kettering Institute. No significant difference was observed in the beta-gamma ratio of fluorescent response.

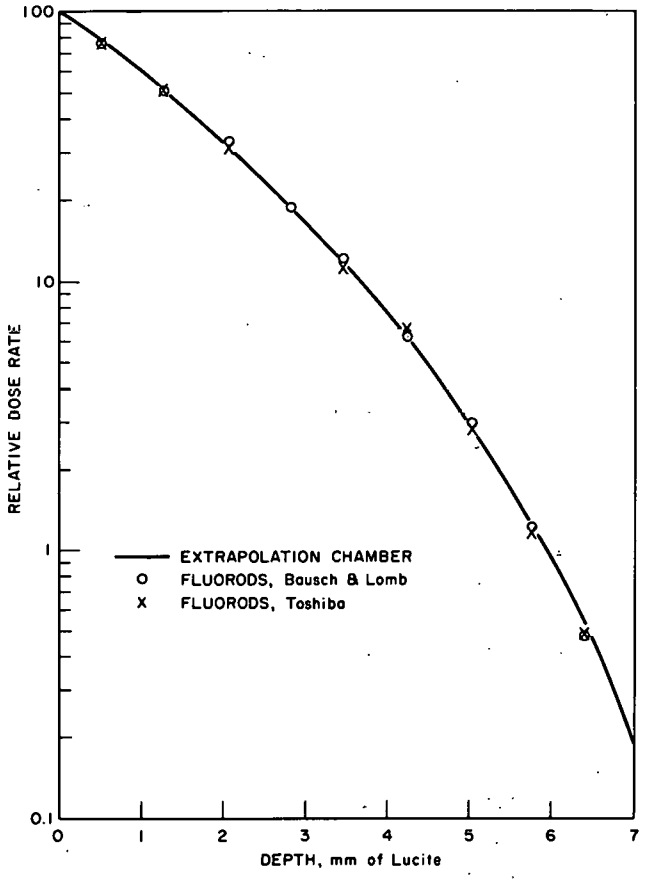

Figure 26

Comparison of depth-dose measurements in Lucite; fluorods vs extrapolation chamber

Temperature Dependence

Although we have not carried out extensive tests, the fluorods seem to be relatively insensitive to temperature in the range of 0 to 25°C Barr[11] and Miyanaga[4] reported temperature coefficients of +0.4%/°C and +0.2%/°C for B and L and Toshiba fluorods, respectively. The maximum variation, therefore, can be no more than 10%.

Conclusion

The use of Schulman and Etzel fluorods for *in vivo* and *in vitro* dosimetry for Sr^{90} beta rays is quite feasible, provided careful precalibration is carried out on a sample of the specific batch of dosimeters to be used. A reproducible technique for calibration employing gelatin phantoms has been described. The convenience in practice of using such gelatin techniques for calibrating beta-ray applicators should not be overlooked. Comparison with the work of other laboratories can always be made if a Co^{60} gamma-ray calibration is included.

The response is linear with dose over a large range and is also independent of dose rate, at least from 24 R/hr to 2400 R/min. If one uses low-Z fluorods the fluorescence does not fade over many months, and, thus, the dosage can be reread at any time. Of the two commercially available materials, the Toshiba fluorods are superior with regard to sensitivity and low pre-dose reading; however, both the Toshiba and the B and L products offer good reproducibility if the B and L reader is slightly modified to provide better alignment of the fluorods.

A bibliography resulting from a literature survey is supplied as Appendix B.

It is a pleasure to acknowledge the encouragement and advice of Mr. L. D. Marinelli, Director of the Radiological Physics Division of this Laboratory. Stimulation of this work and fruitful discussion were also provided by Dr. L. Voyvodic of the High Energy Physics Division and Dr. A. M. Brues of the Division of Biological and Medical Research. We also appreciate the ingenuity of Mr. Edward Fudala in modifying the reader chuck, and the help of Mr. Billie G. Oltman in making some special scintillator measurements.

References

1. H. W. Etzel and J. H. Schulman. J. Chem. Phys. 22, 1549 (1954).
2. G. E. Blair, C. H. Brumley, R. J. Meltzer, and J. L. Rood. Nucleonics 17 (9), 128 (1959).
3. E. D. Gupton, D. M. Davis, and J. C. Hart. Health Phys. 5, 57-62 (1961).
4. I. Miyanaga and H. Yamamoto. Health Phys. 9, 965 (1963).
5. J. Degelman, A. B. Callahan, and G. P. Fulton. Radiation Res. 6, 548 (1957).
6. G. J. Hine and G. L. Brownell. Radiation Dosimetry. Academic Press, Inc. N. Y., 1956. p. 824.
7. A. S. Chhabra. Radiology 79, 1001 (1963).
8. M. Hodara, M. Friedman, and G. J. Hine. Radiology 73, 693 (1959).
9. D. N. Tapper, M. M. Nold, and C. L. Comar. Health Phys. 8, 207 (1962).
10. N. F. Barr, M. Stark, and J. S. Laughlin. Radiology 76, 113 (1961).
11. N. F. Barr, M. B. Stark, J. Hands, and J. S. Laughlin. Health Phys. 7, 48 (1961).

APPENDIX A

Modification of Bausch and Lomb Fluorod Microdosimeter Reader #33

Modification of the B and L reader chuck involves only the 0.055 in. stainless steel plate on the light source side of the chuck. The original plate is removed and used to locate all holes on a new plate. (Ours is 0.050-in. aluminum.) All holes are drilled and counter-bored to duplicate the original, with the exception of the window which admits ultraviolet light to the rods. This hole is first drilled through with a #67 drill; then, from the photocell side, and to a full diameter depth of 0.030 in., the hole is enlarged with a #59 drill. (See Figure 27.) The fluorods will now sit in this hole to a depth of 0.030 in. This is sufficient to maintain reproducible alignment. The small spring in the chuck still provides a firm grip for the rod.

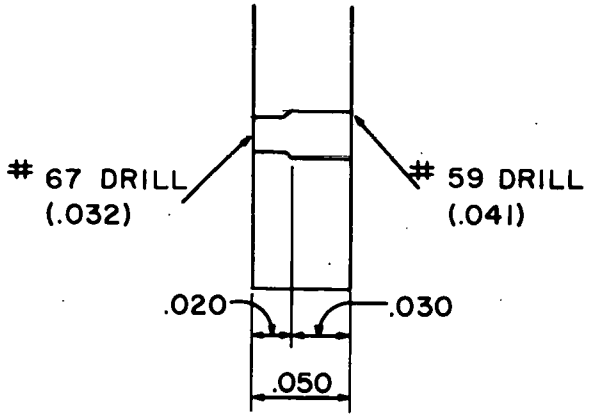

Figure 27

Reader chuck modification

Handling of the rods can also be made more efficient by clipping 5/16 in. long sections of #PE 160 intramedic polyethylene tubing in a #88 Mueller Electric Co. battery clip so that 1/8 in. of tubing protrudes. The rods are slipped into the tubing from the chuck or from the rod holder and are firmly held by the tubing. The clips merely serve as handles and are not opened and closed.

APPENDIX B

Radiophotoluminescence Bibliography

1. N. F. Barr, M. B. Stark, Joan Hands, and J. S. Laughlin. Dosimetry with Fluorods. Radiology 73, 693-705 (1959).

2. N. F. Barr, M. Stark, and J. S. Laughlin. A Comparison of Two Fluorometers Designed to Measure Radiation Induced Fluorescence of Ag-activated Rods. Radiology 76, 113-115 (1961).

3. C. H. Bernard, W. T. Thornton, and J. A. Auxier. Ag Metaphosphate Glass for x ray Measurements in Coexistent Neutron and Gamma Radiation Fields. Health Phys. 4, 236-243 (1961).

4. G. E. Blair. Applications of Radiation Effects in Glasses in Low- and High-Level Dosimetry. J. Am. Ceram. Soc. 43, 426-429 (1960).

5. G. E. Blair, C. H. Brumley, R. J. Meltzer, and J. L. Rood. Commerical Microdosimeter Uses Glass Fluorescence. Nucleonics 17 (9), 128 (1959).

6. J. Degelman, A. B. Callahan, and G. P. Fulton. An Improved Fluorometer for Miniature Glass Rod Detectors. Radiation Res. 6, 548-553 (1957).

7. H. W. Etzel and J. H. Schulman. Silver-Activated Alkali Halides. J. Chem. Phys. 22, 1549-1554 (1954).

8. J. F. Hamilton, F. A. Hamm, and L. E. Brady. Motion of Electrons and Holes in Photographic Emulsion Grains. J. Appl. Phys. 27, 874-885 (1956).

9. R. L. Hayes, M. M. Nold, C. L. Comar, and H. Kakehi. Internal Radiation Dose Measurements in Live Experimental Animals-I. Health Phys. 4, 79-85 (1960).

10. G. Hine, M. Hodara, and M. Friedman. Accuracy of Fluorod Dose Measurements. Radiology 78, 44-48 (1962).

11. M. Hodara, M. Friedman, and G. J. Hine. Radiation Dosimetry with Fluorods. Radiology 73, 693-705 (1959).

12. Sohei Kondo. Neutron Response of Silver-Activated Phosphate Glass. Health Phys. 4, 21-24 (1960).

13. P. K. Lee, E. R. Ballinger, and W. H. Schweitzer. A Heat Treatment which Extends the Usable Range of Ag PO_3 Glass Dosimeters. Los Alamos Report LA-2575 (September 13, 1961).

14. S. J. Malsky, C. G. Amato, and C. Reid. A Miniature Versatile Dosimeter. IRE Trans. ME-7 (3), 193-196 (1960).

15. S. J. Malsky, C. G. Amato, C. B. Reid, C. Spreckels, and L. Maddalone. In Vivo Dosimetry with Miniature Glass Rods. Part I - Physical Aspects and Recent Developments. Am. J. Roentgenol. 85, 568-571 (1961).

16. M. M. Nold, D. N. Tapper, and C. L. Comar. Cs^{137} Dose Measurements in Tissue-II. Health Phys. 8, 217-229 (1962).

17. A. L. Reigert, H. E. Johns, and J. W. T. Spinks. Ag-Phosphate Glass Needles for Measuring Gamma Dose. Nucleonics 14 (11), 134-137 (November 1956).

18. Bernard Roswit. In Vivo Dosimetry with Gold-Sheathed Miniature Glass Rods. Part II - Clinical Applications in Radiation Therapy. Am. J. Roentgenal. 85, 572-581 (1961).

19. J. H. Schulman and H. W. Etzel. Small Volume Dosimeter for x-rays and Gamma-Rays. Science 118, 184-186 (1953).

20. J. H. Schulman, F. J. Ginther, C. C. Klick, R. S. Alger, and R. A. Levy. Dosimetry of x-rays and Gamma-rays by Radiophotoluminescence. J. Appl. Phys. 22, 1479-1487 (1951).

21. J. H. Schulman, W. Shurcliff, R. J. Ginther, and F. H. Attix. Radiophotoluminescence Dosimetry System of the U. S. Navy. Nucleonics 11 (10), 52-56 (October 1953).

22. D. N. Tapper, M. M. Nold, and C. L. Comar. Cs^{137} Dose Measurements in Tissue-I. Health Phys. 8, 207-216 (1962).

23. R. Yokota, S. Nakajima, and E. Sakai. High Sensitivity Silver-Activated Phosphate Glass for the Simultaneous Measurement of Thermal Neutrons, Gamma and/or Beta rays. Health Phys. 5, 219 (1961).

24. I. Miyanaga and H. Yamanoto. Studies on Silver-Activated Metaphosphate Glass on a Personnel Monitoring Dosimeter. Health Phys. 9, 965 (1963).

25. N. F. Barr, M. B. Stark, Joan Hands, and J. S. Laughlin. Dosimetry With Small Silver-Activated Glass Rods. Health Phys. 7, 48 (1961).

26. K. Becker. Phosphate Glass for Routine Personnel Monitoring. U. S. Atomic Energy Commision Report AEC-TR-5781 (February 1963).

MEASUREMENT OF THE COSMIC-RAY FAST NEUTRON BACKGROUND

Jacob Kastner, Billie G. Oltman, Leonidas D. Marinelli,
and Joseph H. Klems

The fast neutron dose being received by man may be an important fraction of the total dose from the natural environment. During the past year, a program has been under-way at Argonne to develop statistically significant data, using pulse shape discrimination associated with large hydrogen-rich organic scintillators, to provide the necessary high efficiency and tissue-like characteristics. For field studies we also wanted reasonable portability.

The greater part of our data has been obtained with a commercially available circuit,* first proposed by Daehnick and Sherr[1] in 1961.

Figure 28 gives the response of NE 213 liquid scintillator to ionizing radiations of several energies. Various volumes of this scintillator were employed either directly coupled to the 6810A or by means of a conical Lucite light pipe. The meson data, for example, were developed by comparing the output at low gain, of a 1 in. x 5 in. right-circular cylinder with that of one 5 x 5 in. The resultant precise linearity is proof that no effective loss of light obtains for scintillations produced at the top of the liquid compared with those near the cathode.

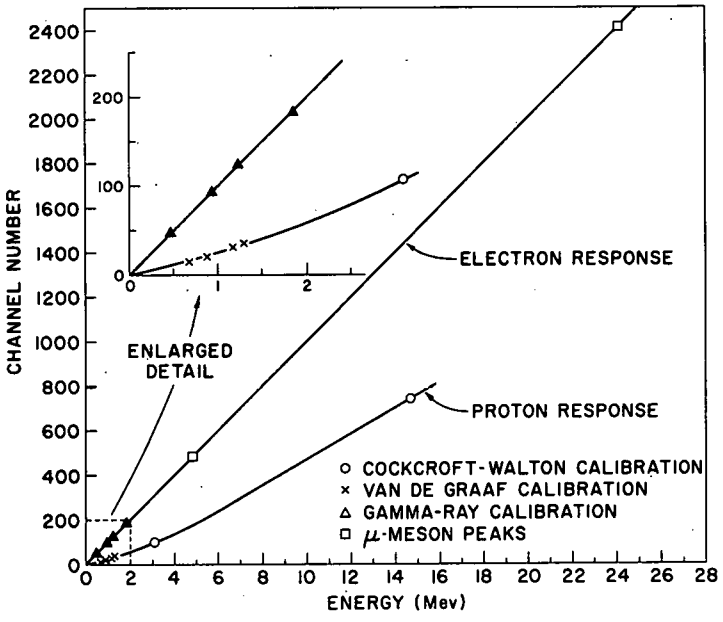

Figure 28

Response of liquid scintillator (NE 213)

*NE 5551, Probe, Nuclear Enterprises, Winnipeg, Canada.

The proton-recoil spectra were analyzed for the incident fast neutron flux and spectral distribution in the usual way. However, because of the large detector volume, corrections are required for the effect of second scattering from hydrogen nuclei as well as for the attenuation of neutron flux in traversing the detector.

In this experiment, an isotropic spatial distribution of neutrons impinges on a cylindrical detector. Although this geometry makes the calculation of multiple scattering and self-absorption correction difficult, we are nonetheless in the process of trying to derive rigorous expressions. In the meantime, we have adapted formulae derived for other geometries on the assumption that they ought to be good approximations.

Correction for Self-Absorption in the Scintillator

Because the incident neutron flux is isotropic, the detector is approximated by a sphere having the same average chord length as the actual cylinder. Wigner's[2] general formula for the average chord length of a lump is 4 (volume/surface). Applying this to a cylinder whose height L is equal to its diameter (2r), we find

$$4\left\{\pi r^2 (2r) \,/\, [2(\pi r^2) + 2\pi r(2r)]\right\} = 4r/3$$

$$= 2L/3 \qquad (1)$$

This is also the average chord length of the inscribed sphere of radius r. The factor by which an isotropic incident neutron flux is attenuated in a spherical detector is given by[3,4]

$$f(aL) = \frac{3}{(aL)^2}\left[\frac{aL}{2} + e^{-aL} - \left(\frac{1-e^{-aL}}{aL}\right)\right] \qquad (2)$$

where $a = a(E) = 2\sigma_H(E) \cdot N_H/V + \sigma_c(E) \cdot N_c/V$

$\sigma_H(E)$ = scattering cross section for hydrogen

$\sigma_c(E)$ = scattering cross section for carbon

N_H/V = hydrogen atoms per unit volume in the scintillator

H_c/V = carbon atoms per unit volume in the scintillator

L = diameter of the spherical detector having the same average chord length as the cylindrical detector.

Correction for Multiple Scattering

Some of the incident neutrons lose their energy to the protons in the scintillator by making more than one collision. The pulses from multiple collisions register as one coincident pulse and distort the observed proton spectrum and, hence, the derived incident neutron spectrum.

A correction factor S_s for multiple scattering is given by Broek[5] for the case of a collinear neutron beam incident on the flat end of a cylindrical detector:

$$S_s = 0.090\ N_H/V\ \tau\sigma_H(E_n) + .077\ N_H/V\ r\ \sigma_H(.068E_n) + 1 \qquad (3)$$

where τ is the height of the cylinder

r is the radius of the cylinder

E_n is the energy of the incident neutron.

It seemed reasonable to apply this formula to our case by simply taking τ to be the average chord length, $2L/3$; and r to be $\tau/2 = L/3$. The distorted incident neutron spectrum is thus corrected by dividing by S_s and $f(aL)$.

A program has been coded in Fortran for the CDC 3600 computer to derive the incident neutron flux from the experimental distribution of proton scintillation with respect to pulse-height analyzer channel number. This program, 1977/RPY 146, was compiled by Mrs. Carol Burleson of the Applied Mathematics Division, and its details are given in Appendix A.

A check of the correction factors was carried out experimentally by comparing the derived Pu-Be neutron spectrum from a 5-in. diameter detector of 1-in. thickness with that from a detector of 5-in. thickness. Figure 29 shows that the approximate corrections are really quite adequate, even though the effect of second scattering is certainly significant in the 5- x 5-in. case. This is shown in Figure 30 where the response to 14.8 MeV neutrons of the 1- x 5-in. detector is compared with that of the 5 x 5 in.

Data were obtained over a period of about two million seconds at various sites in the Argonne area. Preliminary results are given in Table 9 and compared with the data presented by Hess and his co-workers at the University of California Radiation Laboratory.[6]

Measurements of total environmental neutron flux at sea level have been carried out recently by several workers, and it is interesting to see how their data and ours compare with those of Hess et al.

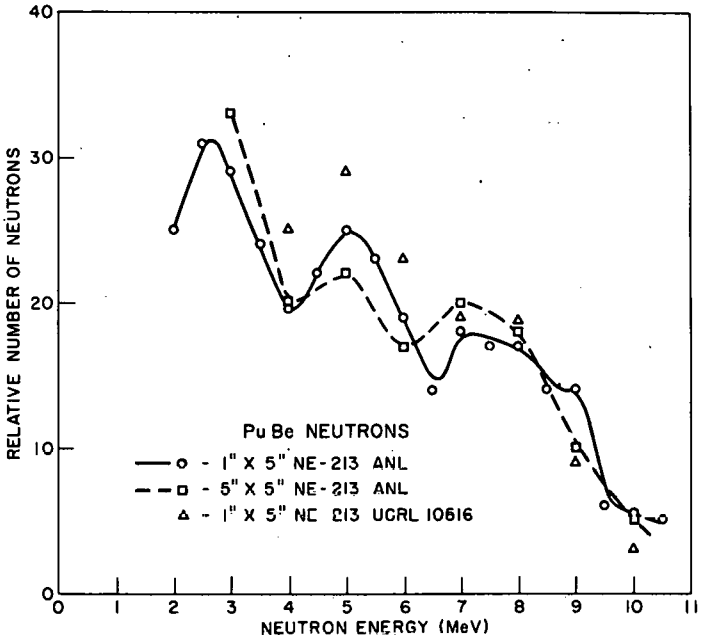

Figure 29

Pu-Be neutron spectrum

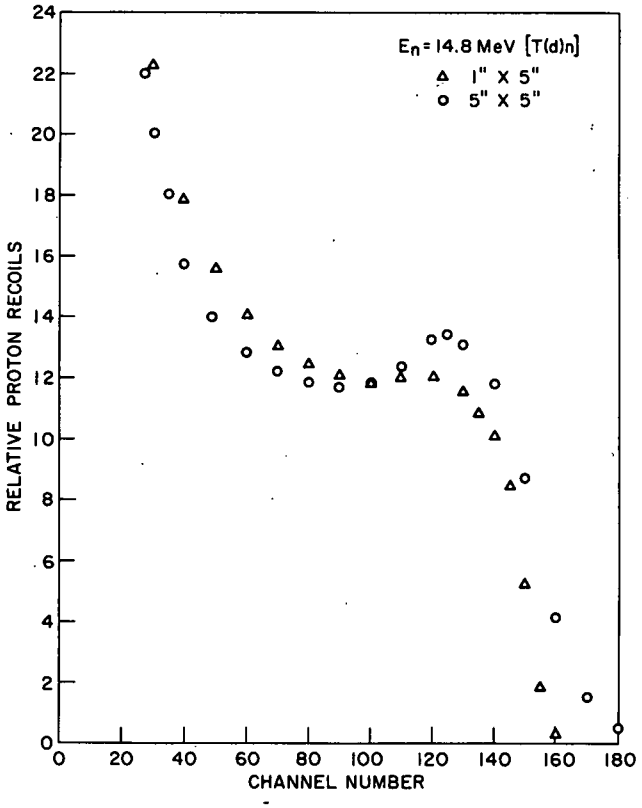

Figure 30

Response of NE 213 liquid scintillator
to 14.8 MeV neutrons

Table 9

Neutron background

Energy, MeV	Neutron/cm²/sec/MeV	
	UCRL	ANL*
1.0	0.00750	0.00360
2.0	0.00250	0.00091
3.0	0.00130	0.00066
4.0	0.00080	0.00038
5.0	0.00050	0.00031
6.0	0.00036	0.00020
7.0	0.00027	0.00015
8.0	0.00020	0.00010

*Time = 1.8×10^6 sec

In view of the many uncertainties in the analysis of the data, precision indexes cannot be supplied. However, it seems reasonable to conclude from Table 10 that the total cosmic-ray neutron flux at sea-level is probably of the order of 0.01 neutron/cm²/sec of which 0.0025 neutron/cm²/sec is between 1-10 MeV.

Table 10

Comparison of environmental neutron flux measurements of various observers

Observer	Cosmic-ray neutron flux, n/cm²/sec		Relative to Hess
	1-10 MeV	Total	
Hess et al.[6]	0.01	0.041	1
Edge[7]		0.013	0.31
Kent[8]		0.0087	0.21
Boella et al.[9]		0.0065	0.16
This experiment	0.0045		0.45

We are indebted to Donald L. Horrocks of the Chemistry Division and to George Ansley of the Electronics Division for their help in the early stages of the pulse-shape discrimination work. We are grateful to Richard Selman for his very many contributions. We appreciate, also, the help of Charles Kelber of Reactor Physics in the problem of scattering corrections.

References

1. W. Daehnick and R. Sherr. Rev. Sci. Instr. 32, 666 (1961).
2. A. Weinberg and E. P. Wigner. Physical Theory of Chain Reactions. University of Chicago Press, Chicago, 1958. p. 715.
3. W. R. Dixon. Nucleonics 8 (4), 68 (1951).
4. K. M. Case, F. de Hoffman, and G. Placzek. Introduction to the Theory of Neutron Diffusion, Vol. 1. U. S. Government Printing Office, Washington, D. C., 1953.
5. H. W. Broek and C. E. Anderson. Rev. Sci. Instr. 31, 1063 (1960).
6. W. Hess, H. W. Patterson, R. Wallace, and E. L. Chupp. U. S. Atomic Energy Commision Report UCRL-8268 (February 1959).
7. R. D. Edge. Nucl. Phys. 12, 182 (1959).
8. R. A. Kent. U. S. Atomic Energy Commission Report HW-SA-2870 (May 25, 1963).
9. G. Boella, et al. Nuovo Cimento 29, 103 (1963).

APPENDIX A

Argonne National Laboratory
Applied Mathematics Division
Program Library 1977/RPY 146

TITLE: Cosmic Ray Neutron Background

PROGRAMMER: Carol Burleson

DESCRIPTION OF THE PROBLEM: Recordings of proton recoils as a function of their energy are made with an organic scintillator. The first phase of the problem, which will be described in this report, proceeds from the experimental distribution of proton counts to the derivation of the incident neutron flux distribution as a function of energy.

The incident neutron flux is isotropic, and all scattering is elastic and Newtonian. The liquid scintillator is enclosed in a cylindrical container. Corrections for multiple scattering and self absorption by the scintillator are included.

MACHINE: CDC 3600, FORTRAN coded

RUNNING TIME: Execution time for the test case submitted was about 6 seconds for 6 values of E(K). In general, the execution time will be about KMAX seconds.

Compilation time for the three subprograms was 24 seconds.

INPUT INFORMATION REQUIRED: Five tables of information, each of which may contain several hundred elements (see listings) and nine individual cards are required as input information for the program.

The program provides options for changing certain parts of the input information for subsequent runs without rereading all of the input listed below. This is done by recycling the program, beginning at some point other than the beginning of the program. If one of these options is selected, the user should be sure to include input information for all READ statements occurring beyond the point from which the program is recycled. (See listings and Program Notes)

Card 1) ESIG(1), DESIG, MLSIG
FORMAT (2F12.6,I6)

ESIG(1) is the first value of the energy in MeV for which the hydrogen elastic scattering cross section is read.

DESIG is the increment in energy (MeV) at which values of the hydrogen elastic scattering cross section is read.

MLSIG is the number of elements in the table of hydrogen cross sections.

Table 1) (SHSIG(LSIG), LSIG = 1, MLSIG)
FORMAT (6E12.6)

SHSIG(LSIG) is the value of the hydrogen elastic scattering cross section $\sigma_H(E)$ at the energy E(LSIG) computed from the input on card 1.

Table 2) (SFHSIG(LSIG), LSIG = 1, MLSIG)
FORMAT (6E12.6)

SFHSIG(LSIG) is the value of the hydrogen elastic scattering cross section in square centimeters at 0.068E(LSIC), viz., $\sigma_H(.068E)$.

Table 3) (SCSIG(LSIG), LSIG = 1, MLSIG)
FORMAT (6E12.6)

SCSIG(LSIG) is the value of the carbon cross section in square centimeters at energy E(LSIG)

Cards 2,3) HNOV, CNOV, OK, V, TAU, R, EL
FORMAT (3E12.6, 3F12.6/F12.6)

HNOV = N_H/V is the number of hydrogen atoms per cubic centimeter in the scintillator.

CNOV = N_C/V is the number of carbon atoms per cubic centimeter in the scintillator.

OK = $1/K$ is the total number of hydrogen atoms in the scintillator.

V is the scintillator volume in cubic centimeters.

TAU is the effective height τ in centimeters of the scintillator in the multiple scattering correction.

R is the effective radius r in centimeters of the scintillator in the multiple scattering correction.

EL is the diameter of the sphere having the same average chord length as the cylindrical detector.

Card 4) KMAX, E(1,3), DELE
FORMAT (I6,2F12.6)

KMAX is the number of values of the energy E(K,M) at which the incident neutron spectrum is calculated.

E(1,3) is the first value of E(K,M) in MeV.

DELE is the increment in the value of the energy (MeV) at which the incident neutron spectrum is calculated.

Card 5) LMAX
FORMAT (I6)

LMAX is the number of energies in the table comprising the standard calibration curve for the pulse-height analyzer.

Table 4) (SCHAN(L), DSCHAN(L), SE(L), L = 1, LMAX)
FORMAT (3F12.6)

SCHAN(L) is the channel number at energy SE(L) on the standard calibration curve for the pulse-height analyzer.

DSCHAN(L) is the derivative of SCHAN with respect to E evaluated at E = SE(L).

Card 6) SCAL, XCAL, XCHINT, EBIN
FORMAT (3F6.2, E12.6)

SCAL is the channel number on the standard calibration curve for the pulse-height analyzer at some chosen calibration energy.

XCAL is the channel number at the current gain setting of the analyzer at the same chosen calibration energy.

XCHINT is the channel number (positive or negative) of the zero-point of energy for the current gain setting.

EBIN is the energy increment (MeV) about E(K,M) used to compute the derivative of proton counts with respect to energy, $\Delta N_p/\Delta E$.

Card 7) T, JMAX, JCHAN
FORMAT (E12.6, 2I6)

T is the elapsed time in seconds during which data was taken.

JMAX is the total number of channels (not channel numbers) for which the number of proton counts are read into the program.

JCHAN is the lowest channel number at the current gain setting for which proton counts are read into the program.

Table 5) (CONTS(J), J = 1, JMAX)
FORMAT (12I6)

CONTS(J) is the number of proton counts N_p in channel (JCHAN-1+J) at the gain setting for the current run.

Card 8) KWRITE
FORMAT (I6)

KWRITE = $\{\frac{1}{2}\}$ controls the set of variables to be output. (See POSSIBLE OUTPUT below.)

Card 9) NEXT
FORMAT (I6)

NEXT is an integer which may be set from 1 to 6 to recycle the program for the next computation. The six options are explained in Program Notes.

POSSIBLE OUTPUT: The output is controlled by the input variables KWRITE. Two options are provided:

1) KWRITE = 1

The output includes the following, appropriately headed:

Input variables V, τ, r, L, T, EBIN, SCAL, XCAL, XCHINT (headed V, TAU, R, L, T, EBIN, SCAL, XCAL, XCHINT).

A table of ΔN_p and $\eta(E)$ as functions of energy (headed DQCONT, ETA, E respectively) where N_p is the differential proton spectrum for the energy bin width 2XEBIN, and $\eta(E)$ is the computed incident neutron flux.

2) KWRITE = 2

In addition to the above, the output includes a table of XCHAN, N_p, N_p (dSCHAN/dE), S_s, and f(aL) as functions of energy (headed XCHAN, PCONTS, QCONTS, SS, FAL, E, respectively), where XCHAN is the computed experimental channel number at energy E, N_p is the number of proton counts in that channel, S_s is the correction factor for multiple scattering, and f(aL) the correction factor for self-absorption.

RESTRICTIONS AND LIMITATIONS: The tables of the hydrogen scattering cross sections $\sigma_H(E)$ and $\sigma_H(.068E)$ need not be given for the same energies at which $\eta(E)$ is to be computed, although values should be given at sufficiently small energy intervals to insure that the necessary interpolation is sufficiently accurate. Similarly, the tables of SCHAN and DSCHAN need not be changed to correspond to each new value of EBIN, but the energy interval at which they are tabulated should be of the same order of magnitude as EBIN.

The assignment of experimental channel number to a given energy is accurate to within $\pm .5$ channels.

The ranges of energy for the tables of σ_H, SCHAN, the input table of proton counts and for the output need not agree.

Scattering from carbon in the scintillator is ignored in the multiple scattering correction.

The computation of the incident neutron flux from the experimental distribution of proton scintillations with respect to pulse-height analyzer channel number can be divided into three parts: 1. the calibration of the analyzer and the subsequent computation of the number of proton scintillations per unit energy as a function of energy; 2. the calculation of the incident neutron distribution from the observed proton distribution using a familiar equation from nuclear physics; 3. the correction of the derived neutron spectrum for multiple scattering and self-absorption in the detector, using formulas for these corrections which are appropriate to the geometry of the experiment.

1. Calculation of the number of proton counts per unit energy, $N_p(E)$

The calibration of the analyzer for the gain setting used during a particular data run is complicated by the fact that the response of the organic scintillator used as a proton detector is not a linear function of the proton energy. A standard calibration curve giving channel number as a function of proton energy is available, however.

For each data run, the channel number XCAL at the current gain setting is determined for protons at some known energy. The channel number SCAL on the standard calibration curve can also be determined for the same energy. In addition, the channel number XCHINT of the zero-point of energy must be determined for each run. Then for energy E,

$$\text{XCHAN(E)} = \left(\frac{\text{XCAL-XCHINT}}{\text{SCAL}}\right)\cdot\text{SCHAN(E)}$$

where

XCHAN(E) is the channel number at energy E for the current gain setting, corrected for non-zero origin, and

SCHAN(E) is the channel number at E on the standard calibration curve.

The data, collected in the form of proton count per channel number, can now be put into the form of proton counts per unit energy with respect to energy, $N_p(E)$. For some energy E, the number of proton counts per channel recorded at E, N_p', is the number of counts in channel number SCHAN(E)-XCHINT. The number of counts per unit energy at E is given by

$$N_p(E) = N_p'(\text{XCHAN(E)-XCHINT}) \cdot \frac{d(\text{XCHAN(E)})}{dE}$$

where

$$\frac{d(\text{XCHAN(E)})}{dE} = \text{number of channels per unit energy.}$$

Because the response of the scintillator is a nonlinear function of proton energy, $\frac{d(XCHAN(E))}{dE}$ must be evaluated from the slope of the standard calibration curve SCHAN(E), viz., $\frac{d(XCHAN(E))}{dE} = \frac{d(SCHAN(E))}{dE} \cdot \left(\frac{XCAL-XCHINT}{SCAL}\right)$.

2. Derivation of the incident neutron spectrum

To derive the incident neutron spectrum from the observed spectrum of protons in the scintillator, the familiar relation for n-p scattering given in reference 5 is employed.

$$\frac{N_p(E)}{V} = \frac{N_H}{V} \int_E^\infty \frac{\sigma_H(E_n)}{E_n} \eta(E_n) dE_n$$

where $N_p(E)$ is the number of recoil protons per unit energy.

N_H/V is the number of free protons per unit volume in the scattering material.

$\sigma_H(E_n)$ is the hydrogen elastic scattering cross section at energy E_n.

$\eta(E_n)$ is the number of incident neutrons per unit energy per unit area at energy E_n impinging on the scattering material.

The result of differentiating both sides of the equation and rearranging factors is

$$\eta(E) = \frac{-1}{N_H/V} \frac{E}{\sigma_H(E)} \frac{dN_p(E)}{dE}$$

In evaluating $\eta(E)$, the following procedure is used:

(a) A set of energies E(K) at which the spectrum $\eta(E)$ is to be evaluated is determined.

(b) A small energy increment EBIN is selected which is of the order of magnitude of the energy resolution of the system. $N_p(E)$ is evaluated at E = E(K) + EBIN and E = E(K) - EBIN for each value of E(K).

(c) Then

$$\eta(E(K)) = \frac{-1}{N_H/V} \frac{E(K)}{\sigma_H(E(K))} \left[\frac{N_p(E(K)+EBIN) - N_p(E(K) - EBIN)}{2 \cdot EBIN \cdot V \cdot T}\right].$$

The additional factors V and T are introduced because the experimental N_p is the total number of proton scintillations observed in a scintillator of volume V during a time T.

3. Correction of $\eta(E)$ for multiple scattering and self-absorption in the absorber.

In this experiment, a spherically symmetric (isotropic) spatial distribution of neutrons is impinging upon a cylindrical detector. This peculiar geometry makes the calculation of multiple scattering and self-absorption corrections difficult. For each correction, a formula derived for a different geometry is adapted for use with the present geometry and is assumed to be a good approximation.

(a) Correction for self-absorption in the scintillator

Since the incident neutron flux is spherically symmetric, the shape of the detector will be approximated by a sphere having the same average chord length as the actual cylindrical detector. The formula for the factor by which a spherically symmetric incident neutron flux is attenuated in a spherical detector is given in reference 3.

$$f(aL) = \frac{3}{(aL)^2}\left[\frac{aL}{2} + e^{-aL} - \left(\frac{1-e^{-aL}}{aL}\right)\right]$$

where $a = a(E) = 2\sigma_H(E) \cdot N_H/V + \sigma_c(E) \cdot N_c/V$

$\sigma_H(E)$ = scattering cross section for hydrogen

$\sigma_c(E)$ = scattering cross section for carbon

N_H/V = hydrogen atoms per unit volume in the scintillator

N_c/V = carbon atoms per unit volume in the scintillator

L = the diameter of the spherical detector having the same average chord length as the cylindrical detector.

(b) Correction for multiple scattering

Some of the incident neutrons lose their energy to the protons in the scintillator by making more than one collision with the protons. The scintillation pulses from all collisions made by any one neutron register as one coincident pulse, thus distorting the observed proton spectrum and the incident neutron spectrum derived from it.

The correction factor used for multiple scattering is given in reference 5. The experimental geometry for which this formula is derived is assumed to be a collinear neutron beam incident upon one face of a cylindrical detector. The correction factor S_s is given by

$$S_s = 0.090\, N_H/V\, \tau\, \sigma_H(E_n) + .077\, N_H/V\, r\, \sigma_H(.068E_n) + 1$$

where τ is the height of the cylinder

r is the radius of the cylinder

E_n is the energy of the incident neutron

To use the above formula for S_s with the geometry of the present experiment, τ is taken as the average chord length and r as half the average chord length of the cylindrical detector.

4. Final expression for $\eta(E)$

The final expression for $\eta(E)$ is obtained by dividing the uncorrected expression for $\eta(E)$ in section 2. by S_s and f(aL).

$$\eta(E) = -\frac{1}{N_H/V}\,\frac{E(K)}{\sigma_H(E(K))}\,\frac{N_p(E(K)+EBIN) - N_p(E(K)-EBIN)}{2\cdot EBIN\cdot V\cdot S_s\cdot f(aL)\cdot T}$$

In the program, $\eta(E)$ is derived from the raw data in three steps, as follows:

(a) The analyzer is calibrated and $\Delta N_p(E(K)) = -[N_p(E(K) + EBIN) - N_p(E(K) - EBIN)]$ is computed for each E(K).

(b) The factor

$$D = \frac{2\ EBIN}{E(K)} \cdot N_H \cdot \sigma_H(E(K)) \cdot S_s \cdot f(aL) \cdot T$$

is computed for each E(K).

(c) The quotient

$$\eta(E(K)) = \frac{\Delta N_p(E(K))}{D}$$

is computed for each E(K).

Program Notes

1. Description of the program

The program is divided into a main program and two subroutines, as follows:

PROGRAM NEUTBAK handles part of the input and all of the output, calls the subroutines, computes E(K) and $\eta(E(K))$, and recycles the program according to the option chosen by the user. The user may select one of six options described below, depending upon which part of the input data he wishes to change after the first run.

NEXT = 1: Tables of hydrogen and carbon cross section are to be changed. Recycle from statement 100 of NEUTBAK.

NEXT = 2: The values of E(K) are to be changed. Recycle from statement 101 of NEUTBAK.

NEXT = 3: The standard calibration table for the detector is to be changed. Recycle from the beginning of CHAN.

NEXT = 4: The calibration of the detector for the current run is to be changed. Recycle from entry point CHANGE1 of CHAN.

NEXT = 5: The table of counts per channel number is to be changed. Recycle from the entry point CHANGE2 of CHAN.

NEXT = 6: Terminate the program.

For each option 1-5, the user must read in again all data included in READ statements subsequent to the point from which the program is recycled, even though these data may be the same as those in the previous run.

SUBROUTINE DCOMP computes the factor D for each value of E(K).

SUBROUTINE CHAN calibrates the detector for the current gain setting and computes $\Delta N_p(E(K))$.

2. Variable definitions

ESIG(LSIG)	The energies for which the tables of cross sections are read into the program.
LSIG	Current value of the index.
DESIG	Difference between consecutive values of ESIG.
MLSIG	Maximum value of LSIG
SHSIG(LSIG)	Hydrogen elastic scattering cross section $\sigma_H(E)$ at ESIG(LSIG)
SFSIG(LSIG)	Hydrogen elastic scattering cross section $\sigma_H(E)$ at .068 ESIG(LSIG).

SCSIG(LSIG)	Carbon elastic scattering cross section $\sigma_C(E)$ at ESIG(LSIG).
HNOV	Number of hydrogen atoms per unit volume in the scintillator, N_H/V.
CNOV	Number of carbon atom per unit volume in the scintillator, N_C/V.
OK	Total number of hydrogen atoms in the scintillator, $N_H = N_H/V \cdot V = 1/K$.
V	Volume of the scintillator.
TAU	τ, the average chord length of the detector (for use in the formula for the multiple scattering correction).
R	r, half the average chord length of the detector (for use in the formula for the multiple scattering correction).
EL	Diameter L of the sphere whose average chord length is the same as that for the detector; for use in the formula for the self-absorption correction.
E(K,M)	E(K,3) are the energies (referred to as E(K) in Appendix A) at which the neutron spectrum is computed. E(K,1) = E(K,3) - EBIN E(K,2) = E(K,3) + EBIN
KMAX	Number of energy values at which the neutron flux is computed.
DELE	Difference in consecutive values of E(K,3)
HSIG(K)	Value of $\sigma_H(E)$ at E(K,3)
FHSIG(K)	Value of $\sigma_H(E)$ at .068 · E(K,3)
CSIG(K)	Value of $\sigma_C(E)$ at E(K,3)
PAL	Interpolation factor for computing values of cross sections at energies E(K,3) from the values read in at energies E(LSIG).
AL	aL the argument in the formula for f(aL).
FAL(K)	f(aL), the correction factor for self-absorption at energy E(K,3).
SS(K)	S_s, the correction factor for second scattering, at energy E(K,3).

DOT(K)	The value of $\sigma_H(E) \cdot f(aL) \cdot S_s \cdot N_H/E$ at $E = E(K,3)$
LPSIG	Values assigned to the index LSIG for use in a DO-loop.
SE(L)	Energies for which the standard calibration table is read.
SCHAN(L)	Channel number corresponding to energy SE(L) on the standard calibration curve.
DSCHAN(L)	$\frac{d(SCHAN(L))}{dE}$ at energy SE(L).
LMAX	Number of values in standard calibration table.
SCAL	Channel number on standard calibration curve at some calibration energy.
XCAL	Channel number at current gain setting for the same calibration energy.
XCHINT	Channel number at zero energy at the present gain setting.
EBIN	Energy increment about E(K,3) for use in evaluating the derivative of the proton spectrum at energy E(K,3).
CALFAC	Calibration factor for analyzer for current gain setting.
LP	Value assigned to index L for use in a DO-loop.
ZCHAN(K,M)	Floating-point variable to which the value of the channel number at E(K,M) for the current gain setting is temporarily assigned.
XCHAN(K,M)	The channel number at E(K,M) for the current gain setting; an integer.
DXCHAN(K,M)	$\frac{dXCHAN(K,M)}{dE}$ at energy E(K,M).
POL	Interpolation factor used in computing XCHAN(K,M) from SCHAN(L) when the energies SE(L) and E(K,M) are not identical.
T	Duration of time for which data (CONTS) was taken.
JMAX	Number of channels for which counts per channel are read.
JCHAN	Channel number of the first channel for which data is read.

CONTS(J)	Proton counts in channel number J+JCHAN-1.
KP	Value assigned to index K for use in a DO-loop. Subsequently, it is the index of smallest value of energy E(K,1) for which data (CONTS) has been read into the program.
KFIN	Index of largest value of energy E(K,2) for which data (CONTS) has been read into the program.
PCONTS(K,M)	Proton counts per channel number found in the channel corresponding to E(K,M).
QCONTS(K,M)	Proton counts per unit energy at energy E(K,M) = $N_p(E(K)\pm EBIN)$
DQCONT(K)	The value $N_p(E(K)-EBIN)-N_p(E(K)+EBIN)$
D(K)	Denominator D (see appendix A) at energy E(K,3).
ETA(K)	Incident neutron spectrum $\eta(E)$.
KWRITE	Integer which controls output option.
NEXT	Integer which controls options for recycling the program.

SPECIFIC PRIMARY IONIZATION BY BETA RAYS

F. F. Rieke

Experiments are being undertaken to measure the number of primary ionization acts per unit path by beta rays of given energy passing through various gases. The method to be used has been employed previously by McClure[1] and consists of measuring, under suitably controlled conditions, the efficiency of a GM tube filled with the gas in question. McClure's results concern H_2 and rare gases only, and the latter are now known to be subject to an ambiguity because admixtures of hydrogen were used to stabilize the operation of the GM tube. (The efficiencies are not additive in gas mixtures.) It is intended that this uncertainty will be cleared up and that data will be obtained for a wider variety of gases. By modifications of the method, information about indirect processes of ionization will also be obtained.

The components of the apparatus, including a small double-focusing beta-ray spectrometer as a source of monoenergetic electrons in the range 0.1-2 MeV, have all been constructed and tested. The complete apparatus is now being assembled.

Reference

1. G. W. McClure. Phys. Rev. 90, 796 (1953).

AN UNUSUAL CASE OF RADIUM TOXICITY*

H. F. Lucas, Jr., R. E. Rowland, C. E. Miller,** R. B. Holtzman, R. J. Hasterlik,† and A. J. Finkel**

Abstract

A case history of a patient with radium toxicity is presented. The patient, before death at age 54, was found to have large amounts of Ra^{226} in a femur amputated in the treatment of an osteoblastic osteogenic sarcoma. The total body burden was estimated by several methods. Whole-body counting showed a body burden of about $0.60 \pm 0.06\ \mu C$ of Ra^{226}. Radiochemical analyses of small sections of the amputated femur gave an estimated burden of about $0.4\ \mu C$ and Rn^{222} breath measurements indicated a burden of about $0.17\ \mu C$ Ra^{226}. Autoradiographic studies indicated a total burden of about $2\ \mu C$, an estimate in agreement with that from bone damage observed in Roentgenograms.

It was estimated that the Ra^{226} had been incorporated into the skeleton about 40 years prior to these measurements. While the patient received a series of weekly injections at about this age, there is a lack of direct evidence that they contained radium. The coefficient of excretion, the ratio of RaD to Ra^{226} in bone samples, and Roentgenographic findings are consistent with exposure to Ra^{226} at about 18 years of age.

The route and rate of intake of the original exposure, as deduced from the hot-spot-to-diffuse ratios in the autoradiographs, are consistent with injection over a period of 3 months and correspond to an intravenous dose of about $360\ \mu C$.

The discrepancies in the estimate of the body burden were apparently due to the extensive turnover of large areas of bone which were subsequently seen in the autoradiographs and microradiographs. The whole-body gamma counting and the chemical methods showed only averages of the remaining Ra^{226}, while the autoradiographs, indicating where activity was present, showed the nature of the original deposits. The importance of the initial amount of radium in the body on the carcinogenic process is discussed.

---

*Published in Am. J. Roentgenol. 90, 1042-1051 (1963).

**Health Division.

†Argonne Cancer Research Hospital, Chicago, Illinois.

8

THE LOW-LEVEL GAMMA COUNTING ROOM: RADON REMOVAL AND CONTROL

Henry F. Lucas, Jr.

An underground counting room has been constructed to permit the continuation of studies requiring the quantitative assay of very low intensity gamma-ray emitting sources. This room was placed underground to provide increased shielding from nearby sources of fast neutrons and from the nucleonic component of cosmic rays.

The air supply for this room is controlled. Airborne radioactive particles are removed by filtration, and the radioactive gases A^{41} and Rn^{222} are eliminated either by aging for several half-lives in large steel tanks or by adsorption on cooled charcoal. Since the flow rate of air into the room is small compared to the volume, the residence time of the air within the underground room is always much longer than the 1.8-hour half-life of A^{41}. The combined effects of dilution and decay should be sufficient to eliminate the problems resulting from radioactive argon. Control of the radon is much more difficult because of its longer half-life (3.8 days) but is very important since variations in the level of Rn^{222} in the atmosphere[1,2] produce background instabilities in the gamma-ray detectors equal to 10 to 20% of background; these instabilities are much larger than can be tolerated. Reduction of the radon concentration to a low level minimizes these instabilities. This report describes the process by which the removal and control of the Rn^{222} in air is accomplished.

Design

Radon was removed by adsorption on cooled (-40 to -80°C) activated charcoal. Since quantitative removal of radon on the charcoal is obtained only if the air (or gas) is free of water and CO_2, the system shown schematically in Figure 31 is required. The specifications for each component were as follows:

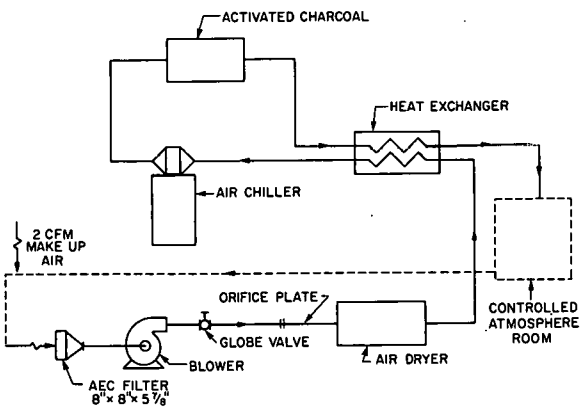

Figure 31

Radon Adsorption Apparatus - Bldg. 203

1. Blower: a turbo compressor with a capacity of 70 cu ft/min at a total pressure of 24 oz/sq in., Spencer turbine model B-70-24 with 1-HP belt drive.

2. Air Dryer: a molecular-sieve water and carbon-dioxide

adsorption unit designed for a flow rate of 30 cfm with an adsorption rate for water of 0.8 lbs/hr and for carbon dioxide of 0.37 lbs/hr. The air leaving the adsorber has a dewpoint of -110°F and contains a maximum of 10 ppm carbon dioxide. A two-bed unit provides continuous operation, with electric regeneration and manual switchover from one drying bed to another. Three-way valves cannot be used (because of excessive external air leakage into the system). Model #BWC-500-F-SP (CIBIEI) Lectrodryer* designed for 100 psig, Sieve type 5A, 1/16 in. pellets is used.

3. Heat Exchanger: an air-to-air heat exchanger capable of cooling 30 cfm of air from 128°F to 0°F with return air at -90°F. Trane Company, bronzed aluminum, two 6 in. units in series.

4. Air Chiller: a low-temperature air cooler capable of chilling 30 cfm of air from 0°F to -90°F. Murphy and Miller SVO-6W-90.

5. Activated Charcoal: activated coconut charcoal 6-8 mesh, 150 lbs, Fisher Scientific Company, Chicago, Illinois.

6. Orifice Plate: 1.100 in. dia., reading, 3.0 in. W.C. (water column) at 30 scfm, 14.7 psia, 90°F.

Operation and Testing

Because the charcoal adsorption chamber would require a high temperature bakeout the initial design called for replaceable charcoal canisters which could be removed for reactivation. They were mounted in a box insulated with 4 in. of fiberglass. Access was provided by a large removal door. The charcoal was contained in 18 canisters (1.5 lbs each) making a bed of 1.5 in. depth. This unit was eventually replaced with another for the following reasons: 1) the door leaked around the gasket; 2) the temperature rise between the chiller and the exit of the charcoal bed was 40-50°C rather than the 11°C calculated; 3) leaks in the chiller housing and the box containing the charcoal canisters could not be repaired without extensive rebuilding.

Before replacing the defective charcoal bed, the possibility of in situ bakeout was evaluated. A 500-Watt electrical heater was installed within the charcoal bed. Power consumption was controlled with an autotransformer. Air from the molecular sieve with a water content of 0.6 ppm[3] was flowed through the bed at a rate of 150 l./min. At a temperature of 130°C the water content of the air leaving the charcoal bed increased to 2.1 mg/l. After 24 hr, a temperature of 145°C was reached, and the water content of the air had decreased to a value less than 0.05 mg/l. Thus it appeared that water was removed from the charcoal at

*Pittsburgh Electrodryer Division, McGraw-Edison Company, Pittsburgh, Pa.

a temperature lower than the upper limit of about 250°C imposed by the gaskets and the limit of about 175°C imposed by the refrigeration system.

The efficiency of radon adsorption by the 18-canister, 27-lb charcoal bed was determined at a flow rate of 9 scfm. At this flow rate, the temperature of the bed was reduced from its initial value of +30°C to -13°C at 2 hours and -48°C at 6 hours after startup. As shown in Figure 32, the radon concentration decreased to a minimum value of 2×10^{-15} C/l. after 8 hours and increased thereafter. Since the radon adsorbed on the charcoal bed at the termination of this experiment was 0.38 μC, retention of radon on the charcoal was excellent, and this system would be suitable for operation for continuous periods of up to a week. However, for the previously mentioned reasons, this charcoal bed was removed and replaced with a different unit.

The new charcoal bed (Figure 33) was designed to contain 150 pounds of 6-8 mesh activated coconut charcoal. This charcoal was contained in a bed having a 12 x 17-in. cross section and a mean depth of approximately 30 in. Three 500-Watt heaters were included for bake-out of the charcoal. In addition, twenty-one copper-constantan thermocouples monitored the temperature of the heaters, the cooling coil, and various regions of the charcoal bed.

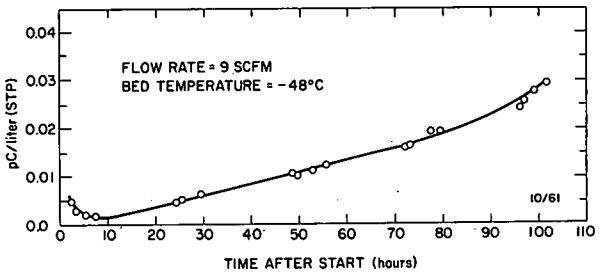

Figure 32

Efficiency of radon adsorption by the 18-canister, 27-lb charcoal bed

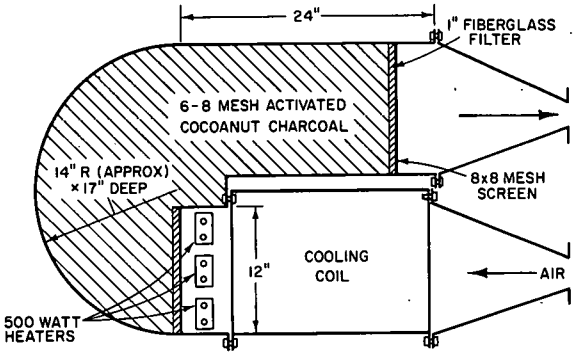

Figure 33

Design of 150-lb charcoal bed

Gaskets were of silicone rubber,* cemented in place. All joints were tested until bubble tight at 1 psi. The temperature of the charcoal bed during bakeout varied from 180°C at the inlet to 140°C near the walls and at the outlet. The temperature of the air entering the charcoal bed when cooling varied from -95 to -90°C as the flow rate varied from 2 to 30 scfm. The temperature of the air near the walls and at the exit of the

*Chorlastic 500 sheets, cement #251, The Connecticut Hard Rubber Co., 407 East Street, New Haven, Connecticut.

charcoal bed was highly dependent on flow rate, being 10, 20, and 40°C higher at flow rates of 30, 3, and 2 scfm, respectively. However, even at 2 scfm, nearly one-third of the charcoal bed was cooler than -70°C.

The radon concentration in the air leaving the charcoal bed has been followed from startup to the present. In one three-week period, a flow rate of 30 scfm for eight hours was followed by a flow rate of 2.0 scfm for the remaining time. Samples of 600 to 1000 liters were collected at 3- to 4-day intervals, and all were found to have radon concentrations of less than 5×10^{-17} C/l. An exact value could not be obtained because of the small amount (a few ppm) of carbon dioxide in the air. While this concentration did not affect the retention of radon on the large charcoal bed, it was necessary to use a Drierite-Ascarite trap in the analysis system, which has been found to release small amounts of radon.[4] Approximately 1 μC of radon was adsorbed on the charcoal at the end of this test period. Thus, retention of radon is extremely good, and reactivation may be required only after several months of continuous operation. Testing is continuing for longer times at 5 scfm.

Radon in Vault Air

The radon concentration of the air in the underground counting room - otherwise known as "the vault" - has been found to be very difficult to control in spite of elaborate precautions taken in the design. Briefly, the vault is a large, concrete box 16 x 30 x 15 ft high (7200 cu ft). It is lined on its inner surface with 28 ga galvanized sheet iron; all joints are lapped and soldered. Gaskets are used on all fastenings to the concrete. Entrance to the vault is gained through an air lock. The temperature is controlled to within ±1°F and the humidity is maintained at less than 50% R.H. at 80°F.

The radon concentration in the vault air has been found to vary from as little as 0.03 pC/l. to as high as 5 pC/l. The higher value was obtained when none of the sources of flush air was being used.

Measurements of the concentration of radon in the vault air over a period of 40 days are summarized in Figure 34. In the first half of this period outside air was pumped through the "aged air system" at a flow rate of 3.5 scfm. The radon concentration varied from 0.2 to 1.1 pC/l. reflecting the variation in the outside air during this period.[1] On July 27, the vault was flushed for 7.5 hours with radon-free air at a flow rate of 30 scfm. The flow rate was then reduced to 2.0 scfm and the radon rapidly increased to about 1 pC/l. However, increasing the flow rate of radon-free air to 3.0 scfm reduced the radon concentration to about 0.12 pC/l.

It seems likely that the large reduction in radon concentration resulting from such a small increase in flush rate was due to the increased pressure differential developed across the walls of the vault. The pressure differential across the air lock is a very sensitive function of flow rate having average values of 0.02, 0.04, 0.1, and 0.2 inch W.C. for input rates of 2, 3, 7, and 10 scfm, respectively. However, large pressure fluctuations about these mean values occur, which are caused by changes in the air temperature as the control units cycle. Generally these are in the range ±0.1 inch W.C. with an occasional value as high as 0.2 inch W.C. - sufficiently large to reverse the pressure gradient completely. The increased pressure due to the 3.0 scfm input of radon-free air presumably had so large an effect because it greatly reduced the number of negative pressure excursions and thus reduced the leakage of relatively highly radioactive air from outside through cracks in the walls.

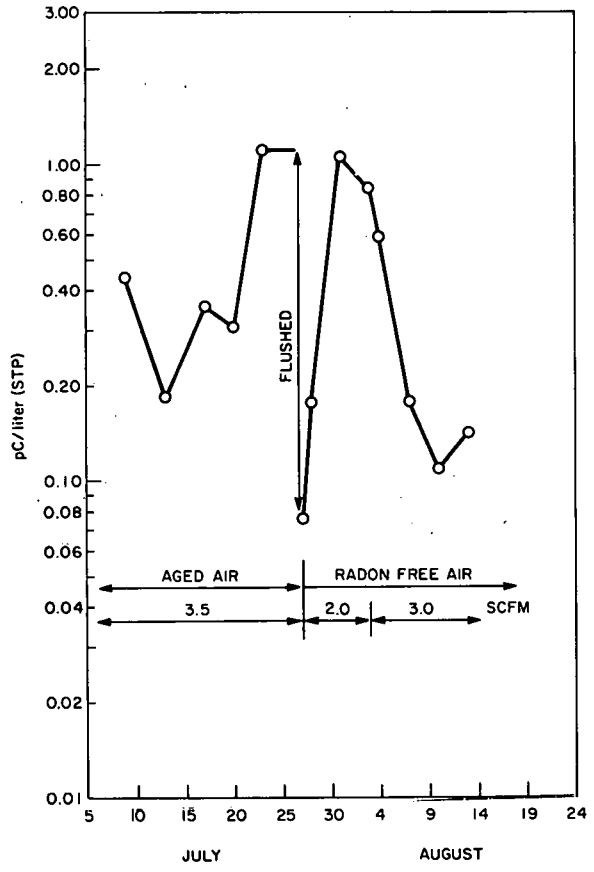

Figure 34

Concentration of radon in vault air

The rate of influx of contaminated air under these conditions can be estimated by the following argument. If we assume that the recirculating fans completely mix the air within the vault, then a flow rate of 3.0 scfm into a volume of 7200 cu ft should produce a "residence half-time" of about 30 hr. Since the input air is also water-free, the relative humidity in the vault (assuming no occupants and no leaks) should be characterized by the same 30-hr half-time. However, because it actually required 40 hr for the relative humidity to drop from 30 to 15%, the leakage of outside air must have been about 0.2 scfm at 100% R.H. or 0.4 scfm at 50% R.H. Similar reasoning suggests that the average rate of radon input to the vault was about 3 pC/min. The radon concentration of the outside air thus appeared to be about 0.3 pC/l. at 50% R.H. or 0.6 pC/l. at 100% R.H.

Several months prior to the above measurements, it had been observed that the concentrations of radon in the air on the uncontrolled side of the air lock doors ranged from 0.4 to 0.9 pC/l. while the relative

humidity during this period was 50 to 60%. A leakage of this air into the vault at an average rate of 0.2 scfm could be obtained if, for four minutes out of each hour, the pressure differential across the air lock became negative by only 0.04 inch W.C. Since negative pressures of this magnitude were observed for six minutes per hour over a two hour period, it appears that the observed radon contamination resulted from the influx of high radon air during brief periods of negative pressure gradient.

It must, therefore, be concluded that the air lock system should be made more effective and that other sources of leakage should be reduced to a minimum. Increased pressure should eliminate all external sources of radon and allow the concentration in the vault air to approach an expected level of 10^{-14} C/l. or lower.

Special thanks are due Frank Markun, Richard Selman, and Robert M. Parr for assistance in the studies in the control of radon. Very great thanks are due William Ware (Plant Engineering) for his work in the design of the radon removal system. I would like to give special thanks to L. D. Marinelli and J. E. Rose for their encouragement and interest.

References

1. H. Moses, A. F. Stehney, and H. F. Lucas, Jr. The Effect of Meteorological Variables upon the Vertical and Temporal Distributions of Atmospheric Radon. J. Geophys. Res. 65 (4), 1223 (1960).

2. H. Moses, H. F. Lucas, Jr., and G. A. Zerbe. The Effect of Meteorological Variables upon Radon Concentration Three Feet Above the Ground. J. Air Pollution Control Assoc. 13 (1), 12 (1963).

3. Linde Molecular Sieves. Form 9693-D, Linde Company Division of Union Carbide Corporation, New York.

4. A. F. Stehney, W. P. Norris, Jr., H. F. Lucas, Jr., and W. H. Johnston. A Method for Measuring the Rate of Elimination of Radon in Breath. Am. J. Roentgenol. 73, 774 (1955).

GENERAL TECHNICAL PROBLEMS IN RADIOLOGICAL PHYSICS*

Leonidas D. Marinelli

Introduction

In the three areas of medicine in which radiological physics is today involved, x-ray diagnosis, radiotherapy, and nuclear medicine, there are certain recurring problems, as well as problems which are specific to a particular area. The distinction will not be discussed per se because it will become evident as we try to cover each field separately.

I. X-Ray Diagnosis

The most widespread medical use of Roentgen rays has been, and is still, for diagnosis. This was also their first use. Toward the end of 1895, Wilhelm Conrad Roentgen persuaded his wife to place her hand on a photographic plate on which he beamed his new rays for 15 minutes. The result was the first radiograph and Roentgen became the first x-ray diagnostician.

Basically, diagnostic techniques involve a properly prepared patient, a radiating source, and the apparatus and materials necessary to record the image resulting from the interactions of the radiation beam and the patient (Figure 35).

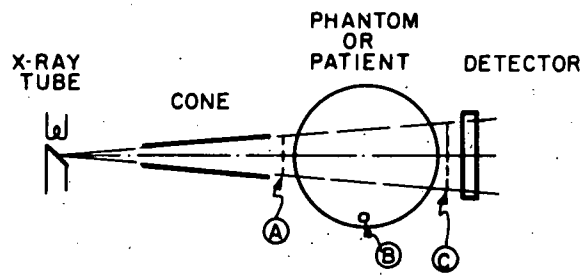

Figure 35

Schematic arrangement for diagnostic radiology. (From H. O. Wyckoff, Reference 4.)

The development of those portions of the diagnostic techniques involving only the adequate preparation of the patient has been practically the unchallenged domain of the roentgenologist. On the other hand, the development of the radiation sources has rested with industry without much aid from others; this is probably because the commercial demand for diagnostic x-ray apparatus has almost always been large enough to support the cost of the development and research instigated and demanded by the diagnosticians.

---

*Presented at the Colloqui Sui Rapporti Tra Fisica E. Medicina, Levico-Roncegno, Italy, September 14-20, 1964.

This situation has led to the establishment of relatively small, but extremely well-informed groups of electrical engineers and industrial research physicists who have transformed the crude tube of Wilhelm Roentgen into today's variety of diagnostic apparatus. As a rule, these groups have dealt directly with the roentgenologist without too much assistance (or interference) from hospital physicists. A very recent result of this teamwork is the registration of detailed radiographic information onto magnetic tape or similar memory devices in order to retrieve it selectively for more deliberate appraisal via television circuits. Along the same line, diagnosticians have also coded the information carried by the radiographic image onto cards suited to automated selection and correlation by means of commercial business machines.

The trend in everyday diagnostic instrumentation, however, seems to be toward a predominance of electronic accessories aimed at more precise control of the image by phototimers, and pulsed operation of grid tubes aimed at shortening the exposure time, resulting in simultaneous reduction of dose to the patient and of blurring due to motion. The advent of the image intensifier has brought electron optics into the field. Without going into many details it seems that the main advantages resulting from this are reduction of patient's dose and increase in image brightness, which have made possible, by allowing constriction of the target size, both amplification of radiographic images and more frequent use of cineradiography.

For improvements in the registration of the image one would have to look into amelioration of some properties of the radiographic film, which has received the consistent attention of only a few major manufacturers throughout the world, and into the fluoroscopic screen which, instead, seems to have been developed practically at random and manufactured by a large number of small firms. A recent advance that promises to increase information in x-ray diagnosis, with a concurrent reduction of dose, is the use of CsI and KI in radiographic intensifying screens.[1] These crystals, well-known for their performance in scintillation spectrometry, seem to excel in all the steps leading to the conversion of x-ray radiation of diagnostic quality into optimal registration on a photographic film. Thus, compared with the generally used screen material, $CaWO_4$, they exhibit: a) a higher absorption coefficient, b) twice the luminescent efficiency per unit of photon energy absorbed and, c) better spectral matching with the sensitivity of x-ray films (since the wavelength of the light emitted is around 4300 Å). Whether these materials will ever become practical will depend on the circumvention of some annoying drawbacks, such as hygroscopy of the crystals.

A novel and recent contribution to the general aim of x-ray diagnosis has been the effort of Dr. B. Jacobson to estimate the amount X_i

of a chemical element i present in a live patient by x-ray spectrophotometry in vivo.[2] This estimate is based on the solution of a set of n simultaneous equations of the type:

$$I_1 = I_{01} \exp - (\mu_{11} X_1 + \mu_{12} X_2 + \ldots\ldots + \mu_{1n} X_n)$$

associated with the transmitted portion I_1 of photons of total energy I_{01} incident on the mass of material containing element i = 1, 2 . . . n, the absorption coefficients of which are designated by μ.

This approach cannot succeed unless the μ's are substantially different; at present this method has shown some measure of success only in the estimate of iodine, hydroxyapatite, and soft tissue. The equations are solved by analog computer methods as illustrated in Figure 36, namely, by interposing the object to be studied beyond three wedges of I^{127}, bone salt, and water in the path of three successive monochromatic x-ray beams originating from a rotating multielement anode and aimed at a properly placed scintillator. The apparatus is set by having the beams cross the wedges at their thickest part; when the object to be measured is interposed, feedback circuits will move the wedges toward their thinner edges until the scintillator registers the pre-set intensity at all wavelengths. By these means the displacement of the wedges will give a measure of the unknown quantities. Some data on bone salt in the metacarpal region which were obtained by these means are shown in Figure 37. Although the sensitivities available can keep the absorbed dose within acceptable limits, this technique needs further improvement to become practical; its possibilities when used with roentgenographic contrast media remain to be explored.

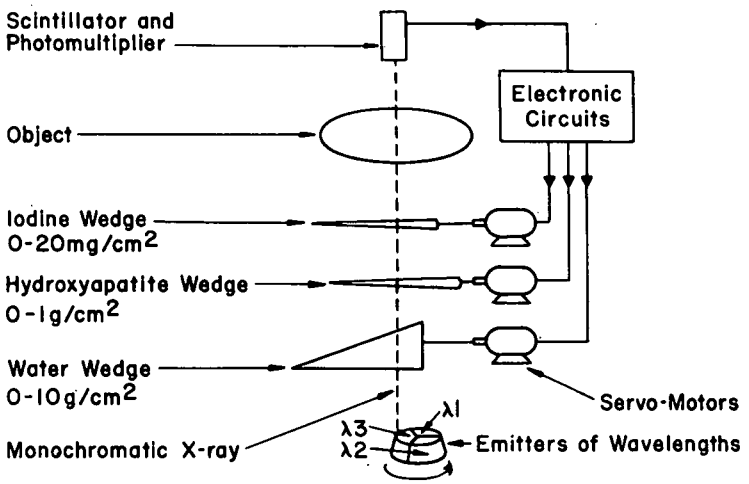

Figure 36

Principle of the analog computer.
(From Reference 2.)

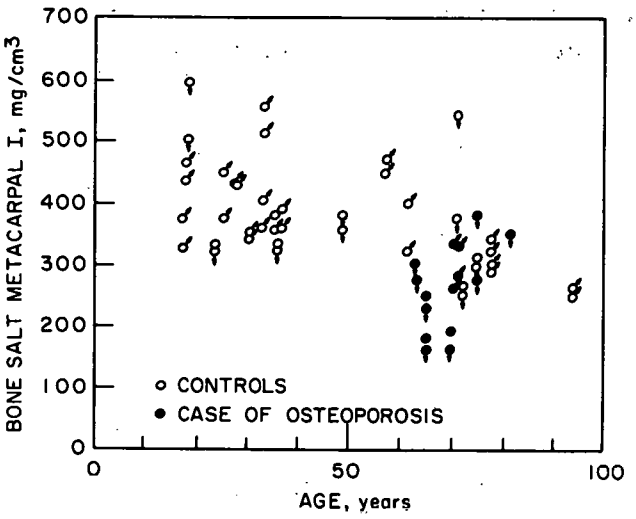

Figure 37

Hydroxyapatite value for the metacarpal bone of the thumb decreases with the age. The values were calculated per unit volume of bone including the marrow. (From Reference 2.)

Until a decade or so ago, the radiological physicist was rather a stranger in the diagnostic department except for his concern over the protection of the operating personnel; most of his efforts were required in therapy. However, with the widespread concern over the genetic material of mankind, the emphasis has turned to the protection of the gonads of the patient. This preoccupation extends to no less than the average gonadal dose of the population of an entire country; and, to be convincing, some evaluation studies have needed very large population sampling, indeed. The remarkable survey made in England a few years ago required exemplary cooperation throughout the country and special skill and devotion on the part of both the hospital physicists and of the radiological profession.(3)

In the U.S.A. there have been two special meetings completely devoted to the reduction of the diagnostic dose to the patient. Although held only three months apart, the overlap in attendance and subject matter was minimal. The written record(4,5) amply demonstrates the vast and intricate interplay of the disciplines involved in the task of maintaining optimal diagnostic objectives with minimum dose. This is because highest operational efficiency consistent with basic knowledge can be attained only by optimizing every step involved in the conveyance of diagnostic information.

In order to keep within the limits of my task, I shall restrict myself to a brief review of the measurements of exposure and absorbed dose in patients undergoing diagnostic procedures; these measurements require the moderate accuracy and stringent economy that make possible convincing mass surveys.

The measurement of exposure to radiation useful in diagnosis and dermatology was accomplished by means of standard air chambers patterned after the basic design of Taylor and Stoneburner(6) soon after the adoption of the Roentgen as a unit. Much more recently, very profuse and detailed data on the design and performance of this type of chamber have been given by Ritz(7) and Allisy and Roux.(8)

In the early thirties measurements of exposure to low voltage x-rays were made in the clinic, not only with thin-walled calibrated thimble chambers but also with the so-called "mesh chamber" originally suggested by Failla and described by Quimby.[9] The design requirements of this chamber, namely, maintenance of maximal transparency and avoidance of interpenetration of the electric field between the electrodes, was recognized early and properly implemented in practice by the Memorial Hospital group; yet it was not reported in the open literature for many years. Only in 1943 did Quimby and Focht[10] report air, skin and depth doses from a Chaoul machine by means of a mesh chamber and by an extrapolation chamber (Figure 38) to which a mesh upper electrode was adapted when the absorption of x-ray by a plastic film proved too severe. Since that time, more detailed descriptions of the design requirements of mesh chambers have been given by Somerwil[11] and by R. K. Clark.[12] To this general category of chambers belongs the recently described "wall-less" chamber of Tranter[13] which is said to agree with the air chamber within a very few percent in the range of 10 to 50 kvp.

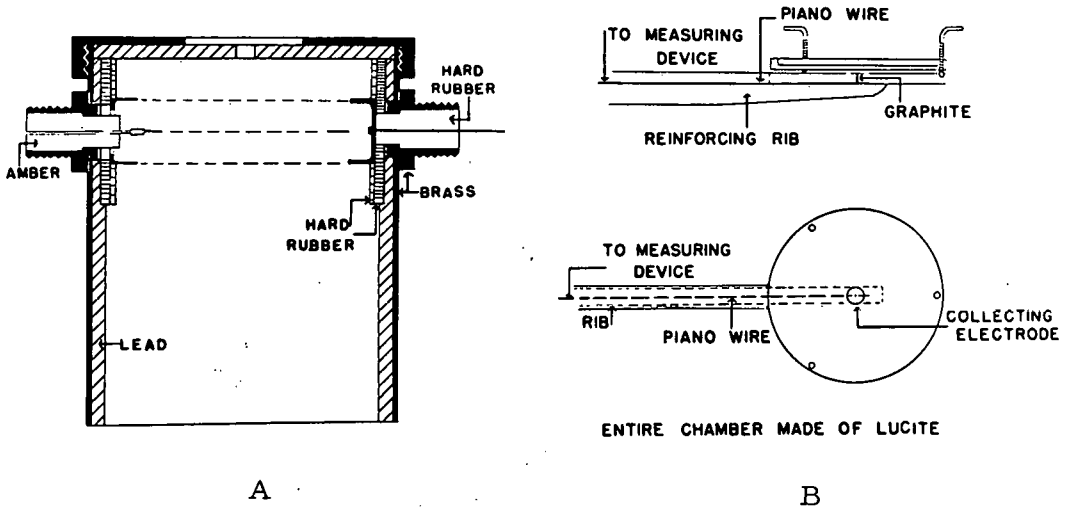

Figure 38

A. Open air chamber of mesh type; B. Small extrapolation chamber. (From Reference 10.)

This precision, by avoiding absorption by the front walls of an ionization chamber, made possible the measurements of air, skin, and depth doses in phantoms;[14,15] it did not solve the problem of measurements in vivo at dose rates and locations pertinent to radiation protection; this problem required the development of rugged thimble chambers capable of energy independence within the diagnostic region of the spectrum. This did not occur until 1953 when a study by Oosterkamp and Proper appeared in Acta Radiologica.[16] In that paper the idea of using an air-filled-cavity chamber with a wall of Z lower than air was first proposed as a means of overcoming the high absorption unavoidably associated with wall thicknesses compatible with ruggedness (Figures 39 and 40).

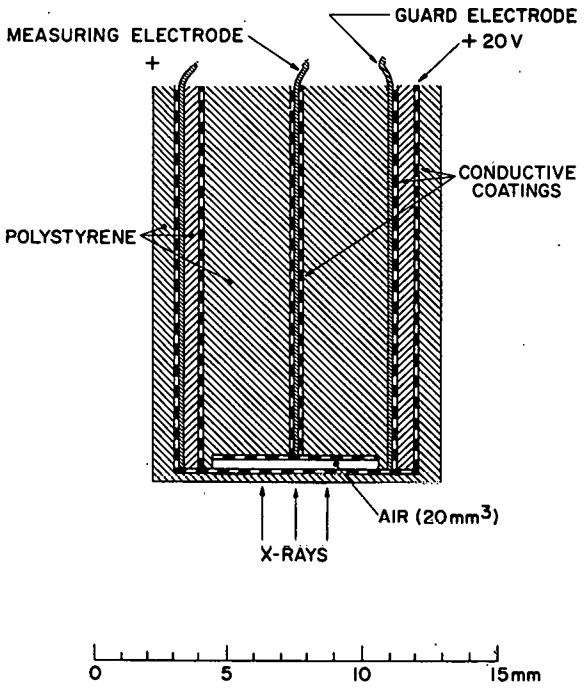

Figure 39

Cross section of flat ionization chamber. (From Reference 16.)

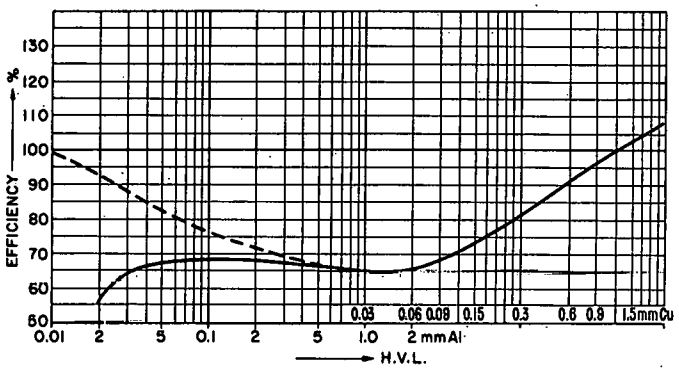

Figure 40

The efficiency of a flat ionization chamber as a function of hvl. (From Reference 16.)

Recently a promising design (Figure 41) has been proposed by Garrett and Laughlin[17] who have taken up the original suggestions of Oosterkamp and Proper and added some original points of their own to achieve a satisfactory isotropic- and energy-independent response from a chamber of modest dimensions (Figures 42 and 43). Concurrently, the performance of similar chambers of good but somewhat more limited characteristics in energy or directional response have been reported elsewhere.

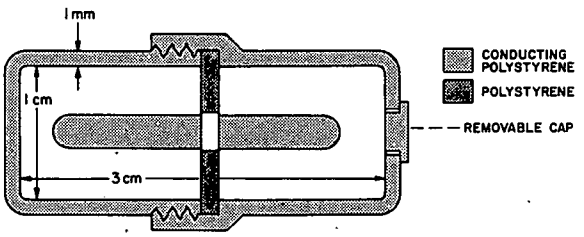

Figure 41

Memorial diagnostic chamber. Cross-section of chamber designed for diagnostic x-ray exposure studies. (From Reference 4.)

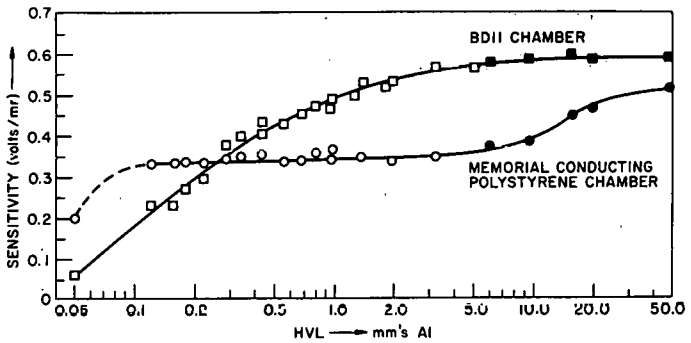

Figure 42

Energy response of thimble chambers. (From Reference 4.)

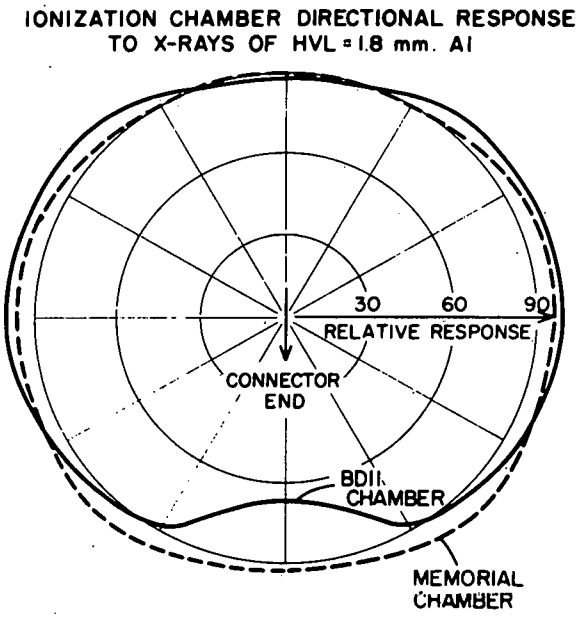

Figure 43

Directional response of thimble chambers. (From Reference 4.)

These designs do represent a significant step forward; however, one must realize that the chamber is also used to measure scattered radiation and it is not basically a standard. Hence, the limits of isotropy and energy independence should be established unequivocally with monochromatic radiation at distances relevant to the use to which these chambers are put. This supplemental information will resolve some of the ambiguities arising in the energy regions of ~0.05 mm Al hvl and ~2-3 mm Al where the responses clearly show a sharp deviation (Figures 40 and 42). At these energies the "clinical diagnostic" spectrum can be investigated with scintillation spectrometers employing either NaI, KI or CsI, and/or proportional counters using the heavy noble gases.

In the field of radiation protection in diagnostic radiology various other needs have been mentioned in the current literature. Some of them have been mentioned in the current literature. Some of them have been expressed especially by governmental safety inspectors of diagnostic equipment. They are as follows:

a) Convenient methods for the appraisal of screen efficiency.

b) Adequate fast response in measuring apparatus to permit correct readings during the typically short times of radiographic and fluoroscopic procedures.

c) Personnel dosimeters designed specifically for this energy range.

d) A better understanding of the behavior of irradiated insulators and the elimination of their defects in condenser dosimeter work.

Other problems also await particular solutions for this energy range. One is direct measurement of the absorbed diagnostic dose in soft tissues in vivo, possibly by an extension of Oosterkamp and Proper's suggestions of a low Z wall chamber filled with tissue gas. A more important problem, perhaps, is measurement, also by direct means, of the distributed absorbed dose in bone marrow. This special topic looks rather large today because, correctly or incorrectly, no dose threshold is assumed in the leukemogenic action of radiation.

At present, our estimates are still heavily dependent on evaluation of rad-to-Roentgen ratios; these calculations, pioneered and detailed by Spiers, require knowledge of the energy spectra of the secondary electrons crossing the marrow-bone interfaces and knowledge of the dimensions of the cavities comprising the trabecular labyrinth.

Some methods aimed at evaluating the integral doses delivered under typical diagnostic procedures have been described by Grimmett,[18] Mayneord[19] and Rossi.[20] The exact role of these measurements in the appraisal of potential leukemogenic action will, of course, remain obscure until the mechanisms involved are clarified. Nevertheless, in the interest of record keeping and of maintaining awareness of the physical agent used, some radiologists have designed ionization chambers, such as shown in Figure 44, which record automatically the total x-ray energy flowing through them on its way to the patient.[21]

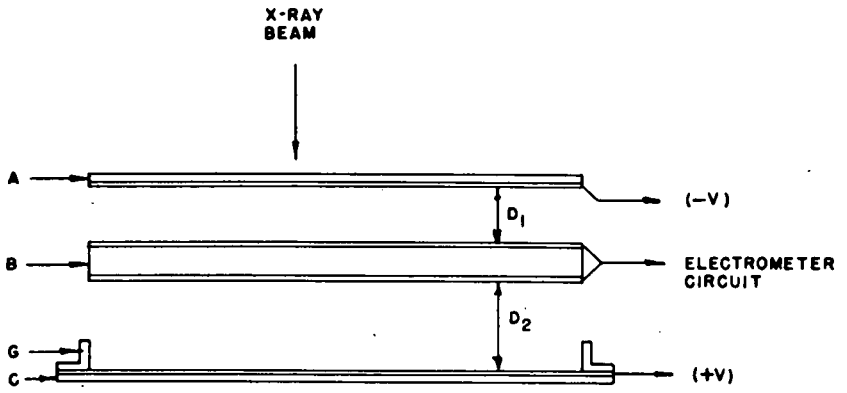

Figure 44

Cross-sectional schematic diagram of the ionization chamber. (From Reference 21.)

I sincerely hope that the use of this conscientious gatekeeper of photons will be imitated widely outside the field of radiology. Instruments thus conceived should improve the vigilance over, and lead to the reduction of more serious offenses against, the public health.

II. Therapy

Roentgen was unquestionably the first diagnostician, but the observer of the first radiobiological effect is much more difficult to identify. Depilation following exposure to x-rays was reported four months after Roentgen's discovery, and severe skin burns suffered by a salesman of x-ray machines were described a few months later. Among the early radiobiologists, one can count Henri Becquerel who accidentally discovered the production of erythema on his own skin as a result of having carried a container of the newly-discovered radium in his vest pocket. More systematic were the animal studies of Pierre Curie who collaborated with two medical men, Bouchard and Balthagard; they found that radium destroyed superficial cancers. The first medical case notes, however, were published in 1904 by Danlos who used the element at the St. Louis Hospital of Paris.

By about 1910 it had become obvious that in addition to the study of the biological responses which had just been begun by such pioneers as Bohn, Bergonié and Tribondeau, and Dominici and Perthes, some quantitative approach to radiotherapy was necessary. It was thus the profession of radiological or hospital physics was born.

The objective of most radiation therapy is the destruction of a tumor with minimal damage to normal structures. It is obvious that to succeed a great deal of care must be exercised in the procedure. Different and, at the same time, rigid requirements have been set for sources of radiation and for spatial source-patient relationships.

Self-contained sources applied within or near the tumor consist usually of radioactive elements, the classical representative of which is Ra^{226}, the well-known daughter of uranium used almost exclusively before 1940. It is in this particular type of therapy that the hospital physicist was first called in to assist in the design of the first moulages conforming with the individual lesion, the first radium teletherapy apparatus, and the first protective containers. Owing to the very high cost of radium in the early twenties, quite a good deal of effort was also devoted, especially in America, to the extraction of radon from radium and to its proper containment in filtered tubes for intracavitary treatments and in needles of smaller diameter for interstitial therapy.

In the two decades from 1910 to 1930 radiotherapy was actively nourished by radiobiological research in which several radiotherapists

participated. Yet, one wonders nowadays just how much of the success in those days depended also on the fact that the early pioneers used radium for the treatment of surface or easily accessible lesions practically in contact with their sources. Under those conditions the influence of the inverse square law limited drastically any accidental overdoses to relatively shallow depths. Moreover, the very high cost of the element limited also the size of the sources and enforced prolonged treatment times even before Regaud's experiments clarified the importance of the time factor in radiation therapy. Also of early vintage are the calculations of the distribution of radiation in interstitial therapy pursued by hospital physicists in various clinics, using the inverse square law and a little-known coefficient of absorption. In practice, these deficiencies could not lead to disastrous consequences because the relevant thicknesses rarely exceed a few centimeters; moreover, in many types of treatments, surgical limitations and anatomical configuration dictated the geometrical array of the sources. The exposure, expressed in milligram-hours of radium (or millicuries destroyed of radon) was sufficient to express a method of treatment with a fair record of reproducibility.

With the advent of the powerful but erratic beams of radiation from the early x-ray tubes, however, the probability of accidental overdosage increased. As a consequence, the absolute necessity of achieving meaningful dosimetry became apparent and so did the desire to achieve through it a rational comparison of various methods of treatment and their eventual improvement.

In the years between the definition of the Roentgen in x-ray therapy (1928) and the Second World War, a good deal of the physicist's activity was spent in attaining a unification of the unit of exposure in both radium and Roentgen therapy. The goal consisted of measuring the exposure rate in Roentgens from a radium source under standard conditions of filtration and distance. Because of the high energy photons emitted by radium it was not possible to reach a satisfactory solution based on the use of the parallel plate chamber, which was, and still is, the standard in the range of photon energies below a few tenths of a megavolt; in 1936 these efforts culminated in the clarification and confirmation of the Bragg-Gray criteria governing the now-famous relationship linking the energy D_m released per unit mass in the walls of a cavity to the ionization J_m produced per unit mass of gas in the cavity itself:

$$D_m = J_m W_g \rho_m \qquad (1)$$

In this expression W_g is the energy necessary to produce one pair of ions in the gas and ρ_m is the ratio of the stopping power of the wall material to that of the gas for the ionizing particles crossing the cavity surface.

For the moment I shall limit my remarks on the role of dosimetry in the field of radiation therapy. I think we are all agreed that investigations leading to an understanding of the basic phenomena in an ionization device have led to satisfactory and reproducible measurements of absorbed dose. It must be realized, however, that the drive for very high accuracy in dose distribution and radiation measurements in general are being met, not infrequently, with skepticism by very competent therapists who have noted the inconsistency between attainment of meticulous physical measurements of the dose on the one hand and the somewhat cruder clinical appraisal of tumor location on the other. This criticism would be justified if dosimetric fastidiousness were carried out in the clinic as an end in itself; the comment is not justified, however, if the accuracy is practiced in schools in order to offer the therapist resident the opportunity to appraise the properties of radiation which he will use for the rest of his life and to develop in him the wholesome skepticism and care so necessary to persons who must delegate some aspects of human welfare to the accuracy of instruments.

It must be realized that the basic principles of dosimetry by gas ionization methods have not changed radically to this day but the variety of the sources in any one institution have. From the so-called superficial (140 kvp) and deep therapy (200 kvp) machines of the early thirties we do have a respectable range of apparatus to face, namely, Grenz machine (10 keV), plesio-therapy (45 keV), diagnostic equipment (25-100 kvp), medium voltage (140 kvp), conventional or orthovoltage (250-500 kvp), supervoltage roentgen rays (1-2 MeV), linear accelerators (1-70 MeV), betatrons and synchrotrons (15-50 MeV), and teleisotope machines (Co^{60}-Cs^{137}). This list comprises sources of continuous output (constant potential, Van de Graaff generators and teleisotope sources) and others which are pulsed from intervals ranging from 1/120 of a second on down to the microsecond region.

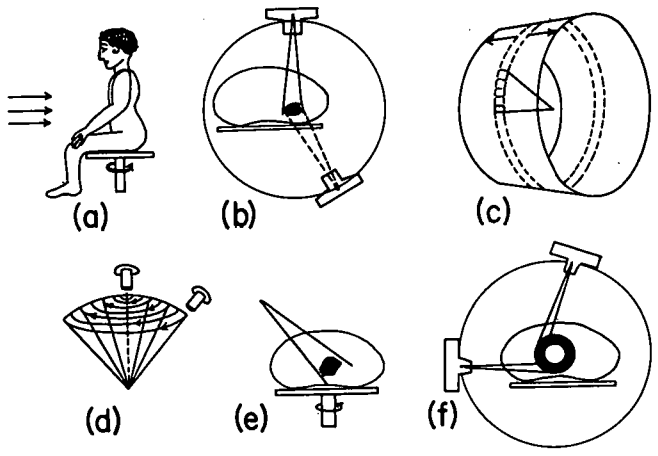

Figure 45

Diagram illustrating the various types of moving field therapy. (From Reference 45.)

From these sources we may obtain either uniform or very asymmetric spatial emissions; in the latter case very fastidious corrections are needed to make the source useful at all. This may be complicated by the fact that the source and the patient may or may not be stationary with respect to each other. An illustration of the different kinds of moving fields in use today is shown in Figure 45.

It is obvious, therefore, that the variety of therapeutic approaches poses continual

challenges to the physicist. His task is still to evaluate the absorbed dose within the body, often in three dimensions when the therapautic objective of tumor cure demands doses approaching closely the tolerance of the tissues adjacent to the lesion. It has been recognized that these studies have reduced the hazard of radiation injuries that may accrue through unrecognized overlapping in multifield techniques. What is highly desirable in this respect is the economical attainment of this spatial information with a modicum of accuracy, say 5 or 10 percent. In the very large centers this ideal may be implemented by computer methods fed by a library of depth dose information; in others, if and when attainable, the quantitative evaluations of the luminescence produced by a therapy technique throughout a suitable plastic phantom will be sufficient for the purpose. If I were to name the most informative and convenient method of exploring isodoses in depth following therapeutic techniques, I would not expect harsh criticism if I were to mention the "proper" photographic emulsion, provided that by "proper" I meant the property of absorbing and registering any type of ionizing energy at a rate proportional to that absorbed in an equal volume of water or soft tissue similarly placed.

This desideratum, however, has not been reached; in everyday therapeutic practice we still rely on the ionization chamber which has proved so versatile in skilled hands as to constitute the standard against which other types of detectors are compared, in most - if not all - circumstances. An example of the few limitations of ionization devices is illustrated by considering whether the chambers are to be used in vivo. If one were to contemplate the insertion of a dosimeter in a lesion, one would have to think in terms of size of a needle of one or two millimeters in diameter; at this point construction and handling of gas ionization chambers with high insulation between electrodes becomes impractical for routine purposes. Here the search for convenient methods, especially for those not requiring high skill, has turned to the investigation of the effects of radiations on liquids and solids. Among liquids the ferrous sulphate dosimeter of Fricke has gained wide recognition in radiation research in general, and, to a more limited extent, in clinical dosimetry.

The discovery of measurable radiation effects on the structural properties of many materials has confronted persons interested in dosimetry with too many choices; these have usually been classified by the process which reveals the effect. Some of them have proved convenient in the investigation of radiation damage in solid materials, a field characterized by extremely high exposures to mixed radiations, such as those prevalent in the interior of nuclear reactors.

When information of this sort and the materials in question become available to the radiological physicist two reactions occur: one is total rejection of the method because of the limited control that the physicist can exercise over the properties of these devices; the other is

blind acceptance of anything that solid science is likely to offer. If the first attitude may lead to delay in useful applications, the second can lead to a tremendous waste of experimental effort and the publication of inane papers. This can be avoided in most instances, since one knows beforehand that one cannot expect satisfactory dosimetry in predictable energy bands when the atomic number of the materials of the detector is far removed from 7.0 and its active volume is much too large to behave as a small gaseous cavity.

The usefulness of solid state Bragg-Gray devices based on radiation damage has been demonstrated by Ritz and Attix under very stringent conditions.(22) They found Mylar films (6μ) satisfactory enough but, unfortunately, useful only from 10^7 to 1.5×10^8 Roentgens; damage in larger thicknesses of anthracene did not follow rigorously the ionization in the air cavity.

Of sensitivity compatible with the ranges of exposure used in radiotherapy are the radiophotoluminescent glasses (10-10^5 Roentgens) in the form of rods of small dimensions (5-15 mm x 1 mm).(23) These have been used in tissue implants and seem to have gained favor in some radiological departments. Their main advantage over ionization chambers of the condenser type is their ruggedness, smaller size and retention of response to radiation. Although their use is most rewarding in the megavolt region, their shortcomings (which might be minimized in the near future) are definite. These are: a) Their Z is relatively high; the suggested corrections brought about by filtration are definitely empirical and have not been demonstrated to apply isotropically. b) In general the response from a batch of rods is likely to be spotty; hence, readings must be constantly checked by the use of several fluorods.

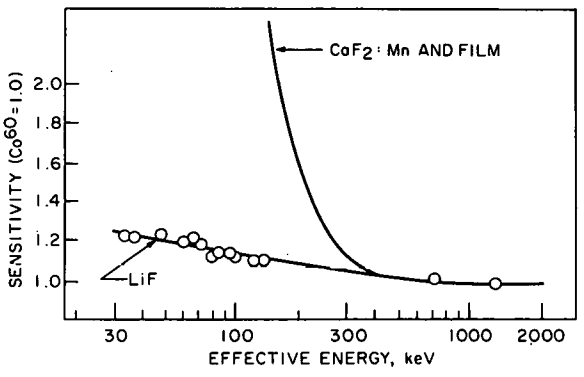

Figure 46

Energy dependence of LiF (TLD-100, Harshaw Chem. Co.) compared with that of other unshielded dosimeters. (From Reference 24.)

Of great promise, because of their sensitivity and low Z, are the measurements of thermoluminescence available from irradiated LiF (Figure 46) for soft tissue(24) and $CaSO_4$ for bone mineral.(25) Although the full signal is destroyed by the measurement, use of aliquots permit a permanent record of the reading; moreover, repeated measurements of the phosphorescence have been suggested as feasible.(26) Special mention must be made of the small amounts of material needed (a few mg) and the small size of the individual crystals available (a few microns); these properties augur

well for their use in real bone trabeculae for the direct measurement of the average dose to the marrow. Thus far, this estimate has been attempted only by indirect means, including the use of a biological dosimeter consisting of a phage culture.[27]

Only brief mention can be made of some applications of these devices that should be suited to the spectrometry and dosimetry of β-ray applicators. In principle, the absorbed dose at any one point of a given material can be always calculated with fair accuracy if one knows the energy spectrum of the ionizing particle crossing a small spherical surface surrounding the point. This information can be obtained, over flat surfaces at least, by means of suitably diffused silicon junctions which, depending on the depth of the depletion layer (10 to 1000 μ), could register the whole energy flow or merely dE/dx. These devices do offer high sensitivity per unit volume and can be used as solid ionization chambers. Their energy response to ionizing particles is practically proportional to energy lost and independent of LET. Recent reviews on the applicability of these methods to dosimetry have been published by Fowler[28] and by Attix and West.[29]

Organic scintillators, both liquid and solid, also offer to the investigator the possibility of acquiring spectrometric and dosimetric information: their sensitivity is high, their cost is relatively low, and their shape can be controlled to a certain extent. Since they are not very sturdy instruments, however, and require skillful handling, they cannot generally be considered ideal instruments for routine dosimetry.

Besides using liquid and solid radiation detectors for the estimate of absorbed dose, the radiological physicist should also inquire into the nature of the mechanisms involved in their response, especially when these are evaluated in terms of absorbed energy. Some stimulating facts may emerge; for instance, if one compares radiation-induced luminescence and biological effects, one notes that both of them are affected by oxygen and that striking differences exist in the efficiency of their response to radiations of high LET. Of particular interest are some preliminary findings of Berlman et al. of our Laboratory.[30] In their investigations of the light emitted by diphenyloxazole (PPO) in various solutions under the action of equal energy of α and β radiation, they found (Table 11) that the ratio of luminescence produced by the first to that of the second was correlated to the intrinsic sensitivities of the solutions to radiation chemical damage. These studies were undertaken with the intent of gaining some information on the excitation of atoms and molecules along the ionizing track. What light they may throw, by analogy or otherwise, on the relative biological effects of radiations of different LET is practically impossible to predict at this time.

Table 11

The α/β ratios from binary solutions composed of various solvents with 8 g/l. of PPO as the common solute*

Solvent	mV	α/β ratio	Gr**
cyclopentane	26.3/54.4	0.052	
hexane	31.9/61.8	0.056	
methyl cyclohexane	37.6/69.7	0.058	
cyclohexane		0.063	14.3
cyclohexene		0.067	
xylene	115.4/142.7	0.087	11.0
ethyl benzene	103.6/126.6	0.088	9.0
toluene	109.7/131.8	0.090	3.1
styrene	7.8/8.4	0.100	1.6
benzene	101.2/109.3	0.100	1.8
C_6D_6	123.2/115.4	0.115	

*From Reference 30.

**The number of free radicals formed per 100 eV energy expended by an ionizing particle in the solvent.

III. Nuclear Medicine

The most recently developed area in radiological physics is that of nuclear medicine. Although the term has been used in conjunction with the few attempts at external radiotherapy employing a nuclear the reactor as a radiation source, nuclear medicine has come to designate those fields of medical research, diagnosis, and therapy in which radioactive isotopes are given internally.

Of these three areas, research and diagnosis are at present the most active and productive. As far as the hospital physicist is concerned, both disciplines require of him the assessment of the distribution of the concentration of a radioelement within the body and its variation with time. The accuracy with which the concentration and/or the localization is required to be known varies considerably; typical examples of the extremes in localization range from the so-called "hot" or "cold" nodules due to I^{131} localization in the thyroid to the distribution of a colloidal substance, such as Au^{198} or Au^{199}, through the reticuloendothelial system of the body.

The first attempts to investigate radioisotope distribution in vivo by holding a shielded G.M. counter by hand over the body have given way to modern automatic scanning. Evidence of the interest in this technique throughout the world is given by the recent publications of the IAEA (1959)[31]

and of the USAEC (1962)[32] and the very recent IAEA meeting in Athens last April 20-24. Commensurate in effort and expense, though probably of no comparable usefulness to clinical medicine, have been the simultaneous developments of sensitive methods for assessing the natural potassium content of human beings and the retention of extremely small amounts of radioactive substances which have gained access into their bodies through fallout of radioactive debris. These methods are also being applied today in long-term experimental studies involving slowly changing physiological parameters; as a rule, in these procedures less emphasis is placed on geometrical resolution.[33-35]

It is impossible within the space at my disposal to do much more than outline the functional requirements of a clinical scanning system. They are: a) the registry of the coordinates of a point in a plane; b) a response related to the concentration below the point in question; and finally, c) the presentation of this information to the physician for proper evaluation.

The first task is accomplished by pantographic methods. The second is achieved by the response of a scintillation crystal properly shielded and supplied with a properly designed collimator; to the latter is assigned the double task of allowing the crystal essentially to "look" at one small region at a time and of suppressing the interference of radiation engendered elsewhere. By more or less complicated means, the crystal response is marked graphically in various ways at the coordinates of the point under the collimator. The result is a scintigram for the diagnostic interpretation of which some selection of the total information gathered is usually done by various electronic means.

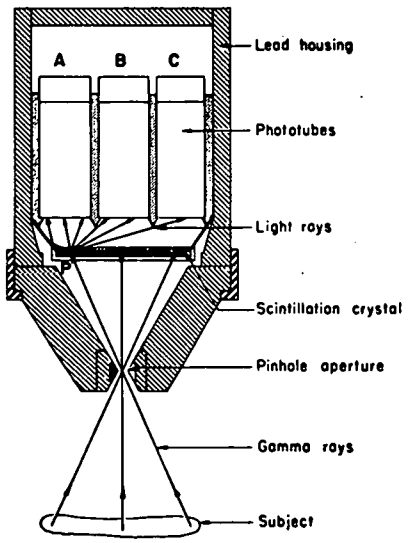

Figure 47

Schematic diagram of the scintillation camera of anger. (From Reference 36.)

An ingenious scanning method at this moment reaching commercial outlets is the so-called "static" approach involving no motion of the crystal with respect to the patient. The principle of image formation is identical to that of the camera obscura in which a relatively thin crystal takes place of the screen. An obviously dense and high Z shield is supplied with a denser central region in which the pinhole aperture is located.[36] The scintillations that occur in the crystal, and their coordinates are carried over to the scintigram by proper electronic circuits (Figure 47). The advantage of this method resides mainly in the higher efficiency and the concurrent benefit of low isotope dosage.

It is well to comment at this point that despite the rapid progress that has been made

in the last few years in automatic scanning,[37] the demands of the clinics themselves[38] have posed numerous problems of practical nature which are being solved effectively, more by careful choice of the radioelements employed than by the alteration of the basic methodology evolved during the last decade.

This trend began with the substitution of one radioisotope of shorter life and emitting gamma rays of lower energy (80-200 keV) for the one which was used initially, just because it was easily available. This choice has led to a sharp reduction of the weight and mass of the crystal-shield structure; the practical advantages that ensue are the attainment of better resolution with less expensive collimators (Figure 48) and the possibility of using several of these to suit the specific anatomical distributions.[39]

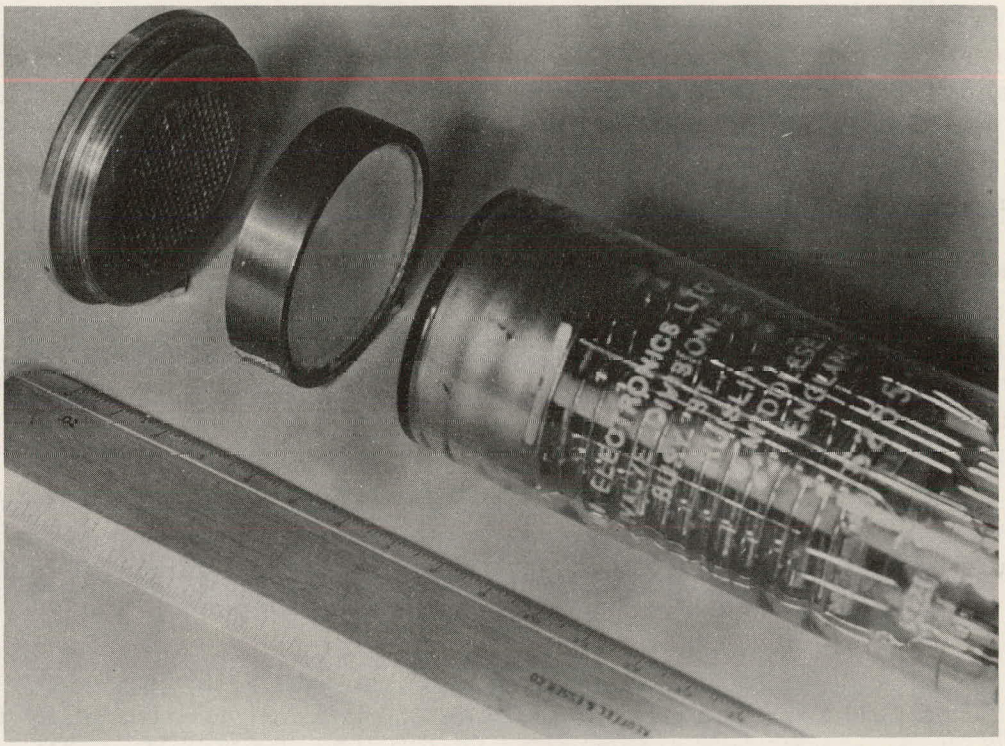

Figure 48

Low energy gamma-ray detector. Collimator thickness 0.55 in.; NaI(Tl) crystal is 1.75 in. x 0.25 in. thick. Lead shield is 0.25 in. thick, adequate for 140 keV. (From Reference 40.)

With the advancing knowledge of biochemical procedures aimed at incorporating radioisotopes in substances which are selectively taken up by various organs in the body, a more recent trend has intervened: namely, first selecting a radioelement with the desirable physical characteristics for optimum scanning and later solving the biochemical problem required by the incorporation of this element in a compound known to localize properly.[40]

In the field of research in intermediary metabolism, the activities of the radiological physicists have been many. The results of their laboratory and mathematical studies concerning iodine and strontium metabolism in the human are too well known to need emphasis here.

In the clinical field, therapeutic applications of radioisotopes do not compare in variety with the diagnostic applications, but the use of I^{131} in the therapy of hyperthyroidism is sufficiently widespread to invite comment. Here the physicist contributes to diagnosis by functional tests with tracer amounts; if I^{131} therapy is indicated, he applies the diagnostic findings to the estimate of the correct absorbed dose. Without his help the evaluation of the correct dose of I^{131} in treatment of hyperthyroidism would have required a much longer time and, under certain circumstances, might have led to erronous conclusions as to the usefulness of the procedure.

The future of internal radioisotope therapy depends critically on the discovery of chemical substances which concentrate in tumor tissue to the virtual exclusion of the rest of the body. It is difficult to make predictions in this direction because so much of the chemistry of the body is unknown. It would seem, on the one hand, that the chemical requirements of this type of therapy should be less rigorous than those of chemotherapy because the radiodestruction of the tumor demands only chemical concentration at the site. In chemotherapy, on the other hand, one would guess that additional chemical properties are needed to interfere with tumor metabolism; yet these very properties may be required to enhance specificity in concentration.

Today only certain types of metastatic thyroid cancer benefit in no uncertain terms from this systemic approach owing to the unique affinity of iodine for functional thyroid tissue. Bold and hopeful is the effort of Bale[44] aimed at achieving therapeutic concentrations of radioelements by immunological tagging.

It is perhaps because the success of systemic treatment by radioelements is basically dependent on biochemistry and is still so limited in the clinic, that internal beta-ray dosimetry is attracting so little attention from radiological physicists. Fundamental problems such as determination of beta-ray point source functions and the evaluation of experimental distributions in situ by practical means are still unresolved. In certain cases the resolution required suggests the use of photographic emulsions containing grains much smaller than those in use today. In others, such as the dose distribution in red bone marrow in trabecular bone containing radioisotopes, the vast photographic information given by autoradiography must be collated in some quantitative fashion by the experimenter. It is obvious that the intricacy of the distribution demands some type of automation. This approach has not been reported for this particular problem, but the radiodiagnostic literature already contains

reference to methods analogous to the ones required here but used for the evaluation of information contained in the radiographic image.(42)

Problems within the exclusive competence of physicists in this field are the standardization of radioactive sources and the spectrometric evaluation of their purity in everyday clinical practice. In the field of beta-ray dosimetry from external sources, absorbed doses in depth can be evaluated via the extrapolation chamber and scintillation counters when the energy of the radiation is fairly large.(43) For very low energy sources such as tritium, C^{14} and S^{35} useful parameters of dosimetric interest can be obtained by mesh chambers(12) and wall-less chambers.(44)

Perhaps the most complicated dosimetric studies that have faced the radiological physicist since the inception of the profession are those involved in accidents due to unscheduled criticality excursions of reactors. The interested person is referred to the original reports which are as lengthy and as detailed as required by the complicated situations in which they occurred.

Before leaving the subject it is well to mention that neutron activation analysis of tissue and fluids may well contribute to a better understanding of the metabolism of tracer elements in the body. Thus far, this technique has proved popular with chemists; it has been found definitely useful in tracer analysis of biopsy or autopsy specimens. It remains to be seen whether partial activation of portions of the body can facilitate quantitative studies of electrolyte and other mineral transport from organs of the body. At first sight, this approach seems especially favorable for elements with large activation cross-section and very short half-lives; it is too early to surmise whether it could aid in the selection of a better radiotherapeutic method.

Prophecy in radiological physics, as in any other field of scientific endeavor, has an exceedingly short-lived accuracy; despite this obstacle I shall conclude this presentation by trying to look quizzically into the future.

The radiological physicist, if he is to play a progressive role in the clinic and in the laboratory, must maintain more than casual contact with fields delving into the effects of ionizing radiation, not only on histological and biomolecular states, but also on the liquid and solid states of inorganic matter. This task will require a greater portion of his time than was the case in the past.

Qualitatively, however, his role may remain unchanged; namely, he is likely to exploit for the immediate benefits of medicine and radiology the discoveries of the future Roentgens, Curies, Rutherfords, and Fermis, who, like these illustrious men, will remain physicists and devote most of

their activities to unraveling the mystery of matter and will rarely enter into biomedical problems.

As in the past, the field will be populated also by trainees in the life sciences and medicine who will complement the physicists in their task by contributing the skills and knowledge acquired in medical and biological schools. The result of this collaboration should lead to more rapid, beneficial advances.

References

1. M. Ter-Pogossian. The Efficiency of Radiographic Intensifying Screens, Technological Needs for Reduction of Patient Dosage from Diagnostic Radiology, ed. Murray L. Janower. Charles C. Thomas, Springfield, Ill., 1963. p. 215.

2. B. Jacobson. X-Ray Spectrophotometry In Vivo. Am. J. Roentgenol. 91, 202 (January 1964).

3. U. K. Ministry of Health, Dept. of Health for Scotland. Radiological Hazards to Patients, Second Report to Committee. Her Majesty's Stationery Office, London, 1960.

4. M. L. Janower, ed. Technological Needs for Reduction of Patient Dosage from Diagnostic Radiology. Charles C. Thomas, Springfield, Ill., 1963.

5. R. D. Moseley, Jr., and J. H. Rust, eds. The Reduction of Patient Dose by Diagnostic Radiologic Instrumentation. Charles C. Thomas, Springfield, Ill., 1963.

6. L. S. Taylor and C. F. Stoneburner. The Measurement of Low Voltage X-Ray Intensities. Bur. Std. J. Res. 9, 769 (December 1932).

7. V. H. Ritz. Design of Free-Air Ionization Chambers for the Soft X-Ray Region (20-100 kV). Radiology 73, 911 (December 1959).

8. A. Allisy and A. M. Roux. Contribution à la mesure des rayons roentgen dans la domaine de 5 à 50 kV. Acta Radiol. 55, 57 (January 1961).

9. E. H. Quimby, C. Lucas, A. N. Arneson and W. S. MacComb. A Study of Back-Scatter for Several Qualities of Roentgen Rays, Radiology 23, 743, Dec. 1934.

10. E. H. Quimby and E. F. Focht. Dosage Measurements in Contact Roentgen Therapy. Am. J. Roentgenol. 50, 653 (November 1943).

11. A. Somerwil. A Grid Ionization Chamber of Special Design for the Measurement of Soft Radiations, Acta Radiol. 37, 44 (January 1952).

12. R. K. Clark, S. S. Brar, and L. D. Marinelli. Ionization of Air by Beta Rays from Point Sources. Radiology 64, 94 (January 1955); also The Ionization in Free Air around Point Sources of Beta Radiation. Argonne National Laboratory Report ANL-5201 (August 1954).

13. F. Tranter. An Ion Chamber with a Wall of Air. Selected Topics in Radiation Dosimetry. International Atomic Energy Agency, Vienna, 1961. p. 131.

14. L. D. Marinelli and L. S. Taylor. The Measurement of Ionizing Radiations for Biological Purposes. Radiation Biology, Vol. I, High Energy Radiation, ed. A. Hollaender. McGraw-Hill Book Co., Inc., N. Y., 1954. p. 145.

15. L. D. Marinelli. Radiation Dosimetry and Protection. Ann. Rev. Nucl. Sci. 3, 249 (1953).

16. W. J. Oosterkamp and J. Proper. Free-Air and Thimble Ionization Chambers for Grenz-Ray Dosimetry. Acta Radiol. 37, 33 (January 1952).

17. R. Garrett and J. S. Laughlin. A Diagnostic X-ray Exposure Dose Chamber. Health Phys. 2, 189 (October 1959). (See also Reference 4.)

18. L. G. Grimmett. Contributions to Radium Therapy. Am. J. Roentgenol. 41, 432 (March 1939).

19. W. V. Mayneord and J. R. Clarkson. Energy Absorption, II. Brit. J. Radiol. 17, 151 (May 1944); ibid. 177 (June 1944).

20. H. H. Rossi, R. Liebowitz, and F. de Friess. Measurement of Integral Dose in Unit Density Phantoms of Uniform Cross Section, Radiology 72, 104 (January 1959).

21. R. H. Morgan and W. F. Ciceric. Measurement of Radiant Energy Delivered to Patients in Diagnostic Radiology. The Reduction of Patient Dose by Diagnostic Radiologic Instrumentation, ed. R. D. Moseley, Jr., and J. H. Rust. Charles C. Thomas, Springfield, Ill., 1963. p. 60.

22. V. H. Ritz and F. H. Attix. A Solid State Bragg-Gray Cavity Chamber, Symposium on Radiation Effects and Dosimetry, 1960. ASTM, Special Tech. Publ. 286.

23. F. H. Attix. Dosimetry by Solid State Devices. U. S. Naval Research Laboratory Report 5777. Washington, D. C., June 1962.

24. J. R. Cameron, D. Zimmerman, G. Kenney, R. Buch, R. Bland and R. Grant. Thermoluminescent Radiation Dosimetry Utilizing LiF. Health Phys. 10, 25 (January 1964).

25. J. H. Schulman, F. H. Attix, E. J. West, and R. J. Gintha. New Thermoluminescent Dosimeter. Rev. Sci. Instr. 31, 1263 (December 1960).

26. J. H. Schulman and E. J. West. Phosphorescence Method of Reading Thermoluminescent Dosimeters. Rev. Sci. Instr. 34, 863 (August 1963).

27. N. Aspin and H. E. Johns. The Absorbed Dose in Cylindrical Cavities within Irradiated Bone. Brit. J. Radiol. 36, 350 (May 1963).

28. J. F. Fowler. Solid-State Dosimeters for In-Vivo Measurements. Nucleonics 21, 60 (October 1963).

29. F. H. Attix and E. J. West. Thermoluminescent Dosimeters on Recoverable Satellites. U. S. Naval Research Laboratory Report 5938. Washinton, D. C., May 1963.

30. I. B. Berlman, R. Grismore and B. G. Oltman. Study of α/β Ratios of Organic Scintillation Solutions. Trans. Faraday Soc. 59 (No. 489, Part 9), 2010 (September 1963).

31. Medical Radioisotope Scanning. International Atomic Energy Agency, Vienna, 1959.

32. R. M. Kniseley, G. A. Andrews, C. C. Harris and E. B. Anderson, eds. Progress in Medical Radioisotope Scanning. Oak Ridge Inst. of Nuclear Studies, Oak Ridge, Tennessee, 1963. U.S. Atomic Energy Commission Report TID-7673 (1963).

33. G. R. Meneely, ed. Radioactivity in Man. Charles C. Thomas, Springfield, Ill., 1961.

34. Whole Body Counting. International Atomic Energy Agency, Vienna, 1962.

35. L. D. Marinelli, C. E. Miller, H. A. May and J. E. Rose. Low Level Gamma-Ray Scintillation Spectrometry: Experimental Requirements and Biomedical Applications. Advances in Biological and Medical Physics, 8, 81 (1962).

36. H. O. Anger. Scintillation Camera. Rev. Sci. Instr. 29, 27 (January 1958).

37. J. P. Kriss. Radioisotope Scanning in Medical Diagnosis. Annual Review of Medicine, 14, 381 (1963).

38. M. Blau and M. A. Bender. Biological Aspects in the Choice of Scanning Agents. Nucleonics 22, 55 (January 1964).

39. H. Endlich, P. Harper, R. Beck, W. Siemens and K. Lathrop. The Use of I^{125} to Increase Isotope Scanning Resolution. Am. J. Roentgenol. 87, 148 (January 1962).

40. P. V. Harper, R. Beck, D. Charleston and K. A. Lathrop. Optimization of a Scanning Method Using Tc^{99m}. Nucleonics 22, 50 (January 1964).

41. W. F. Bale and I. L. Spar. Studies Directed Toward the Use of Antibodies as Carriers of Radioactivity for Therapy. Advances in Biological and Medical Physics, 5, 285 (1957).

42. P. H. Meyers. Evaluation of a Computer-Retrieved Radiographic Image. Radiology 81, 201 (August 1963).

43. A. S. Chhabra. Sr^{90}-Y^{90} Beta Ray (and Bremsstrahlung) Depth-Dose Measurements in Lucite. Radiology 79, 1001 (December 1962); also Radiological Physics Division Semiannual Report, Argonne National Laboratory, Argonne, Ill., 1961. ANL-6474, p. 24.

44. P. Failla and G. Failla. Measurement of the Dose in Small Tissue Volumes Surrounding "Point" Sources of Radioisotopes. Radiation Res. 13, 61 (July 1960).

45. H. E. Johns, ed., Physics of Radiology, 2nd Edition (Charles C. Thomas, Springfield, Ill., 1961).

120 - W

Lead-210

Pb^{210} (RaD) IN INHABITANTS OF A CARIBBEAN ISLAND

Richard B. Holtzman

Abstract

The mean concentration of lead-210 in vertebrae of Puerto Ricans was 0.118 pC/g ash. The value in males, 0.133 pC/g ash, was significantly higher than the 0.088 pC/g ash in females. These values are significantly lower than those in similar groups of mid-continent (midwestern U.S.) residents, 0.196 for males and 0.156 for females. These lower values in island dwellers are attributed to the lower atmospheric concentration of Pb^{210} over the oceans with the consequently lower exposure of these people.

Discussion

The distribution of Pb^{210} (RaD) in human populations is of particular interest because this nuclide, along with its daughter Po^{210}, contributes 20% or more of the natural radiation dose to the skeleton.(1) In turn, the dose from natural radiation (cosmic rays, gamma rays, Ra^{226}, etc.) accounts for 90% or more of the total skeletal radiation dose (natural and fallout) exclusive of the uncertain dose received from medical X-ray exposure.(2)

Geographical variations in Pb^{210} concentration are to be expected on the basis of a previously proposed mechanism for the acquisition of the nuclide. In the United States about one half the activity is acquired by intake from food and the rest by inhalation, the contribution from skeletal Ra^{226} being negligible.(1) The concentration of Pb^{210} in air, however, should be lower over the ocean than over the continents because of the known lower concentrations over the ocean of the Pb^{210} precursor, Rn^{222}.(3,4) The atmospheric concentrations of Pb^{210} measured in England(5) and those measured at the 80th meridian air sampling stations are consistent with this concept.(6) Consequently, the Pb^{210} content in populations breathing ocean air should be lower than that in similar populations breathing continental air. This effect may be further enhanced by a lower intake from food, if, by analogy with the uptake of Sr^{90} in plants, a substantial fraction of the Pb^{210} in food is acquired from atmospheric precipitation.(7)

Skeletal concentrations of Pb^{210} have been determined previously in residents of various geographical locations: in England, by Hill and Jaworowski;(8) in the eastern United States, by Hursh;(9) in the midwestern United States, by Holtzman;(1) and in Germany by Groos, Sattler, and Stahlhofen.(10) However, little variation is to be expected among these groups,

since the subjects are mainly from continental regions with the exception of England. Unfortunately, since only a few samples were reported from England and the concentrations were given in units of activity per gram of wet bone, no accurate comparison is possible (vide infra).[11] To verify the hypothesis of regional variation, the Pb^{210} concentration in bone from residents of a Caribbean island, Puerto Rico, was measured.

Specimens of vertebra were obtained at autopsy from each of 28 residents, 19 male and 9 female, in the vicinity of the city of San Juan between January and August of 1961. Each specimen was ashed in a muffle furnace at 900°C, dissolved in concentrated hydrochloric acid, and diluted to 0.5 N acid. The Pb^{210} was determined by the previously described method of plating out its daughter Po^{210} onto a silver disk, which was then counted for alpha particles.[1] Although some Po^{210} was probably lost during the ashing process, the interval of one year between ignition and measurement allowed the Po^{210} to reach virtual radioactive equilibrium with the Pb^{210}, a fact confirmed by subsequent re-analysis of the samples.

The loss of Pb^{210} at the 900°C ashing temperature appears to be negligible as shown by tests with samples of human rib, vertebra, and joint, and bovine mandible. Each was homogenized in a mortar; part of each was ashed at 900°C and another part wet-ashed in nitric and perchloric acids.[1] The ratio of Pb^{210} in the dry-ashed to wet-ashed samples was 1.06 ± 0.10 (standard error).

Table 12 presents the data on the Puerto Rican subjects arranged in order of increasing Pb^{210} concentration. The ages range from 21 to 109 years and the concentrations from 0.049 to 0.237 pC/g ash. Little

Table 12

Pb^{210} concentration in the bone of residents of San Juan, Puerto Rico

Sample No.	Age, years	Sex	Pb^{210}, pC/g ash ± E*	Sample No.	Age, years	Sex	Pb^{210}, pC/g ash ± E*
1	34	F	0.049 ± 0.005	15	45	F	0.111 ± 0.009
2	23	F	0.053 ± 0.007	16	29	M	0.113 ± 0.013
3	45	M	0.064 ± 0.006	17	109	F	0.115 ± 0.012
4	66	F	0.064 ± 0.010	18	45	M	0.117 ± 0.012
5	24	M	0.074 ± 0.009	19	51	M	0.125 ± 0.013
6	29	F	0.080 ± 0.004	20	51	F	0.126 ± 0.011
7	61	M	0.083 ± 0.012	21	54	M	0.139 ± 0.008
8	67	M	0.083 ± 0.009	22	66	M	0.165 ± 0.015
9	39	F	0.085 ± 0.007	23	67	M	0.170 ± 0.013
10	85	M	0.093 ± 0.011	24	25	M	0.180 ± 0.012
11	73	M	0.100 ± 0.011	25	68	M	0.187 ± 0.011
12	46	M	0.107 ± 0.007	26	58	M	0.187 ± 0.013
13	26	F	0.107 ± 0.011	27	78	M	0.195 ± 0.014
14	24	M	0.108 ± 0.012	28	44	M	0.237 ± 0.016

*E = 90% confidence limit

correlation between age and concentration is apparent. Table 13 shows, for the entire group and for the males and females separately, the mean concentrations of Pb^{210}, the range of values and the number of samples; similar data are presented for the "trabecular" bone samples (rib, vertebra, iliac crest, and talus) taken from the Midwest study.[1]

Table 13

Mean concentrations of Pb^{210} found in the specimens of bone obtained from residents of Puerto Rico and of the Midwest

Subjects	Region				P**
	Puerto Rico		Midwest		
	Age, years	Pb^{210}, pC/g ash ± E*	Age, years	Pb^{210}, pC/g ash ± E*	
Total	51 ± 21	0.118 ± 0.054	57 ± 13	0.184 ± 0.144	< 0.005
Range	23 - 109	0.049 - 0.237	18 - 90	0.053 - 0.454	
No. of samples		28		67	
Male	53 ± 19	0.133 ± 0.049	60 ± 11	0.196 ± 0.096	< 0.001
Range	24 - 85	0.064 - 0.237	34 - 85	0.059 - 0.453	
No. of samples		19		47	
Female	47 ± 27	0.088 ± 0.028	52 ± 16	0.156 ± 0.108	< 0.005
Range	23 - 109	0.049 - 0.126	18 - 90	0.053 - 0.454	
No. of samples		9		20	

*E is the standard deviation (of a single measurement).

**P is the probability that the mean value for a given Puerto Rican group is essentially identical with that of the analogous Midwest group.

The data from each study appear to be approximately normally distributed. The mean age and sex classifications are also comparable, the Puerto Rican subjects being slightly, but not significantly, younger than those of the Midwest study. The mean value of Pb^{210} concentration in each Puerto Rican group is about 60% that of its Midwest analog. The differences are significant based on Student's t'-test (t-test modified for the nonidentities of the variances of the groups);[12] for the complete groups and female groups, $P<0.005$; for the male groups, $P<0.001$. The Puerto Rican male group also shows a mean value significantly higher than that of the female ($P<0.005$). It might be noted that the significance of the difference between the mean values of the Midwest male and female groups is questionable ($P<0.1$), possibly because of the greater Midwest population inhomogeneity as indicated by the larger fractional variance and the more extensive geographical areas sampled.

That the mean Pb^{210} concentrations are higher in the male than in the analogous female groups is probably due to the greater metabolic activity of the former. This greater activity implies (and is seen in the "Recommended Daily Dietary Allowances")[13] that, per unit body weight, males consume more food (and air) and consequently more Pb^{210} than females.

These comparisons are consistent with the hypothesis that, for human skeletons, the atmosphere constitutes a significant source of Pb^{210}, whether absorbed through direct inhalation or precipitation on foodstuffs. The relative contributions of diet and inhalation cannot be determined from the present data.

Additional support for the hypothesis that the atmosphere is a significant source of Pb^{210} could be inferred from Table 14. The average of 0.110 ± 0.037 pC/g ash in cortical bone from Germany is essentially identical to the 0.105 ± 0.100 pC/g ash found in cortical bone from the Midwest study. In England, where one would expect a lower atmospheric concentration of Pb^{210}, the few available measurements[8] indicate an average concentration in vertebrae (assuming an ash-to-wet weight ratio of 0.25[11]) very similar to that of the Puerto Rican samples. The mean values of both groups appear to be significantly lower than the comparable Midwest value for "trabecular" bone ($P<0.005$). The data of Hursh[9] for eastern U.S. are not directly comparable since whole-body rather than skeletal ash was measured.

Table 14

Regional variation of the Pb^{210} content of bone ash*

Bone	Region			
	Midwest, pC/g ash	Puerto Rico, pC/g ash	England, pC/g ash	Germany, pC/g ash
Trabecular	0.184 ± 0.144 (67)	0.118 ± 0.054 (28)	0.103 ± 0.019 (5)	- -
Cortical	0.105 ± 0.100 (61)	- -	- -	0.110 ± 0.037 (20)

*Numbers in parentheses - number of samples in study.

In summary then, skeletal concentrations of Pb^{210} appear to be higher in residents of continental regions than in those of islands. Further information is needed, however, before definite conclusions can be drawn concerning the importance of the atmosphere as a source of this nuclide. The concentration of Pb^{210} should be determined in the diet and in the atmosphere, and a larger sampling of the populations should be taken. Most important, comparison should be made of data from populations which, except for Pb^{210} concentrations in the air, are more nearly similar than those studied here.

I thank Dr. J. Rivera of the U. S. Atomic Energy Commission Health and Safety Laboratory and Dr. C. Galindo of the University of Puerto Rico for supplying the samples.

References

1. R. B. Holtzman. Health Phys. 9, 385 (1963).

2. R. A. Dudley. Low Level Irradiation. American Association for the Advancement of Science, Publication No. 59, Washington, D. C., 1959. p. 7.

3. L. B. Lockhardt, Jr., R. A. Baus, R. L. Patterson, Jr., and I. H. Blifford, Jr. Naval Research Laboratory Report, NRL-5208 (1958).

4. F. Barreira. Science 190, 1092 (1961).

5. W. M. Burton and N. G. Stewart. Nature 186, 584 (1960).

6. L. B. Lockhardt, Jr., R. L. Patterson, Jr., A. W. Saunders, Jr., and R. W. Black. Radiological Health Data 4(2), 71 (1963).

7. R. S. Russel. Radioisotopes in the Biosphere. The University of Minnesota Press, Minneapolis, 1960. Ch. 19.

8. C. R. Hill and Z. S. Jawarowski. Nature 190, 353 (1961).

9. J. B. Hursh. Science 132, 1666 (1960).

10. E. Groos, E. L. Sattler, and W. Stahlhofen. Atomkernenergie 8, 32 (1963).

11. R. B. Holtzman. Health Phys. 8, 315 (1962).

12. A. Hald. Statistical Theory with Engineering Applications. John Wiley and Sons, Inc., New York, 1952. p. 412 ff.

13. Food and Nutrition Board, National Research Council, Revised 1953. In Handbook of Chemistry and Physics, 38th Ed. Chemical Rubber Publishing Co., Cleveland, Ohio, 1956. p. 1813.

THE KINETICS OF ALKALINE EARTH TRACER METABOLISM*

Richard B. Holtzman

Abstract

In mammals the fractional retention R at time t after a single injection of an alkaline earth tracer has been shown to follow a power function which has only two adjustable constants:

$$R = \left[\frac{t + \gamma}{\gamma}\right]^{-b}$$

It is suggested here that this equation is theoretically sound; it is derived from a differential equation describing an n^{th} order kinetic reaction, and it is otherwise consistent with the principles of reaction kinetics. It is assumed that 1) the tracer is deposited onto a purely inorganic system of bone crystal (hydroxyapatite) of constant mass and surface area and is bathed in a solution of constant calcium concentration; 2) the fraction of the tracer in solution is negligible; and 3) the specific activity of the calcium deposited with the tracer at t = 0 remains constant throughout time, i.e., the traced calcium does not mix with the other calcium in the system. The parameters of the equation are then $b = 1/(n-1)$ and $\gamma = (b/k)c_0^{-1/b}$ where n is the order of the reaction, k the rate constant, and c_0 the ratio of the calcium deposited with the tracer to that present in the system. The proposed mechanism is recrystallization (only the dissolution component is observed). This theory is consistent with the experimental results that R is independent of the amount of tracer injected and that R and the apparent value of b are dependent on the calcium content of the diet.

Application of these equations to the case of a continuous and constant uptake of tracer yields finite values for the predicted retention, rather than the infinite level predicted by the simple power function.

---

*Abstract of paper presented at the Twelfth Annual Meeting of the Radiation Research Society, Miami Beach, Florida, May 17-20, 1964. Abstract published in Radiation Research 22, 198 (1964).

A RIGOROUS LEAST-SQUARES ANALYSIS OF COMPLEX GAMMA-RAY SPECTRA WITH PARTIAL COMPENSATION FOR INSTRUMENTAL INSTABILITY*

Robert M. Parr and Henry F. Lucas, Jr.

Abstract

The least-squares method for analyzing multichannel gamma-ray spectra is one of great power and versatility, but its full potential is difficult to realize because of instrumental instabilities. For sources having low or moderate activities and for which the counting times range from a few minutes to several hours, the most important instabilities are long term drifts in zero-energy channel intercept and gain. A computer routine based on the use of a special reference source is described, which can detect changes in zero-intercept of as little as 0.05 channels (for a 512 channel analyzer), and in gain of as little as 0.1%. By prior transformation of the data to compensate for these effects, and by the use of appropriate weighting factors in the least-squares analysis, the goodness of fit is dramatically improved. Often, the goodness of fit indicator "chi-squared over degrees of freedom" is reduced from a value in excess of three to a value which does not differ significantly from unity. The weighting procedure described takes into account the statistical errors in both the complex spectrum which is to be analyzed, and in the reference spectra which are its components. These computer methods have been applied to the analysis of gamma spectra from biological materials containing low activities of the natural series of radionuclides, and of atomic fallout products.

*IEEE Trans. NS-11 (3), 349 (1964).

Th

THE RELATIVE ACTIVITIES OF THORIUM DAUGHTER ISOTOPES IN THE TISSUES OF THOROTRAST PATIENTS. A PROGRESS REPORT.

Robert M. Parr

Introduction

Thorotrast is a colloidal preparation of thorium dioxide which was used extensively as a contrast medium in diagnostic radiology between the years 1930 and 1945. It is a radioactive substance containing isotopes of the Th^{232} decay series which, depending on the exact mode of administration, may be retained in the body over very long periods of time. As was pointed out by Marinelli,(1) the patients who received injections of this material during the years it was in common usage now constitute an invaluable and irreplaceable source of data on the clinical effects of long-term irradiation in man.

Of fundamental importance in any study of the effects of chronic irradiation is the accurate determination of radiation dose. Unfortunately, in the case of thorotrast patients, dosimetry is a problem of great complexity since thorium decays to its final stable state of Pb^{208} through a series of radioactive daughters. Some of these are sufficiently long lived to be metabolized in a way quite different from their parent, Th^{232}. Rundo(2) and Kaul(3) have studied the equilibrium status of some of the daughter isotopes in the tissues of a small number of patients and have shown that very marked degrees of radioactive disequilibrium exist. However, their conclusions were based on an extremely small number of measurements, and there remains an urgent need to confirm these findings and to extend the measurements to a greater variety of tissues.

Therefore, as an initial step in determining the radiation doses received by the tissues of thorotrast patients, procedures have been developed for elucidating the equilibrium status of thorium daughter isotopes in small samples of tissue. These methods have been applied to the analysis of some tissues from thorotrast patients and also from a small number of experimental animals which had been given injections of this material.

Analytical Method

Principle of the Method

The procedures which were developed for stydying the isotopes of the Th^{232} decay series listed in Table 15 relied principally on the use of gamma-ray spectrometry without any prior chemical processing of the samples. Only the parent isotope Th^{232} itself was not determined by these

means. In this case a chemical extraction of the thorium was carried out, and the Th^{232} was determined by alpha spectrometry. Throughout, emphasis was placed on the use of computer methods for processing all the experimental data in order to facilitate the analysis of large numbers of samples.

Table 15

Physical characteristics of Th^{232} and its radioactive daughters

Serial number of daughter isotope	Isotope	Half-life	Particle emitted and energy, MeV	Principal gamma ray energies*	Serial number of daughter isotope group
0 (parent)	Th^{232}	1.4×10^{10} yr	α 4.10	-	0 (parent)
1	Ra^{228}	5.85 yr	β 0.053	-	1
2	Ac^{228}	6.13 hr	β 1.55	0.34; 0.97; others up to 1.64	2
3	Th^{228}	1.91 yr	α 5.42 (0.83) 5.33 (0.17)	-	3
4	Ra^{224}	3.64 days	α 5.67	0.241 (weak)	4
5	Em^{220}	54.5 sec	α 6.28	-	
6	Po^{216}	0.16 sec	α 6.77	-	
7	Pb^{212}	10.6 hr	β 0.36	0.239	5
8	Bi^{212}	60.5 min	α (0.337) 6.05 β (0.663) 2.20	0.73 (weak)	6
9	Po^{212}	0.3 μsec	α 8.78	-	
10	Ti^{208}	3.1 min	β 1.77	0.58; 2.62; and others	

*Only gamma rays greater than 0.10 MeV in energy and more than 1% abundant are listed.

The analysis of the gamma-ray spectrometer data was complicated somewhat by the fact that only three of the eleven radioisotopes which comprise the Th^{232} decay series contribute significantly to the gamma spectrum of thorotrast: Ac^{228}, Pb^{212}, and Tl^{208}. Consequently, gamma measurements on living tissue samples, as in whole body counting, or single measurements of autopsy or biopsy samples, do not afford a very complete understanding of the status of the whole series of daughter isotopes. However, considerably more data can be obtained from autopsy and biopsy samples which are first encapsulated to prevent a possible loss of thoron and then counted at various subsequent times in order to follow the growth and decay of their radioactive components. Analysis of the growth and decay curves provides estimates of several of the daughter activities which cannot otherwise be determined directly.

For obvious reasons the encapsulated samples can rarely be placed in the spectrometer without a delay of at least 15 minutes after the moment of death or removal of the biopsy sample from the body. It follows, therefore, that the radioactive growth and decay curves must obey the laws of a six-component system since all the daughter isotopes can be combined into

the six groups listed in Table 15. Thus, for example, it takes only about 15 minutes for Tl^{208} to grow into equilibrium with its parent Bi^{212}, and only about 1 microsecond for Po^{212} to reach equilibrium. Therefore, on the time scale defined above, Bi^{212}, Po^{212}, and Tl^{208} must behave as a single isotope group with an apparent half-life of 60.5 minutes.

Unfortunately, this arrangement into groups of isotopes is not quite a perfect description of the in vivo situation. For example, group 4 (Table 15) undoubtedly breaks down in vivo into the two subgroups Ra^{224} and Em^{220} + Po^{216}. Therefore it is not possible to determine directly the in vivo activities of Em^{220} and Po^{216} by the procedure outlined above. This is a serious limitation of the method since both these isotopes contribute significantly to the total radiation dose from thorotrast; but it should be emphasized that it in no way invalidates the determination of Ra^{224} or any other of the daughter isotopes.

Gamma-ray Spectrometry

All gamma spectra were recorded by means of a Nuclear Data ND-120 pulse height analyzer and a 4- x 4-inch well-type NaI crystal. The standard counting conditions required a 5-ml sample contained in a small snap-top plastic tube to be counted inside the well of the crystal.

Although the gamma spectrum of thorotrast is derived almost entirely from groups 2, 5, and 6 of Table 15, there is an additional small contribution from Ra^{224} in group 4, which produces a low intensity spectrum virtually indistinguishable from that of Pb^{212}. In order to unscramble the spectra it has been found convenient to ignore this Ra^{224}, essentially by treating it as Pb^{212}, and then to apply a correction later in the analysis of the growth and decay curves.*

The spectrum unscrambling procedures required a knowledge of the individual gamma spectra of 1) pure Ac^{228} free of its daughters, 2) pure Pb^{212} free of its daughters, and 3) Bi^{212} in equilibrium with its daughters. The appropriate radioactive reference sources were prepared by a combination of solvent-extraction and ion-exchange procedures from commercially available samples of thorium metal and carrier-free Th^{228} solution. Their spectra are shown in Figure 49.

Spectrum unscrambling was carried out by the "matrix method" which involves dividing each spectrum into a number of bands and solving an appropriate set of simultaneous equations. It is expected that the method of least squares will soon be employed instead since it promises greater accuracy and sensitivity and a superior evaluation of errors.[4]

*The x-ray region below 100 keV has been entirely ignored in this discussion owing to the complexity of its components and the difficulty in applying corrections for self-absorption within the samples.

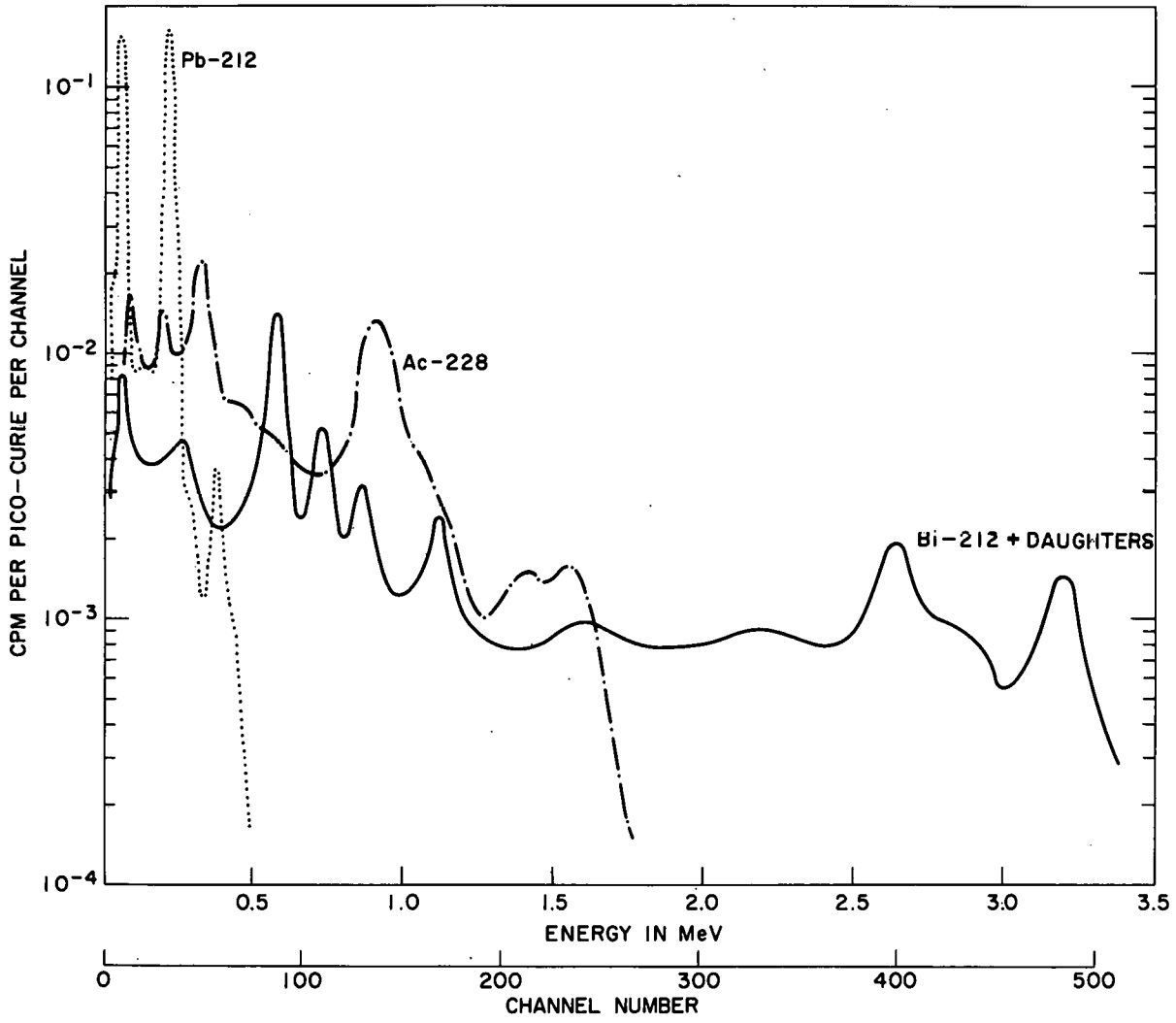

Figure 49

Gamma-ray spectra of thorium daughter isotopes

Analysis of Growth and Decay Curves

The measurements which define all the necessary parameters of the growth and decay curves extend over a period of roughly four weeks from the time that a sample is prepared for analysis. During this time the activity of Ra^{228} can be regarded as a constant since its half-life is almost six years. Consequently, it is legitimate to regard Ra^{228} as the ultimate parent of the series of daughter isotopes listed in Table 16. The relationships between their activities at different times are given by the expressions in column 4, where, after Kirby,[5] each Bateman coefficient F_{ij} has the form:

$$F_{ij},\ (i > j) = (-1)^{i-j}\,[\lambda_{(j+1)} \cdot \lambda_{(j+2)} \cdots \lambda_{(i)}]$$

$$\times\left[\frac{e^{-\lambda(j)t}}{[\lambda(j) - \lambda(j+1)][\lambda(j) - \lambda(j+2)](\ldots..)[\lambda(j) - \lambda(i)]} + \ldots.\right.$$

$$\left. \ldots + \frac{e^{-\lambda(i)t}}{[\lambda(i) - \lambda(j)][\lambda(i) - \lambda(j+1)](\ldots..)[\lambda(i) - \lambda(i-1)]}\right]$$

$$F_{jj} = e^{-\lambda_j t}$$

In this expression, $\lambda_1, \lambda_2, \ldots \lambda_6$ are the appropriate decay constants for the isotope groups listed in Table 16. As an example, the coefficients which define the activity of Bi^{212} as a function of time are illustrated in Figure 50.

Table 16

Analysis of growth and decay curves

Serial number of isotope group	Isotope	Activity at zero-time*	Activity at time t after zero-time (where each coefficient F_{ij} is a function of t)**
1	Ra^{228}	A_1^0	$F_{11}A_1^0$
2	Ac^{228}†	A_2^0	$F_{21}A_1^0 + F_{22}A_2^0$
3	Th^{228}	A_3^0	$F_{31}A_1^0 + F_{32}A_2^0 + F_{33}A_3^0$
4	Ra^{224}, Em^{220}, Po^{216}	A_4^0	$F_{41}A_1^0 + F_{42}A_2^0 + F_{43}A_3^0 + F_{44}A_4^0$
5	Pb^{212}†	A_5^0	$F_{51}A_1^0 + F_{52}A_2^0 + F_{53}A_3^0 + F_{54}A_4^0 + F_{55}A_5^0$
6	Bi^{212}, Po^{212}, Tl^{208}†	A_6^0	$F_{61}A_1^0 + F_{62}A_2^0 + F_{63}A_3^0 + F_{64}A_4^0 + F_{65}A_5^0 + F_{66}A_6^0$

*"Zero-time" is the time of death, or, in the case of a biopsy sample, the time at which it is removed from the body.

**F_{ij} is the activity of isotope group i at time t in a sample initially containing unit activity of pure isotope group j.

†These isotopes are essentially the only gamma emitters in the Th^{232} decay series (see text).

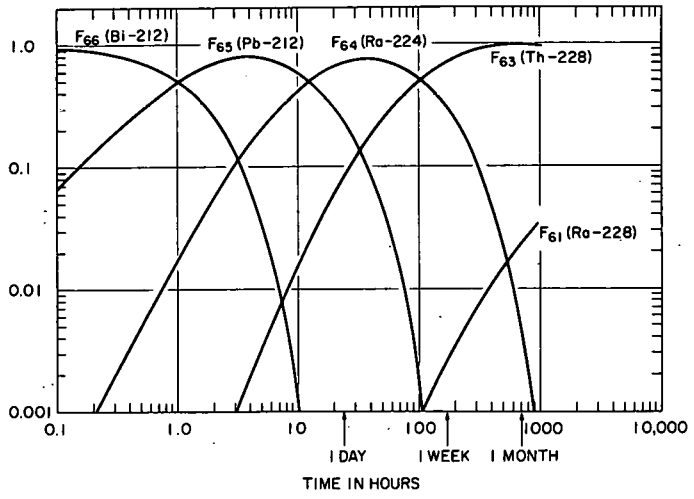

Figure 50

Bateman coefficients defining Bi^{212} activity

Each of the activities $A_1^0,\ldots,A_6^0$ can be estimated from the growth and decay curves by solving sets of simultaneous equations. Thus, two measurements of the Ac^{228} activity are sufficient to provide estimates of the two unknowns A_1^0 and A_2^0. Only four unknowns then remain to be determined, and four measurements of the Bi^{212} activity are sufficient to define their values.

The times at which measurements should be made in order to provide the best sensitivity and resolution can be judged by inspection of Figure 50 and corresponding graphs of the other Bateman coefficients. Ideally, four measurements should be made as follows:

Measurement	Hours from zero time
1	<0.5
2	~6
3	~50
4	~400

The correction for the small contribution from Ra^{224} which is ignored in the spectrum unscrambling procedure can be made by a method of successive approximations. Once approximate values of the coefficients A_1^0, A_2^0, A_3^0, and A_4^0 have been obtained (in the way described above), it is a simple matter to make allowance for the Ra^{224} by first using the appropriate expression in Table 16 to calculate the Ra^{224} activity.

Determination of Th^{232}

The Th^{232} determinations were carried out some time after the completion of all the gamma measurements. The samples were wet ashed in concentrated nitric acid, and the thorium was chemically separated by a dibutyl phosphate extraction.(6) The ratio of Th^{232}/Th^{228} was determined by alpha spectrometry using a Frisch Grid ionization chamber, and the Th^{232} activity was then estimated using the previously evaluated Th^{228} activity. This method did not require a knowledge of the chemical yield of the extraction procedure.

Results

Despite the fact that many thousands of people are probably still alive who were injected with thorotrast during the 1930's and 1940's,(1) it has proved to be very difficult to obtain any of their tissues for analysis. Most of the human measurements so far were of autopsy samples from terminal cancer patients who had been injected with thorotrast just a few weeks prior to death (Table 17). The remaining human tissue samples were comprised of a few specimens of blood and a single sample of aspirated bone marrow (Table 18).

Table 17

Autopsy samples from thorotrast patients

Sample code	Duration of burden, days	Volume of thorotrast administered, ml	Tissue	Th^{232}*	Ra^{228}*	Th^{228}*	Ra^{224}*
02	49	50 (batch 12878)	liver	?	23 ± 1 (0.16)	144 ± 5 (1.00)	85 ± 4 (0.59)
			spleen	?	64 ± 2 (0.17)	372 ± 12 (1.00)	277 ± 22 (0.75)
			rib**	?	3.3 ± 0.1 (0.27)	12.4 ± 0.5 (1.00)	17 ± 2 (1.4)
			vertebra**	?	6.3 ± 0.2 (0.23)	28 ± 1 (1.00)	22 ± 3 (0.79)
			(injection material)†	(2.6 ± 0.1)	(0.51)	(1.00)	(1.00)
03	49	23 (batch 12878)	liver	(2.4 ± 0.1)	24 ± 1 (0.17)	143 ± 5 (1.00)	93 ± 4 (0.65)
			spleen	(2.5 ± 0.1)	25 ± 1 (0.18)	137 ± 4 (1.00)	102 ± 4 (0.74)
			rib**	(2.2 ± 0.1)	0.7 ± 0.2 (0.18)	3.8 ± 0.3 (1.00)	4.1 ± 0.5 (1.08)
			vertebra**	(2.3 ± 0.1)	1.9 ± 0.1 (0.63)	3.0 ± 0.1 (1.00)	3.9 ± 0.2 (1.30)
			(injection material)†	(2.6 ± 0.1)	(0.51)	(1.00)	(1.00)

*Picocuries per gram of fresh tissue at time of death. Numbers in parentheses are activities relative to Th^{228}.

**Fresh bone containing some bone marrow.

†Th^{232} activity: approximately 0.024 μc/ml.

Table 18

Blood and bone marrow samples from thorotrast patients

Sample code	Duration of burden	Volume of thorotrast administered, ml	Tissue	Ra^{228}*	Ac^{228}*	Th^{228}*	Ra^{224}*	Pb^{212}*	Bi^{212}*
57	> 10 years	?	cells	-2	-2	-1	-1	87	93
			plasma	2	2	2	3	4	?
59	11 years	?	marrow**	8	8	8	3	40	?
70	7 days	23	cells	5	3	-2	1	67	?
			plasma	1	5	-2	7	3	?
71	20 days	23	cells	1	-1	-1	3	73	?
			plasma	4	-3	0	8	-4	?
Estimated standard deviations				±2	±4	±2	±3	±5	±10

*Picocuries in a 5-ml sample.

**Marrow containing a small but undetermined quantity of whole blood.

One of the most difficult problems in working with human tissues is that of obtaining the samples soon enough to provide estimates of the Bi^{212} activities, i.e., within an hour of death. It was mainly for this reason, but also in the hope that the metabolic behavior of thorotrast in experimental animals might throw some light on its behavior in man, that a number of experiments with rats were carried out. The thorotrast (usually about 0.5 ml) was injected through the tail vein, and the animals were sacrificed after various different intervals of time. Analyses of their tissues yielded the results recorded in Table 19.

For a variety of reasons the measurements are rather fragmentary in nature. Many were made at a time when the analytical methods were still in a rudimentary stage of development, and a number of the samples could not be prepared for analysis soon enough to provide estimates of the

shorter lived activities. Finally, a large number of the Th^{232} determinations still remain to be completed.

Table 19

Analysis of rat tissues

Sample code	Duration of burden	Tissue	Ra^{228}*	Ac^{228}*	Th^{228}*	Ra^{224}*	Pb^{212}*	Bi^{212}*
29 Thorotrast batch 13098	6 hours	liver	310 (0.27)	617 (0.53)	1171 (1.00)	198 (0.17)	620 (0.53)	655 (0.56)
		spleen	58 (0.27)	118 (0.56)	212 (1.00)	26 (0.12)	86 (0.41)	102 (0.48)
		kidney	34	22	6	43	206	511
		whole blood	11	14	16	2	110	67
		(injection material)	(0.80)	(0.80)**	(1.00)	(1.0)**	(1.0)**	(1.0)**
34 Thorotrast batch 13098	3 days	liver	275 (0.22)	198 (0.16)	1226 (1.00)	266 (0.22)	123 (0.10)	9 (0.01)
		spleen	86 (0.24)	48 (0.14)	355 (1.00)	59 (0.17)	15 (0.04)	-
		kidney	0	-2	4	9	196	273
		whole blood	-6	-2	3	6	56	22
		tail	33 (1.00)	23 (0.70)	33 (1.00)	47 (1.43)	31 (0.94)	-
		bone	160 (5.5)	161 (5.5)	29 (1.0)	225 (7.8)	111 (3.8)	-
		(injection material)	(0.80)	(0.80)**	(1.00)	(1.0)**	(1.0)**	(1.0)**
65† Thorotrast batch 13098	20 days	liver	17 (0.26)	19 (0.29)	66 (1.00)	20 (0.30)	30 (0.45)	16 (0.24)
		spleen	0	6	0	3	11	29
		kidney	1	18	0	3	92	150
		tail	225 (0.12)	216 (0.12)	1810 (1.00)	1751 (0.97)	-	-
		(injection material)	(0.98)	(0.98)	(1.00)	(1.00)	(1.00)	(1.00)
67†† Thorotrast batch 13098	41 days	liver	150 (0.22)	147 (0.22)	663 (1.00)	250 (0.38)	92 (0.14)	34 (0.05)
		spleen	31 (0.27)	29 (0.26)	113 (1.00)	31 (0.27)	16 (0.14)	9 (0.08)
		kidney	-1	0	4	5	94	182
		tail	75 (1.34)	67 (1.20)	56 (1.00)	61 (1.09)	57 (1.02)	41 (0.73)
		(injection material)	(0.98)	(0.98)	(1.00)	(1.00)	(1.00)	(1.00)
72 Thorotrast batch 09940	35 days	liver	1357 (0.68)	1185 (0.59)	2002 (1.00)	1072 (0.58)	696 (0.35)	500 (0.25)
		spleen	190 (0.66)	185 (0.64)	288 (1.00)	126 (0.44)	72 (0.25)	52 (0.18)
		kidney	14 (0.54)	20 (0.77)	26 (1.00)	17 (0.65)	58 (2.2)	90 (3.5)
		tail	81 (2.3)	86 (2.5)	35 (1.00)	76 (2.2)	61 (1.7)	50 (1.4)
		bone	75 (5.0)	80 (5.3)	15 (1.00)	52 (3.5)	27 (1.8)	-
		(injection material)	(0.80)	(0.80)	(1.00)	(1.00)	(1.00)	(1.00)
Estimated standard deviations			±2 pC or ±5%‡	±4 pC or ±5%‡	±2 pC or ±5%‡	±3 pC or ±5%‡	±5 pC or ±5%‡	±10 pC or ±10%‡

*Picocuries of activity at time of death in total sample analyzed (numbers in parentheses are activities relative to Th^{228}). The samples analyzed were liver, approximately 70% of total; spleen, approximately 90% of total; kidney, approximately 90% of total;[2] tail, 4-cm length containing site of injection; bone, 1-2 g of fresh bone largely devoid of marrow.

**No actual measurements of the equilibruim status of the shorter lived daughters at the time of injection were made in this case, but measurements on two other samples of injection material indicate that none of the shorter lived daughter activities was more than 5% below radioactive equilibrium with its parent.

† Apparently a poor injection since most of the thorotrast was located subcutaneously in the tail.

†† Apparently a poor injection since a large proportion of the injected thorotrast could not be accounted for.

‡ Whichever error estimate is the larger.

Determination of Errors

The calculation of the errors arising from the statistics of the counting procedures is very complicated since the experimental data are made to undergo a double matrix inversion process. Each inversion introduces correlation between the matrix coefficients, and in this way a series of covariance terms arises which has to be taken into account in

calculating the errors rigorously. The program for doing this has not yet been completed and, therefore, the errors quoted are those which have been determined experimentally by multiple counting of some of the samples.

Discussion

Autopsy Samples from Thorotrast Patients

The most significant observation which can be made about the figures in Table 17 concerns the behavior of the 3.6-day Ra^{224}. Between 25 and 40% of that forming within the liver and spleen was evidently escaping and finding its way in part to the skeleton. Rundo[2] observed a similar washout from liver and spleen in each of three patients who had been injected with thorotrast many years previously. Kaul[3] on the other hand observed only about a 10% washout of Ra^{224} in several long-term thorotrast patients. Therefore, it is difficult to say on the basis of current knowledge what the usual metabolic behavior of this isotope is, and whether it is the same at early and late times.

A number of interesting deductions can be made from a comparison of the Ra^{228}/Th^{232} ratios in liver, spleen, and injection material (Table 17). It can be calculated that approximately 65% of the Ra^{228} which was present in the injection solution existed in a free, readily excretable form. This implies that 65% of the Th^{228} which was being formed while the thorotrast was still in its ampoule - about 25% of the <u>total</u> activity of Th^{228} in the ampoule - should also have been in a free form, not associated with the thorotrast particles. Following intravenous injection, monomeric tracer thorium such as this accumulates preferentially in the skeleton,[7] and, therefore, one would expect to observe a depression of the Th^{228}/Th^{232} ratios in liver and spleen, and an elevation in bone. Unfortunately, the measurements are not definitive about this, but certainly there does not appear to be a pronounced accumulation of Th^{228} in the skeleton. This suggests strongly that the free Th^{228} had become adsorbed onto the surface of the thorotrast particles, which would be an important observation if it could be substantiated, since the location of the Th^{228} presumably has a bearing on the escape of its daughter Ra^{224} from the liver and spleen. However, the constancy of the Th^{228}/Th^{232} ratios can be explained in another way, for the free Th^{228} may have become bound on the walls of the thorotrast ampoule prior to injection, in which case there would have been no free Th^{228} present in the injection material. Experiments with other thorotrast ampoules (alas, the one in question had been thrown away) gave highly variable results. In some of them a large proportion of the total activity <u>was</u> tightly bound to the glass, while in others, only a negligible activity was retained in this way. The factors which determine adsorption onto the walls of the ampoules have yet to be discovered.

Blood Samples from Thorotrast Patients

The only clearly demonstrable activity in whole blood appeared to be Pb^{212} (probably in equilibrium with its daughter Bi^{212}) and this was contained almost entirely in the cellular fraction (Table 18). The ratio Ra^{224}/Pb^{212} for whole blood appeared to be much smaller than the value of 0.25 reported by Rundo.[2] Considering the long biological half-life of lead in the liver (about 2000 days[8]), it is reasonable to assume that most of the Pb^{212} found in the blood did not come by diffusion of lead itself from the reticuloendothelial system, but rather that it was produced by thoron decaying within the bloodstream. The data on Pb^{212} metabolism reported by Stover[9] suggest that the concentrations of thoron in the blood were approximately double those of Pb^{212}.

Rat Tissues

The most complete series of measurements made so far were of a variety of rat tissues (Table 19). Not all the injections were completely satisfactory, but nevertheless a certain pattern in the behavior of the isotopes following intravenous injection could be discerned.

The long-lived isotopes Ra^{228} and Th^{228} were deposited mainly in the liver and spleen in the way anticipated for isotopes bound to the thorotrast particles. However, a certain proportion of the injected Ra^{228} behaved as free ionic radium and was either excreted or incorporated into the skeleton. Curiously, the proportion of free radium appeared to vary quite markedly with the different batches of thorotrast used (compare animals 67 and 72), but no explanation of this phenomenon has yet been discovered.

The 6-hr Ac^{228} contained in the injection material was taken up by the liver and spleen more readily than its parent Ra^{228} (animal 29). After three days the situation was reversed, and there was an actual deficiency of Ac^{228} in the liver and spleen. At later times the Ac^{228}/Ra^{228} ratio did not depart significantly from the expected value of unity.

A large proportion of the Ra^{224} produced by Th^{228} in the liver and spleen was either excreted or incorporated into the skeleton. As with the other radium isotope, the metabolism of Ra^{224} appeared to vary with the different batches of thorotrast used.

Most interesting of the isotopes were Pb^{212} and Bi^{212}, which apparently escaped fairly readily from the liver and spleen and became concentrated in the kidney. The Bi^{212} activity in the kidney was usually about double that of Pb^{212}. Up to the present time the radiation dose received by the kidney has not been thought very large. However, there are several high-energy alpha and beta particles associated with the decay of Bi^{212} (Table 15), and since there is virtually no ThO_2 present in the kidney to reduce their effects by self-absorption, the radiation dose may be quite appreciable.

Conclusions

The incomplete nature of the results presented here hardly warrants any general statement about the radiation doses delivered to the tissues of thorotrast patients. Indeed, from the standpoint of dosimetry this project has served better to demonstrate the complexities of the problem than to point to its solution. The Pb^{212} measurements, for example, are of rather questionable value since this isotope is not itself an alpha emitter and contributes only insignificantly to the total radiation dose. However, it happens that Pb^{212} is one of the most easily determined of the thorium daughter isotopes, and, therefore, it is natural to ask what possible uses these measurements have. Three possibilities are:

1) The estimation of Bi^{212}. This is a much more important isotope dosimetrically than Pb^{212}, and also much more difficult to determine on account of its very short half-life. Rundo[2] assumed that Pb^{212} and Bi^{212} are always in equilibrium, but the results of Table 19 demonstrate conclusively that this is not generally true. However, if some rationale could be discerned in the Pb^{212}/Bi^{212} ratios, the Pb^{212} measurements would be of undoubted value.

2) The estimation of Em^{220} and Po^{216}. These are the parents of Pb^{212} and they account for a substantial fraction of the total radiation dose from thorotrast. According to Stover[9] their activities in blood are directly proportional to the activity of Pb^{212}, but unfortunately it is not known whether such a simple relationship obtains in any other tissues.

3) The estimation of the total body burden of thorotrast in long-term patients. It is possible that the measurement of Pb^{212} in blood could be used to estimate the total body burden of thorotrast in a living patient. This would be a much simpler method than the current alternative techniques of whole body counting and thoron breath analysis, and there are many more laboratories in the world equipped to make such measurements.

In addition to these uncertainties, many other problems remain to be solved. It is known that thorotrast forms large aggregates of particles within the liver and spleen and that, as a consequence, the radiation doses are reduced to a considerable but unknown extent by self-absorption. Rotblat and Ward[10] have made estimates of the magnitude of this effect, but their measurements were made by autoradiography and took no account of the washout of the short-lived thorium daughters *in vivo*.

There now seems to be a possibility that the self-absorption can be measured directly since recent experiments in this division have shown that ThO_2 is thermoluminescent. Possibly, therefore, thorotrast can be used as its own dosimeter. However, this still leaves unanswered the question: what is the dose *distribution* in the tissues from each daughter

isotope - is it fairly uniform, or is it concentrated in the regions around each thorotrast aggregate? The absolute location of each daughter isotope - whether within the aggregates, or on their surfaces, or in the bulk of the tissue - is obviously an important factor which has to be known.

Another serious problem arises from the continual process of redistribution of thorotrast aggregates in the liver and spleen.[11] The kinetics of this process have not yet been determined, but evidently they could be very important if the microdistribution of dose within these organs were found to be very uneven. Finally there is a problem of deciding what RBE factor to use for all the alpha particles emitted by thorotrast.

I am indebted to a number of people for providing tissue samples for analysis. The human tissue specimens were supplied by Dr. M. L. Griem and Dr. G. S. Fisher. The rat experiments were made with the assistance of Dr. D. J. Simmons and Mr. J. E. Farnham. In addition I wish to express my sincere thanks to Mr. H. F. Lucas, Jr., for much valuable advice and encouragement.

References

1. L. D. Marinelli. The Effects of Chronic Low Levels of Radiation in Man: the Contribution of Epidemiological Studies. Trans. 9th Intern. Cong. of Radiology, ed. B. Rajewsky, Georg Thieme Verlag, Stuttgart, 1960. pp. 1234-1238.

2. J. Rundo. Measurement and Dosimetry of Radioactive Isotopes Deposited within the Human Body, with Special Reference to Colloidal Thorium Dioxide, following Intravenous Injection. Thesis, University of London, 1958.

3. A. Kaul. Gamma Spectrometric and Histo-Autoradiographic Investigations of the Distribution and Excretion of Thorium and its Daughters in Thorotrast Patients. Proc. IAEA Symposium on Assessment of Radioactive Body Burdens in Man, Heidelberg, May 1964, in press.

4. R. M. Parr and H. F. Lucas. A Rigorous Least Squares Analysis of Complex Gamma Ray Spectra with Partial Compensation for Instrumental Instability. IEEE Trans. NS-11 (3), 349 (1964).

5. H. W. Kirby. Decay and Growth Tables for the Naturally Occurring Radioactive Series. Anal. Chem. 26, 1063 (1954).

6. A. H. Stehney, D. E. Wallace and F. H. Ilcewicz, Butyl Phosphates as Extractants of Thorium from Bone. Argonne National Laboratory Report on Biological, Medical and Biophysics Programs, January 1956. ANL-5518, p. 18.

7. R. G. Thomas, R. Lie and J. K. Scott. Thorium Distribution and Excretion Studies I: Patterns following Parenteral Administration. Health Phys. 9, 153 (1963).

8. Report of Committee II, International Commission on Radiological Protection. Health Phys. 3, 217 (1960).

9. B. J. Stover. Pb^{212} (ThB) Tracer Studies in Adult Beagle Dogs. Proc. Soc. Exptl. Biol. Med. 100, 269 (1959).

10. J. Rotblat and G. Ward. Tissue Dosage from Thorotrast in the Body. Nature. 172, 769 (1953).

11. M. Faber. Thorotrast in Man. The Carrier State and the Sequelae. Some Aspects of Internal Radiation. Pergamon Press, New York, 1962. p. 473-498.

RAPID SPECTROPHOTOMETRIC METHOD FOR THE DETERMINATION OF LEAD IN BONE ASH*

F. H. Ilcewicz, R. B. Holtzman, and H. F. Lucas, Jr.

Abstract

The measurement of the absorbance of the chloro complex of lead (II) in 9 M hydrochloric acid at 271 mμ provides a simple and rapid method for the analysis of microgram quantities of lead in bone ash. Interfering ions, e.g., iron (III) and copper (II), were removed by extraction with triisooctylamine. The effect of the concentration of hydrochloric acid and calcium phosphate (bone ash) on the absorbance was studied. The optimum experimental condition was attained when bone ash was dissolved in 9 M hydrochloric acid at a concentration of 0.2 g ash/ml of acid. Beer's law was obeyed for lead concentrations up to 16 μg/ml. The sensitivity was 0.1 μg/ml and the standard error for calcium phosphate-lead standards was ±2%. The procedure has been used for determinations of lead in samples of bone ash in which the concentrations ranged from 6 to 80 ppm.

*Published in Analytical Chemistry 36, 1132 (1964).

CALCIUM ACCRETION AND BONE FORMATION IN DOGS

An Experimental Comparison between the Results of Ca^{45} Kinetic Analysis and Tetracycline Labeling

W. R. Lee,* J. H. Marshall, and H. A. Sissons*

In recent years much work has been carried out on the uptake by bone of radioactive isotopes, particularly those of calcium and strontium. These isotopes appear to act as tracers for calcium between blood and the rest of the body and have contributed much to knowledge of calcium metabolism. It has been found that calcium is rapidly taken up by the skeleton after its injection into the blood; if the rate of elimination of the tracer from the body is known, measurement of the rate of clearance of calcium from the blood allows calculation of the rate of calcium accretion.(1) Work on the anatomical sites of uptake of bone-seeking isotopes has made it clear that there is preferential deposition of these substances in regions of active bone formation and that there is a correlation between the amount of bone formation in the skeleton and the rate of calcium accretion. But it has also become apparent(2) that exchange processes with the calcium of existing bone tissue also contribute to long-term radioisotope uptake so that calcium accretion cannot be directly equated with bone formation.

A number of meanings have been attached to the terms "accretion" and "accretion rate." In this paper we use these terms in an operational sense simply to describe what is measured as A in the Bauer-Carlsson-Lindquist equation (Equation 1).

Until recently, it was not possible to make a quantitative evaluation of bone formation. It has been observed, however, that tetracycline antibiotics are deposited in bone and that they outline the surfaces on which bone formation is occurring at the time of injection.(3) It is possible, therefore, through the use of two tetracycline injections separated by a known time interval, to determine, for any skeletal site, the rate at which bone is deposited on forming surfaces. Accordingly, the rate of calcium accretion as determined by calcium-45 analysis was compared with the rates of bone formation in different parts of the skeleton as determined by double tetracycline labeling.

Materials and Methods

Two mongrel bitches were used for the experiment. One (dog P) was a puppy three to four months old; the other (dog N) was one to two years old. The experiment lasted twelve days, during which time the

*Institute of Orthopaedics, London.

animals were kept in metabolism cages and fed a standard dog diet. The general outline of the experiment was as follows. On day zero, each animal received a marker dose of dimethylchlortetracycline (20 mg/kg) by intravenous injection. On day six, the radioisotope Ca^{45} was injected. On day ten, a second marker dose of tetracycline was injected. Both animals were sacrificed on day twelve. Blood, urine, and fecal samples were collected from the time of Ca^{45} injection until sacrifice. The two tetracycline labels outlined the new bone formed in a ten-day interval. The Ca^{45} injection near the middle of this interval provided data for the calculation of accretion rate.

The complete skeleton was dissected from each animal, and the soft tissues were removed from the individual bones. Except for the vertebral column, each skeleton was separated into two halves, the left half being taken for radiochemical analysis, the right half for histology and autoradiography. In this way, specimens from comparable locations in the skeleton were used for isotope and tetracycline studies. One lumbar vertebra from each animal was taken for microscopic analysis, the rest of the vertebral column being analyzed radiochemically. The bones for histological and isotope analysis (femora, humeri, and lumbar vertebra, parietal bone, iliac crest, and rib) were fixed in absolute alcohol.

Radiochemical Procedures

High specific activity Ca^{45} (700 mC/g Ca) was injected intravenously as the chloride in aqueous solution. Dog P, weighing 4.5 kg, received 104 μC or 23 μC/kg. Dog N, weighing 10.0 kg, received 260 μC or 26 μC/kg. The volumes of solution injected were 2.0 ml and 5.0 ml, respectively. Urine and feces were collected daily from the metabolism cages. Blood samples were taken in heparin-rinsed syringes at 1/2, 1, 2, 4, and $7\frac{1}{2}$ hr and at 1, 2, 3, 4, and 6 days after injection. The samples were immediately centrifuged and the plasma decanted.

The fecal and bone samples were ashed overnight in silica crucibles at 600°C. The ash was weighed, dissolved in HCl, and diluted to 100 ml or 250 ml in volumetric flasks. After thorough agitation, 0.05-ml aliquots were pipetted in duplicate to nickel planchets and dried under a heat lamp. Blood plasma and urine aliquots (0.05 ml) were pipetted in duplicate directly to planchets and dried without heat. The planchets were counted under a thin end-window Geiger counter mounted in a lead shield. At least 1000 counts were timed for each planchet. The counting rates were corrected for background and converted to activities by comparison with Ca^{45} standard planchets pipetted from dilutions of the injection solution. All activities refer to the date of injection.

Repeated preparation and counting of samples gave a standard deviation of 3% for plasma and of 4% for bone. Corrections for self-absorption were determined by adding a known Ca^{45} activity to samples

of urine and plasma and to each of the solutions of bone and feces. Sources were prepared as already described, and the fractional self-absorption was measured by comparing the counting rates with that from a Ca^{45} standard. Correction was made for the relatively small activity already contained in each sample. The resulting relation between self-absorption and source thickness, measured in terms of the weight of ash per unit volume of parent solution, was used to correct for the small volume of water added with the Ca^{45}. Source preparation, counting, and correction for self-absorption yielded values with an estimated standard error of 4% in measurements of plasma activity and 7% in measurements of the activity of bone and excreta.

The skeletal content of Ca^{45} at sacrifice was obtained by doubling the Ca^{45} activities measured for the half of the skeleton which was analyzed. The activity in the lumbar vertebra which was taken for microscopic analysis was taken into account by averaging the activity in adjacent vertebrae.

The recovery of the injected Ca^{45} in the six-day collection of excreta and in the terminal skeleton was 98% for dog P and 95% for dog N. Soft tissue was not analyzed.

The calcium concentration of plasma and of solutions prepared from samples was measured by titration with EDTA, using photometric detection of the endpoint with murexide as an indicator. Titrations were made in duplicate and were compared with calcium standards. Plasma calcium averaged 10.4 mg/100 ml for dog P and 9.7 mg/100 ml for dog N. The total skeletal calcium was 57 g for dog P and 150 g for dog N.

Evaluation of Calcium Accretion Rate

Bauer, Carlsson, and Lindquist[1,4] have described a method of calculating an accretion rate A from data on the specific activity of the blood and the retention of activity in the body following a single intravenous injection of a calcium-like radioisotope. This accretion rate is defined by the following equation*

$$q R = E S + A \int_0^t S \, dt \qquad (1)$$

where

q is the activity of tracer injected into the blood in microcuries

R is the fractional retention of this activity in the body as a function of time (dimensionless)

*A term referring to the resorption of radioactive bone in the original equation has been omitted in Expression 1 because this term is set equal to zero whenever the equation is used to calculate A.

S is the specific activity of the blood (plasma) as a function of time in microcuries per gram calcium

A is the accretion rate for the whole body in grams calcium per day.

E is the rapidly-exchangeable calcium in grams.

The usual method of solving this equation involves the assumption that within a certain interval of time the values of A and E can be considered to be independent of the time after injection at which they are calculated. Equation 1 is written for two different times t_1 and t_2. These two equations are then solved simultaneously for A yielding

$$A = q\left[\frac{S_1R_2 - R_1S_2}{S_1I_2 - I_1S_2}\right] \tag{2}$$

where I_1 represents the time integral of S from time zero to time t_1, etc.

An equivalent way to solve Expression 1, which does not involve the above assumption, results from letting the interval between times t_1 and t_2 become very small so that one calculates A from the values and slopes of S and R at a single time (Expression 33, Reference 5).

$$A = \frac{qR(\lambda_S - \lambda_R)}{S + \lambda_S I} \tag{3}$$

where

λ_S is the rate constant of the tangent to the curve S at a particular time t. Note that $\lambda_S = -(1/S)(dS/dt)$.

λ_R is the corresponding rate constant for R. Note that $\lambda_R = -(1/R)(dR/dt)$.

I is the time integral of S from time zero to time t.

The interval between injection and the time at which A is calculated has some effect upon the result. Bauer, Carlsson, and Lindquist[4] used Expression 2 with time t_1 = 5 days and t_2 = 10 days for measurements in man. In the present experiment, Expression 3 was used, and a time of five days after injection was chosen. The slow variation of A with time after injection is discussed below.

Histological Procedures

Preparation of Sections. After fixation and the removal of soft tissues, blocks of bone were embedded in methyl methacrylate. Undecalcified sections were cut on a milling machine, and the sections for

fluorescence microscopy were ground by hand between glass plates;[6] 100-μ sections were used for microradiography, but for study of the tetracycline markers sections were ground to a thickness of 20-30 μ and were mounted in Fluorfree* mountant.

Fluorescence Microscopy. In the presence of calcium, tetracycline has a peak fluorescence at 520 μ when activated by a light of 410 mμ wavelength.[7] The light source used was a 250-Watt mercury vapor lamp which was fitted to an optical bench, along with a 2-in. collecting lens, a filter holder, and a monocular microscope. The most suitable primary filter was found to be a Corning 57-59, together with the Chance OB 10, which transmits light of 410-440 mμ.[8] A glass ultraviolet filter (Cooke, Troughton & Sims M1683) which transmits light of wave length greater than 520 mμ was used as a secondary filter in the microscope body. With this filter system, dimethylchlortetracycline markers appear as a bright yellow line against a dark green background. Bone itself shows some green autofluorescence, but this can readily be distinguished from the fluorescence of the tetracycline marker.

Measuring Technique. The bone formation rate was determined by measuring the area of new bone enclosed by the markers in a complete section of a particular bone block, and also the total area of bone present in the same section. For a thin section these areas can be assumed to be proportional to the respective volumes of tissue present. The area components were measured using the Leitz integrating eyepiece micrometer.[9] With this instrument, the intersection of a horizontal and vertical crosswire is made to traverse a series of paths across a square area in the microscope eyepiece. The movement of the horizontal crosswire can be activated by any one of 6 measuring micrometer screws, so that the length of intercept corresponding to each of 6 tissue components can be recorded separately. This is, in effect, a way of integrating for area, the total intercept distance for each component, giving a measure of the relative area it occupies in the section. In cortical bone, five components - periosteal and endosteal new bone, new bone of secondary osteons, pre-existing bone, and vascular space - were recorded. Each field in which measurements were made corresponded to an area of tissue 2 x 2 mm in size, and these fields were evenly distributed throughout the section (Figures 51 and 52). Repeatability tests on sections of cortical bone showed that it was necessary to sample at least 50% of the total area of bone in a section to achieve a standard error of less than 10% for the area of new bone. There was a considerable variation between the individual values obtained for different areas in any one section, but there was a good agreement between the mean values from sections taken from the same block. The mean value obtained from 2 or 3 sections was, therefore, assumed to be representative of the block from which they were taken.

*G. T. Gurr Ltd.

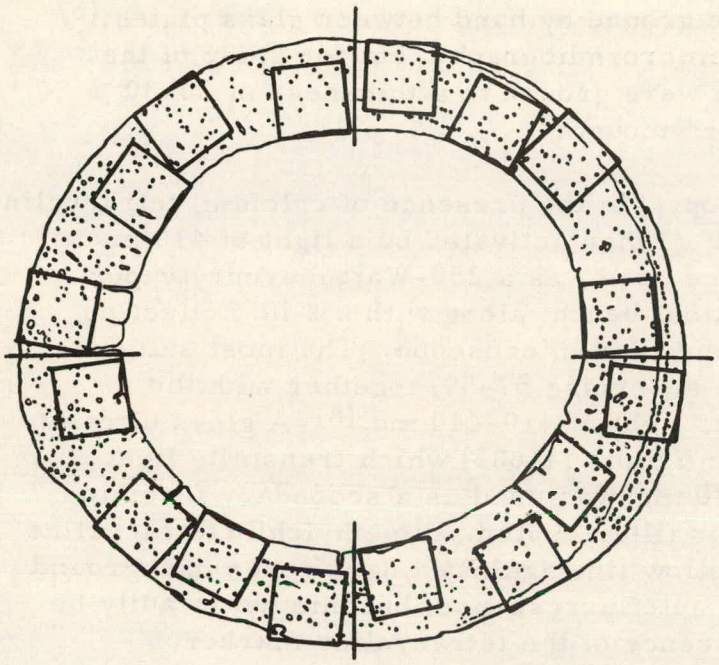

Figure 51

Sketch of fields measured by tetracycline method

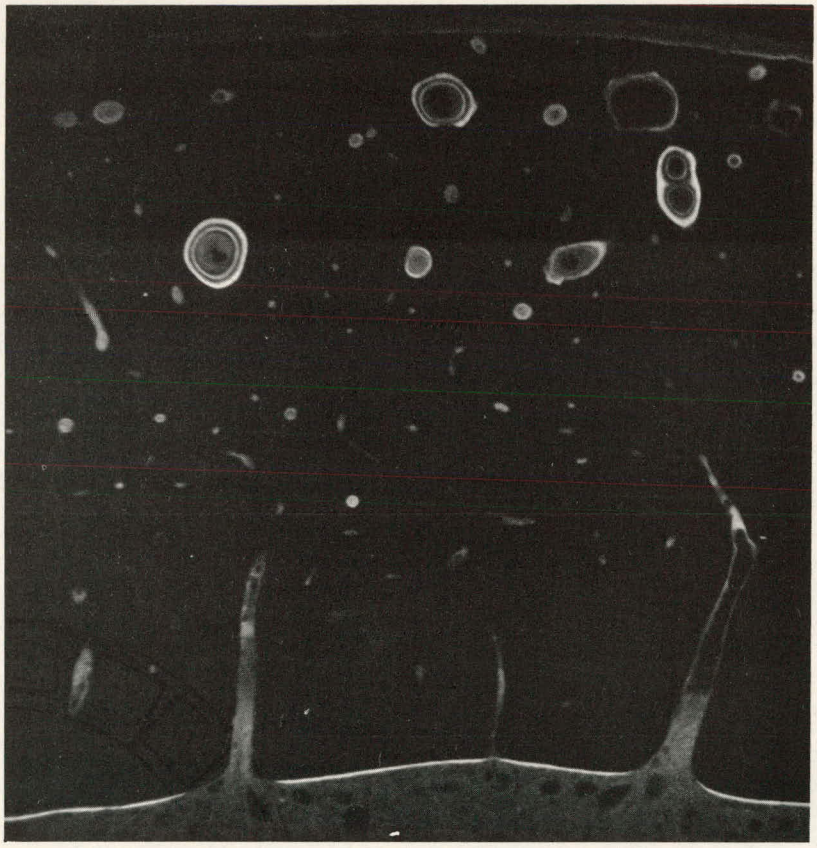

Figure 52

Ultraviolet photograph of typical field in the femoral shaft of dog N

Cancellous bone was less suitable for quantitative analysis than the cortex of the shafts of the long bones because a high proportion (approximately 50%) of the surfaces with tetracycline markers were sectioned

obliquely. As the sections were relatively thick (20-30 μ), the obliquely-sectioned markers appeared wide and flared, and it was difficult to determine accurately the area of new bone enclosed by them. With the integrating eyepiece micrometer, values were first obtained for the surfaces with clear markers. These clearly gave an underestimate for the bone formation rate since the surfaces of formation with flared markers were disregarded. In order to achieve a better approximation, the mean intercept distance derived from the clear markers was determined, and this value was recorded wherever a flared surface was encountered in the fields scanned. The total value thus obtained is put forward as a reasonable approximation for the bone formation rate.

Autoradiographic Procedure

The blocks of bone embedded in methyl methacrylate were cut on a milling machine into sections at least 150 μ thick. Contact autoradiographs were made on Eastman Type A autoradiographic plates. Included in each development batch were calibration plates exposed to plaster-of-Paris radiators[10] which contained known aliquots of the injection solution per unit weight. The darkening of the autoradiographs and calibration plates was measured with a microscope-densitometer with an aperture of 30 μ. The diffuse component was measured at numerous locations for each section, and the values were averaged. The standard deviation of these values for each section was 10-15%. Care was taken to avoid areas of new bone growth as indicated by tetracycline lines and high localized uptake of Ca^{45}. The specific activity of the diffuse component was calculated by relating the measured darkening values to the activity per gram of the plaster-of-Paris radiators[2] and assuming the calcium content of the embedded bone to be 0.25 g Ca/g bone.

Results

Isotope Data

The specific activity of the blood plasma as a function of time after injection is shown in Figures 53 and 54, together with the time integral of the plasma specific activity obtained by numerical integration. The retention of activity in the body was obtained by subtracting from the injected dose the cumulative fecal and urinary excretion, allowing one day for fecal delay. The retained activity divided by total skeletal calcium (the average specific activity of the body) is also shown in Figures 53 and 54. The percent retention of activity as a function of time after injection is listed in the first column of Tables 20 and 21.

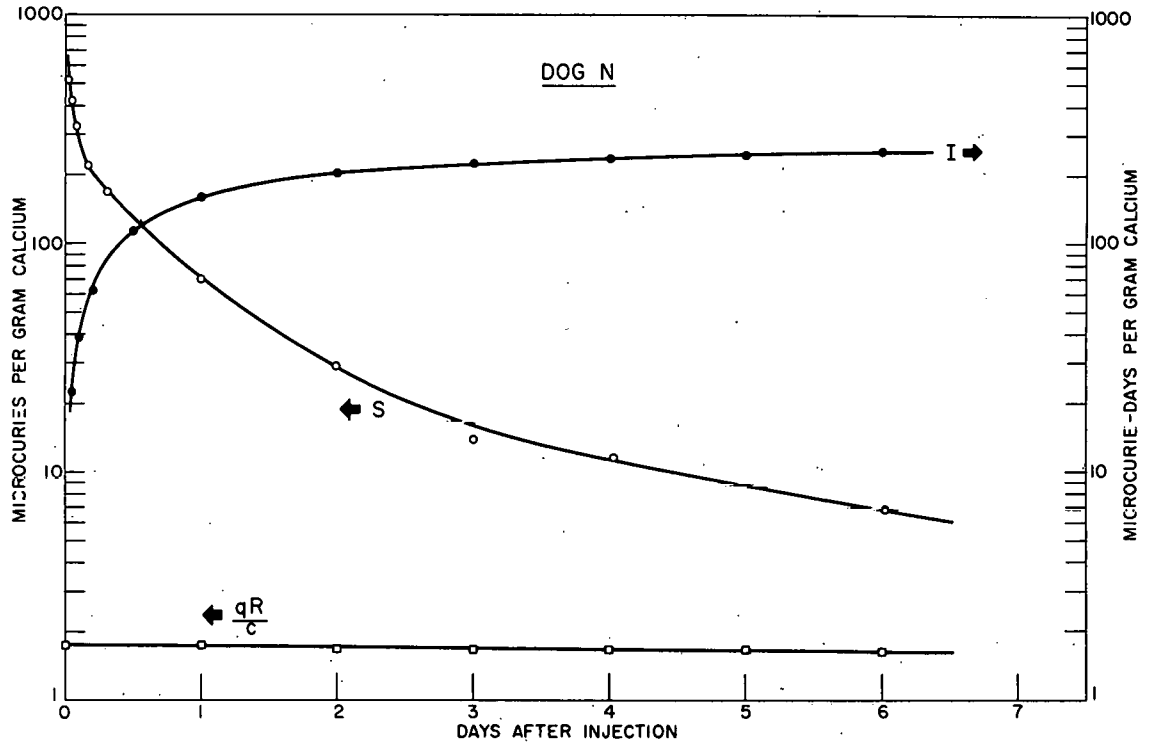

Figure 53

Data for the specific activity of blood plasma vs time after injection (curve S). The time integral of curve S from time zero to time t is given by curve I. The average specific activity of the body vs time is given by the curve labeled qR/c, where q is the activity injected (260 μC), c is skeletal calcium (150 g) and R is the fractional retention of the injected activity vs time as determined from collection of excreta.

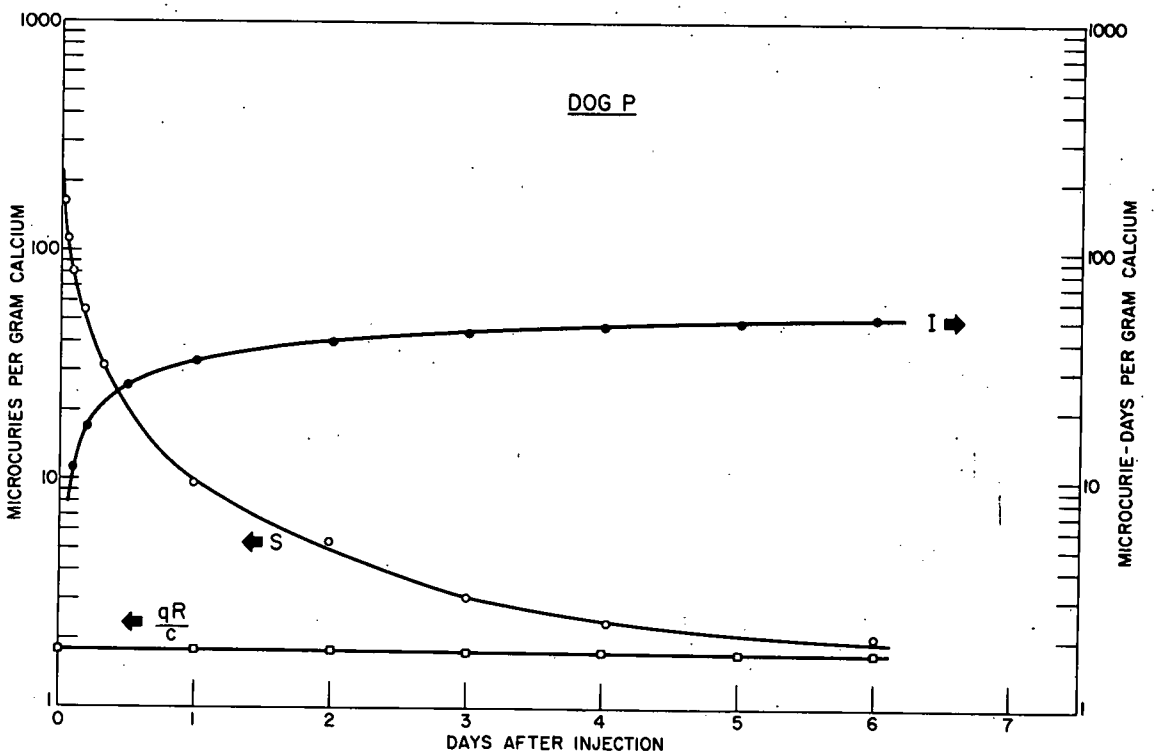

Figure 54

Same as Figure 53 except q = 104 μC and c = 57.7 g Ca

Table 20

Dog N. Isotope results.

Quantities correspond to those in Expression 3

Injected activity q = 260 μC;
skeletal calcium c = 150 g.

t, days	R, %	S, μC/g Ca	I, μC-days/g Ca	λ_S, day^{-1}	λ_R, day^{-1}	A/c, %/day
1	99.8	72.0	160	1.1	0.02	0.75
2	96.2	29.0	202	0.76	0.015	0.68
3	95.5	16.0	223	0.45	0.01	0.62
4	94.3	11.5	236	0.28	0.008	0.58
5	94.0	8.8	246	0.26	0.008	0.57
6	93.2	6.9	253	-	-	-

Table 21

Dog P. Isotope results.

Quantities correspond to those in Expression 3

Injected activity q = 104 μC;
skeletal calcium c = 57.7 g.

t, days	R, %	S, μC/g Ca	I, μC-days/g Ca	λ_S, day^{-1}	λ_R, day^{-1}	A/c, %/day
1	99.2	10.0	33	1.0	0.006	4.1
2	98.7	5.0	40	0.57	0.004	3.6
3	98.4	3.1	44	0.37	0.003	3.3
4	98.1	2.5	47	0.19	0.003	2.9
5	97.8	2.1	49	0.14	0.002	2.7
6	97.6	1.8	51	-	-	-

The accretion rate for the whole body was calculated from these data by means of Expression 3. The values of S, I, λ_S, and λ_R taken from smooth curves through the data are shown in Tables 20 and 21 together with the values of A that result from calculation at different times after injection. The values of A for the time of five days after Ca^{45} injection are

A_5/c = 2.7 %/day for dog P

A_5/c = 0.57 %/day for dog N.

These values refer to A in grams Ca/day divided by the total skeletal calcium c in grams. From the errors of the input data, we estimate that these values are good to within 10-15%.

The specific activity (activity/g Ca) of individual blocks of bone and of the skeleton as a whole is shown in Tables 22 and 23. Also shown in these tables are local values of accretion rate based upon the whole body value for five days and upon the local specific activity according to the relation:

$$\text{Local accretion rate} = \text{Whole body accretion rate} \times \frac{\text{Local specific activity}}{\text{Whole body specific activity}} \quad (4)$$

The application of this relation is discussed below.

Table 22

Dog N. Isotope analysis of skeleton.

For paired bones, the values of Ca^{45} activity relate to both sides of the skeleton. The local accretion rates are based on Expression 4.

Site	Block	Activity, μC	Specific activity, μC/g Ca	Accretion rate, %/day
Femur; upper end	NA	6.3	1.95	0.72
Femur; proximal shaft	NCPL	0.79	0.69	0.26
Femur; midshaft	NCML	0.59	0.58	0.21
Femur; distal shaft	NCDL	1.24	1.17	0.43
Femur; lower end	NCER	8.4	1.98	0.73
Tibia, fibula, rest of femur	-	20.8	1.54	0.57
Humerus, radius, ulna	-	31.3	1.43	0.53
Vertebrae; lumbar	NJ	14.2	2.16	0.80
Vertebrae; thoracic (mostly)	-	15.9	1.92	0.71
Vertebrae; cervical (mostly)	-	14.0	1.78	0.66
Vertebrae; cervical; tail; sternum	-	15.2	1.71	0.63
Ribs	-	18.6	1.75	0.65
Pelvis, scapula (except iliac crest)	-	22.0	1.85	0.69
Iliac crest	NL	2.03	3.36	1.24
Skull (except mandible)	-	30.7	1.39	0.52
Mandible	-	16.5	1.64	0.61
Carpus and tarsus	-	13.0	0.77	0.29
Whole skeleton		232.6	1.54	0.57

Table 23

Dog P. Isotope analysis of skeleton.

For paired bones, the values for Ca^{45} activity relate to both sides of the skeleton. The local accretion rates are based on Expression 4.

Site	Block	Activity, μC	Specific activity, μC/g Ca	Accretion rate, %/day
Femur; proximal shaft	PCPR	0.57	1.19	1.9
Femur; midshaft	PCMR	0.41	0.87	1.4
Femur; distal shaft	PCDR	0.81	1.46	2.3
Femur; lower end	-	4.4	2.72	4.2
Tibia, fibula, rest of femur	-	10.4	1.75	2.7
Humerus, radius, ulna	-	14.9	1.91	3.0
Vertebrae; lumbar	-	6.6	2.13	3.3
Vertebrae; (other); tail; sternum		15.1	1.88	2.9
Ribs, carpus, tarsus	-	15.9	1.62	2.5
Pelvis, scapula, mandible	-	15.1	1.70	2.7
Skull (except mandible)	-	15.5	1.43	2.2
Whole skeleton		99.7	1.73	2.7

Rate of New Bone Formation

Dog N (aged 1 to 2 years): Table 24. The values are expressed, for any particular skeletal site, as the amount of new bone formed per day as a percentage of the total amount of bone present in the section. The values have been subdivided to show the contribution of endosteal new bone formation and secondary osteon formation; there was no appreciable periosteal new bone formation at the sites studied in this dog.

Table 24

Dog N. Bone formation rate at different skeletal sites.
Values for cortical bone. The total values are each the sum of the three components.

Site	Section	Bone formation rate, %/day			
		Total	Secondary osteon formation	Endosteal bone formation	Periosteal bone formation
Femur; proximal shaft	NCPR 9	0.14	0.11	0.08	0.03	-
	NCPR 16		0.13	0.09	0.04	-
	NCPR 20		0.17	0.12	0.05	-
Femur; midshaft	NCMR 3	0.07	0.075	0.075	-	-
	NCMR 11		0.067	0.067	-	-
	NCMR 15		0.076	0.076	-	-
Femur; distal shaft	NCDR 8	0.24	0.26	0.21	0.05	-
	NCDR 13		0.25	0.20	0.05	-
	NCDR 16		0.21	0.18	0.03	-
Humerus; midshaft	NH 1	0.08	0.09	0.08	0.005	-
	NH 2		0.08	0.06	0.02	-
Rib	NP 1	0.56	0.57	0.52	0.05	-
	NP 2		0.55	0.49	0.06	-
Parietal	NN 1	0.06	0.05	0.05	-	-
	NN 2		0.06	0.06	-	-

The values obtained in the midshafts of the femur and humerus are of the same order of magnitude, less than 0.1%/day, and the contribution of secondary remodeling accounts for most of this. A similar value was obtained for the parietal bone.

The metabolic activity in the proximal and distal parts of the femoral shaft was about 2-3 times that of the midshaft. The values obtained from the different sections in these situations varied more than those from the midshaft because of the increase in the activity of bone remodeling toward the ends of the bone. The rate of new bone formation in the midshaft of the 5th rib was higher than in any of the other sites - 0.6%/day.

In the cancellous bone of Dog N, Table 25, the wide range of growth activity encountered in different parts of the same bone, together with the irregular shapes of many of the bones, further complicates the task of determining an over-all value for the bone formation rate which could reasonably be compared with the Ca^{45} data for the corresponding bone specimen. For each of these sites, however, the final value for the

bone formation rate took into account the variation of activity in different parts of the section, and an attempt was made to allow for the volumes of the various anatomical subdivisions (epiphysis, metaphysis, and diaphysis) and the actual amount of bone each contained.

Table 25

Dog N. Bone formation rate at different skeletal sites.

Approximate values for cancellous bone. The total values take into account the volume of each anatomical subdivision and the actual amount of bone it contains.

Site	Section	Bone formation rate, %/day			
		Total	Epiphysis	Metaphysis	Diaphysis
Femur; upper end	NA 5	0.59	0.70	0.13	1.01	0.96
	NA 7		0.47	0.09	0.80	0.60
Femur; lower end	NCER 7	0.45	0.48	0.19	0.82	-
	NCER 8		0.41	0.18	0.73	-
Iliac crest	NL 1	1.45	1.48	-	1.84	1.09
	NL 2		1.42	-	1.92	1.06
Lumbar vertebral body	NJ 1	0.63	0.72	0.29	1.05	0.53
	NJ 2		0.54	0.25	0.92	0.49

Dog P (aged 3 to 4 months): Table 26. The values are expressed in the same way as already noted, the values being subdivided to show the amounts of periosteal and endosteal new bone formation, and that related to secondary osteon formation.

Table 26

Dog P. Bone formation rate at different skeletal sites.

Values for cortical bone. The total values are each the sum of the three components.

Site	Section	Bone formation rate, %/day			
		Total	Secondary osteon formation	Endosteal bone formation	Periosteal bone formation
Femur; proximal shaft	PCPL 1	2.4	2.1	1.1	0.6	0.4
	PCPL 4		2.1	1.3	0.5	0.3
	PCPL 8		3.0	2.0	0.4	0.6
Femur; midshaft	PCML 9	1.7	1.6	0.6	0.03	1.0
	PCML 13		1.7	0.6	0.07	1.0
	PCML 17		1.7	0.7	0.01	1.0
Femur; distal shaft	PCDL 9	2.6	3.3	2.8	0.3	0.2
	PCDL 14		2.5	2.0	0.5	0.0
	PCDL 19		2.1	1.6	0.5	0.0
Humerus; midshaft	PH 1	1.3	1.1	0.7	0.0	0.4
	PH 2		1.5	0.8	0.1	0.6
Rib	PP 1	3.4	3.5	1.3	1.2	1.0
	PP 2		3.3	1.0	0.9	1.4
Parietal	PN 1	1.1	1.2	0.2	0.8	0.2
	PN 2		1.0	0.4	0.5	0.1

The rates of new bone formation in the midshafts of the limb bones were of the order of 1-2 %/day. The values for the proximal and distal femoral shafts were higher, approximately 2.5%/day, but the difference

between the ends of the femur and the midshaft was not as great as in the older animal. Bone formation in the rib was again higher than in other sites, and was about 3.4%/day.

In the midshaft of the long bones, it appears that periosteal bone formation makes the greatest contribution, being responsible for about 60% of the total value. In the proximal and distal parts of the femoral shaft, however, the greatest contribution appears to be made by bone formation related to secondary osteon formation, although in this material growth was so rapid that it was not always easy to make a clear distinction between periosteal growth and secondary osteon formation. Endosteal bone formation was present at every skeletal site, and in the parietal bone it was the most important factor. In the rib, each of the three types of bone formation was represented.

Autoradiographic Data

The specific activity of the diffuse component in different regions of cortical bone is shown in Tables 27 and 28. Typical autoradiographs from which these measurements were made are shown in Figures 55 and 56.

Table 27

Dog N. Specific activity of the diffuse component and the corresponding rate of calcium uptake (augmentation rate). The latter values are based on Expression 5.

Site	Section	Specific activity, μC/g Ca	Augmentation rate, %/day
Femur; proximal shaft	NCPR 3 NCPR 13 NCPR 18	0.25 { 0.23 0.26 0.27	0.09
Femur; midshaft	NCMR 2 NCMR 9 NCMR 14 NCMR 18	0.25 { 0.25 0.26 0.24 0.24	0.09
Femur; distal shaft	NCDR 15 NCDR 25	0.30 { 0.33 0.27	0.11
Humerus; proximal shaft	NHP 2 NHP 10 NHP 18 NHP 24	0.27 { 0.24 0.24 0.27 0.33	0.10
Humerus; midshaft	NHM 1 NHM 7 NHM 11 NHM 21	0.26 { 0.26 0.27 0.26 0.25	0.10
Humerus; distal shaft	NHD 7 NHD 15	0.34 { 0.36 0.32	0.13

Table 28

Dog P. Specific activity of the diffuse component and the corresponding rate of calcium uptake (augmentation rate). The latter values are based on Expression 5.

Site	Section	Specific activity, μC/g Ca	Augmentation rate, %/day
Femur; midshaft	PCML 3 PCML 7 PCML 11 PCML 18	0.16 { 0.16 0.17 0.15 0.14	0.25
Humerus; proximal shaft	PHP 4 PHP 12 PHP 15	0.19 { 0.18 0.14 0.24	0.30
Humerus; midshaft	PHM 9 PHM 13 PHM 21 PHM 33	0.19 { 0.22 0.19 0.18 0.17	0.30
Humerus; distal shaft	PHD 3 PHD 15 PHD 20	0.18 { 0.14 0.18 0.22	0.28

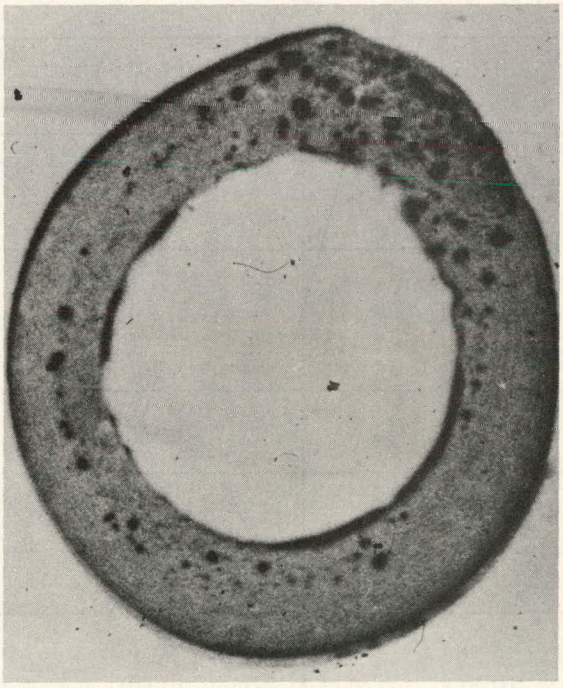

Figure 55

Ca^{45} autoradiograph on Type A plate of femoral midshaft of dog N

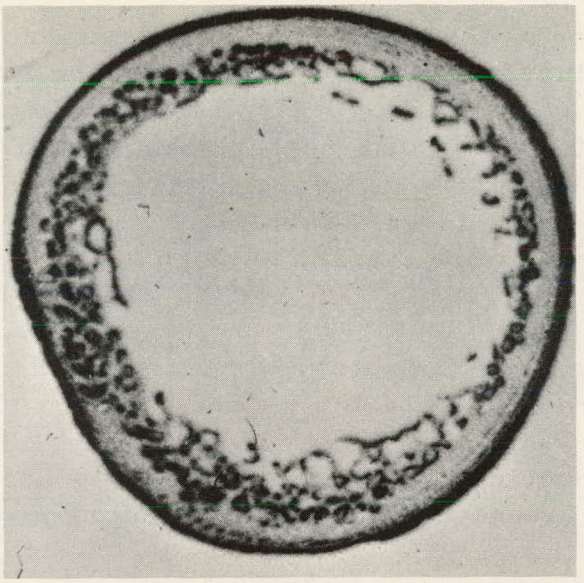

Figure 56

Ca^{45} autoradiograph on Type A plate of femoral midshaft of dog P

The measurements for both dogs were made in regions of periosteally-formed bone. In particular, the measurements for the mid-shaft of the femur in both dogs were made in a region of non-Haversian bone lying between the periosteum and the band of forming and recently-formed Haversian systems, shown by the gray region extending around part of the circumference of the autoradiographs in Figures 55 and 56. In dog N, this region represented almost half the area of a section. In dog P, this region was only a small part of the area of a section because much of the periosteally-formed bone showed some slow residual laminar bone formation as indicated by the long parallel lines of tetracycline labeling within the cortex (Figure 57).

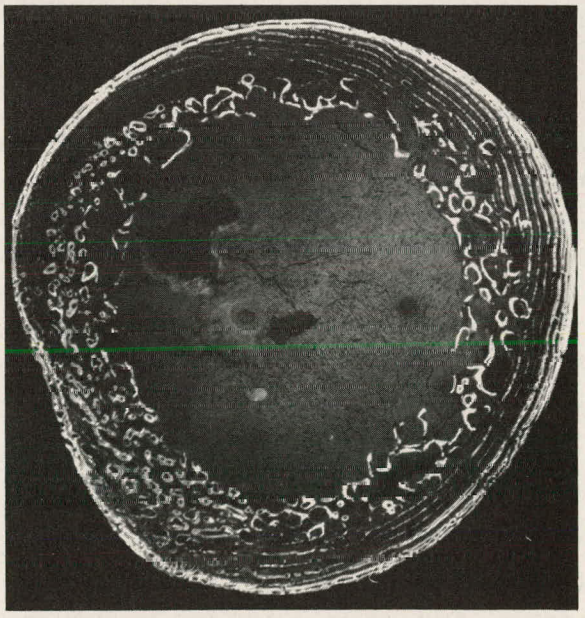

Figure 57

Ultraviolet photograph of femoral midshaft of dog P

In the distal femoral shaft of dog N, there were no broad areas of non-Haversian bone and the diffuse values were somewhat higher. The proximal and distal parts of the femoral shaft of dog P showed such active bone growth and corresponding hotspots that diffuse measurements could not be made.

The measurements in the humerus were similar to those in the femur.

The rate of calcium uptake (augmentation rate) indicated by each measured diffuse specific activity was calculated from the relation

$$\text{Augmentation rate} = \frac{\text{Whole body}}{\text{accretion rate}} \times \frac{\text{Specific activity of diffuse component}}{\text{Average specific activity of body}}. \quad (5)$$

The resulting rates are also listed in Tables 27 and 28.

Discussion

Isotope Data

The most striking aspect of the isotope data is the large difference in the level of the specific activity of the plasma in the two dogs. The younger rapidly-growing dog (P) had values only about one-fifth those of the older dog (N) during most of the period of observation. The almost five-fold difference in the accretion rates for the two animals (2.7%/day and 0.57%/day) is largely a reflection of this plasma difference.

A similar age-dependence of accretion rate has been described by Bauer et al.:[4] The accretion rate in the tibia shafts of three-month old rats is given as 2.4%/day and in the femur shafts of old rats as 0.7%/day. In normal human beings Bauer finds the accretion rate for adults to be about 0.05%/day, for adolescents about 0.3%/day, and for infants about 1%/day. In the present experiment the accretion rate for the older dog was only one-fifth that for the young pup. However, it was still more than three times as high as the accretion rate that may be calculated from the data for sixteen-month-old beagle dogs injected with Sr^{90} by Stover and Atherton[11] (0.17%/day). If, as is probable, this difference is due to age alone, it would suggest that dog N was not much over a year in age.

The retention of Ca^{45} was more than 90% in both dogs but was particularly high in dog P. Values for plasma specific activity and whole body retention similar to those for dog P have been reported by Stover, Atherton, and Arnold[12] for a five-month-old beagle injected with Ca^{45} and sacrificed at 24 hours.

The slow decrease of the value of accretion rate with time after injection as shown in Tables 20 and 21 stems primarily from the curvature of the semilogarithmic plot of plasma specific activity versus time. In human data a straight segment in such a plot is often found beginning about two days after injection. This initial two-day period is interpreted as the time required for mixing within the exchangeable pool. Subsequent departure of the data from the straight segment of the plot is thought to indicate the beginning of the return of deposited activity from the bone to the blood, whether by resorption or by slow exchange. An excellent review of the status of this subject as it applies to human data has been given by R. P. Heaney.(13) In the present experiment, although the difference between the values of A for adjacent days is probably not significant, there is a real tendency over a period of several days for A to decrease with time. One must, therefore, choose a time for the calculation of A and the effect of this choice must be borne in mind in comparing the Ca^{45} and tetracycline results. The time of five days, which has been chosen in the present experiment, is intended to be comparable to the times usually used for human data but also to be short enough to minimize the possible effects of the resorption of activity.

The use of Expression 4 to derive the local values of accretion rate shown in Tables 22 and 23 introduces an assumption the effect of which can now be estimated. Expression 4 depends upon the assumption that the slope of the retention curve for activity in an individual block of bone is the same as the slope λ_R of the retention curve for the body as a whole (Expression 3). An estimate of the maximum error in a local accretion rate that could arise from this assumption can be made as follows. In a block of cortical bone the slope of the retention curve of activity may be less than that of the body as a whole. In fact, if all of the activity in the block arose from a one-way transfer of calcium from blood to bone with no return of activity to the blood, then the activity in the block would rise in direct proportion to the time integral I of the plasma specific activity. None of the activity would be considered exchangeable, and the value of A would be calculated from Equation 1 with E set equal to zero. From the five-day values for R and I given in Tables 20 and 21 it follows that in this extreme situation a local value of accretion rate for dog N would be 16% higher, and for dog P would be 33% higher, than the value calculated from Expression 4. In bone which turns over more rapidly than the average for the skeleton as a whole, the possible error due to this retention curve assumption would be in the opposite direction and of comparable magnitude. The actual error due to this assumption is probably only a fraction of the above limits. The significant point for the subsequent comparisons with the tetracycline data is this: The possible error in the local values of accretion rate in Tables 22 and 23 due to the use of Expression 4 is such as to make values of accretion rate below the skeletal average a little too low and to make values above the skeletal average a little too high.

For the sake of consistency, the values of the rate of calcium uptake in the diffuse component have been calculated on the same basis (Expression 5).

Isotope and Autoradiographic Data

The rates of calcium uptake in the diffuse component (augmentation rate) for these two dogs are comparable to the rates reported[14] for dogs of comparable ages. The ratio of the specific activity of the diffuse component to the average specific activity of the skeleton (i.e., the ratio, diffuse/uniform label, discussed by Rowland[15]) is lower than the value of one-half expected in older animals. In dog P the diffuse/uniform label is about one-tenth and in dog N it is about one-sixth (based on data from femur and humerus six days after injection). These low values appear to be a result of the high rates of bone growth in these animals. If one compares the values for these two dogs it appears that accretion rate may decrease more rapidly with age than does augmentation rate so that the diffuse component becomes a more important contribution to the total activity the older the animal.

Combined Histological and Isotope Results

Dog P. There are three locations in which the tetracycline and Ca^{45} measurements can be directly compared in this animal. These are the blocks of bone from the proximal, middle, and distal shaft of the femur (see Table 29 and Figure 58). In all three sites the accretion rates were

Table 29

Ca^{45} and tetracycline values for comparable regions of bone. The rates are expressed as %/day and are taken from Tables 22, 23, 24, 25, and 26.

Site	Block	Calcium accretion rate, Ca^{45}	Bone formation rate, tetracycline
Dog N			
Cortical bone			
Femur; proximal shaft	NCP	0.26	0.14
Femur; midshaft	NCM	0.21	0.07
Femur; distal shaft	NCD	0.43	0.24
Cancellous bone			
Femur; upper end	NA	0.72	0.6
Femur; lower end	NCE	0.73	0.4
Iliac crest	NL	1.24	1.4
Lumbar vertebral body	NJ	0.80	0.6
Dog P			
Cortical bone			
Femur; proximal shaft	PCP	1.9	2.4
Femur; midshaft	PCM	1.4	1.7
Femur; distal shaft	PCD	2.3	2.6

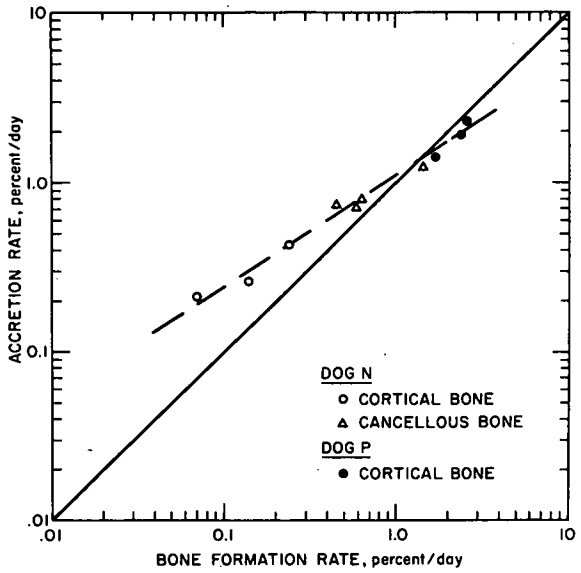

Figure 58

Plot of Table 29

found to be 10-20% lower than the rates of bone formation. This difference may be due in part to the retention curve assumption discussed above, which tends to give somewhat low values of accretion rate for such sites. There is probably some resorption of Ca^{45} activity in this animal during the five-day period after injection, and this also would tend to lower the values of accretion rate. However, resorption of bone containing tetracycline labels (some of which was observed) would remove Ca^{45} as well as tetracycline; both the measured accretion rate and the measured bone formation rate would be lowered and their comparison would not be much affected. The diffuse component in the femur shaft of this animal does not represent much of the activity because its specific activity is low and because it occupies only a small part of the area of a cross section of bone. One may conclude that in this rapidly-growing animal, the bone formation rate and the accretion rate measured five days after injection are equal within about 20% in the regions of cortical bone studied.

Dog N. In the older dog there are seven locations in which the tetracycline and Ca^{45} measurements can be directly compared (Table 29 and Figure 58). In the cortical bone of the midshaft of the femur, where the lowest rate of bone formation was found, the accretion rate was about three times the rate of bone formation. In sites where higher rates of bone formation were found, the proximal and distal parts of the femoral shaft, the ratio was about a factor of two. In each of these three locations the observed magnitude of the diffuse component is sufficient to account for most of the difference between the two rates (Table 27). Note that these diffuse measurements were for non-Haversian bone and hence are indicative primarily of long-term exchange.(2)

Finally, in the cancellous bone of the remaining four sites, the ends of the femur, a lumbar vertebra, and a small segment of the iliac crest, the approximate values for the rate of bone formation were comparable to the accretion rate.

Summary

1. The rates of bone formation in a number of skeletal sites in a puppy and in an adult dog were directly measured by double tetracycline labeling.

2. In the same animals the Bauer-Carlsson-Lindquist accretion rate was measured using Ca^{45}.

3. Accretion rates were calculated five days after injection. Data for shorter times of calculation are included.

4. In the rapidly-growing puppy the accretion rate was comparable to the bone formation rate at all sites studied.

5. In the adult dog, the values were comparable in cancellous bone, but in cortical bone the accretion rate was two to three times the bone formation rate.

6. Most of the difference between accretion rate and bone formation rate in adult cortical bone was due to the diffuse component and, hence, to long-term exchange.

7. The ratio of the diffuse component to the uniform label in the puppy was about one-tenth, and in the dog was about one-sixth, based on data from femora and humeri six days after Ca^{45} injection.

8. Despite the important differences between the accretion rate and the bone formation rate that were found to exist in regions where there was only a small amount of bone formation, there was a strong correlation between the two rates. The value of the accretion rate as a parameter of bone metabolism is clear.

References

1. G. C. H. Bauer, A. Carlsson, and B. Lindquist. Evaluation of Accretion, Resorption and Exchange Reactions in the Skeleton. Kgl. Fysiograf. Sallskap. Lund, Forh. 25, 1 (1955).

2. J. H. Marshall, R. E. Rowland, and J. Jowsey. Microscopic Metabolism of Calcium in Bone. Radiation Res. 10, 213 (1959); ibid. 258 (1959).

3. W. H. Harris, R. H. Jackson, and J. Jowsey. The in vivo Distribution of Tetracyclines in Canine Bone. J. Bone Joint Surg. 44A, 1308 (1962).

4. G. C. H. Bauer, A. Carlsson, and B. Lindquist. Mineral Metabolism, ed. C. L. Comar and F. Bronner, Academic Press, New York, 1961. Vol. I, Part B, pp. 609-76.

5. J. H. Marshall. Theory of Alkaline Earth Metabolism. J. Theoret. Biol. 6, 386 (1964).

6. J. Jowsey. The Use of the Milling Machine for Preparing Bone Sections for Microradiography and Microautoradiography. J. Sci. Instr. 32, 159 (1955).

7. D. A. Buyske, H. J. Eisner, and R. G. Kelly. Concentration and Persistence of Tetracycline and Chlortetracycline in Bone. J. Pharmacol. Exptl. Therap. 130, 150 (1960).

8. O. W. Richards. Fluorescence Microscopy. Analytical Cytology, ed. R. C. Mellors. McGraw-Hill, New York, 1955.

9. E. Schuchardt. Das Integrationsverfahren in der mikroskopischen Technik. Handbuch der Mikroskopie in der Technik, ed. Freunel, 1, 565 (1957).

10. R. A. Dudley and B. M. Dobyns. The Use of Autoradiographs in the Quantitative Determination of Radiation Dosages from Ca^{45} in Bone. Science 109, 327 (1949).

11. B. J. Stover and D. R. Atherton. Metabolism of Sr^{90} in Adult Beagle Dogs. Proc. Soc. Exptl. Biol. Med. 99, 201 (1958).

12. B. J. Stover, D. R. Atherton, and J. S. Arnold. Comparative Metabolism of Ca^{45} and Ra^{226}. Proc. Soc. Exptl. Biol. Med. 94, 269 (1957).

13. R. P. Heaney. Evaluation and Interpretation of Calcium-Kinetic Data in Man. Clinical Orthopaedics 31, 153 (1963).

14. J. H. Marshall. Microscopic Metabolism of Calcium in Bone. Bone as a Tissue, ed. K. Rodahl, J. T. Nicholson, and E. M. Brown. McGraw-Hill, New York, 1960. p. 144.

15. R. E. Rowland. Some Aspects of Human Bone Metabolism Deduced from Studies of Radium Cases, Clinical Orthopaedics 28, 193 (1963).

OSTEOLATHYRISM IN MICE AND INHIBITION OF THE ENDOSTEAL BONE REACTION IN ESTROGEN-TREATED MICE BY AMINOACETONITRILE*

AAN

D. J. Simmons, A. M. Pankovich,**
and A. M. Budy†

Abstract

The effect of aminoacetonitrile (AAN) on the skeletons of young mice injected with estrogen was studied histologically and microradiographically. AAN (0.5, 2.5, 5, 10, or 20 mg) was administered daily during the first week of treatment alone or in combination with a single injection of 1 mg estradiol valerate on the first day. The animals were sacrificed at intervals of 7 days for a period of 4 weeks. The bone reaction leading to ossification of the marrow cavities as a consequence of estrogen treatment was diminished by 5-20 mg AAN, and the effect was roughly proportional to the dose of the nitrile. The metaphyseal trabeculae (distal femur) of the AAN-treated mice developed a mosaic appearance. While administration of the nitrile alone induced the formation of periosteal hyperostotic and osteocartilaginous hyperostotic fibrous bone tissue over the femoral shafts late in the posttreatment recovery period; combined treatment with estrogen potentiated these changes during the treatment period itself. The cortical bone tissue was also demineralized by combined treatment, and fused osteocyte lacunae regularly appeared as an apparent sequela of both cell enlargement and degradation of perilacunar matrix. Conversely, estrogen completely protected the epiphyseal cartilages against degenerative changes (abnormal vascular invasion, rents, etc.) after low doses of AAN (0.5-2.5 mg) during the treatment period, but the hormone was only partially effective after higher doses of AAN. It was suggested that aminoacetonitrile disrupts both the formation of new bone collagen and the integrity of collagenous structures deposited prior to the treatment.

Introduction

Estrogen administered to mice stimulates ossification of the medullary cavities of most of the skeletal elements.[1,2] The endosteum becomes an actively proliferating tissue. New bone is formed centripetally and if treatment is prolonged, the marrow cavity may become completely obliterated. Potentiation of the endosteal bone reaction has been ascribed to

* This work was partially supported by Research Fellowship No. DPD-12,985, United States Public Health Service Grant No. A-4225 Met., and the Atomic Energy Commission [At(11-1)-787] awarded to Dr. Franklin C. McLean, Physiology Department, The University of Chicago, Chicago, Illinois.

** Department of Surgery (Orthopaedics), The University of Chicago Clinics, Chicago, Illinois.
† Department of Physiology, The University of Chicago, Chicago, Illinois.

increased vascularization or to some unspecified local insult to the primitive connective tissue cells of the marrow. These cells respond by modulating to osteoblasts.[2,3] Although attempts have been made to inhibit this new bone formation with testosterone,[2,4,5] the results have not been conclusive; nor is the role of the pituitary growth hormone well established.[6]

An increasing number of reports indicate that nonendocrine agents such as β-aminopropionitrile (BAPN) and aminoacetonitrile (AAN) and their analogs are effective inhibitors of ground substance formation in connective tissues, that is, they reduce the hexosamine content of bone[7,8] and inhibit collagen polymerization.[9-12] It is not known whether these compounds or their metabolites disrupt collagen formed prior to administration, but they do cause extensive multiple lesions of mesodermal tissues, particularly in the skeletal and vascular systems. These include epiphyseal tearing and slipping, periosteal new bone formation, reduction of endochondral bone formation, kyphoscoliosis, dislocations, degenerative arthritis, and dissecting aneurysm of the aorta. Clinically, the changes are known as osteolathyrism, and the complete syndrome can be produced after inclusion of Lathyrus odoratus L. seeds in the diet or treatment with nitrilic compounds for prolonged periods. In the rat, estrogen apparently inhibits the development of lathyrism[13,14] and retards the regression of the skeletal lesions after temporary AAN treatment.[15] In the rat, the hormone suppresses osteoclastic resportion only of bone of endochondral origin.[16,17] In the present experiments the estrogen-treated mouse has been used to observe the effect of AAN on both newly forming and old collagenous tissues, and to determine whether AAN will interfere with estrogen-induced new bone formation.

Materials and Methods

In a preliminary experiment, 12 CF_1 mice, 30-35 days old, were divided into four groups. Group 1 received intraperitoneally a total of 1.0 mg estradiol valerate (Delestrogen*) in 0.5-mg doses on the first and third day; group 2 received 10 mg AAN intraperitoneally daily for 6 days; group 3 received both estradiol valerate and AAN; group 4 served as controls. The nitrile was not neutralized prior to the injection. Three mice from each group were sacrificed on the 7th day. At autopsy, the left femurs and tibias were removed and fixed in 95% alcohol and Susa solution, respectively. The remaining carcasses were eviscerated and stained with alizarin red S to ascertain the gross effects of the agents upon the skeleton. The femurs were embedded undecalcified in methyl methacrylate and cut longitudinally at 75-100 μ on a high-speed rotary saw. The sections were microradiographed on Kodak Spectroscopic Plates 649-0. The tibias decalcified in Susa solution were embedded in paraffin, sectioned longitudinally and stained by the gentian violet technique described by Selye.[15]

* Delestrogen was generously supplied by Dr. E. C. Reifenstein, Jr., Squibb Institute, New Brunswick, N. J.

Since the preliminary study indicated that AAN could suppress endosteal bone formation in mice, a second and more extensive experiment was designed to establish the dose at which AAN was most effective. The experimental plan was similar to the preliminary one except that groups were composed of 6 mice and estradiol valerate was administered in a single 0.5 mg-dose subcutaneously on day 1. Control mice received sesame oil or water. Other groups received an intraperitoneal injection of either 5, 10 or 20 mg AAN alone or 0.5, 2.5, 5, 10, or 20 mg AAN daily for 6 days in combination with the single subcutaneous dose of estrogen. At autopsy at the end of the first, second, third, and fourth weeks, the mice were x-rayed. The femurs were fixed in 10% neutral formalin or 95% alcohol and sections were prepared for microradiography and histology as before. Paraffin-embedded sections were stained with hematoxylin, eosin, and azure II. The lengths of the long bones were obtained from x-rays.

Results

Preliminary Experiment

The epiphyseal cartilages of the lower femurs of mice treated with AAN appeared somewhat thicker than those of the controls in microradiographs (Figures 59A and 59C). Combined treatment with AAN + estrogen appeared to suppress the endosteal bone reaction which was well established at the end of the first week in the group receiving estrogen alone (Figures 59B and 59D).

Dose-Dependent Changes

Control and Estrogen-Treated Groups. After one week the epiphyseal cartilage of the femurs of the estrogen-treated animals was thinner than that of the controls (Figure 59). The metaphyseal trabeculae were thicker and longer and the cortex exhibited a slight endosteal reaction. The undifferentiated mesenchymal cells of the marrow were modulating to osteoblasts, and these cells lined the free surfaces of the trabeculae. At two weeks, the endosteal reaction had spread proximally to the neck of the femur, and long narrow trabeculae filled the distal third of the bone. The growth cartilage was thinner than in the controls and the ossification front was slightly irregular. Occasionally, sites of epiphyseal-diaphyseal union were observed. By the fourth week, the endosteal reaction was much less intense. Fewer osteoblasts lined the older trabeculae, but heavy confluent deposits owing to remodeling filled the distal half of the shaft and epiphyseal medullary spaces.

Epiphyseal Cartilages. The epiphyseal cartilages of the mice treated (Figure 60) at the three dose levels with AAN were uniformly thicker than those of the controls. Columns of chondrocytes in the proliferating zones were short, disoriented, and separated by wide areas of acellular matrix.

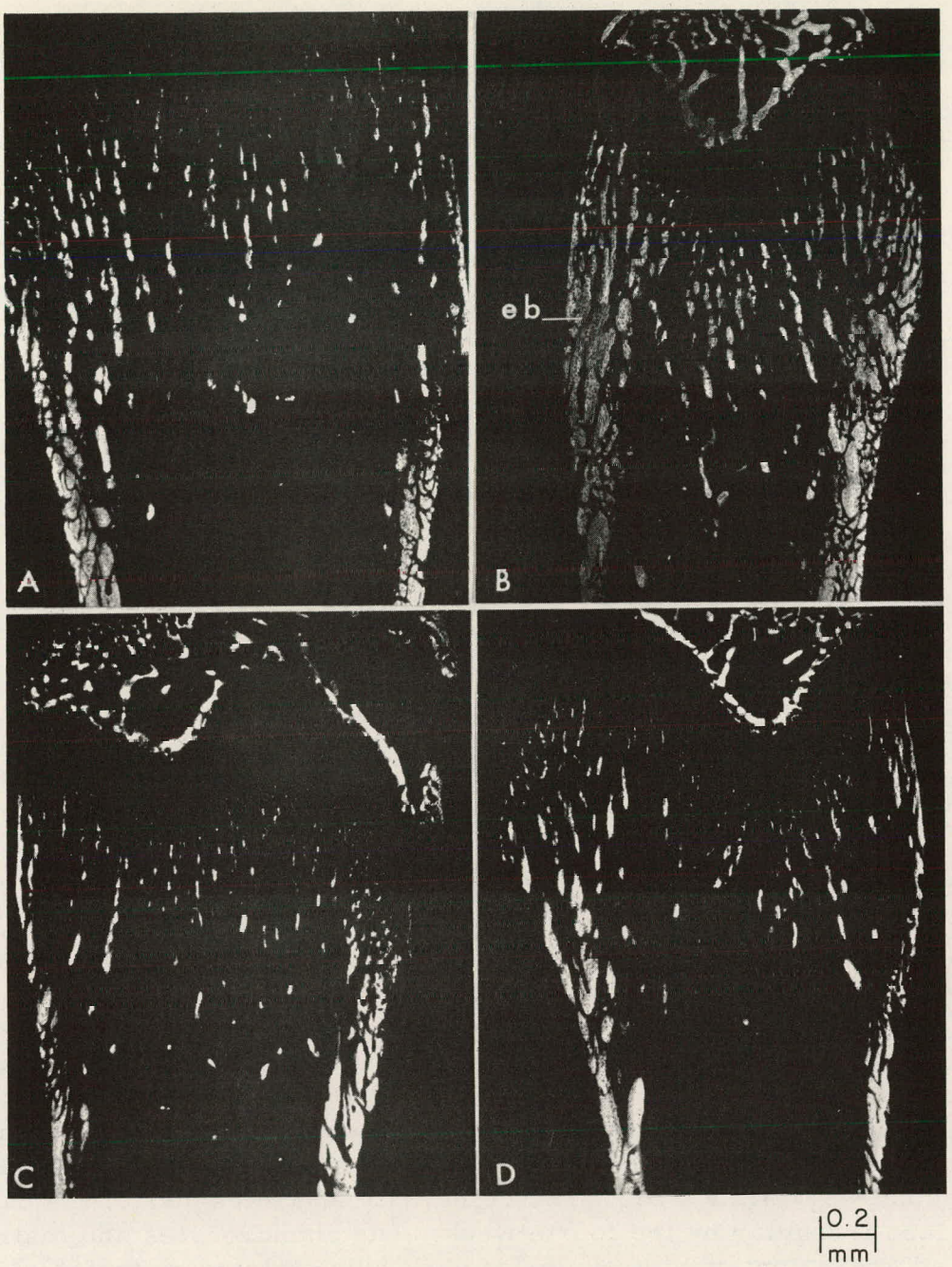

Figure 59

Microradiographs of longitudinal sections of femurs from mice after one week of treatment. A. Control; B. Aminoacetonitrile-treated (eb, endosteal bone); C. Estrogen-treated; D. Aminoacetonitrile estrogen-treated. Note the absence of endosteal bone formation in the metaphysis of the mouse in D.

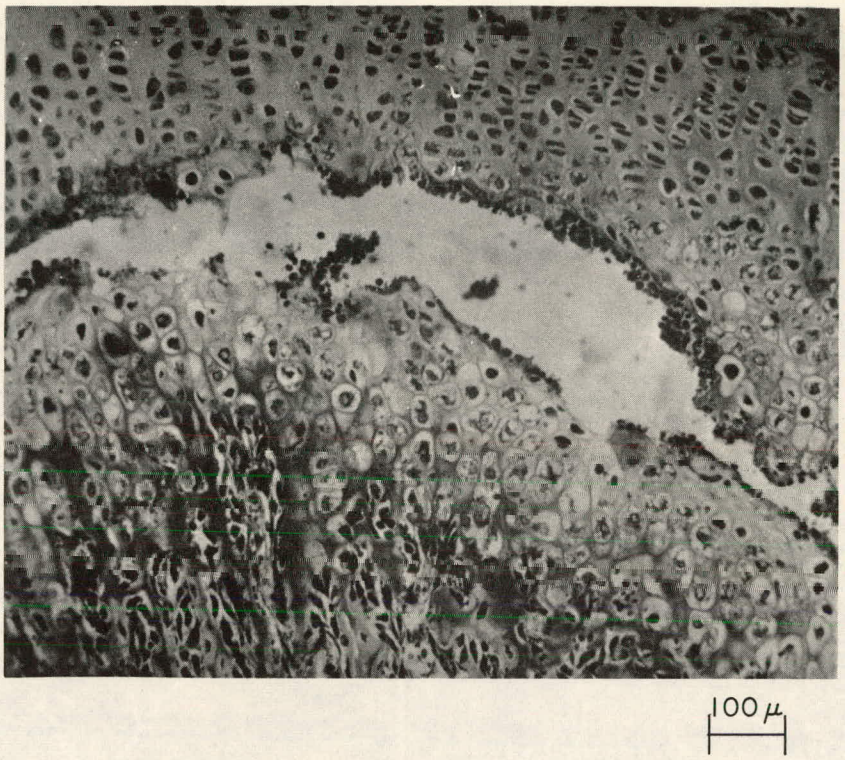

Figure 60

Photomicrograph of a large rent in the proliferating zone of the thickened distal femoral epiphyseal cartilage from a mouse 1 week after daily treatment with 5 mg AAN

Removal of the hypertrophic zone cells by invading metaphyseal vessels was irregular, and the ossification front appeared discontinuous. After 5 mg AAN, the tissues may also have been disrupted by large tears and vascular spaces (Figures 61 and 62). Bony fusion of the epiphysis and metaphysis occurred in a few animals after 20 mg. Regression of these changes was generally apparent during the posttreatment recovery periods although occasional foci of vascular erosion were still seen at the end of the second week after 5 mg. The cellularity and thickness of the cartilage were less irregular by the fourth week. The chondrocytes and matrix in affected areas contained granules of dark blue staining material which may represent calcium salts.

Estrogen preserved the cartilage after low doses of AAN + estrogen (AAN + E) during the treatment period. Thickening of the plate was slight after 5 mg AAN + E, but the foci of vascular erosion were smaller and less severe than in mice treated with the nitrile alone. The protective influence of estrogen was not apparent after 10-20 mg AAN + E. While the cartilages were approximately as thick as those of the mice treated with estrogen alone, owing to regressive changes during the posttreatment period, the damage to the plates was persistent and possibly exaggerated. Small tears not found at one week, for example, were present at two weeks after 2.5 mg AAN + E.

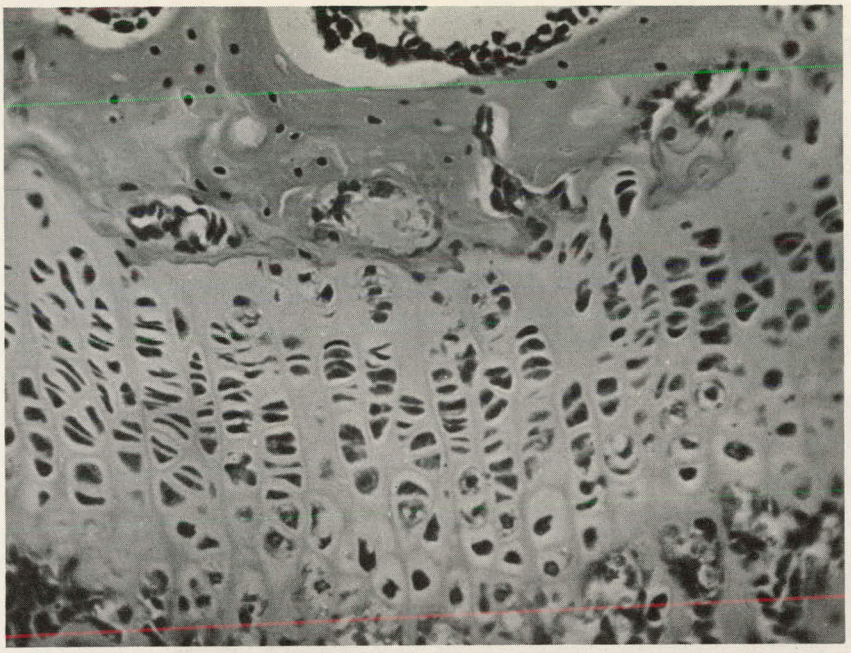

Figure 61

Photomicrograph of the distal end of the femur from a control mouse showing the normal structure of the epiphyseal cartilage

Figure 62

Photomicrograph of vascular lesions in the proliferating zones of the epiphyseal cartilage from the distal femur of a mouse 1 week after daily treatment with 5 mg AAN. Note the disorganization of the cell columns.

Slipped Epiphyses. Slipped epiphyses were not common in AAN-treated mice, although the cartilage and metaphysis of one animal dead after receiving 6 injections of 20 mg AAN was irregularly dissected by bands of muscle and dense connective tissue which also appeared under the periosteum (Figure 63). Animals of the four-week recovery period which were treated with 5 mg AAN + E seemed disposed toward an increased incidence of epiphyseal slippage. In several instances muscle fibers seemed to enter the bone along transverse tears in the periosteum and cartilage perhaps following rotation of the epiphysis on the bony metaphysis.

Figure 63

Photomicrograph showing slipped epiphysis in the distal femoral epiphyseal cartilage from a mouse dead after 6 injections of 20 mg AAN per day. The cartilage and metaphysis are irregularly dissected by muscle bands (M).

Articular Cartilage Degeneration. Foci of degeneration, apparent either as a simple loss of cartilage tissue or as fibrous invasion, occurred on the joint surfaces after 5 mg AAN during the first week. No further evidence of joint deterioration occurred during the recovery period. The extent of damage after combined treatment with AAN + estrogen was similar and not dose dependent, although the tissue was sometimes replaced by bone trabeculae.

Metaphyseal Bone. Demonstrable changes occurred in the metaphyses of the bone, and some of the effects of the nitrile were persistent throughout

the period of observation. The numbers of the osteoblasts in the zone of endochondral ossification and those lining the trabeculae did not seem to be reduced by AAN, and, in fact, 5-10 mg AAN or AAN + E seemed to intensify modulation to osteoblasts at the ossification front. The trabeculae were thinner after AAN treatment and had a mosiac appearance (Figures 64 and 65); their distribution and form were also quite irregular at one week, but they became more massive than the controls at two weeks. At four weeks the distinction between the groups was slight, with the exception of the fine structure of the bone. The dark blue staining granules observed in cartilage after AAN treatment were also observed in the cytoplasm of osteoclasts in mice injected with 20 mg AAN, and a few were observed in osteoblasts and the osteogenic precursor population. The deposits were particularly dense after combined AAN and estrogen treatment.

While osteoblastic activity in the metaphysis was undiminished in the first week after 0.5-5 mg AAN + E, the ossification front was discontinuous and there was extensive osteoclastic resorption. Osteoid deposition on calcified spicules of cartilage was delayed by 10-20 mg AAN + E. In all cases, the numbers of trabeculae were diminshed by combined treatment, and they were individually abnormal as noted above (Figure 65), short and relatively more massive than in the mice treated with estrogen. Large vesicular spaces occured in subepiphyseal areas (Figure 66). The intensity of the endosteal reaction was reduced after 2.5-10 mg AAN + E or restricted to areas where trabecular bone was already established after 20 mg AAN + E. Although most bones show masses of confluent trabeculae in the distal half of the shaft, there are relatively more vascular spaces and the most proximal and newly formed trabeculae are thinner than those in the estrogen controls.

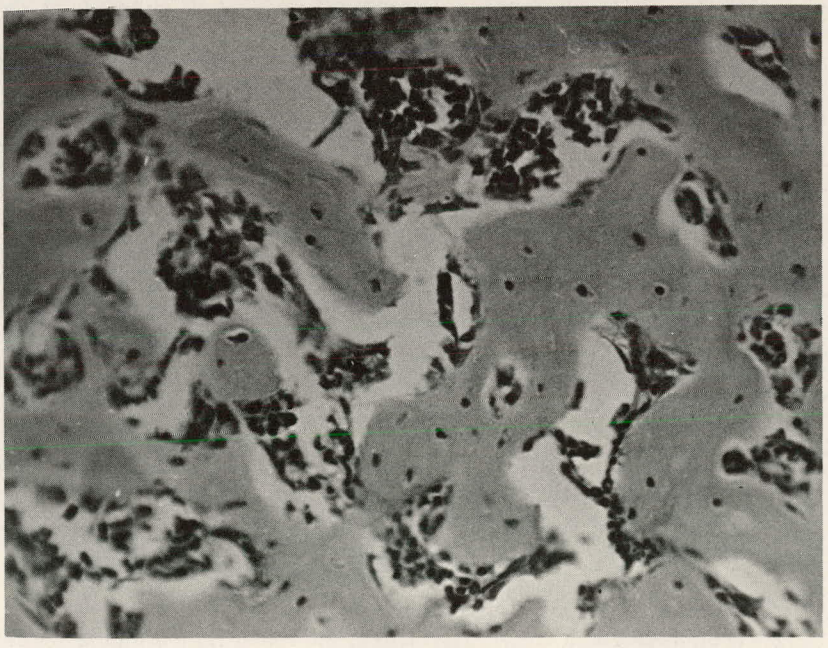

Figure 64

Photomicrograph of normal endosteal bone trabeculae in the distal femur from a mouse which had received estrogen

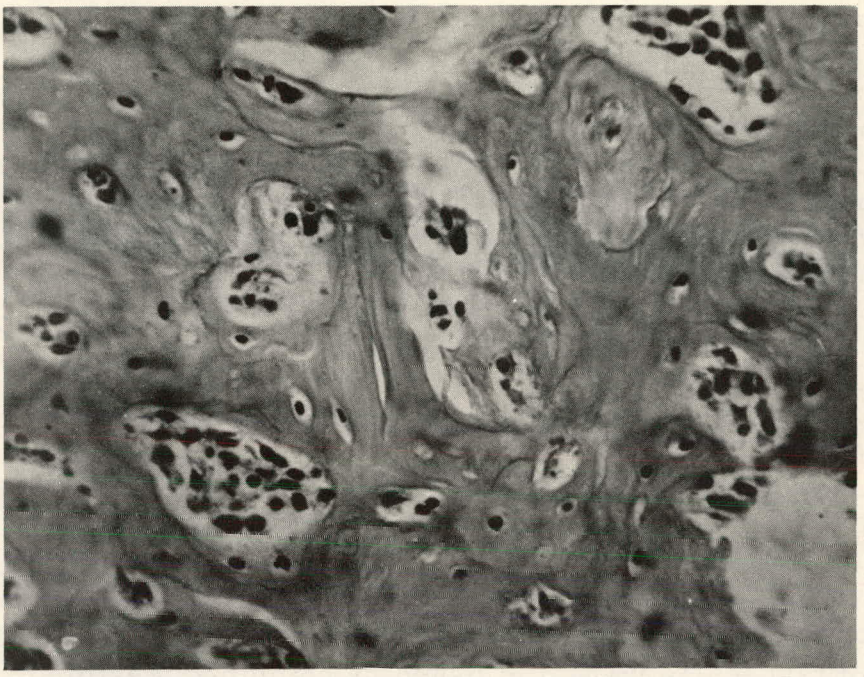

Figure 65

Photomicrograph of abnormal endosteal bone trabeculae in the distal femur from a mouse 1 week after treatment with 5 mg AAN per day. Note the mosaic structure of the trabeculae lined by numerous osteoblasts.

Figure 66

Photomicrograph of the distal end of the femur from a mouse 1 week after treatment with 20 mg AAN per day and estrogen. Note large vesicular spaces at the border between the cartilage and metaphyseal bone.

Cortical Bone

Normal and Estrogen-treated Mice. The shaft of the femur normally contains dense lamellar bone demarcated into zones of periosteal and endosteal growth by regular cement lines which enclose a few small vascular spaces. While the lacunae of osteocytes are usually elongated and narrow, the cells in areas of tendon insertion along the neck and trochanters tend to be more ovoid and less precisely aligned along lamellae, and the circumlacunar matrix is often disrupted by small rents. The periosteum over the neck of the femur in very young animals may be somewhat thicker. Estrogen treatment does not alter the appearance of this bone.

Small rents were commonly observed in the shaft and it is probable that some defect in the collagen fibers became pronounced during fixation and dehydration of the tissues preliminary to sectioning. The tissues simply fixed in alcohol and microradiographed were not similarly distrupted.

Periosteal Hyperostoses in AAN and AAN + E-treated Mice. Changes in the old collagenous tissue owing to AAN were present in the proximal half of the bone. The periosteum thickened and became loosely attached to the shaft after treatment with 5 mg AAN. Hemorrhagic areas were observed during the first week. Metaplasia of proliferating periosteal cells resulted in periosteal hyperostotic fibrous bony tissue formation (callus) after 10-20 mg AAN early in the recovery period (Figures 67 and 68). Basophilic granules and globules were scattered throughout the developing callus tissue.

Figure 67

Photomicrograph of midshaft cortical bone from a mouse injected with 10 mg AAN per day and sacrificed after the first week post-treatment recovery period. Note the formation of periosteal hyperostotic fibrous bone (F).

Figure 68

Microradiograph of midshaft cortical bone from a mouse injected with 5 mg AAN per day and sacrificed after the first week posttreatment recovery period. Note the formation of periosteal hyperostotic bone (F) and destruction of the underlying cortical tissue (C).

The severity of these changes was even more marked in the group injected with combined AAN + E. Thickening and loosening of the periosteum with subsequent callus formation occurred after the administration of AAN + E during the treatment period. Cortical damage was consistent with the 5-mg AAN level in the second week after 2.5 mg AAN + E, and one mouse exhibited a large vesicular space at the level of the midshaft. During the treatment period, callus formed over large areas of the neck and midshaft after 5-10 mg AAN + E and both lacunae and matrix were severely altered (Figure 69). Fused lacunae regularly appeared in microradiographs owing to cell enlargement and reduction of radiopaque perilacunar matrix. The bony tissue was of low mineral density indicating demineralization. Osteoclasts were conspicuous in the callus tissue. Repair was most complete at the end of the experiment in mice treated with 5 mg AAN + E, but the periosteum remained loosely attached to the shaft.

Osteocartilaginous Hyperostosis. Periosteal proliferation also formed osteocartilaginous hyperostotic fibrous bone (Figures 70 and 71) on the proximal third of the shaft in a mouse during the recovery period three weeks after injections of 20 mg AAN. Estrogen, however, initiated this change during the treatment period at this dose and in a few mice which had received 10 mg AAN + E. The cartilage component, composed largely of disorganized hypertrophic cells and a few discoid cells typical of the proliferating zone of epiphyseal cartilages, was bound by a narrow outer band of fibrillar bone and a larger inner zone of irregular trabeculae.

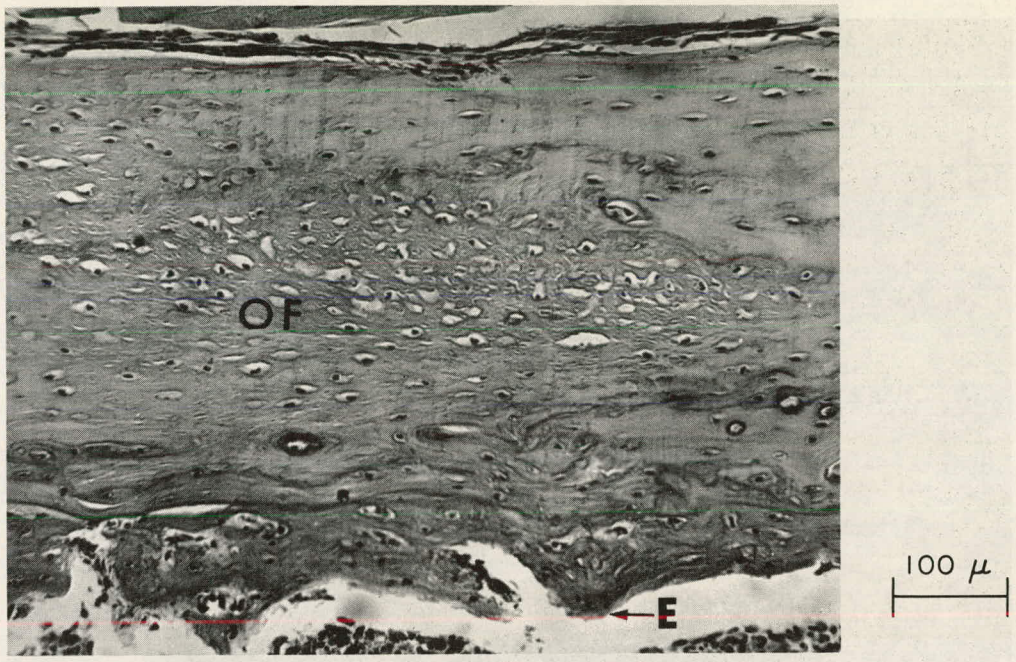

Figure 69

Photomicrograph of midshaft cortical bone from a mouse injected with 20 mg AAN per day and estrogen and sacrificed after the third week posttreatment recovery period. Note the enlargement and apparent fusion of osteocytes plus the degradation of the perilacunar matrix (OF). An endosteal reaction is present (E).

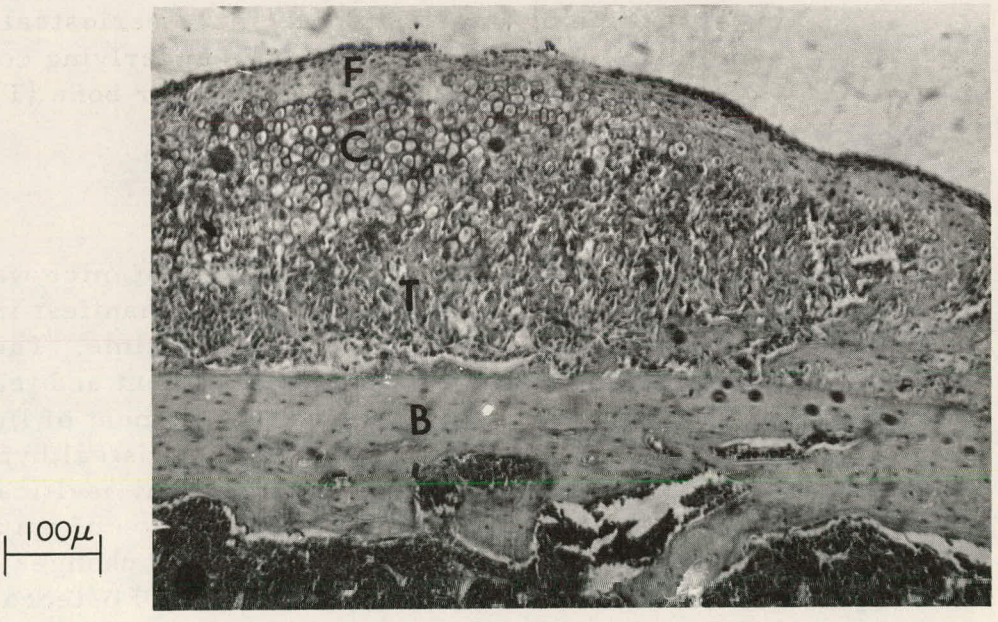

Figure 70

Photomicrograph of the proximal shaft of a femur from a mouse dead after 4 daily injections of 10 mg AAN. Note the formation of an osteocartilaginous periosteal hyperostosis. Limiting sheath of fiber bone (F); Medial zone of cartilage (C); Inner zone of trabecular bone (T); Cortex (B).

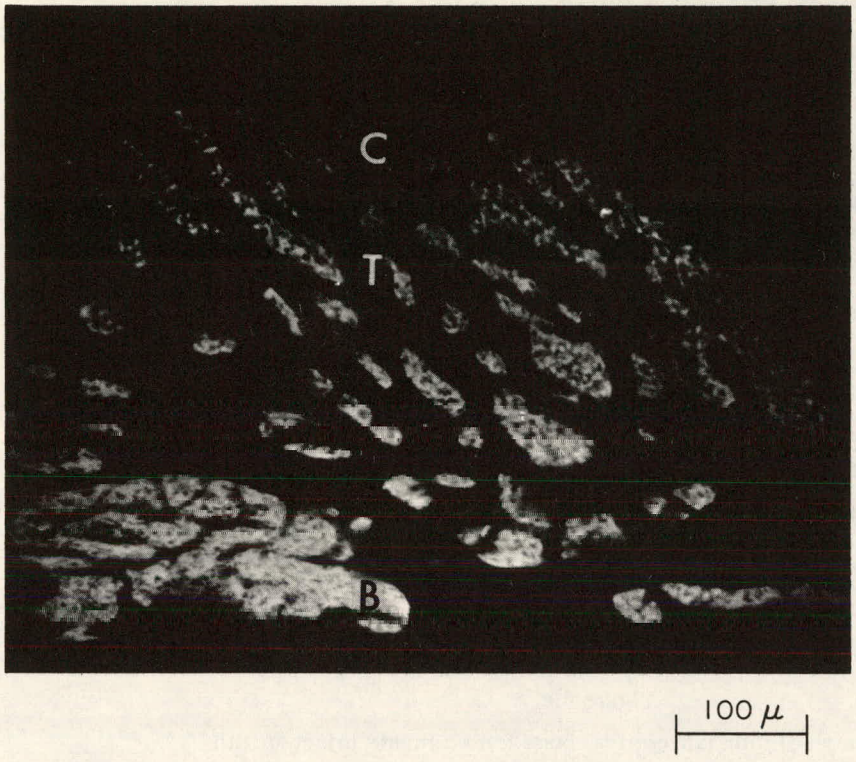

Figure 71

Microradiograph of the proximal shaft of a femur from a mouse injected with 20 mg AAN per day and estrogen, and sacrificed at the end of 1 week. Note the formation of an osteocartilaginous periosteal hyperostosis and destruction of the underlying cortical bone (B); Cartilage (C); Trabecular bone (T).

Discussion

The effect of injected AAN on the skeleton of mice was dose-dependent and certain of the anomalies have been manifest in other species after feeding lathyrogens for prolonged periods of time. The principal skeletal involvements in these mice were enlargement and tearing of the growth cartilage in the proliferative zones, detachment of ligamentous and tendinous insertions and subsequent growth of periosteal hyperostotic tissue (callus), and faulty and/or delayed endochondral ossification and mineralization patterns resulting from the disruption of epiphyseal cartilage structure. With the exception of degenerative joint changes, the incidence of slipped epiphyses and periosteal hyperostotic and osteocartilaginous hyperostotic tissue increased after combined treatment with estrogen and higher levels of AAN (5-20 mg).

The prime target of lathyrogens is the ground substance, in particular the synthesis of chondroitin sulfate.[18,19] Disruption of these important biochemical events would result in aberrant mineralization of tissues. Sulfated mucopolysaccharides are irregularly distributed in rat tissues after treatment with nitrilic compounds.[20] The appearance of darkly basophilic granules in the matrix of the cartilage plate in the hypertrophic zones, probably representing calcium salts, confirms the observations of Borle et al.[21] These granules were also present in the fibrous bone of developing callus tissue and are comparable to a) the globules of amorphous metachromatic substance present between young fibroblasts in the periosteum of lathyritic rats[13,22] and chicks[23] and b) the globules of PAS-positive material in the calcifying zones in healing fracture callus.[24] These granules and globules, present in larger numbers only after 20 mg AAN, were found in callus tissue, between the trabeculae in the metaphysis, and within osteoclasts. Combined treatment of AAN + E increased the incidence of these cellular and extratrabecular deposits.

The appearance of bone cells was normal after nitrile treatment, although early senescence, disappearance, and modulation of osteoblasts to spindle-shaped cells has been reported in BAPN-treated suckling rats.[25] In this study AAN did not stimulate the modulation of cells to osteoclasts although this event was observed by Clemmons and Angevine[25] in BAPN-injected rats and in rats fed a diet including L. odoratus seeds.[26] There is also little evidence to suggest that the functional activity of osteoblasts is impaired by AAN treatment. Periosteal fibrous hyperostotic tissue and endochondral trabecular formation continued at all dose levels, although AAN reduced the numbers of trabeculae and partially inhibited the endosteal bone reaction after very high doses.

It seems clear from this study that AAN partially suppressed the proliferation of endosteal bone in estrogen-treated mice. While the effect after the subcutaneous injection of 0.5-2.5 mg AAN + E was negligible, progressively fewer trabeculae were formed with increasing doses of AAN. The effect was greater when estrogen was administered intraperitoneally. Estrogen enhances collagen synthesis in bones of mice.[27] Augmentation of the potentially mitotic osteoblast population has been demonstrated with tritiated thymidine labeling in the metaphyses of mice as early as 6 hours after a single dose of estradiol valerate.[3] The trabeculae which formed under the influence of AAN and AAN + E were abnormal and the fibrillar structure appeared loosely organized, perhaps owing to disruption of the pattern of cross linking and polymer formation.[28] Distorted endochondral trabeculae have previously been described in rats by Menzies and Mills,[29] and by Ponseti and his co-workers.[13] Some workers have compared the mosaic structure of rat lathyritic bone to a Pagetoid condition,[13,30-33] but cement lines characteristic of this disorder were absent in mice.

There is also evidence that lathyrogenic compounds attack mature collagen. While this study showed that the effect of AAN on the osteocytes and matrix in the midshaft of the femur was negligible, combined treatment with estrogen consistently resulted in osteocyte enlargement and perilacunar matrix degradation and demineralization of bone. These features are similar to the condition in AAN + E treated rats described by Selye[22] and may result from the disrupting of lateral intramolecular links in collagen.[34] Lipp[35] and, more recently, Bélanger et al.[36] have commented that osteocytes possess some latent characteristics usually attributed to osteoclasts and that under certain conditions (parathyroid treatment) they may show intralacunar resorption. Osteoporotic-like bone resulting from lathyritic compounds has been described[26,30] and, in these mice, the cortical tissue was dissected by large vessels and the tissue was remodeled in areas of periosteal hyperostotic bone formation. Focal lacunar enlargement occurs in osteoporosis. Lathyritic collagen may lack tensile strength.[9]

References

1. W. U. Gardner and C. A. Pfeiffer. Proc. Soc. Exptl. Biol. Med. 37, 678 (1938).

2. M. R. Urist, A. M. Budy, and F. C. McLean. J. Bone Joint Surg. 32-A, 143 (1950).

3. D. J. Simmons. Clin. Orthopedics No. 26, 176 (1963).

4. H. K. Suzuki. J. Bone Joint Surg. 40-A, 435 (1958).

5. D. J. P. Barker and J. N. Crossley. Nature 194, 1088 (1962).

6. W. U. Gardner and D. H. Clouet. Anat. Rec. 88, 433 (1944).

7. A. A. Castelliani and C. Castelliani-Bisi. Proc. Soc. Exptl. Biol. Med. 98, 318 (1958).

8. I. V. Ponseti and F. Aleu. J. Bone Joint Surg. 40-A, 1093 (1958).

9. C. I. Levene and J. Gross. J. Exptl. Med. 110, 771 (1959).

10. A. Van den Hooff, C. I. Levene, and J. Gross. J. Exptl. Med. 110, 1017 (1959).

11. J. Gross. Biochim. Biophys. Acta 74, 314 (1963).

12. G. R. Martin and P. Goldhaber. Biochim. Biophys. Acta 69, 568 (1963).

13. I. V. Ponseti and R. S. Shepard. J. Bone Joint Surg. 36-A, 1031 (1954).

14. H. Selye and P. Bois. Rev. Can. Biol. 15, 281 (1956).

15. H. Selye. Rev. Can. Biol. 16, 1 (1957).

16. M. R. Urist, A. M. Budy, and F. C. McLean. Proc. Soc. Exptl. Biol. Med. 68, 324 (1948).

17. B. Lindquist, A. M. Budy, F. C. McLean, and J. L. Howard. Endocrinology 66, 100 (1960).

18. A. E. Sobel, M. Burger, B. C. Deane, H. G. Albaum, and K. Cost. Proc. Soc. Exptl. Biol. Med. 96, 32 (1957).

19. Y. K. Shintani and H. E. Taylor. Lab. Invest. 11, 697 (1962).

20. L. F. Bélanger. Proc. Soc. Exptl. Biol. Med. 88, 150 (1955).

21. A. B. Borle, M. J. Karnovsky, and G. Nichols, Jr. Am. J. Physiol. 197, 124 (1959).

22. H. Selye. Acta Anat. 33, 146 (1958).

23. W. Dasler and R. V. Milliser. Proc. Soc. Exptl. Biol. Med. 98, 759 (1958).

24. E. Storey and G. Varasdi. Brit. J. Exptl. Pathol. 39, 376 (1958).

25. J. J. Clemmons and D. M. Angevine. Am. J. Pathol. 33, 175 (1957).

26. A. F. Gardner. Oral Surg. 12, 876 (1959).

27. G. Vaes and G. Nichols, Jr. Endocrinology 70, 890 (1962).

28. G. R. Martin, J. Gross, K. A. Piez, and M. S. Lewis. Biochim. Biophys. Acta 53, 599 (1961).

29. D. W. Menzies and K. W. Mills. J. Path. Bacteriol. 73, 223 (1957).

30. W. B. Bean and I. V. Ponseti. Circulation 12, 185 (1955).

31. S. Wawzonek, I. V. Ponseti, R. S. Shepard, and L. G. Wiedenmann. Science 121, 63 (1955).

32. V. P. Amato, M. Sliema, and R. Bombelli. J. Bone Joint Surg. 41-B, 600 (1959).

33. P. Ramamurti and H. E. Taylor. J. Bone Joint Surg. 41-B, 590 (1959).

34. C. I. Levene. J. Exptl. Med. 116, 119 (1962).

35. W. Lipp. Acta Anat. 22, 151 (1954).

36. L. F. Bélanger, J. Robichon, and D. H. Copp. Anat. Rec. 145, 206 (1963).

DIURNAL VARIATIONS IN THE METABOLIC ACTIVITY OF BONE AND CARTILAGE*

David J. Simmons and George Nichols, Jr.**

It was reported earlier that the amount of glycine-2-C^{14} - a labeled precursor for collagen formation - incorporated by cells forming the proteinaceous matrix of bone and cartilage was dependent upon the clock hour at which the tracer was administered.(1) Peak cellular incorporation in intact epiphyseal-metaphyseal segments from the distal femurs of rats occurred at 13:00 while minimal utilization was found at 01:00-03:00. However, because the tracer was labeled in both alpha and carboxyl carbon atoms, it was possible that the results partly reflected metabolic processes other than collagen synthesis. Since DNA synthesis in mouse cartilage is known to vary diurnally,(2) other biochemical events dependent upon 1-carbon fragments derived from glycine, such as porphyrin (DNA, RNA) and protein biosynthesis or carbon dioxide and lactate formation, might presumably exhibit marked daily rhythms as well. The proportion of the tracer actually secreted from the cells as collagen was similarly unknown. In addition, the possibility existed that the amount of radioglycine incorporated into bone was inversely related to the levels of glycine introduced into the circulation from the diet; rats are nocturnal animals and feed more actively at night. Several experiments were performed to answer these questions.

Methods

An in vivo experiment was designed to study the influence of diet on the utilization of glycine-2-C^{14} by bone and cartilage cells. Twelve 30- to 35-day old albino rats (Sprague Dawley) were divided into four groups of three animals each. For two weeks the rats were individually housed and exposed to a photoperiod of 12 hours (09:00-21:00) alternating with 12 hours of darkness (21:00-09:00). Half the colony was fasted 18-24 hours before treatment to empty their stomachs and intestines. The rats were injected when the greatest differences in tracer uptake by the tissues would be expected.(1) Three fed and three fasted rats received 35 μC glycine-2-C^{14} intravenously via the tail vein at 09:00-10:00 (Day Group); the remainder were injected at 01:00-02:00 (Night Group). Each animal also received an intravenous injection of 1 μC strontium-85 at the same time to investigate the influence of dietary calcium intake on the differential incorporation of strontium reported previously.(3) The

*This work was supported in part by Grant AM00854(C9), National Institutes of Health, U.S. Public Health Service.

**Department of Medicine, Harvard Medical School, Boston 15, Massachusetts.

Night Group was treated first to determine if the earlier results[1] were due to stress attendant upon frequent visits to the animal quarters. The animals were sacrificed by ether anaesthesia an hour after injection.

At autopsy, the femurs were removed. The bones of the left side were fixed in 95% alcohol and divided into distal, epiphyseal-metaphyseal, and shaft segments. These were stripped of soft tissues, ashed overnight at 600 deg, and assayed for their Sr^{85} activity in a well-type scintillation detector. The bones of the right side were fixed in 10% neutral formalin, cleaned of soft tissues, split longitudinally, and sliced into epiphysis, cartilage plate, metaphyseal, and shaft segments with a razor blade. The head of the femur was discarded. Following decalcification in 10% EDTA (pH 7.4), the segments were dissolved in concentrated formic acid (0.5 ml/mg tissue). Aliquots (0.1 ml) of this crude extract were transferred to planchets, evaporated and assayed by a thin end-window Geiger tube sensitive to the beta rays from C^{14}. The assays were performed in triplicate and measured against known standards.

An in vitro attempt was made to confirm and to evaluate the in vivo results obtained with crude tissue extracts with respect to various metabolic parameters in bone. The experiment was designed to study the metabolism of cells in chips of cartilage-free metaphyseal bone obtained by the technique of Borle et al.[4] from rats sacrificed at 10:00 and 03:00, approximately the hours of peak and minimal activity recorded in a previous experiment.[1] It was based upon knowledge that bone cells incorporate glycine (Figures 72 and 73) and that, with time, the label becomes incorporated into newly formed collagen. It was reasoned that any differential cell activity would also be reflected in the collagen fraction, and it would then be possible to gain corollary information about rates of bone formation.

Glycine-1-C^{14}, labeled in the carboxyl carbon, was used since this tracer would permit discrimination between that fraction of molecular glycine incorporated intact into the cells and newly formed collagen and that utilized in other metabolic pathways. The end points of cellular metabolism measured in this study were CO_2 and lactate production by the cells and the distribution of calcium between bone and the incubating medium. These phenomena seem at least qualitatively related. Schartum and Nichols[5] have shown that a steady-state distribution of calcium between bone and its surrounding medium is attained in vitro within two to three hours after the beginning of incubation, and that this is maintained as a function of the solubility of bone mineral and the acid produced by bone cell metabolism. It was further hoped that investigation of these parameters might furnish evidence of periodic changes of parathyroid gland activity implied by previously observed fluctuations in osteoclast frequency.[1] The immediate advantage of such an in vitro system is that the patterns of radioglycine uptake and mineral metabolism would be less subject to the effects of differential dietary intake or urinary protein elimination at various clock hours.

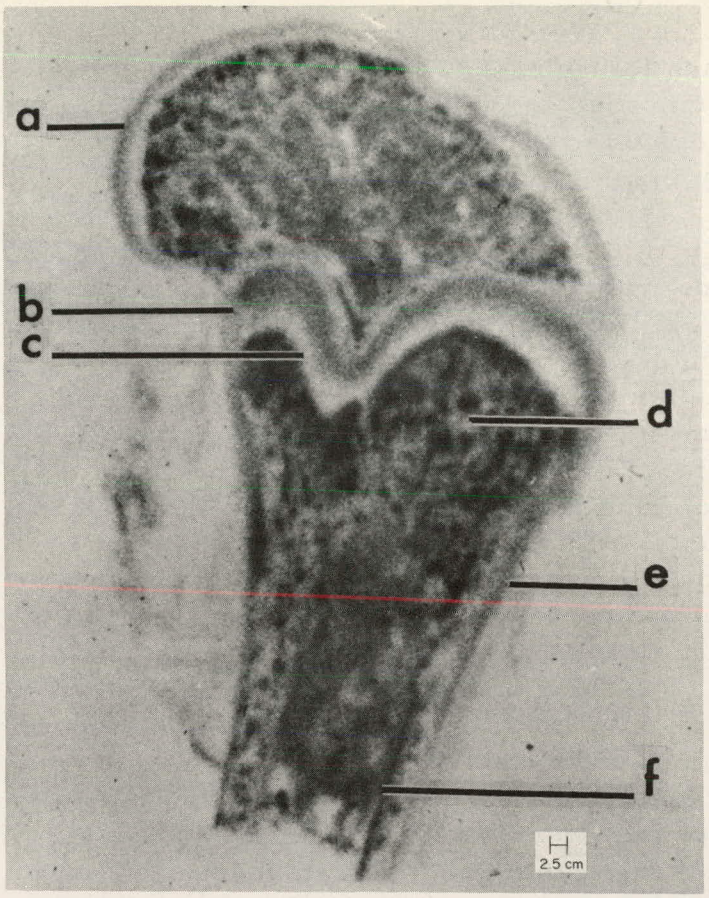

Figure 72

A contact autoradiograph of the distal end of the femur from a rat 1 hour after an injection of glycine-2-C^{14}. a, articular cartilage; b, proliferating zones and c, zone of hypertrophic cells of the epiphyseal growth cartilage; d, metaphysis; e, periosteum; f, endosteum.

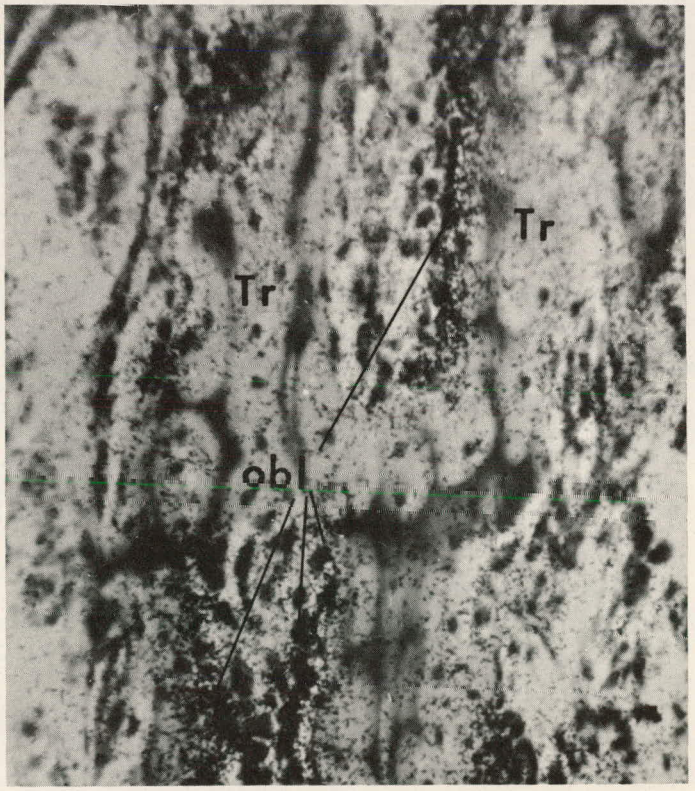

Figure 73

High resolution autoradiograph of the distal femoral metaphysis from a rat 1 hour after an injection of glycine-2-C^{14}. Tr, trabeculae; obl, osteoblasts.

Sixteen albino rats (Charles River Strain), 55 days old, were divided into two groups of 8 animals each following a two-week conditioning period. The animals had not been singly housed and the photoperiod had been somewhat longer than in the previous experiment (light: 06:00-21:00; darkness: 21:00-06:00). The animals were killed by decapitation at 10:00-10:30 and at 03:00-03:30. At autopsy, the long bones of the hind limbs were removed and quickly chilled in ice-cold Krebs Ringer medium. Cartilage-free metaphyseal bone fragments from the ends of the femurs (distal) and tibias (proximal) from two animals were pooled and placed in flasks containing 3.0 ml calcium-free Krebs Ringer medium buffered with bicarbonate at pH 7.4. The femurs and tibias were evaluated separately. Glucose was present in a concentration of 11.1 mM. Each flask also contained 0.6 μC glycine-1-C^{14} (New England Nuclear Corp., specific activity = 0.66 mC/mM) and 0.5 mM carrier glycine. Glucose, important as a substrate for the incorporation of glycine into the organic matrix of bone fragments,[6] and carrier glycine were present in approximately twice the plasma concentration reported for rats.[7] The flasks were sealed and incubated in a metabolic shaker at 37.5 deg under an atmosphere of 95% oxygen and 5% CO_2 for 2 hours to permit incorporation of the isotope by surviving cells. After incubation, the incubation medium and half the bone chips were removed for analysis. The remaining portion of bone was reincubated in fresh medium containing only C^{12} glycine for an additional 4 hours to determine the fate of the labeled glycine in the bone cells. The suitability of this system, which can adequately support living tissue for periods much longer than 6 hours, has been discussed by Schartum and Nichols and coworkers.[5,8]

At the end of each incubation, the medium was immediately centrifuged and aliquots transferred to Conway microdiffusion units for the determination of total and radioactive carbon dioxide.[9] Conway No. 1 units were modified by the technique of Flanagan and Nichols[8] to include a filter paper strip moistened with 1.6 N NaOH. At the end of diffusion, these strips were transferred to scintillation vials for radioactivity measurements. Additional aliquots of the medium were used for the determination of a) lactate production[10] and b) the steady-state distribution of calcium between the bone chips and their surrounding medium by titration using a murexide indicator against EDTA.[11]

The bone chips removed from the flasks at the end of each incubation period were blotted dry, weighed, and divided into two equal samples. One sample was extracted with 2.0 ml of 0.1 N NaOH at room temperature with constant shaking for 16 hours. The supernatant after centrifugation at 2500 rpm was designated the cell fraction and contained all the tissue DNA.[9] This alkali extract contains extracellular material as well (e.g., polysaccharides), but RNA and cellular organelles are destroyed. Collagen and bone mineral remain insoluble. Aliquots were taken for

determinations of total cell nitrogen (cell mass) following micro-Kjeldahl digestion, and of DNA following the hot 5% TCA extraction method of Schneider.[12] The radioactivity of DNA in an aliquot of the hot TCA extract was also measured. The bone residue after alkali extraction, was decalcified by three changes in 10% EDTA (pH 7.4) at 2 deg with continuous shaking for 48 hours, washed with water and acetone and defatted in a 1:1 ethanol-ether solution to give the collagen fraction. The samples were air dried and dissolved in 2.0 ml concentrated formic acid with mild heating in a water bath. Aliquots were removed for collagen (noncellular) nitrogen determination and transferred to scintillation vials for radioactivity measurements. The second sample of bone chips was decalcified and defatted by the procedure described above and extracted by the hot TCA method.[12] While this treatment frees DNA and RNA from the tissue proteins, it is probable that hot 5% TCA extracts some collagen as gelatin.[13] After centrifugation, RNA was determined spectrophotometrically and corrected for DNA.[12] An aliquot of the supernatant was measured for the total activity residing in the nucleic acid and collagen fractions. However, in view of the low specific activity of the alkali-insoluble collagen after two hours' incubation, the short period (15 min) of TCA extraction, and the absence of attendant changes in the radioactivity of the TCA-extractible RNA collagen fractions,[13] the measurements of RNA activity are probably not influenced greatly by any collagen extracted at this early time. The radioactivity of RNA, therefore, could be estimated since the values for DNA obtained from the cell fraction after alkali extraction were known. All lactate, calcium, DNA and RNA, and collagen nitrogen analyses were performed with a Coleman Junior spectrophotometer. A Coleman and a Zeiss spectrophotometer (QM P 11) were used for cell nitrogen determinations.

Radioactive counting was performed in an automatic Packard Tri-Carb liquid scintillation counter. The composition of the scintillation fluid has been described by Flanagan and Nichols.[8] The samples were internally standardized throughout the experiment with C^{14}-benzoic acid in toluene. Recoveries were of the order of 75-90%.

Results

In Vivo Studies

Localization of Glycine-2-C^{14} in Bone. The gross localization of the tracer an hour after injection is seen in a contact autoradiograph from the distal end of a femur (Figure 72). High resolution autoradiographs (Figure 73) indicated that the hotspots in the metaphysis represented incorporation of the tracer in osteoblasts lining the trabeculae; radioglycine was also found between the cells and the borders of the trabeculae. Some of the material has evidently been secreted from the cells as a part of newly synthesized collagen.

Effect of diet on the Utilization of Glycine-2-C^{14} and Strontium-85

The day-night rhythm again was apparent in this study (Table 30). The bones of fasted rats appeared to retain slightly greater amounts of radioglycine than fed rats at 09:00 and 01:00. The day-night rhythm is generally less pronounced after fasting. In the femur, there was a significantly greater incorporation of the tracer (circa 40%) in metaphyseal segments of fasted rats at 09:00, but the dietary program otherwise had little effect and the fraction of the total activity retained by the different segments in the two groups is essentially the same (Table 31). When the isotope was administered at 01:00, only the epiphyseal segments of fasted rats contained more radioactivity than those of the fed rats ($p < .01$), but similar differences did not occur in the regions of most active growth and remodelling of bone tissue. Most of the injected activity is retained by the growth cartilages, and it would appear, furthermore, that this is the only tissue in the femur exhibiting the periodic changes in glycine uptake observed in earlier experiments utilizing intact epiphyseal-metaphyseal segments.

Table 30

Percent glycine-2-C^{14}/mg matrix

	Clock Hour	Femur	Tibia
Fasted	09:00	2.35	2.20
	01:00	1.85	2.02
		(-21.3%)	(-8.2%)
Fed	09:00	1.75	2.00
	01:00	1.19	1.54
		(-32.0%)	(-23.0%)

( ) = % change in the retention of radioglycine

This study did not confirm the previous finding[3] that there was a relationship between the clock hour and Sr^{85} retention in the ends of the bones (Table 32) an hour after injection. The fasted rats seemed to retain more of the tracer dose than fed animals, but the differences are not statistically significant with the possible exception of rats injected at 01:00 ($p > .1 < .05$). Isotopic retention in the shafts is very uniform.

Table 31

Percent retention of glycine-2-C^{14}/mg bone

	Clock Hour		Shaft	Metaphysis	Epiphyseal Cartilage Plate	Epiphysis
Fasted	09:00	M	.0048	.0055	.0080	.0052
		S.E.	.0003	.0004	.0009	.0005
		N	(3)	(3)	(3)	(3)
		•	20.4	23.4	34.0	22.1
	01:00	M	.0039	.0040	.0052	.0054
		S.E.	.0005	.0002	.0001	.0002
		N	(3)	(3)	(3)	(3)
		•	21.1	21.6	28.1	29.2
		p	N.S.	N.S.	<.05	N.S.
Fed	09:00	M	.0043	.0032	.0059	.0041
		S.E.	.0007	.0002	.0004	.0005
		N	(3)	(3)	(3)	(3)
		•	24.6	18.3	33.7	23.4
	01:00	M	.0024	.0033	.0035	.0027
		S.E.	.0002	.0006	.0001	.0003
		N	(3)	(3)	(3)	(3)
		•	20.2	27.7	29.4	22.7
		p	N.S.	N.S.	<.05	N.S.

N = No. rats
• = Per cent of total activity in bone

The irregularities observed in glycine retention are probably due to sample contamination. It was difficult to assure complete separation of the different regions of the bones by the hand-sectioning technique. The epiphyseal cartilage of the femur, for example, is W-shaped on longitudinal section and this segment doubtless contained some metaphyseal and epiphyseal bone.

In view of the equivocal results achieved with the crude formic acid extracts, studies were undertaken using more sensitive in vitro methods.

Table 32

Microcuries of Sr^{85} retained per mg bone ash

Diet	Clock Hour	Femur		Tibia	
		Distal End	Shaft	Proximal End	Shaft
Fasted	09:00	.043	.014	.047	.012
		±.003	±.002	±.005	±.001
		(3)	(3)	(3)	(3)
	01:00	.039	.013	.040	.010
		±.002	±.001	±.005	±.005
		(3)	(3)	(3)	(3)
		N.S.	N.S.	N.S.	N.S.
Fed	09:00	.037	.011	.041	.010
		±.004	±.001	±.003	±.004
		(3)	(3)	(3)	(3)
	01:00	.031	.011	.030	.008
		±.002	±.001	±.001	±.001
		(3)	(3)	(3)	(3)
		N.S.	N.S.	N.S.	N.S.

In Vitro Studies

Radioglycine was more avidly utilized by bone cells (cpm/μg DNA) at 10:00 than at 03:00 after the initial 2-hour incubation period (Table 33). The differences between the bones were marked at these clock hours. Very little activity was initially found in the collagen fraction expressed as cpm/mg collagen N. The subsequent rate of collagen formation during reincubation in nonradioactive medium for 4 hours, measured by the loss of activity from the alkali-soluble cell fraction and the increase in activity in the alkali-insoluble collagen fraction, was also much greater at 10:00. There was no significant difference in the specific activity of the cell fractions at the end of this period. Only the corresponding changes observed for the tibias at 03:00 were in poor agreement. In general, collagen formation seemed to be somewhat greater in tibias than in femurs.

Table 33

Distribution of glycine-1-C^{14} incorporation in cell and collagen fractions of metaphyseal bone

Bone	Clock Hour		Hours of Incubation 2	Hours of Incubation 4	% Change
			cpm cells/μg DNA		
Femur	10:00	M	8304	2104	-74.7
		S.E.	231	154	
		N	6	6	
	03:00	M	6353	2682	-57.8
		S.E.	301	392	
		N	8	6	
		p	<.01	N.S.	
Tibia	10:00	M	7508	1370	-81.8
		S.E.	230	435	
		N	8	6	
	03:00	M	3523	1468	-58.3
		S.E.	845	128	
		N	8	6	
		p	<.01	N.S.	
			cpm collagen/mg collagen N		
Femur	10:00	M	879	3363	+73.9
		S.E.	139	960	
		N	6	8	
	03:00	M	447	1111	+59.8
		S.E.	165	320	
		N	8	8	
		p	>.001	>.001	
Tibia	10:00	M	405	1628	+75.1
		S.E.	52	144	
		N	8	8	
	03:00	M	164	1161	+85.9
		S.E.	62	297	
		N	6	6	
		p	>.001	N.S.	

Variations in cellular nitrogen occurred (10:00 > 03:00, Table 34), although the reason is uncertain in view of the relatively constant values obtained for DNA in the cell fraction (Table 35) and the apparent proportionality of DNA and cell nitrogen to the wet weight of the tissue.*(4) Changes in bone incorporation, changes in cell size, or in the degree of cell breakdown during incubation were possible. For this reason, the radioactivity in the cells was expressed as cpm/μg DNA (an index of cell number), although the choice obviates a quantitative estimation of the distribution of the glycine label within the tissue. The cellular nitrogen data, a possible index of attendant changes in the populations of the different bone cells, is considered in the discussion.

The results of the analyses to determine if the differential rates of glycine incorporation into bone fragments were similarly reflected by changes in the metabolism of glycine by bone cells, e.g., purine and pyrimidine synthesis and CO_2 and lactate formation, are reported in Tables 34-37.

Table 34

Cell nitrogen, mg cell N/100 mg bone

Bone	Clock Hour		Hours of Incubation 2	4
Femur	10:00	M	.639	.640
		S.E.	.219	.087
		N	8	8
	03:00	M	.439	.312
		S.E.	.058	.058
		N	8	8
		p	N.S.	>.05<.02
Tibia	10:00	M	.503	.491
		S.E.	.033	.067
		N	8	8
	03:00	M	.234	.201
		S.E.	.058	.064
		N	8	8
		p	>.01<.001	>.05<.02

Table 35

Content and specific activity of DNA and RNA from the metabolism of glycine-1-C^{14}

Bone	Clock Hour		2 Hour Incubation DNA μg/100 mg bone	DNA cpm/μg	RNA μg/100 mg bone	RNA cpm/μg
Femur	10:00	M	691	438	326	87
		S.E.	75	68	17	34
		N	8	8	8	6
	03:00	M	507	307	233	27
		S.E.	10	44	14	10
		N	8	8	8	8
		p	N.S.	N.S.	>.02<.01	N.S.
Tibia	10:00	M	597	504	291	18
		S.E.	31	110	16	2
		N	8	6	8	6
	03:00	M	618	235	223	15
		S.E.	24	50	14	2
		N	8	6	8	6
		p	N.S.	N.S.	>.01<.001	N.S.

DNA and RNA (Table 35). There were no apparent differences between the amount of DNA in the cellular fractions at the two time periods. However, total RNA values were significantly higher at 10:00 commensurate with the increase in bone protein synthesis. The specific activities of DNA and RNA (cpm/μg/100 mg bone), after the initial incubation periods, at 10:00 and at 03:00 were similar, suggesting that the metabolism of glycine-1-C^{14} and the utilization of the carboxyl carbon for nucleic acid synthesis were not subject to diurnal variations.

*It should be noted in the studies of Borle, Nichols, and Nichols(4) that all animals were sacrificed at approximately the same clock hour.

Table 36

Metabolism of glycine-1-C^{14} to CO_2

Bone	Clock Hour		2 Hour Incubation (CO_2 cmp/μmole CO_2)
Femur	10:00	M	95
		S.E.	14
		N	8
	03:00	M	101
		S.E.	11
		N	8
		p	N.S.
Tibia	10:00	M	126
		S.E.	8
		N	8
	03:00	M	131
		S.E.	56
		N	6
		p	N.S.

Table 37

Lactate production by metaphyseal bone cells, μmoles lactate/hr/μg DNA

Bone	Clock Hour		Hours of Incubation 2	Hours of Incubation 4
Femur	10:00	M	3.23	3.51
		S.E.	.35	.33
		N	8	6
	03:00	M	3.20	2.41
		S.E.	.19	.26
		N	8	6
		p.	N.S.	<.001
Tibia	10:00	M	3.35	4.05
		S.E.	.24	.18
		N	8	8
	03:00	M	2.53	3.17
		S.E.	.33	.47
		N	8	8
		p	<.001	<.001

CO_2, Lactate, and Calcium in the Incubation Medium (Tables 36, 37, 38). The amount of C^{14} - glycine decarboxylated by metaphyseal bone cells, expressed as cpm CO_2/μmole in the medium, was constant at 10:00 and 03:00 after the first 2-hour incubation period (Table 36). However, lactate production (Table 37), derived from the glycolytic cycle of the cell protoplasm, was significantly increased at 10:00 in the tibias (22-25%); this difference (30%) was observed in femurs only following reincubation in nonradioactive medium. The variability between the bones may be related to the somewhat greater metabolic activity of tibias compared to femurs indicated by differences in rates of collagen synthesis (Table 33). That the fragments of metaphyseal bone incubated at 10:00 were also able to maintain higher steady-state distributions of calcium between the tissue and surrounding medium is consistent with observations of differential cell metabolism (Table 38). The changes between lactate production and the medium calcium were nearly proportional, although no stoichiometric relationship between these phenomena[5,14,15] has as yet been shown.

Table 38

Steady state of calcium between bone and incubation medium, m moles/liter Ca in incubation medium

Bone	Clock Hour		Hours of Incubation 2	Hours of Incubation 4
Femur	10:00	M	1.23	1.57
		S.E.	.08	.10
		N	8	8
	03:00	M	0.96	1.00
		S.E.	0.02	0.06
		N	8	8
		p	<.01	<.001
Tibia	10:00	M	1.28	1.37
		S.E.	0.08	0.13
		N	8	8
	03:00	M	1.00	1.01
		S.E.	0.04	0.04
		N	8	8
		p	<.02	<.05

Discussion

Whereas previous studies have demonstrated that mitotic[1,16] and biochemical events in cartilage cells - DNA synthesis[2] and mucopolysaccharide formation[17] - have a diurnal rhythm, the information about bone tissues has been less definitive. The in vitro study presented in this paper using cartilage-free bone has confirmed the results obtained heretofore in vivo that the functional activity of bone cells has a diurnal period. Moreover, the combination of techniques has yielded new information about the relationship between bone formation and resorption.

The high resolution autoradiographs of radioglycine uptake in vivo in the metaphyses indicated that the tracer was deposited principally in osteoblasts lining the trabeculae an hour after injection and that some of the tracer had already been secreted by the cell as a part of newly synthesized collagen molecules. The in vitro study indicated that very little of the total activity incorporated by the bone is in the collagen fraction after 2 hours, and that most of the cellular activity is transferred to the matrix during the succeeding 4 hours. These results are consistent with findings obtained by autoradiographic[18,19] and metabolic techniques[8,13] reported from other laboratories studying the fate of glycine and proline as collagen precursor substances in bone. The present observations go further and indicate that the amount of bone matrix synthesized and formed by osteoblasts is dependent upon the clock hour. The functional activity of osteoblasts is maximal at 10:00 and least at 03:00. This effect was not altered importantly by fasting rats prior to experimentation. The in vitro results also obviate the possibility that the changes are due to diurnal variations in urinary protein elimination. Clinical studies by Altman and Stellate[20] failed to reveal a particular pattern of protein excretion in man.

The relative constancy of the amount of DNA in metaphyseal cells found in this experiment is consistent with the uniform labeling index of osteoblasts at different clock hours following tritiated thymidine administration.[2] Moreover, it supports the autoradiographic evidence that osteoblasts seldom, if ever, undergo mitosis,[2,21-24] and that increases in the osteoblast census are dependent upon the directed modulation of undifferentiated osteoprecursor cells. DNA probably cannot simultaneously support its own replication and the production of RNA in animal tissues.[25]

Bone cell RNA synthesis is significantly increased at 10:00, and this is compatible with an increased bone protein (collagen) synthesis at this time. While the fundamental task of both osteoblasts and chondrocytes is to produce their respective matrices, the life cycle of the cells is quite different. The maintenance of growth cartilage structure, at least, requires that the cells renew themselves by division, and daily

periodic patterns of DNA synthesis[2] and mitosis,[1,16] as well as mucopolysaccharide formation[17] (ground substance), in cartilage have been described. Osteoblasts constitute a metaplastic population of cells competent to modulate morphologically and functionally to other bone cell types, and only in this sense do they constitute a renewal system. It is probable that there is a periodic intensity of cellular modulation in bone from undifferentiated reticular and preosteoblast cells (osteoprecursor cells) to the more highly specialized osteoblasts and osteoclasts. Circadian (circa diem) rhythms in the percentage area of the rat metaphysis occupied by osteoclasts have been found in a previous study,[1] and the phenomenon raises several questions.

Was there in fact an increase in the numbers of these cells or simply a change in their size and/or configuration? Are the frequency changes meaningful in terms of the functional activity of the osteoclast? Finally, what stimulated the changes? The first question cannot be answered completely, but the fact that the in vitro steady-state distribution of calcium between the bone and the incubation medium increased significantly at the period of peak osteoclast frequency is a circumstance suggesting that the metabolic and morphologic changes are indeed interrelated. The differences between the high (10:00) and low (03:00) bone cell nitrogen values reported in this study could be readily explained if osteoclastic resorption of metaphyseal bone were suppressed at 03:00. There is some experimental evidence to support this thesis. Borle and his coworkers[14] and Vaes and Nichols[15] found lower nitrogen levels in rats administered estrogen, and it is known that estrogen-treated rats fail to resorb endochondral metaphyseal trabeculae.[26,27] A plausible answer to the final question rests upon two assumptions: a) that there is a diurnal pattern of parathyroid gland secretion, and b) that the reduced motor activity of rats during the environmental photoperiod is accompanied by metabolic acidosis. If a transitory acidotic state were realized, increased parathyroid gland secretion might occur followed by both an increase in osteoclast numbers and in the basic rate of calcium and phosphorus removal (higher steady-state) from the skeleton.[28] Parathormone (PTE) will stimulate bone lactate formation[14] and the direction of the change observed in this study would also seem to suggest that the basic level of parathyroid gland secretion is subject to diurnal variations. Although aerobically, bone citrate production is small compared to lactate, citrate more effectively than lactate influences calcium mobilization from bone and may, then, also be involved in the maintenance of greater concentrations of calcium in the incubation medium at 10:00.[14] Because Vaes and Nichols[15] found no correlation between changes in bone mineral mobilization and changes in rates of cellular citrate metabolism or citrate concentration in bone and medium, PTE may only initially serve to stimulate bone resorption by increased acid production. The calcium content in the incubation medium probably reflects the changes in the passive solubility of bone mineral as well.[29] In addition, PTE will reduce the

kidney tubular reabsorption of phosphate; the hyperphosphatemic and hyperphosphaturic changes which follow PTE administration might also be expected to stimulate calcium withdrawal from bone.[30] However, these sequelae of presumed metabolic acidosis occur at a time when bone formation is most active, and Gaillard[31] reported that PTE impaired radioglycine uptake by osteoblasts in cultured embryonic mouse bone. While this effect has also been seen in vitro following the administration of PTE to mice[32] and rats,[33] it is probable that endogenous parathormone levels (4 I.U./hr)[34] are never as high as the dose of PTE required experimentally to demonstrate preferential osteoclast formation or to reduce collagen synthesis. Selye,[35] in fact, has shown that physiologic levels of PTE (5 I.U.) stimulate osteoblastic activity in rats without previous osteoclast formation and fibrous transformation of the bone marrow.

Alternative mechanisms which would influence a change in the endogenous activity of the parathyroid gland are, of course, possible. Because rats feed most actively at night, the absorption of large amounts of calcium from the gut into the circulation might tend to suppress the cellular synthesis of parathyroid hormone[36,37] and/or its release from the gland. This would result in a low osteoclast frequency and function. The effect of the adrenal cycle must also be considered. Reduced collagen formation during the environmental dark period might be expected in this study owing to the increased levels of circulating adrenal cortical hormones at this time.[38] Moreover, Stoerk and his coworkers[39] have presented indirect experimental evidence that the blood calcium lowering effect of hydrocortisone (within three hours) administered to parathyroidectomized rats is corrected by a compensatory hyperactivity of the parathyroids in the intact animal. These results, which suggest that there is a simultaneous daily period of parathyroid and adrenal activity, are not incompatible with the interpretation of the osteoclast frequency and the metabolic changes formed in this study. The first histologic evidence of increased osteoclast formation in bones induced by administered parathyroid extract occurs after 6-12 hours.[40]

In view of studies in rabbits by Okada[41] employing the lead acetate vital staining technique, this description of periodic bone formation in the metaphysis is probably valid for osteon formation in cortical bone as well. Whatever the mechanism, it is possible to infer from these parallel cytologic and biochemical investigations that the daily periods of most active metaphyseal bone formation and resorption are not out of phase. They are coincident, and remodeling processes are most intense early in the environmental photoperiod.

Summary

In vivo and in vitro studies of the metabolism of bone cells in the metaphyses of the rat femur (distal) and tibia (proximal) have established that collagen synthesis and new bone formation are diurnally regulated.

Significantly greater amounts of glycine-1-C^{14} were initially incorporated by osteogenic cells (principally osteoblasts) at 10:00 than at 03:00, and the subsequent rate of bone formation by these cells was also faster at 10:00. While DNA values did not vary at these clock hours, the content of RNA was significantly higher at 10:00, consistent with the increased bone protein synthesis. The greatest production of bone lactate and the maintenance of a higher steady-state distribution of calcium between the bone and the incubation medium (release of Ca^{++} from the tissue) also occurred at 10:00. It was concluded that the daily periods of most active metaphyseal bone formation and bone resorption are perhaps coincident, and that tissue remodeling is most intense in rats during the early part of the environmental photoperiod.

References

1. D. J. Simmons, Argonne National Laboratory, Radiological Physics Division, Summary Report, July 1962-June 1963. ANL-6769, p. 142.

2. D. J. Simmons. Clin. Orthopaedics 26, 176 (1963).

3. D. J. Simmons, Argonne National Laboratory, Radiological Physics Division, Semiannual Report, January through June, 1962. ANL-6646, p. 110.

4. A. B. Borle, N. Nichols, and G. Nichols, Jr. J. Biol. Chem. 235, 1206 (1960).

5. S. Schartum and G. Nichols, Jr. J. Clin. Invest. 41, 1163 (1962).

6. G. M. Vaes and G. Nichols, Jr. Endocrinology 70, 890 (1962).

7. P. L. Oltman. Blood and Other Body Fluids, ed. D. S. Dittmer. Federation of American Societies for Experimental Biology, Washington, D. C., 1961.

8. B. Flanagan and G. Nichols, Jr. J. Biol. Chem. 237, 3686 (1962).

9. E. J. Conway. Microdiffusion Analysis and Volumetric Error. Crosby, Lockwood and Son, London, 1947.

10. S. B. Barker and W. H. Summerson. J. Biol. Chem. 138, 535 (1941).

11. A. D. Kenny and V. H. Cohn. Anal. Chem. 30, 1366 (1958).

12. W. C. Schneider. Methods in Enzymology, ed. S. P. Colowick and N. O. Kaplan. Academic Press, Inc., New York, 1957. Vol. III, pp. 680-684.

13. B. Peterkovsky and S. Udenfriend. J. Biol. Chem. 238, 3966 (1963).

14. A. B. Borle, N. Nichols, and G. Nichols, Jr. J. Biol. Chem. 235, 1211 (1960).

15. G. Vaes and G. Nichols, Jr. J. Biol. Chem. 236, 3323 (1961).

16. D. J. Simmons. Nature 202, 906 (1964).

17. D. J. Simmons. Experimentia 20, 137 (1964).

18. J. Carneiro and C. P. Leblond. Exptl. Cell. Res. 18, 291 (1959).

19. R. W. Young. Anat. Rec. 143, 1 (1962).

20. K. A. Altman and R. Stellate. Clin. Chem. 9, 63 (1963).

21. R. W. Young. J. Cell Biol. 14, 357 (1962).

22. N. F. Kember. J. Bone Joint Surg. 42-B, 824 (1960).

23. M. Owen. J. Cell Biol. 19, 19 (1963).

24. M. Owen and S. MacPherson. J. Cell Biol. 19, 33 (1963).

25. E. S. Canellakis. Ann. Rev. Biochem. 31, 271 (1962).

26. M. R. Urist, A. M. Budy, and F. C. McLean. Proc. Soc. Exptl. Biol. Med. 68, 324 (1948).

27. D. D. Dziewiatkowski, F. Bronner, N. DiFerrante, and R. M. Archibald. J. Biophys. Biochem. Cytol. 3, 151 (1957).

28. R. V. Talmage and F. W. Kraintz. Gen. Comp. Endocrinol. 1, 341 (1961).

29. C. C. Johnston, E. B. Miner, D. M. Smith, and W. P. Deiss, Jr. J. Lab. Clin. Med. 60, 689 (1962).

30. A. R. Lavender, T. N. Pullman, H. Rasmussen, and I. Aho. The Parathyroids, ed. R. O. Greep and R. V. Talmage. C. C. Thomas, Springfield, Ill., 1961. pp. 406-412.

31. P. J. Gaillard. The Parathyroids, ed. Greep and Talmage. C. C. Thomas, Springfield, Ill., 1961. pp. 20-45.

32. G. M. Vaes and G. Nichols, Jr. Endocrinology 70, 546 (1962).

33. C. C. Johnston, W. P. Deiss, Jr., and E. B. Miner. J. Biol. Chem. 237, 3560 (1962).

34. B. N. Premachandra and H. T. Blumenthal. Proc. Soc. Exptl. Biol. Med. 107, 842 (1961).

35. H. Selye. Endocrinology 16, 547 (1932).

36. L. G. Raisz and J. E. Obrien. Am. J. Physiol. 205, 816 (1963).

37. S. I. Roth and L. G. Raisz. Lab. Invest. 13, 331 (1964).

38. R. H. Follis, Jr. Proc. Soc. Exptl. Biol. Med. 76, 722 (1951).

39. H. C. Stoerk, A. C. Peterson, and V. C. Jelinek. Proc. Soc. Exptl. Biol. Med. 114, 690 (1963).

40. M. Heller, F. C. McLean, and W. Bloom. Am. J. Anat. 87, 315 (1950).

41. M. Okada. Shanghai Evening Post (Medical Edition), September 1943.

AN UNDERGROUND LABORATORY FOR HIGH SENSITIVITY GAMMA-RAY COUNTING

Harold A. May, John B. Corcoran, and Paul Hess

Introduction

The sources of residual background counts observed in low-level gamma-ray scintillation counting systems have been studied extensively, and methods of minimizing them have been discussed in previous reports from this Division. The background arises, in large part, from activity within the scintillating crystal, the optical reflector or other parts of the crystal container, and from the attached phototube. The radioactive elements found to be responsible are almost all naturally-occurring long-lived isotopes appearing as contaminants within the materials involved, and thus their elimination of reduction can best be accomplished by careful selection of materials of exceptional purity. The half-lives of these trace elements are always very great compared to the duration of experimental studies, so that their background contribution is, at least, constant in time.

We have shown[1] that a significant fraction of the cosmic-ray produced background stems from interactions of high-energy nuclear-active particles (neutrons and protons) within or in the environs of the crystal assembly and its shield. This component may best be reduced in intensity to the point where its effect is much less than those from other background sources by the additional shielding of a suitable thickness of earth, water, or other low Z material. Since fluctuations in the intensity of nucleons due to normal barometric pressure changes may be as great as 25% over a period of a few hours, this attenuation is of particular value.

In the period covered by this report we have occupied and made a few preliminary tests of an underground laboratory area (called the vault) designed to reduce the background contributed by cosmic-ray nucleons to a completely negligible amount. The vault is located at the west end of Building 203, with access via hydraulic elevator from the existing calibration garage area. The experimental area is 30 ft long, 16 ft wide, and 15 ft high; an entryway, shower and locker, and instruments rooms having much lower ceilings provide access, while minimizing direct or "geometrical" leakage of radiation into the vault from above via the elevator shaft. Three vertical shafts are also provided, consisting of sections of 20-in. diameter steel pipe extending to depths of 15 ft (two shafts) and 35 ft below the floor of the vault. These are to be used in further studies of the background contributed by cosmic-ray muons and may also be of some value in the evaluation of ultra-pure materials of

counter construction, or other very low activity samples. Since the blue clay into which these shafts are sunk is known to contain much more radium and thorium than typical surface soil, further shielding within the shaft is required. Approximately five tons of mercury is on loan from the AEC stockpile for this purpose. Plan and elevation views of the facility are shown in Figure 74. The reinforced concrete roof of the vault

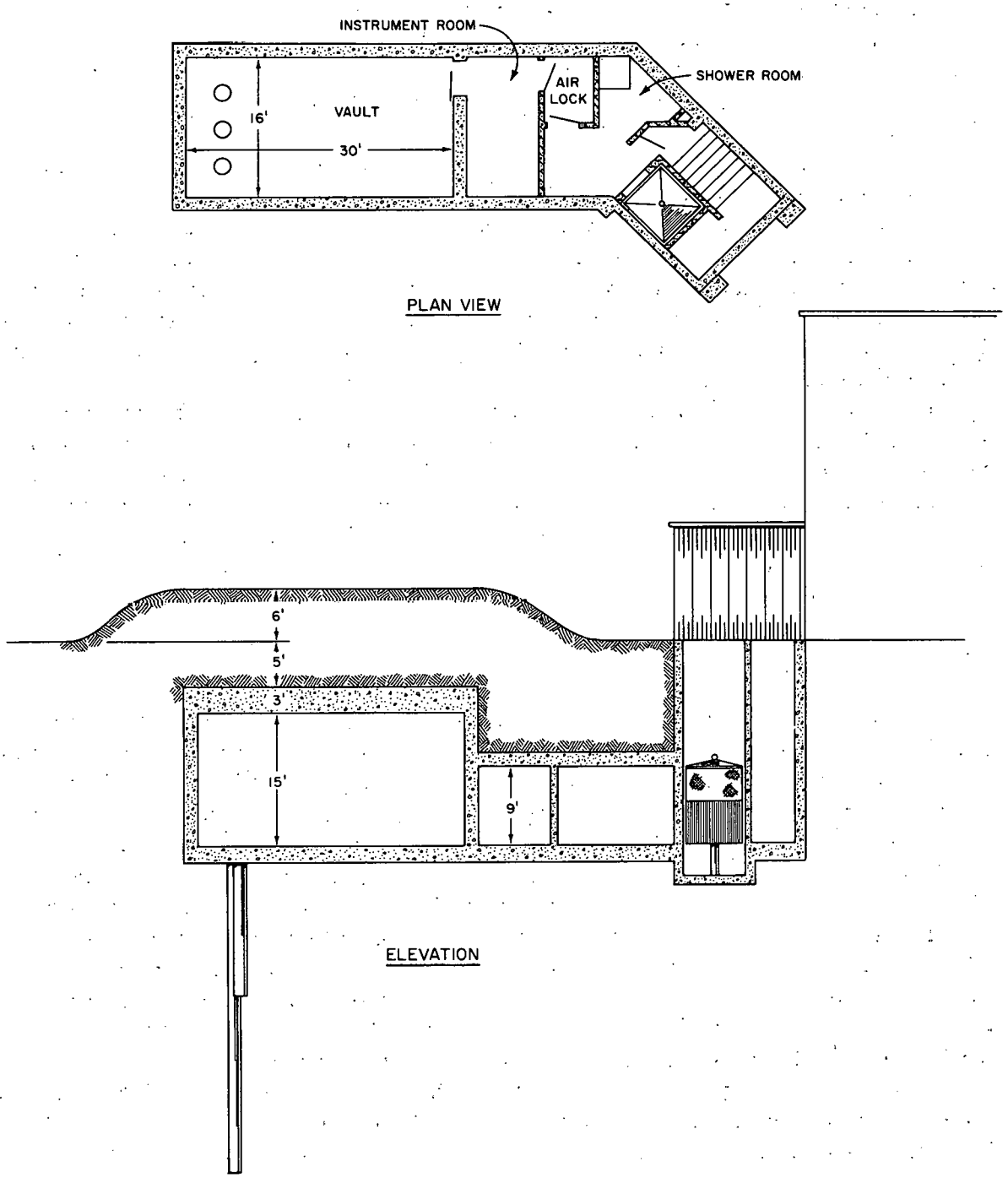

Figure 74

Underground vault for low level gamma spectrometry

is 3 ft thick, its upper surface is 5 ft below grade, and an additional 6 ft of earth is mounded over the vault. Thus the minimum shielding is about 450 g cm^{-2}, increasing to ~620 g cm^{-2} in the vertical direction at the center of the room. Assuming a value of 135 g cm^{-2} as the mean free pathlength of cosmic-ray nucleons in earth, the flux penetrating to the vault should be about 4% of that which is incident, or approximately 7.3% of that in the basement area where the iron rooms and other low-level counters have been located heretofore. The attenuation of neutrons from nearby accelerators, which have on some occasions interfered with our counters, is many times greater than this.

The value of such shielding may be seriously compromised by excessive radon and thoron gas in the vault. In order to keep this concentration well below the outside ambient level, the vault and instrument room are completely lined with galvanized steel sheets with all overlapping joints sealed with soft solder. Access is via an air lock, the air within the controlled area being maintained at a slight positive pressure. This air may come from aged air tanks, or from an air-treatment plant designed to reduce the radon level to some 2-4 x 10^{-5} pC/l. (i.e., of the order of 10^{-4} times the concentration in the outside ambient "feed" air.)* Initial testing of these facilities has revealed that the walls and airlock are not as tight as had been hoped for, with the result that much higher flow rates are required to maintain the required pressure differential. Full discussion of the performance of the system must, therefore, be deferred until a later report.

Neutron Background

We have attempted to measure the fast neutron flux within the vault over the energy range of roughly 0.5 to 15 MeV, where the response of the conventional "long counter" is reasonably flat.[2] In the absence of any nearby sources, this flux consists solely of evaporation neutrons produced in the surrounding materials, which should be proportional to the intensity of the cosmic-ray nucleonic component. The use of the "long counter" was determined by availability rather than choice, for its small volume and consequent low counting rate in the weak fluxes with which we are concerned is a serious limitation to the measurement accuracy. The results of a series of observations in the vault vs Building 818, a surface location with no effective shielding and well removed from all sources of "man-made" neutrons, are tabulated in Table 39. By way of comparison, we have previously reported[3] gross counting rates from 0.554 to 0.643 cpm at surface locations comparable to Building 818, and a BF_3 counter background of 0.171 ± 0.009 cpm. The

*See discussion by Henry F. Lucas, Jr., page 91, for greater details of the radon removal system.

counting rate within the vault is found to be reduced by a factor of about 8, relative to the surface, although because of statistical uncertainties this may vary from 5.5 to 13.

Table 39

Observations of neutron background in the vault and Building 818

Location	Total counting time, min	Counting rate, cpm
Underground vault	13,220	0.1845 ± 0.0075*
BF_3 tube in cadmium (tube background)	8,530	0.1578 ± 0.0106
Net increase from cosmic rays		0.0367 ± 0.013
Building 818	9,070	0.458 ± 0.0158
BF_3 tube in cadmium	19,670	0.165 ± 0.0055
Net increase from cosmic rays		0.293 ± 0.017

*Uncertainties shown are based on counting statistics only, at the 0.9 confidence level.

Considerable difficulty has been experienced in completely eliminating sporadic counting due to noise pickup within the electronic system which, in the presence of such low true counting rates, should be identically zero. Operation of the preamplifier filaments from a well-filtered dc source, and use of a doubly-shielded cable between the preamplifier and the main amplifier aid in keeping signal-carrying paths at low impedance to noise frequencies, and thus greatly reduce the direct pickup of radiated noise signals. These measures seemed to be sufficient at the time our previous runs in the ZGS building were made. When the present runs were started, erratic results persisted until the neutron detector output was placed in anticoincidence with a noise channel. The latter consisted of a conventional linear amplifier which received signals from a noise antenna - a 20-ft piece of hook-up wire taped along the outside of the preamplifier cable - and from the ac line via a small coupling capacitor. This noise channel furnishes a gating pulse of 20 milliseconds' duration, while the output of the detector channel is delayed some 10 milliseconds before being applied to the anticoincidence circuit. Such long gating periods appear to be necessary for suppression of transients associated with shock excitation of inductive elements in the power supplies. When functioning properly, the system is capable of completely eliminating noise counts produced by triggering a 100-Watt soldering gun operated from the same ac outlet and held within a few feet of the detector.

Since the anticoincidence measures cannot suppress noise counts arising in the input stage of the preamplifier, the data output register was paralleled with an Esterline-Angus recorder, so that any short periods of rapid counting could be detected. For some of the data recorded in Building 818, portions of the record which showed higher-than-average counting rates were rejected in this manner, without discarding the entire run. Since the onset and termination of such noise bursts are usually gradual, the determination of the portions of the record to be rejected is arbitrary and subjective. Thus the data of Table 39 are undoubtedly of less significance than might be inferred from the error estimates as calculated from counting statistics alone. This is further attested by analysis of the six consecutive data runs of intrinsic counter background in the vault (line 2 of Table 39) totaling 8530 min. A chi squared test of the normal distribution about the mean yields the value $\chi^2 = 4.84$, which with five degrees of freedom indicates a 43% probability of being exceeded. On the other hand, similar analysis of the eleven consecutive data runs in the vault yield a value of $\chi^2 = 35.1$. Since cosmic rays at this location appear to contribute no more than 25% of the total rate, it does not seem likely that fluctuations in their intensity (except for the remote possibility of a solar flare disturbance) can be responsible for the observed spread of values. Thus it must be admitted that while the tabulated figures support the theoretical attenuation, the degree of agreement is only qualitative.

Muon Intensity

The relative muon intensity within the vault has been determined by observing the counting rate in the muon through-peak of a 7-in. diameter by $3\frac{1}{2}$ in. thick NaI crystal. The most probable energy loss of a 1 GeV muon in 3.5 in. (the crystal normally being oriented with the axis vertical) of this material is about 42 MeV. The distribution in actual energy loss per event, as given by the Landau theory,[4] results in a broad peak with a pronounced tail on the high energy side. In our measurements the peak is further broadened by the distribution in energy of the incident muons, and by the variation in path lengths through the crystal due to the wide viewing angle of the detector and the $\cos^2$ variation of intensity vs direction of the incident particles. Both of these factors introduce shifts in the pulse-height distribution dependent upon the extent and geometry of shielding; since these are small and difficult to account for, the total counting rate between the low- and high-energy half-maximum points at roughly 30 and 55 MeV, respectively, are shown in Table 40. Correlation of these relative counting rates with well-known measurements of the vertical muon flux vs depth underground, utilizing a GM tube coincidence telescope, do not appear to be particularly significant. This is not too surprising, in view of the great difference in the detectors and geometries involved. These figures should be proportional to the total number of muons intersecting the local shielding at each location and, hence, contributing to the low-energy gamma-ray background.

Table 40

Total counting rate between low- and high-energy half-maximum points at 30 and 55 MeV, respectively

Location	Shielding, g cm^{-2}		Through-peak, cpm
Surface	8-in. iron	155	128
Basement, Building 203	concrete	80	114
	+		
	iron	155	
Underground vault	earth and concrete	550	64
	+		
	lead	100	
Bottom of 15 ft shaft	same as vault		33

Gamma Ray Background

We have not had an opportunity as yet to move the 8-in. thick iron cave, within which many of the previously-reported measurements have been performed, into the underground vault. Therefore, the measurements to be reported here have been made with a temporary cave of 2 x 4 x 8-in. lead bricks, surrounding a 3-in. diameter by 5-in. long crystal detector. By assembling this upon a 19-in. diameter heavy steel base plate, with the entire cave being rigidly clamped together by means of a second identical plate fastened to the base with tie rods, it was possible to transport the cave in toto between our former basement location and the vault, and also to lower it to the bottom of one of the vertical shafts. The possibility of some activity being present upon or within the lead bricks cannot be overlooked. Such local contamination would result in an abnormally high apparent background and reduce the fraction (but not the absolute number) contributed by cosmic rays. The use of lead as a shield guarantees a large net difference, due to the nature of the interactions of cosmic-ray nucleons in high Z materials. Furthermore, construction of a cylindrical shield from rectangular bricks inevitably results in many voids in the shielding so that the effective thickness is difficult to ascertain. For these reasons, the results do not permit more than a very rough estimate of background reduction expected in a more conventional iron shield. The background rates observed in the temporary shield at three locations are summarized in Table 41.

Tables 42-44, reproduced directly from the output data sheets prepared by the CDC type 160A computer, list the mean counting rates observed for successive 100-min runs within selected energy bands. Below each

column are shown several parameters which characterize the statistical variations in the background. The abbreviations employed are explained at the top of each table, except for "CF V," which is the coefficient of variation, i.e., the observed standard deviation divided by the mean counting rate. It may be noted that in each location this coefficient, and, hence, the value of chi squared, is extremely large for the lowest energy band. This is certainly due to noise counts in the lowest channels; hence this band has been disregarded in further analysis.

Table 41

Background counting rate in 3 x 5-in. NaI crystal, in 4-in. lead cave

Energy	Basement	Underground vault	δ	Foot of 35-ft shaft
100-400 keV	102.2 ± 1.2	76.4 ± 0.9	25.8 = 25%	71.3 ± 0.8
400-600 keV	33.2 ± 0.7	22.7 ± 0.5	10.5 = 32%	20.3 ± 0.4
0.60-1.3 MeV	56.9 ± 0.8	40.5 ± 0.6	16.4 = 29%	40.0 ± 0.7
1.3-1.6 MeV	10.0 ± 0.3	7.1 ± 0.3	2.9 = 34%	7.3 ± 0.3
1.6-3.0 MeV	14.1 ± 0.4	8.0 ± 0.2	6.1 = 43%	5.8 ± 0.3
0.10-3.0 MeV (Total)	216.5 ± 2.3	154.8 ± 1.2	61.7 = 28%	144.8 ± 1.0

For each value of χ^2, there is a corresponding probability, $P(\chi^2)$, which expresses the relative chance of this value being equaled or exceeded by a single set of observations, if the test hypothesis - in this case, that all fluctuations form a normal distribution about the mean, with standard deviation $[\overline{N}/t]^{1/2}$ - is a valid one. It follows that there is a 90% probability $\chi^2_{lo} \leq \chi^2_{obs} \leq \chi^2_{hi}$, where $P(\chi^2_{lo}) = 0.95$ and $P(\chi^2_{hi}) = 0.05$. To aid in comparing results for the three locations, the observed values of chi squared, and limits, are collected in Table 45.

Two possible sources of nonstatistical fluctuations may be considered: apparent changes in counting rate due to drift in the energy vs channel number, and true count-rate variations. The former is usually the result of temperature changes in thermally-sensitive portions of the system, although uniform drifts associated with component aging or photomultiplier instability cannot be completely overlooked. The RIDL 400-channel analyzer and Hamner stable high voltage supply utilized during this study were located in the vault during accumulation of all the data. Since the vault temperature is stabilized to about $\pm\frac{1}{2}^{\circ}$F, and since these circuits had been operating for a number of days prior to the start of these runs, any fluctuations introduced by them should be insignificant and of the same magnitude in all locations. Gain shifts associated with changes in crystal detector temperature in the basement location cannot be ruled out, although they appear unlikely, considering the statistical behavior of the higher energy bands.

Table 42

Background variations in A-Wing basement of Building 203. 17-20 July 1964, all runs are 100-min, RIDL analyzer used, 3 x 5-in. crystal. The crystal is in a castle of lead bricks, the castle walls are 4 in. thick.

Legend C/M = counts per minute in the selected energy band, N = number of measurements, T = time duration of measurements, DSIG = variation from the mean in units of the expected counting deviations at the ninety percent confidence level, SD = standard deviation of the observed counting rates, ERMN = expected counting error of the mean = SQRT (mean/(N*time)), CHISQ = chi square = for I=1,N (C/M(I) - mean)**2/(C/M(I)/1)

DATA PROCESSING JACK CORCORAN - PROGRAM 1839/RPY 3T2 F2 BACKGROUND ANALYSIS

CHANNELS	10 - 20		21 - 53		54 - 74		75 - 167		168 - 209		210 - 399		21 - 399	
ENERGY (MEV)	0 - .100		.100 - .400		.400 - .600		.600 - 1.3		1.3 - 1.6		1.6 - 3.0		.100 - 3.0	
RUN	C/M	DSIG	C/M	DSIG	C/M	DSIG	C/M	DSIG	C/M	DSIG	C/M	DSIG	C/M	DSIG
19	41.97	-.7	103.02	.4	33.19	.0	57.67	.6	10.77	1.3	15.10	1.4	219.75	1.3
20	41.29	-1.4	100.14	-1.2	33.74	.5	57.74	.6	10.16	.2	14.12	-.0	215.90	-.2
21	41.93	-.8	103.35	.6	33.22	.0	57.91	.8	9.81	-.4	14.15	-.0	218.44	.8
22	42.30	-.4	100.11	-1.2	31.72	-1.5	56.34	-.4	9.99	-.0	13.36	-1.3	211.52	-2.0
23	42.42	-.3	102.53	.1	33.29	.1	56.74	-.1	10.25	.3	14.62	.7	217.43	.3
24	44.62	1.6	102.90	.4	34.33	1.2	57.83	.7	10.55	.9	14.72	.8	220.33	1.5
25	41.71	-1.0	103.20	.5	33.17	.0	57.77	.7	10.10	.1	13.82	-.5	218.06	.6
26	42.24	-.5	103.49	.7	33.66	.5	58.64	1.4	9.97	-.1	14.67	.8	220.43	1.6
27	42.51	-.2	100.57	-1.0	33.24	.0	57.63	.7	9.88	-.3	13.88	-.4	215.40	-.4
28	43.41	.5	102.13	-.0	33.29	.1	58.03	.9	10.33	.5	14.41	.4	218.19	.7
29	42.56	-.2	103.21	.5	34.01	.8	56.04	-.6	9.94	-.1	14.35	.3	217.55	.4
30	42.35	-.4	101.04	-.7	31.78	-1.4	56.33	-.4	10.06	.0	14.15	-.0	213.36	-1.2
31	41.64	-1.1	101.53	-.4	33.37	.2	56.72	-.1	9.44	-1.1	14.07	-.1	215.13	-.5
32	43.63	.7	102.68	.2	34.20	1.0	56.41	-.3	10.19	.2	14.58	.6	218.06	.6
33	43.02	.1	100.41	-1.0	33.83	.6	57.06	.1	9.87	-.3	13.62	-.8	214.79	-.6
34	43.37	.5	100.42	-1.0	32.92	-.2	55.64	-1.0	9.99	-.0	14.33	.2	213.30	-1.3
36	44.80	1.8	103.00	.4	33.30	.1	57.73	.6	9.57	-.9	14.20	.0	217.80	.5
37	43.54	.6	102.07	-.0	32.50	-.7	55.86	-.8	9.91	-.2	14.05	-.1	214.39	-.8
38	42.63	-.1	102.92	.4	33.57	.4	56.40	-.3	10.42	.7	13.81	-.5	217.12	.2
39	42.07	-.6	100.53	-1.0	32.86	-.3	55.08	-1.4	10.33	.5	14.27	.1	213.07	-1.4
40	42.81	-.0	102.47	.1	33.34	.1	57.43	.4	10.11	.1	13.80	-.5	217.15	.2
41	43.25	.4	103.19	.5	33.02	-.1	57.23	.2	9.50	-1.0	14.20	.0	217.14	.2
42	42.26	-.5	103.68	.8	33.03	-.1	56.66	-.1	10.05	.0	14.13	-.0	217.55	.4
43	42.91	.0	102.26	.0	33.12	-.0	56.26	-.4	10.02	-.0	14.00	-.2	215.66	-.3
46	42.71	-.0	100.61	-.9	32.62	-.5	57.49	.4	10.36	.6	13.59	-.9	214.67	-.7
47	43.08	.2	99.88	-1.4	31.33	-1.9	56.07	-.6	9.86	-.3	13.54	-1.0	210.68	-2.4
48	42.25	-.5	102.84	.3	32.79	-.4	56.37	-.4	10.40	.6	13.93	-.3	216.33	-.0
49	42.57	-.2	100.81	-.8	32.62	-.5	56.21	-.5	9.80	-.4	14.59	.6	214.03	-1.0
50	42.69	-.1	103.13	.5	32.51	-.7	57.07	.1	10.51	.8	14.10	-.0	217.32	.3
51	42.60	-.1	103.06	.5	33.40	.2	56.33	-.4	9.91	-.2	14.95	1.2	217.65	.4
52	42.17	-.6	103.86	.9	33.25	.0	56.79	-.0	9.78	-.5	14.69	.8	218.37	.7
53	43.63	.7	102.20	-.0	32.41	-.8	56.68	-.1	9.79	-.4	13.85	-.5	214.93	-.6
54	43.43	.5	102.90	.4	32.82	-.3	56.27	-.4	9.83	-.4	14.45	.4	216.27	-.0
55	43.07	.2	102.54	.1	32.86	-.3	56.12	-.6	9.82	-.4	14.16	.0	215.50	-.3
56	42.58	-.2	103.40	.7	33.60	.4	56.49	-.3	9.80	-.4	13.72	-.7	217.01	.2
57	43.25	.4	103.64	.8	34.32	1.1	58.42	1.2	10.14	.1	14.16	.0	220.68	1.7
58	42.46	-.3	102.90	.4	34.31	1.1	56.70	-.1	10.28	.4	13.93	-.3	218.12	.6
59	45.19	2.1	101.86	-.2	33.81	.6	56.86	-.0	10.10	.1	13.94	-.3	216.57	.0
MEAN	42.81 C/M		102.22		33.16		56.87		10.04		14.15		216.46	
S D	.834 C/M		1.190		.692		.810		.290		.394		2.319	
CF V	.0195		.0116		.0208		.0142		.0289		.0278		.0107	
ERMN	.1061 C/M		.1640		.0934		.1223		.0514		.0610		.2386	
CHISQ	59.24		51.72		54.06		42.59		30.95		40.30		92.36	

Table 43

Background variations in the RPY low background vault. 16-17 July 1964, all runs are 100-min, RIDL analyzer used, 3 x 5-in. crystal. The crystal is in a castle of lead bricks, the castle walls are 4 in. thick

Legend C/M = counts per minute in the selected energy band, N = number of measurements, T = time duration of measurements, DSIG = variation from the mean in units of the expected counting deviations at the ninety percent confidence level, SD = standard deviation of the observed counting rates, ERMN = expected counting error of the mean = SQRT (mean/(N*time)) CHISQ = chi square = for I=1,N (C/M(I) - mean)**2/(C/M(I)/1)

DATA PROCESSING JACK CORCORAN - PROGRAM 1839/RPY 3T2 F2 BACKGROUND ANALYSIS

CHANNELS	10 - 20		21 - 53		54 - 74		75 - 167		168 - 209		210 - 399		21 - 399	
ENERGY (MEV)	0 - .100		.100 - .400		.400 - .600		.600 - 1.3		1.3 - 1.6		1.6 - 3.0		.100 - 3.0	
RUN	C/M	DSIG	C/M	DSIG	C/M	DSIG	C/M	DSIG	C/M	DSIG	C/M	DSIG	C/M	DSIG
3	76.17	25.5	74.91	-1.0	23.23	.5	41.37	.7	6.82	-.6	8.25	.5	154.58	-.0
4	36.76	-2.7	76.51	.0	21.66	-1.4	40.70	.1	6.99	-.2	7.88	-.2	153.74	-.5
5	44.25	4.3	77.28	.6	23.88	1.3	40.54	.0	6.86	-.5	7.65	-.7	156.21	.7
6	44.64	4.6	75.72	-.4	22.41	-.4	40.20	-.3	7.50	.8	7.96	-.0	153.79	-.4
7	30.53	-9.8	76.50	.0	22.33	-.5	40.36	-.1	7.70	1.3	8.10	.2	154.99	.1
8	35.98	-3.5	76.48	.0	22.76	.0	41.16	.5	7.14	.0	7.83	-.3	155.37	.2
9	35.48	-4.1	76.72	.2	22.82	.0	40.30	-.2	6.72	-.8	7.94	-.0	154.50	-.1
10	31.77	-8.3	75.91	-.3	22.61	-.1	40.35	-.1	6.95	-.3	7.98	-.0	153.80	-.4
11	32.51	-7.4	76.78	.2	23.04	.3	40.04	-.4	7.10	.0	8.30	.6	155.26	.2
12	31.26	-8.9	77.27	.6	23.19	.5	40.44	-.0	7.53	.9	8.10	.2	156.53	.8
13	30.47	-9.9	75.27	-.7	22.78	.0	40.31	-.2	6.67	-1.0	8.04	.1	153.07	-.8
14	31.08	-9.1	77.28	.6	23.13	.4	41.36	.7	6.86	-.5	7.99	.0	156.62	.9
15	31.75	-8.3	76.37	-.0	22.19	-.7	40.67	.1	6.74	-.8	8.19	.4	154.16	-.2
16	42.93	3.1	77.99	1.0	22.50	-.3	39.00	-1.4	7.64	1.1	7.61	-.8	154.74	-.0
17	53.94	11.9	76.52	.0	22.85	.1	41.44	.8	7.07	-.0	8.05	.1	155.93	.5
18	42.57	2.8	74.77	-1.1	22.78	.0	40.22	-.2	7.26	.3	7.86	-.2	152.89	-.9
MEAN	39.50	C/M	76.39		22.75		40.52		7.09		7.98		154.76	
S D	11.913	C/M	.893		.504		.612		.337		.191		1.167	
CF V	.3015		.0116		.0221		.0151		.0475		.0240		.0075	
ERMN	.1571	C/M	.2185		.1192		.1591		.0665		.0706		.3110	
CHISQ	3917.19		15.74		16.81		13.98		23.61		6.96		13.20	

Table 44

Background variations at the bottom of the 35-ft shaft in the RPY vault. 13-15 July 1964, all runs are 100-min, RIDL analyzer used, 3 x 5-in. crystal. The crystal is in a castle of lead bricks, the castle walls are 4 in. thick

Legend C/M = counts per minute in the selected energy band, N = number of measurements, T = time duration of measurements, DSIG = variation from the mean in units of expected counting deviations at the ninety percent confidence level, SD = standard deviation of the observed counting rates, ERMN = expected counting error of the mean = SQRT (mean/(N*time)) CHISQ = chi square = for I=1,N (C/M(I) - mean)**2/(C/M(I)/1)

DATA PROCESSING JACK CORCORAN - PROGRAM 1839/RPY 3T2 F2 BACKGROUND ANALYSIS

CHANNELS	10 - 20		21 - 53		54 - 74		75 - 167		168 - 209		210 - 399		21 - 399	
ENERGY (MEV)	0 - .100		.100 - .400		.400 - .600		.600 - 1.3		1.3 - 1.6		1.6 - 3.0		.100 - 3.0	
RUN	C/M	DSIG	C/M	DSIG	C/M	DSIG	C/M	DSIG	C/M	DSIG	C/M	DSIG	C/M	DSIG
1	34.82	3.9	71.69	.2	19.72	-.7	38.96	-1.0	6.88	-.9	5.55	-.7	142.80	-1.0
2	29.11	-2.1	72.46	.8	20.18	-.1	38.79	-1.1	7.53	.5	5.75	-.2	144.71	-.0
3	29.26	-1.9	71.76	.3	20.05	-.3	38.87	-1.1	7.19	-.2	5.91	.1	143.78	-.5
4	28.67	-2.6	71.79	.3	20.20	-.1	39.28	-.7	6.92	-.8	5.75	-.2	143.94	-.4
5	29.82	-1.3	69.32	-1.4	20.56	.3	39.37	-.6	6.78	-1.2	5.62	-.6	141.65	-1.6
6	28.21	-3.2	71.78	.3	20.14	-.2	40.44	.4	7.66	.7	5.76	-.2	145.78	.4
7	28.72	-2.6	70.69	-.4	20.85	.7	39.99	-.0	7.24	-.1	6.05	.4	144.82	.0
8	29.20	-2.0	71.86	.3	20.70	.5	40.18	.1	7.09	-.4	5.66	-.5	145.49	.3
9	29.34	-1.9	71.75	.3	20.41	.1	39.67	-.3	7.10	-.4	5.48	-.9	144.41	-.1
10	31.39	.3	70.58	-.5	19.98	-.4	39.82	-.1	7.73	.9	5.73	-.3	143.84	-.4
11	35.82	4.8	71.80	.3	19.70	-.8	39.83	-.1	7.30	-.0	5.52	-.8	144.15	-.3
12	43.91	11.8	70.39	-.6	19.73	-.7	41.30	1.2	7.20	-.2	5.78	-.1	144.40	-.1
13	30.88	-.1	72.12	.5	20.49	.2	38.58	-1.4	7.48	.3	6.14	.6	144.81	.0
14	28.98	-2.3	71.50	.1	20.02	-.3	40.49	.4	6.98	-.7	5.46	-1.0	144.45	-.1
15	28.72	-2.6	70.45	-.6	20.12	-.2	40.13	.1	6.95	-.8	6.31	1.0	143.96	-.4
16	27.81	-3.7	71.38	.0	20.55	.3	40.26	.2	7.44	.3	5.95	.2	145.58	.3
17	28.52	-2.8	71.83	.3	19.99	-.4	40.01	-.0	7.15	-.3	6.07	.5	145.05	.1
18	29.18	-2.0	71.43	.0	20.71	.5	41.38	1.2	7.11	-.4	6.27	.9	146.90	1.0
19	28.31	-3.1	71.96	.4	19.85	-.6	40.54	.4	7.17	-.2	5.25	-1.6	144.77	-.0
20	28.04	-3.4	69.78	-1.1	21.05	.9	39.89	-.1	7.46	.3	5.69	-.4	143.87	-.4
21	28.70	-2.6	71.37	.0	20.74	.5	39.73	-.2	7.28	-.0	6.46	1.4	145.58	.3
22	33.38	2.4	70.59	-.5	19.83	-.6	40.26	.2	7.54	.5	6.11	.6	144.33	-.2
23	42.44	10.6	71.82	.3	20.70	.5	39.83	-.1	7.27	-.0	5.87	.0	145.49	.3
24	43.20	11.2	70.67	-.4	20.76	.6	40.27	.2	7.09	-.4	6.13	.6	144.92	.0
25	32.39	1.4	71.89	.4	20.51	.2	40.34	.3	7.06	-.5	6.01	.3	145.81	.5
26	32.31	1.3	71.88	.4	19.69	-.8	39.69	-.3	7.75	.9	6.19	.8	145.20	.2
27	33.80	2.8	71.20	-.0	19.71	-.8	40.06	.0	7.14	-.3	5.80	-.1	143.91	-.4
28	27.93	-3.5	69.79	-1.1	20.35	.0	41.32	1.2	7.60	.6	5.75	-.2	144.81	.0
29	31.77	.7	70.59	-.5	20.04	-.3	40.39	.3	7.40	.2	5.79	-.1	144.21	-.2
30	27.72	-3.8	72.11	.5	20.28	-.0	40.55	.5	7.21	-.2	5.98	.3	146.13	.6
31	27.83	-3.6	72.29	.6	20.80	.6	39.33	-.6	7.78	1.0	6.24	.9	146.44	.8
32	29.63	-1.5	71.24	-.0	20.51	.2	40.14	.1	7.91	1.3	5.64	-.5	145.44	.3
33	28.56	-2.8	72.25	.6	21.09	1.0	39.96	-.0	7.61	.6	5.63	-.5	146.54	.8
34	28.96	-2.3	71.49	.1	19.98	-.4	41.07	.9	7.55	.5	5.93	.1	146.02	.6
35	27.68	-3.8	71.90	.4	20.24	-.0	40.01	-.0	7.09	-.4	5.68	-.4	144.92	.0
0	32.20	1.2	70.10	-.8	20.40	.1	39.90	-.1	7.20	-.2	6.00	.3	143.60	-.6
MEAN	31.03 C/M		71.31		20.29		40.01		7.30		5.85		144.79	
S D	4.274 C/M		.794		.402		.668		.280		.271		1.069	
CF V	.1377		.0111		.0198		.0167		.0384		.0463		.0073	
ERMN	.0928 C/M		.1407		.0750		.1054		.0450		.0403		.2005	
CHISQ	1680.42		31.26		27.88		39.12		37.44		43.97		27.75	

Table 45

Observed values and limits for chi squared

Location	Basement		Underground vault		Foot of 35-ft shaft	
No. of runs	38		16		36	
Energy band	χ^2	$P(\chi^2)$	χ^2	$P(\chi^2)$	χ^2	$P(\chi^2)$
100-400 keV	51.7	0.05	15.7	0.39	31.3	0.65
400-600 keV	54.1	0.03	16.8	0.33	27.9	0.80
0.6-1.3 MeV	42.6	0.25	14.0	0.52	39.1	0.3
1.3-1.6 MeV	30.95	0.75	23.6	0.07	37.4	0.36
1.6-3.0 MeV	40.3	0.33	7.0	0.96	44.0	0.14
0.1-3.0 MeV (Total)	92.4	~0.00	13.2	0.59	27.7	0.80
90% Probability	52.0	0.05	25.0	0.05	49.0	0.05
Limits	23.8	0.95	7.26	0.95	22.0	0.95

Neglecting the figures for the total energy span covered, since these are not independent of the individual energy band results, it is apparent that only three of the fifteen χ^2 values are suspiciously high. Two of these are with the detector in the basement, where fluctuations outside of statistics would be most expected. The fact that both are below 600 keV suggests that the fluctuations may be caused by variations in the ambient radon, which in this location is in equilibrium with the outside air. Fluctuations of the two energy bands are well correlated during successive time intervals, but show no significant increase at night, as might result from radon build-up near the ground during a strong temperature inversion. The lack of such a trend is not, however, inconsistent with the meteorological conditions during the counting period.

While the evidence is preliminary and subject to revision when more extensive data are obtained under better-controlled conditions, we are led to conclude that a real improvement in the stability of the gamma-ray background has been demonstrated, due to reduced radon levels and fluctuations therein within the vault. Further experiments are planned to see if differences in cosmic-ray-induced fluctuations are detectable.

References

1. May, Harold, and L. D. Marinelli. Cosmic Ray Contribution to the Background of Low Level Scintillation Spectrometers. Natural Radiation Environment, Proc. Intern. Symp. on the Natural Radiation Environment, Rice University, Houston, Texas, April 11-13, 1963, Ed. J. A. S. Adams and W. M. Lowder (Univeristy of Chicago Press, Chicago, 1964. pp. 463-480.

2. Marion, J. B., and J. L. Fowler, Eds. Fast Neutron Physics. Interscience Publishers, New York, 1960. Vol. 1, p. 362.

3. May, Harold. Neutron Production in Massive Shields and Effect Upon the Low-Energy Gamma-Ray Background. Argonne National Laboratory Radiological Physics Division Semiannual Report, January through June, 1962. ANL-6646, p. 62.

4. Rossi, H. High Energy Particles. Prentice-Hall, New York, 1952. p. 32.

MULTICHANNEL ANALYZER DATA PROCESSING ON THE CDC 160-A COMPUTER

J. B. Corcoran

The use of multichannel analyzers in the Radiological Physics Division has increased steadily over the years of their availability. Certain applications such as gamma-ray spectroscopy have evolved to a considerable degree of sophistication, resulting in high rates of data production and often using large-scale computers to analyze the data. Newer applications have steadily developed, some of which bear no resemblance to the usual pulse-height mode of operation. These newer applications differ widely in their data-processing requirements. Some need only modest arithmetical operations that can be done on a small computer or by hand, if necessary. Others are in various interim stages of developing analytical techniques that will eventually utilize computers. Some of the fledgling developments want nothing more than a print-out of the contents of the analyzer memory.

Although the individual uses of multichannel analyzers vary widely, some aspects of their data processing are common to many or all. All of the analyzers in the Radiological Physics Division include punched paper tape output devices. All require error checking of this paper tape. Almost all need a print-out of the data as it appears on the paper tape or after arithmetical operations such as dividing by time, subtracting background, etc. Many call for some sort of graphic representation of the data. In practice, numerous other details of data processing consistently recur, oftentimes in unrelated applications.

These considerations, together with the necessity of coping with the prodigious quantities of data coming out of these instruments, have led to the development within the Division of an organized approach to multichannel analyzer data processing through a system for generating special-purpose computer programs. The system, referred to hereafter as 1839/RPY, is designed with versatility and flexibility as its primary features. It is intended to provide the full range of computer facilities to any multichannel analyzer application, regardless of the anticipated volume or the stage of development of the applications. New or revised programs can be produced quickly and with a minimum of additional programming effort.

All 1839/RPY programs use the Control Data Corp. 160-A computer, which has a high-speed paper tape reader (350 frames/sec), and a wide variety of peripheral equipment including a paper tape punch, input-output typewriter, punched card reader, card punch, high-speed printer, magnetic tape units, and X-Y plotter. All of this equipment is utilized by one section or another of the 1839/RPY system to provide the

desired versatility of operation. The computer's comparatively small memory is the principal limitation to its use in processing multichannel analyzer data. However, where a large computer is required, the paper-tape data are transcribed to magnetic tape on the CDC 160-A, and the magnetic tape fed to the larger computer.

The 1839/RPY system consists basically of three parts, 1) a LIBRARY of subroutines on a reel of magnetic tape, 2) an EDIT program which allows a subroutine on the library tape to be replaced by a revised version and also allows new subroutines to be added to the library, and 3) an ASSEMBLY program which extracts selected subroutines from the library tape and assembles them into a working program.

The LIBRARY consists of three general types of subroutines, READ, ARITHMETIC, and OUTPUT.

READ subroutines are written for a specific format paper tape. They give the read commands to the paper tape reader, do extensive error checking of the paper tape data (keeping a tally of any errors encountered) and store the data in a designated gross-data storage area of the computer memory. This section of the memory is allocated a maximum of 512 six-digit numbers. A lesser number of channels is stored as a subset, and a five digit number is stored as a six-digit number with a leading zero. This gross data storage method allows all arithmetic subroutines and many output subroutines to apply to data from any analyzer. The limited memory space of the 160-A restricts the 1839/RPY system to analyzers of 512 or fewer channels.

An individual READ subroutine is written for each different format paper tape in use in the division. It is comparatively little work to write a separate read routine for each type of analyzer, but it would be technically infeasible to modify the electronics of the various analyzers to punch out a common format paper tape.

ARITHMETIC subroutines perform operations such as dividing by the time duration of the run to reduce each channel to counts per minute, subtracting background, summing the net counts in selected groups of channels, etc.

OUTPUT subroutines either print out the information or prepare it for further processing by another program or computer. These subroutines include printing out the gross and/or net data, printing out the subgroup totals, writing the data onto magnetic tape, and punching the subgroup sums on cards. The punched card output is usually used as input data for special-purpose programs written in FORTRAN for the 160-A or similar small computers. The magnetic tape output is usually the input data for the more analytical programs on the larger computers, such as least squares fitting.

The ASSEMBLY program is the means by which a data-processing program is assembled from the subroutines on the library tape.

The assembly program is loaded into the 160-A computer and the library tape positioned on a magnetic tape unit. The input to the assembly program consists of punched cards that designate the library subroutines desired, instructions for the STOP and JUMP switches on the computer console, and page heading legends for the print-out sheets. This input is fed to the assembly program, which assembles the data processing program and punches it out in machine language on paper tape (equivalent to a binary deck), which is labeled and filed. In subsequent use of the program, the machine language is loaded into the 160-A from the paper tape, making it unnecessary to repeat the assembly routine. The console switches provide a selection of data-processing options and the means of halting the program between data runs.

STACK PLUME RISE DETERMINATIONS AS AFFECTED BY METEOROLOGICAL AND ENGINEERING FACTORS

Harry Moses, Gordon H. Strom,* and James E. Carson

Introduction

When estimating downwind ground concentrations resulting from the emission of a gaseous stack effluent, the effective stack height must be known. Under many, but not all, meteorological conditions, ground level concentrations may be calculated to an acceptable degree of accuracy by means of one of the well-known diffusion formulas, such as those of Bosanquet and Pearson;[1] Sutton;[2] Cramer, Record, and Vaughan;[3] or Gifford.[4] The latter two are modifications of Sutton's formula. The effective stack height is usually defined as the actual stack height plus the height of plume rise above the stack due to the effluent's buoyancy and momentum. Also, as discussed by Wippermann and Klug,[5] in problems where a minimum stack height must be determined to prevent ground concentrations above a permissible level, information on plume rise is essential.

Recent literature shows that investigators in the United States and abroad have proposed no less than fifteen formulas for calculating plume rise.[6-20] None has been universally accepted, primarily because it has been impossible to establish the validity of any one from the quality and quantity of available plume-rise and meteorological data. The paucity of acceptable data is due to the difficulties inherent in carrying out satisfactory measurements; nevertheless, investigation of the factors controlling plume rise is of such importance that increased effort in this area is warrented. With more data, decisions concerning the selection of stack heights and other stack parameters to minimize concentrations of noxious materials over residential or other critical areas will be made with more confidence and will have greater validity.

Height-of-Rise Formulas

Of the many formulas for calculating plume rise appearing in the literature, some are based on theoretical foundations, while others are strictly empirical. Even those which are considered theoretical base one or more parameters on experimental data obtained in the wind tunnel, in the laboratory, or in the field. This paper discusses in detail three of the most widely used formulas. Two are completely empirical: the Davidson-Bryant[9] and the Holland[10] formulas. The Bosanquet[7] formula is semi-empirical.

*Professor of Aeronautics and Astronautics, New York University, New York.

As expected, each author uses his own notation in presenting his formula. To facilitate comparison and to serve as an aid in later discussions of this paper, the uniform set of symbols presented below has been adopted.

Δh	Computed rise of the plume center line above the stack
Δh_{obs}	Observed plume rise
h	Stack height
d	Inside diameter of stack
V_s	Mean stack effluent velocity
U	Mean horizontal wind speed
ΔT	Temperature excess of effluent gas over ambient air (°K)
T_s	Stack gas temperature (°K)
C_p	Specific heat of effluent at constant pressure
C_{pa}	Specific heat of ambient air at constant pressure
m	Molecular weight of effluent
m_a	Molecular weight of air
P	Ambient pressure
P_{std}	Standard pressure = 760 mm of Hg
ρ	Density of effluent (actual)
ρ_0	Density of effluent at standard temperature and pressure
T_0	273°K = standard temperature
C	Bosanquet diffusion coefficient (assumed equal to 0.13)
g	Acceleration of gravity
t	Time
Q	Volume of stack gas emitted per second
Q_H	Heat emission rate in g-cal/sec
Q_H'	Heat emission rate in megawatts
L	Horizontal distance from point of emission
θ	Potential temperature (°K)
Z	Vertical height coordinate
G	Vertical gradient of potential temperature = $\frac{\partial \theta}{\partial Z}$ in °K/meter

χ_{max}	Maximum ground concentration of contaminant in units of mass per unit volume. The maximum is with respect to horizontal distance from the stack.
$(\chi_{max})_{max}$	Maximum ground concentration of contaminant in units of mass per unit volume. The maximum is with respect to both horizontal distance from the stack and wind speed.
x_{max}	Downwind distance at which χ_{max} is observed
S	Source strength in units of mass/sec
e	Base of Napierian logarithms = 2.7183
π	3.1416
C_z	Sutton's vertical diffusion coefficient
C_y	Sutton's horizontal diffusion coefficient
n	Another Sutton diffusion coefficient
Δh_{cal}	Calculated plume rise as used in Stümke's analysis with no correction applied
Δh^*_{cal}	Calculated plume rise with Stümke's[17] correction applied
N	Number of observations
K	Stümke correction factor (see Equation 15)
C_θ, C_J, μ, λ, ν	Adjustable Stümke parameters

The Davidson-Bryant Formula

Using Bryant's wind-tunnel data,[21] Davidson[9] suggests the formula

$$\Delta h = d\left(\frac{V_s}{U}\right)^{1.4}\left(1+\frac{\Delta T}{T_s}\right). \qquad (1)$$

Any consistent system of units may be used.

Davidson states that the factor $(V_s/U)^{1.4}$ is in fair agreement with Bryant's experimental data on plume rise due to momentum. To account for rise due to buoyancy, Davidson proposes using the multiplying factor $\left(1+\frac{\Delta T}{T_s}\right)$. He further indicates that this formula should be applied to "stacks of moderate or great height" but does not define these terms.

The Holland Formula

Rupp, Beall, Bornwasser, and Johnson[14] give the height of rise of a chimney effluent without bouyancy as

$$\Delta h = 1.5\, d \frac{V_s}{U} \tag{2}$$

based on wind tunnel experiments using ammonium chloride as a tracer. Holland,[10] using photographs of plumes of three power stations, modifies this relation by adding a buoyancy term to bring into closer agreement calculated and observed plume rises. The Holland formula is

$$\Delta h = \frac{1.5\, d\, V_s + 4 \times 10^{-5}\, Q_H}{U} \tag{3}$$

where Δh and d are in meters, V_s and U are in meters per second and Q_H is the heat emission rate in gram calories/sec. Assuming standard atmospheric pressure (760 mm of mercury) and that the effluent has the same molecular weight and specific heat as air, the formula simplifies to

$$\Delta h = 1.5 \frac{V_s}{U} d \left(1 + 1.8 \frac{\Delta T}{T_s} d\right). \tag{4}$$

For other pressures, and effluents of other molecular weights, or specific heats, one may use the formula

$$\Delta h = 1.5 \frac{V_s}{U} d \left(1 + 1.8 \frac{C_p}{C_{pa}} \times \frac{P}{P_{std}} \times \frac{m}{m_a} \times \frac{\Delta T}{T_s} \times d\right). \tag{5}$$

The stack and experimental effluent data upon which Holland's formula is based are shown in Table 46.

Since the height of plume rise depends on atmospheric stability as well as on the parameters given in the equation, Holland suggests that 10 to 20 per cent of the rise given by the equation be added for unstable and an equal amount subtracted for inversion conditions.

Davidson presents no field data in his original paper, but Holland does. Both formulas have been criticized on the grounds that they are empirical. Since they are both empirical, they should not be applied to ranges of variables outside those used in their formulation. Holland's formula has been further criticized because it is dimensionally incorrect, unless the constant modifying Q_H has dimensions.

Table 46

Stack, effluent, and meteorological parameters
for effective stack height
(Investigation by Holland)

	X-10 pile	X-10 steam plant	Watts bar steam plant
Stack height, m	61	55	49
Stack orifice diameter, m	1.75	2.75	4.27
Exit velocity, m/sec	20.1	2.2	15.2
Exit temperature, °K	355	478	450
Volume emission rate, m^3/sec	51.9	12.8	141.6
Heat emission rate, cal/sec	830 000	710 000	6 600 000
Wind speeds:*			
0.4-2.7 mps	4	19	69
3.1-6.7 mps	4	14	24
7.2-9.4 mps	3		
Temperature lapse*	10	18	42
Temperature inversion*		16	51

*Number of observations.

The Bosanquet Procedure

Bosanquet, Carey, and Halton[6] published a technique for calculating height of plume rise which has received wide attention and use. Nonhebel[22] reported that the Beaver Committee in England[23] applied this formula to stack data and found that it gave too high a thermal rise for large plants. Bosanquet was asked to re-examine his original calculations and published a revised technique[7] which is described below.

Bosanquet first considered the rise of a "cold" plume, i.e., one whose density is the same as that of the ambient air. The height of rise when $V_s/U > 0.48$ is given as

$$\Delta h = \frac{\left(\frac{2}{3} Q V_s\right)^{1/2}}{C\pi^{1/2} U}\left\{1.311 - \frac{0.615}{\left[\left(\frac{V_s}{U}\right)^2 + 0.57\right]^{1/2}}\right\}$$

$$= \frac{\left(\frac{2}{3}\frac{\pi d^2}{4} V_s^2\right)^{1/2}}{C\pi^{1/2} U}\left\{1.311 - \frac{0.615}{\left[\left(\frac{V_s}{U}\right)^2 + 0.57\right]^{1/2}}\right\} \qquad (6)$$

$$= 3.14\, d \frac{V_s}{U}\left\{1.311 - \frac{0.615}{\left[\left(\frac{V_s}{U}\right)^2 + 0.57\right]^{1/2}}\right\}.$$

For values of $\frac{V_s}{U} < 0.48$

$$\Delta h = \frac{\left(\frac{2}{3} Q V_s\right)^{1/2}}{C\pi^{1/2} U} \times 0.9 \left(\frac{V_s}{U}\right)^{1/2}$$

$$= \frac{\left(\frac{2}{3} \pi \frac{d^2}{4} V_s^2\right)^{1/2}}{C\pi^{1/2} U} \times 0.9 \left(\frac{V_s}{U}\right)^{1/2}$$

$$= 2.83\, d \left(\frac{V_s}{U}\right)^{1.5} \tag{7}$$

where Q is the volumetric flow rate in m^3/sec and C is a diffusion coefficient and assumed equal to 0.13.

If the density of the effluent is less than that of the atmosphere at the point of emission, Bosanquet gives the relation

$$\Delta h = A\, U \left\{ f_I(X) + f_{II}(X_0) - \frac{0.615\, X_0^{1/2}}{\left[\frac{V_s^2}{U} + 0.57\right]^{1/2}} \right\} \tag{8}$$

where

$$A = \frac{1}{2\pi C^2} \frac{g\, Q\, \Delta T}{T\, U^4} \tag{9}$$

$$X = \frac{t + t_0}{A} \tag{10}$$

$$X_0 = \frac{t_0}{A} \tag{11}$$

$$t_0 = \frac{4\, V_s\, T}{3\, g \Delta\, t} \tag{12}$$

$$t = \frac{L}{U} \tag{13}$$

where g is the acceleration of gravity, L is the horizontal distance from the point of emission to the point where Δh is measured, and t is the time needed

for an element of plume to travel from the stack to the distance L. Equation 8 gives the height of the plume center line above stack height as a function of travel distance, L; it does not necessarily give the maximum rise.

Bosanquet has presented tables of $f_I(X)$ and $f_{II}(X_0)$, where the quantities X and X_0 are calculated from the stack and meteorological measurements. Tables 47 and 48 of this report are taken directly from

Table 47

Values of $f_I(X)$

X	$f_I(X)$	X	$f_I(X)$	X	$f_I(X)$	X	$f_I(X)$	X	$f_I(X)$	X	$f_I(X)$	X	$f_I(X)$
0.0010	0.0059	0.010	0.0323	0.10	0.170	1.0	0.767	10	2.33	100	4.50	1000	6.79
0.0012	0.0067	0.012	0.0370	0.12	0.193	1.2	0.852	12	2.49	120	4.68	1200	6.97
0.0014	0.0075	0.014	0.0414	0.14	0.215	1.4	0.930	14	2.64	140	4.83	1400	7.13
0.0016	0.0083	0.016	0.0456	0.16	0.235	1.6	1.00	16	2.75	160	4.97	1600	7.26
0.0018	0.0091	0.018	0.0497	0.18	0.255	1.8	1.07	18	2.86	180	5.08	1800	7.38
0.0020	0.0098	0.020	0.0537	0.20	0.274	2.0	1.13	20	2.95	200	5.19	2000	7.48
0.0025	0.0116	0.025	0.0632	0.25	0.319	2.5	1.27	25	3.16	250	5.41	2500	7.71
0.0030	0.0133	0.030	0.0721	0.30	0.360	3.0	1.39	30	3.33	300	5.59	3000	7.89
0.0035	0.0149	0.035	0.0806	0.35	0.398	3.5	1.50	35	3.48	350	5.74	3500	8.04
0.0040	0.0164	0.040	0.0887	0.40	0.434	4.0	1.59	40	3.61	400	5.88	4000	8.18
0.0045	0.0179	0.045	0.0965	0.45	0.469	4.5	1.68	45	3.72	450	5.99	4500	8.29
0.0050	0.0194	0.050	0.104	0.50	0.501	5.0	1.76	50	3.82	500	6.10	5000	8.40
0.0060	0.0222	0.060	0.119	0.60	0.562	6.0	1.90	60	4.00	600	6.28	6000	8.58
0.0070	0.0249	0.070	0.132	0.70	0.619	7.0	2.03	70	4.15	700	6.43	7000	8.74
0.0080	0.0274	0.080	0.145	0.80	0.671	8.0	2.14	80	4.28	800	6.57	8000	8.87
0.0090	0.0299	0.090	0.158	0.90	0.720	9.0	2.24	90	4.40	900	6.69	9000	8.99
0.0100	0.0323	0.100	0.170	1.00	0.767	10.0	2.33	100	4.50	1000	6.79	10000	9.09

Table 48

Values of $f_{II}(X_0)$

X	$f_{II}(X_0)$	X	$f_{II}(X_0)$	X	$f_{II}(X_0)$	X	$f_{II}(X_0)$	X	$f_{II}(X_0)$	X	$f_{II}(X_0)$	X	$f_{II}(X_0)$
0.0010	-0.0028	0.010	-0.0138	0.10	-0.044	1.0	0.155	10	1.99	100	9.9	1000	37.0
0.0012	-0.0032	0.012	-0.0156	0.12	-0.045	1.2	0.212	12	2.28	120	11.1	1200	40.9
0.0014	-0.0036	0.014	-0.0172	0.14	-0.046	1.4	0.269	14	2.58	140	12.2	1400	44.5
0.0016	-0.0039	0.016	-0.0186	0.16	-0.046	1.6	0.380	16	2.88	160	13.2	1600	47.8
0.0018	-0.0043	0.018	-0.0200	0.18	-0.045	1.8	0.325	18	3.15	180	14.1	1800	50.9
0.0020	-0.0046	0.020	-0.0213	0.20	-0.043	2.0	0.43	20	3.41	200	15.0	2000	53.8
0.0025	-0.0054	0.025	-0.0242	0.25	-0.037	2.5	0.56	25	4.01	250	17.1	2500	60.6
0.0030	-0.0061	0.030	-0.0268	0.30	-0.030	3.0	0.69	30	4.56	300	19.0	3000	66.8
0.0035	-0.0068	0.035	-0.0291	0.35	-0.020	3.5	0.80	35	5.07	350	20.7	3500	72.4
0.0040	-0.0075	0.040	-0.0312	0.40	-0.010	4.0	0.91	40	5.54	400	22.3	4000	77.7
0.0045	-0.0081	0.045	-0.0331	0.45	0.002	4.5	1.02	45	6.00	450	23.9	4500	82.6
0.0050	-0.0087	0.050	-0.0347	0.50	0.014	5.0	1.12	50	6.43	500	25.3	5000	87.4
0.0060	-0.0099	0.060	-0.0375	0.60	0.041	6.0	1.32	60	7.24	600	28.0	6000	96.1
0.0070	-0.0110	0.070	-0.040	0.70	0.068	7.0	1.50	70	7.98	700	30.5	7000	104.1
0.0080	-0.0120	0.080	-0.042	0.80	0.096	8.0	1.67	80	8.68	800	32.8	8000	111.6
0.0090	-0.0129	0.090	-0.043	0.90	0.125	9.0	1.84	90	9.33	900	35.0	9000	118.6
0.0100	-0.0138	0.100	-0.044	1.00	0.155	10.0	1.99	100	9.95	1000	37.0	10000	125.3

Bosanquet's paper. The height of plume rise may then be determined from Equation 8. Values of $f_I(X)$ and $f_{II}(X_0)$ when the arguments X and X_0 are outside the limits of Tables 47 and 48 may be determined from the following expressions:

When X is very large

$$f_I(X) = \ln X - 0.12, \tag{14}$$

when X is very small

$$f_I(X) = 1.054\ X^{3/4}. \tag{15}$$

When X_0 is very large

$$f_{II}(X_0) = 1.311\ X_0^{1/2} - \frac{1}{2} \ln X_0 - 1, \tag{16}$$

and when X_0 is very small

$$f_{II}(X_0) = -0.527\ X_0^{3/4}. \tag{17}$$

In a stable atmosphere, the maximum plume rise may be determined by assigning a value to $t + t_0$ by means of the expression

$$t + t_0 = 1.527 \left(\frac{2T}{gG}\right)^{1/2} \tag{18}$$

where G is the gradient of potential temperature in (°K/m). If $t + t_0$ is greater than 200 sec, the value of 200 should be used; if $t + t_0$ is equal to or less than 200, the actual value should be used.

Empirical Correction Factor

The most extensive comparative study to date is given by Stümke,[17] who tested eight formulas with observed plume rises from three large stacks, two in Germany and one in England (see Comparison of Formulas, below).

In an attempt to reduce the difference between observed and calculated values, Stümke determined a multiplying factor, K, for each of the formulas in the following way:

Let Δh_{cal} represent the height of rise calculated by a given formula and Δh_{obs} the observed rise. Then K is defined by the relation

$$\frac{1}{K} = \frac{1}{N} \sum \frac{\Delta h_{cal}}{\Delta h_{obs}} \tag{19}$$

when N is the number of observations. If we let Δh^*_{cal} represent the calculated rise after applying the K factor, then

$$\Delta h^*_{cal} = K \, \Delta h_{cal} \tag{20}$$

and

$$\frac{1}{N} \sum \frac{\Delta h^*_{cal}}{\Delta h_{obs}} = 1. \tag{21}$$

For example, Holland's formula becomes

$$\Delta h^*_{cal} = \frac{K (1.5 \, V_s \, d + 4 \times 10^{-5} \, Q_H)}{U} \tag{22}$$

and when K = 2.92, the value determined by Stümke for Holland's formula,

$$\Delta h^*_{cal} = \frac{4.38 \, V_s \, d + 11.7 \times 10^{-5} \, Q_H}{U} \tag{23}$$

The K factor is essentially a type of regression coefficient between Δh_{cal} and Δh_{obs}. Since the K values given by Stümke (see Table 49) are based on data from only 3 stacks, their validity for other stacks awaits tests with further measurements.

Table 49

Values of Stümke's K factor

Investigators \ Formula	Davidson-Bryant	Holland	Bosanquet
Moses & Strom	1.63	1.86	0.75
Stümke	6.69	2.92	0.75
Rauch	-	3.09	-

A different modification to Holland's formula is suggested by Thomas[19] based on measurements of plume rise taken at the Johnston Steam Plant of the Tennessee Valley Authority in the U.S.A. Thomas found that values provided by Holland's formula are too low, and proposes that the buoyancy factor be doubled. Holland's formula is then modified to read

$$\Delta h = \frac{1.5\ V_s\ d + 8 \times 10^{-5}\ Q_H}{U} . \qquad (24)$$

Worked Example

To illustrate the use of each of the above formulas, the following worked example based on an actual run at Duisburg, Germany, on September 16, 1959, is presented.

The observed data are:

V_s = stack effluent velocity = 11.53 m/sec

d = stack diameter = 3.5 m, then

Q = volumetric flow rate = $\frac{\pi d^2}{4} V_s$ = 110.93 m^3/sec

T = ambient air temperature = 291°K

T_s = effluent temperature = 405°K

ΔT = difference between ambient air temperature and stack gas temperature = 114°K

g = acceleration of gravity = 9.8 m/sec^2

C = Bosanquet's diffusion coefficient = 0.13

U = average wind velocity = 7.32 m/sec

L = distance from stack = 500 m

Δh_{obs} = observed height of rise = 68.0 m.

1) Davidson-Bryant Calculation

$$\Delta h_{cal} = d\left(\frac{V_s}{U}\right)^{1.4}\left(1 + \frac{\Delta T}{T_s}\right)$$

$$= 3.5\left(\frac{11.53}{7.32}\right)^{1.4}\left(1 + \frac{114}{405}\right)$$

$$= 8.5 \text{ m.}$$

2) Holland Calculation

$$\Delta h = \frac{1.5\ V_s\ d + 4 \times 10^{-5}\ Q_H}{U} = \frac{1.5\ (11.53)(3.5) + 4 \times 10^{-5}\ (2.65) \times 10^6}{7.32}$$

$$Q_H = \rho \frac{\pi d^2}{4} V_s\ C_p\ \Delta T = \frac{\rho_0 T_0}{T_s} \frac{\pi d^2}{4} V_s\ C_p\ \Delta T = \frac{1293 \times 273}{405} \frac{\pi d^2}{4} V_s\ C_p\ \Delta T = 2.65 \times 10^6$$

Δh_{cal} = 23 m.

3) Bosanquet's Formula

$$t_0 = \frac{4}{3}\frac{V_s\ T}{g\ \Delta T} = \frac{4}{3}\cdot\frac{11.53 \times 291}{9.8 \times 114} = 3.99$$

$$t = \frac{L}{U} = \frac{500}{7.32} = 68.31$$

$$t + t_0 = 72.30$$

$$A = \frac{1}{2\pi\ C^2}\frac{g\ Q\ \Delta T}{T\ U^4} = \frac{9.8}{2(3.1416)(0.13)^2}\frac{110.93 \times 114}{291(7.32)^4} = 1.40$$

$$X_0 = \frac{t_0}{A} = \frac{3.99}{1.40} = 2.85$$

$$X = \frac{t + t_0}{A} = \frac{72.30}{1.40} = 51.64$$

$$f_I(X) = 3.85 \text{ (from Table 47)}$$

$$f_{II}(X_0) = 0.65 \text{ (from Table 48)}$$

$$\Delta h = A\ U\left\{f_I(X) + f_{II}(X_0) - \frac{0.615\ X_0^{1/2}}{\left[\left(\frac{V_s}{U}\right)^2 + 0.57\right]^{1/2}}\right\}$$

$$= 1.4\ (7.32)\left\{3.85 + 0.65 - \frac{0.615\ (2.85)^{1/2}}{\left[\left(\frac{11.53}{7.32}\right)^2 + 0.57\right]^{1/2}}\right\}$$

$$= 40.0 \text{ m.}$$

The variability of Δh_{cal} shown in this case is not at all atypical. In this example, the Bosanquet's formula is nearest the correct value, but all three (two grossly) underestimate the observed Δh.

The values of Δh^*_{cal} (computed with Stümke's K correction factor) are

$$\Delta h^*_{cal} = K\ \Delta h_{cal} = (6.69)(8.5) = 56.9 \text{ m (Davidson-Bryant).}$$

$$\Delta h^*_{cal} = K\,\Delta h_{cal} = (2.92)(23.0) = 67.1 \text{ m (Holland).}$$

$$\Delta h^*_{cal} = K\,\Delta h_{cal} = (0.75)(40.0) = 30.0 \text{ m (Bosanquet).}$$

It can be seen that the value given by Bosanquet is now less accurate than before, while the values of the other two are closer to the observed height.

Definition of Height of Rise

The height of rise has been defined differently by the various authors; this lack of uniformity is reflected in the formulas and computed heights.

Davidson[9] indicates that his formula refers to a point when the plume slope is less than 0.1. Holland[10] indicates very generally that the height of rise may be considered as the height at which the plume levels off. Bosanquet[7] indicates the height of rise is the height at which the effects due to the emission, i.e., buoyancy and momentum, have died away. The point at which this is reached may be determined from Equation 18. Authors, such as Priestley,[13] Scorer,[16] or Sutton[18] use other criteria.

Critical Wind Speed

According to Sutton,[2] the maximum concentration at the ground from a point source such as a stack at height h is

$$\chi_{max} = \frac{2S}{\pi e}\,\frac{1}{Uh^2}\,\frac{C_z}{C_y} \tag{25}$$

where S is the mass of material emitted per second, χ_{max} the concentration in mass per unit volume, U is the wind speed, and C_z and C_y are Sutton's diffusion coefficients, and e and π have their usual values, 2.7183 and 3.1416, respectively. If we take into account the effective stack height, which is the actual height plus the plume rise, then this equation becomes

$$\chi_{max} = \frac{2S}{\pi e}\,\frac{1}{U(h+\Delta h)^2}\,\frac{C_z}{C_y}. \tag{26}$$

The concentration, χ_{max}, represents the maximum with respect to the horizontal distance from the source. The magnitude of χ_{max} is a function of wind speed and effective stack height as shown in Equation 26. By substituting the expression for Holland's formula in Equation 26, differentiating χ_{max} with respect to U, and setting $(\partial \chi_{max})/\partial U = 0$, we find a double maximum for the concentration, i.e., a maximum with respect to horizontal distance from the source as well as a maximum with respect to wind speed. To illustrate, let

$$B = 1.5\ V_s\, d + 4 \times 10^{-5}\ Q_H \tag{27}$$

Holland's formula for plume rise then becomes

$$\Delta h = \frac{1.5\ V_s\, d + 4 \times 10^{-5}\ Q_H}{U} = \frac{B}{U} \tag{28}$$

and

$$\chi_{max} = \frac{2S}{\pi e}\frac{C_z}{C_y}\frac{1}{U\left(h+\frac{B}{U}\right)^2} \tag{29}$$

Upon differentiating χ_{max} with respect to U and setting $(\partial\chi_{max})/\partial U = 0$, χ_{max} has a maximum when $U = B/h$. This value of U is called the "critical wind speed" by Hawkins and Nonhebel.[24] Substituting $U = B/h$ in Equation 29, we have

$$(\chi_{max})_{max} = \frac{S}{2\pi e}\frac{C_z}{C_y}\frac{1}{Bh} \tag{30}$$

In deriving Equation 30 it was assumed that the ratio C_z/C_y is independent of wind speed. This assumption is not strictly valid, but may serve as an approximation. Thomas[19] points out that his field measurements have verified this expression.

According to Sutton's formula for atmospheric diffusion, the horizontal distance at which maximum concentration occurs is

$$\chi_{max} = \left(\frac{h}{C_z}\right)^{2/(2-n)} \tag{31}$$

When the plume rise is added, Equation 26 becomes

$$\chi_{max} = \left(\frac{h+\Delta h}{C_z}\right)^{2/(2-n)} \tag{32}$$

Obviously, the distance at which the maximum occurs is farther away from the stack and χ_{max} is lower when the plume rise is included. In assessing the hazard or nuisance expected from a given stack an examination of climatological wind records would be most useful in determining the frequency with which $(\chi_{max})_{max}$ values are expected in a given direction.

Factors Affecting Plume Rise

Properties of the Plume

Whether the effluent is gaseous or contains particulates determines, in part, the concentration of materials reaching the ground. Particulates having a diameter of less than 20 μ, i.e., having a fall velocity of the order of 1-2 cm/sec, may be considered as gaseous. In this paper, only plumes having gaseous characteristics are considered.

Two other properties of the plume, momentum and buoyancy, substantially affect ground concentrations. Buoyancy may be either positive or negative. Plumes having negative buoyancy are denser and usually colder than the surroundings and will fall to the ground more rapidly. It is to be noted that the reduction in pressure due to aerodynamic effects in the lee of a stack or associated building will also cause the plume to descend even though it has positive buoyancy. The plume rise equations may be modified to handle true negative buoyancy in the plumes, but the authors are not aware of such measurements appearing in the literature.

A plume with positive buoyancy will rise above the stack top, and its lower edge will come to the ground after a longer time and at a greater distance from the stack than in the previous case. The resulting ground concentrations are therefore appreciably less.

Meteorological Conditions

The two meteorological factors of importance in determining the behavior of the smoke plume are: 1) wind, which includes turbulent fluctuations in speed and direction as well as the mean speed and direction, and 2) stability. Under light wind conditions, plumes such as those associated with power-generating plants, which have considerable amounts of momentum and positive buoyancy, will rise tens to hundreds of meters above the stack. Under stronger wind conditions, the plume levels off more quickly. The exact relation between plume rise and wind speed has not yet been determined: in the Holland formula[10] it may be seen that the plume rise varies as $(1/U)$; in the Davidson-Bryant technique[9] it varies as $(1/U)^{1.4}$. In the Bosanquet procedure[7] for cold plumes with values of V_s/U less than 0.48, the plume rise varies as $(1/U)^{1.5}$; when $V_s/U > 0.48$, the relation is not simple. In Bosanquet's formula with buoyancy the variation of Δh with wind is much more complex. Sutton[18] suggests that the plume rise varies as $(1/U)^3$, while others (Priestley[13] and Scorer[16]) give more complicated relations. Thus, the problem is not resolved.

The character of turbulence in the atmosphere may be classified, though quite crudely, into two types: mechanical and convective. When the

winds are strong, appreciable mixing takes place and the atmospheric vertical temperature gradient tends toward the adiabatic lapse rate (neutral). Surface roughness, such as trees, buildings, and terrain irregularities, markedly affects the air flow. Under these conditions, the turbulence is predominantly mechanical. At these times, the wind direction may be of importance in determining the character of the smoke plume, since the roughness characteristics in one direction are usually quite different from those in another. Large upwind roughness elements, tens or even hundreds of stack heights away, may influence the air flow and therefore plume behavior.

The stability of the atmosphere, determined by the vertical gradient of potential temperature, $\frac{\partial \theta}{\partial Z}$, markedly influences the character of turbulence. During a sunny day, the ground becomes heated more rapidly then the air above. As a result, the air layers nearest the ground become warmer than layers higher up, thus enhancing vertical mixing since the atmosphere becomes unstable. Especially when the winds are light, i.e., less than 5 mph, large convective eddies appear and convective turbulence predominates. These eddies may have periods of the order of minutes or tens of minutes and are influenced by the nonuniform distribution of thermal properties of the soil such as albedo (reflectivity), emissivity, conductivity and diffusivity. Plowed fields, lakes and rivers, forests, crops, buildings, roads, railroads, and even the shadows of passing clouds provide inhomogeneities in the thermal properties of the ground surface. The inhomogeneities are often referred to as "thermal roughness." Since a smoke plume is a visual atmospheric tracer, the vertical and horizontal oscillations of air parcels are depicted in the sinuosities of the smoke plume.

During sunny days with higher winds, an intermediate condition exists, exhibiting the effects of both mechanical and convective turbulence. On a clear night, when winds are light, the ground cools by radiation more rapidly than the air above, and an inversion, a condition where the temperature increases with height, forms. Under these conditions, the atmosphere is stable and the intensity of mixing, particularly in the vertical direction, is considerably lower than under unstable conditions. Plume rise is ordinarily reduced under stable conditions, at least in part because the rising plume will lose its buoyancy as the difference between plume and air temperature is reduced, since the temperature of the air increases with height.

Illustrations of Meteorological Factors Influencing Plume Behavior

Figure 75 shows five different plume patterns which result from meteorological effects.

Figure 75a is the looping plume. One sees a serpentine configuration typical of daytime conditions with clear skies and intense solar heating characteristic of pronounced convective turbulence.

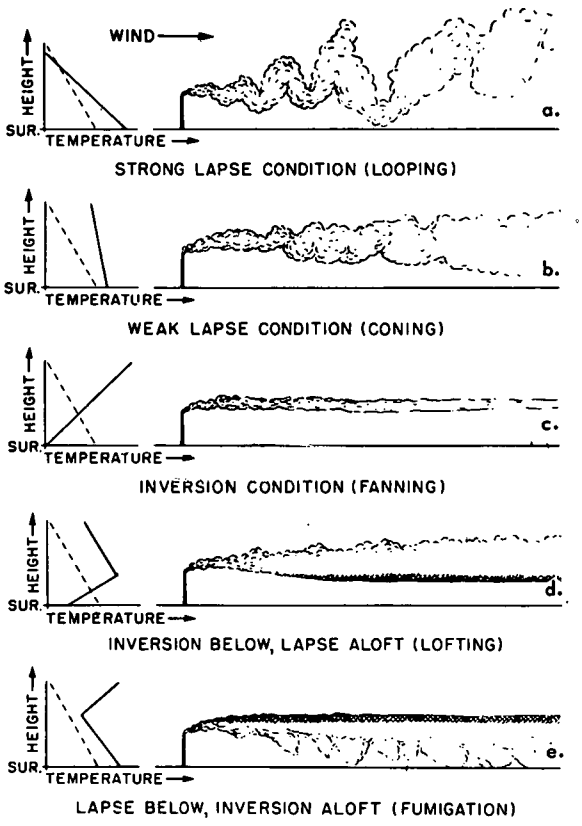

Figure 75

Schematic representation of stack gas behavior under various conditions of vertical stability. --- represents dry adiabatic lapse rate.(25)

Figure 75b illustrates coning which occurs under high wind and near neutral stability conditions. Mechanical turbulence dominates.

Fanning in Figure 75c occurs under conditions of extreme stability. This configuration occurs during a nocturnal inversion, although it may also be seen just before sunset and shortly after sunrise. The vertical component is suppressed more than the horizontal so that the plume's horizontal width is typically greater than its vertical thickness. Photographs from high towers or from aircraft show that this type of plume may undergo appreciable lateral fluctuation similar to that of a meandering river.

Figure 75d shows that when lofting plume conditions prevail, conditions are most favorable from an air pollution standpoint. Under these conditions, ground concentrations are quite low, since part of the plume is rapidly dispersed upward and diffusion toward the ground is suppressed. This type of plume is usually observed in the late afternoon or early evening.

Figure 75e shows the fumigating plume which may be considered as the complement of the lofting plume. The fumigating pattern occurs in the early morning when the inversion is being destroyed from the ground upward. When instability reaches the level of the plume, the lower portions of the plume are brought to the ground rapidly, while the upper part may still remain intact. These conditions may result in extremely high ground surface concentrations.

Plume rise formulas can not be applied to lofting or fumigating plumes.

Short Term Variation in Plume Rise

It is important to realize that even if any one of the formulas adequately described the mean height of rise in a given sampling period, the

actual plume rise over shorter intervals would vary by a factor of two or more, as is illustrated in Figures 76 and 77. The individual points in Figures 76 and 77 show the observed height of rise as a function of distance downwind from the stack. Each point represents the centerline height based on 3 exposures on the same negative made during an interval of from $\frac{1}{2}$ to $1\frac{1}{2}$ min. Figure 76 is based on a series of 15 runs taken during a 35-min interval, and Figure 77 is based on a series of 10 runs taken in a 31-min interval. Only those curves showing the highest and lowest plume rises are shown. It is evident from these diagrams that the plume center line is still rising. Also shown are the Holland and Davidson-Bryant calculated values of plume rise (both with and without Stümke's K correction), as well as the values of plume height vs distance from the stack computed from Bosanquet's 1957 formula.

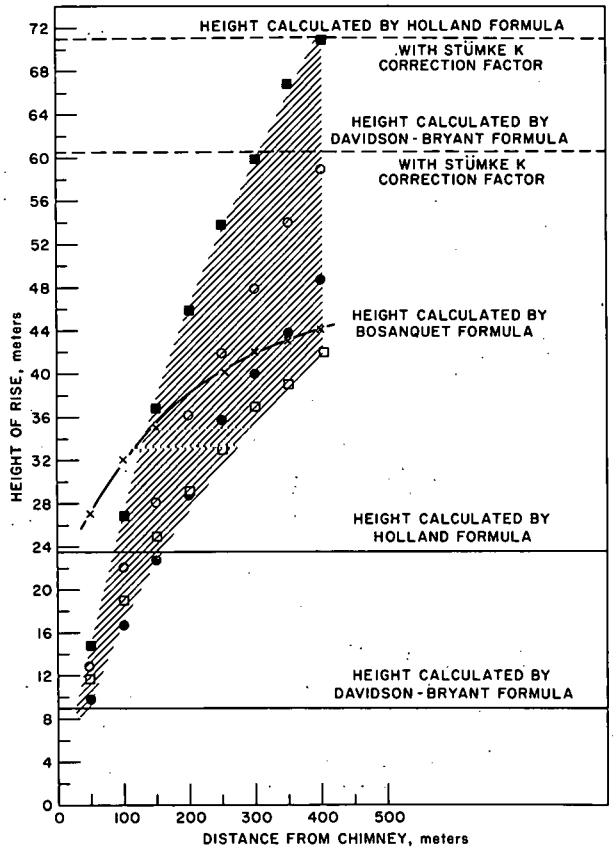

Figure 76

Plume rise as a function of distance based on 15 runs. Individual symbols ○ and ■ indicate the two highest runs and ● and □ indicate the two lowest runs. Hatching indicates areas where intermediate plume rise measurements were obtained. The symbol × indicates height calculated from Bosanquet's formula. Data taken from Rauch at Duisburg, Germany, on September 15, 1959.(41)

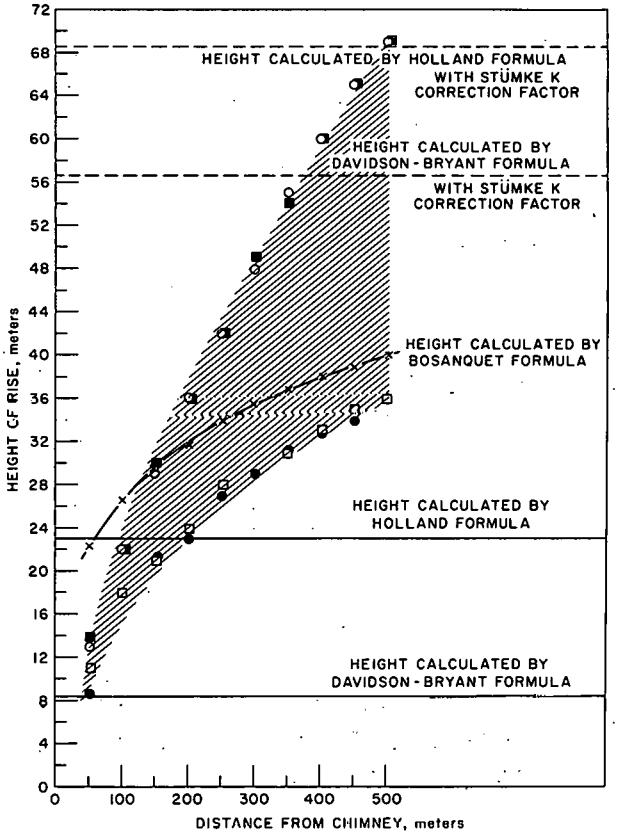

Figure 77

Plume rise as a function of distance based on 10 runs. Individual symbols ○ and ■ indicate the two highest runs and ● and □ indicate the two lowest runs. Hatching indicates areas where intermediate plume rise measurements were obtained. The symbol × indicates height calculated from Bosanquet's formula. Data taken from Rauch at Duisburg, Germany, on September 16, 1959.(41)

In Figure 76, the height of the plume at 400 m ranged from 42 to 71 m; in Figure 77, the heights, at 500 m downwind, ranged from 36 to 69 m. In each case, the pertinent stack and meteorological parameters were given as approximately constant over the entire sampling period. One is, therefore, forced to conclude that an unmeasured atmospheric influence, such as large convective eddies, brought about this variation.

The effect of the eddies is also illustrated in Figure 78 and 79 (based on the same data as Figures 76 and 77), which give the height of the plume at 400 m and 450 m, respectively, as a function of time. These variations are irregular, i.e., show no significant pattern. A similar irregularity is demonstrated by time-lapse movies of smoke plumes which show strikingly the rapid variations in azimuth and height, as well as superimposed sinuosities.

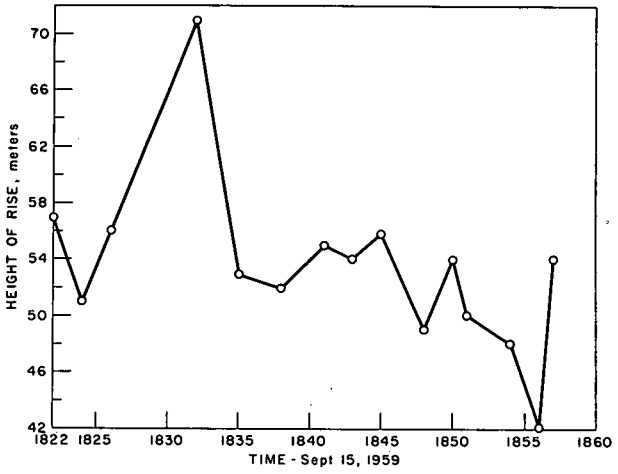

Figure 78

Time variation of plume rise at a horizontal distance of 400 m from stack. Data taken by Rauch at Duisburg, Germany, on September 15, 1959.(41)

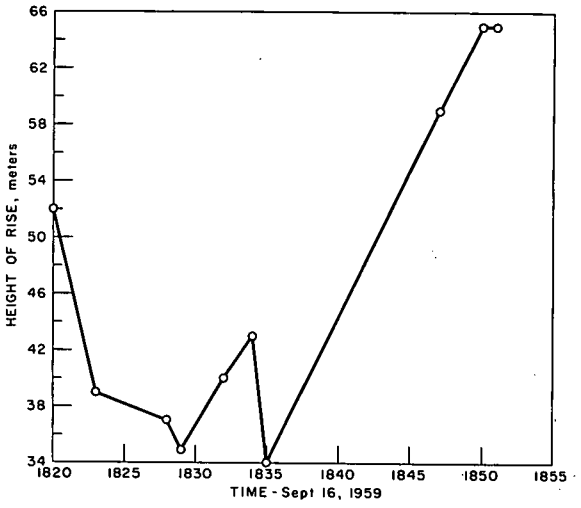

Figure 79

Time variation of plume rise at a horizontal distance of 450 m from stack. Data taken by Rauch at Duisburg, Germany, on September 16, 1959.(41)

Shape of Stack

Jensen and Franck(26) performed a wind-tunnel study in which the effect of the shape of the stack near the emission point on plume rise was investigated. Three stacks were used, all having the same height and cross-sectional area, as illustrated in Figure 80. It was found that the greatest rise occurred with the rectangular stack directed along the wind, the second best was the circular stack, and the worst was the rectangular stack with the long axis perpendicular to the wind. The square stack provided lower plume rises than the circular stack. Several values of the ratio of stack velocity to wind speed and different roughness conditions were used.

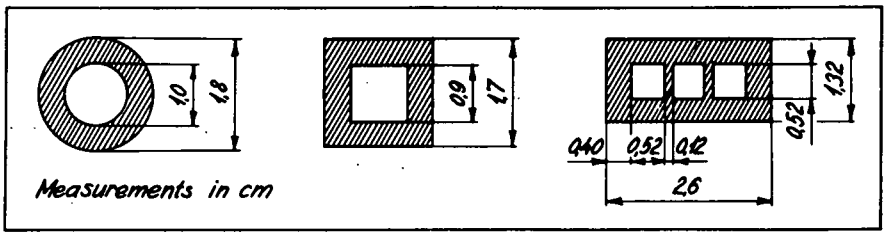

Figure 80

Cross-sections through chimney models.[26]

Aerodynamic effects at the lee of a stack produces von Karman eddies and a region of reduced pressure, which draws the effluent down along the side of the stack, a phenomenon called downwash. When the effluent is colored, the stack surface near the top takes on coloration. Sherlock and Stalker[27] studied this phenomenon in a wind tunnel and their results are summarized in Figure 81, which shows the relation between wind velocity and stack effluent velocity and the occurrence of downwash. It is evident from this figure that if V_s/U exceeds about 1.5, downwash will be minimized.

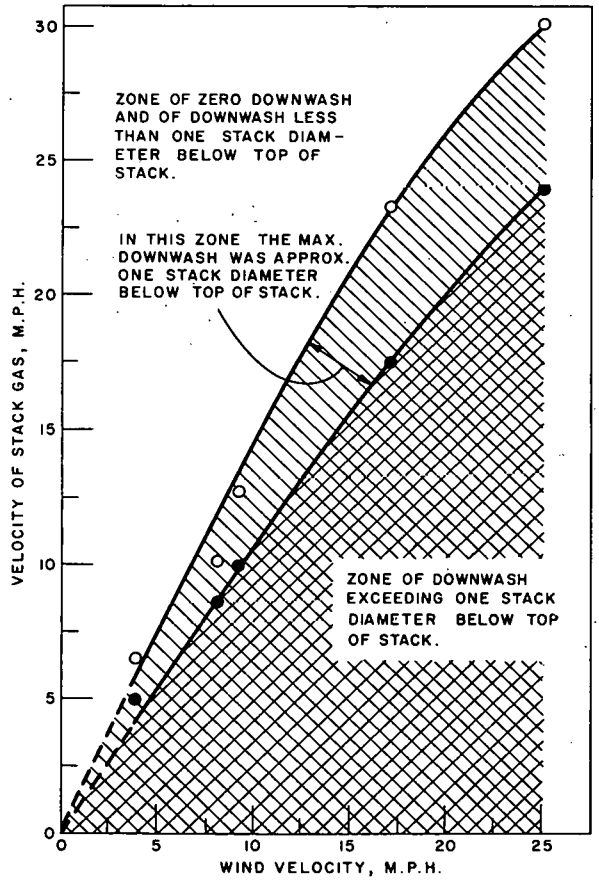

Figure 81

Critical relations between wind velocity and stack-gas velocity in the control of downwash.[27]

Shape of Buildings

Mechanical eddies created by buildings and other obstructions to air flow strongly affect plume rise in a manner not easily predicted by theoretical considerations. Field or wind-tunnel experiments are usually needed to determine the effects. An interesting study of airflow around buildings in a wind tunnel was reported by Evans[28] in which he shows the effect of buildings of various shapes and orientations with respect to the wind. Figures 82 through 84, taken from that study, show the flow around buildings made up of one or more cubical blocks.

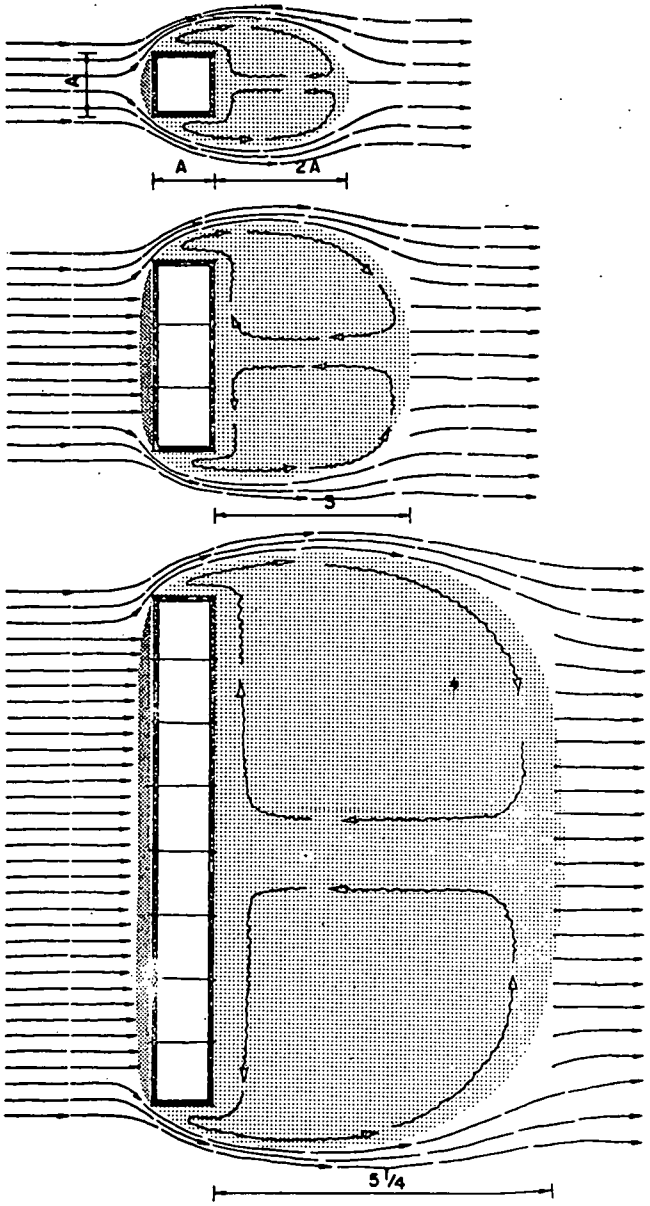

Figure 82

Variation of air flow patterns with increasing building length. Wind perpendicular to large dimension of building.[28]

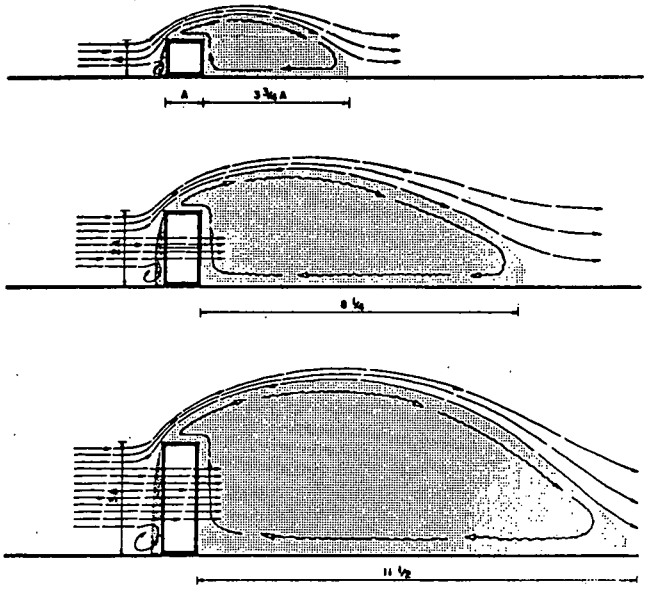

Figure 83

Variation of air flow patterns with increasing building height.(28)

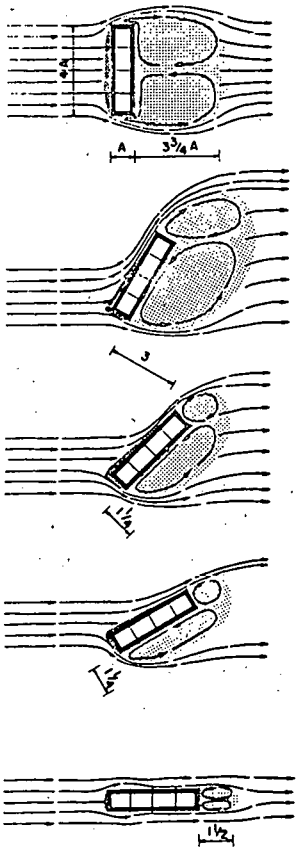

Figure 84

Variation of building air flow patterns with change in wind direction.(28)

Figure 82 is a plan view showing the effect on the downwind eddy pattern of increasing the building length with the wind oriented perpendicular to the long dimension. This figure shows that the longer the building the larger the downwind eddy.

Figure 83 is an elevational view of the cubical blocks. With an increase in building height, both the vertical and the downwind horizontal dimensions of the eddy increase. Of interest is the ratio of the downwind eddy dimension to building height which appears to be about 4:1. Further, note the return flow not only at the ground level, but also at the roof top. Similar results were found by Halitsky.(29) This figure indicates that the building effect is somewhat smaller than that indicated by the $2\frac{1}{2}$ times rule, discussed below.

Figure 84 is a plan view and shows the effect of orientation of a long building with respect to wind direction. A wind blowing perpendicular to the largest dimension of such a building will provide greater turbulence

and stronger downdrafts than a wind in the longitudinal direction. In view of this, the orientation of a rectangular building should, if at all possible, be selected to allow the prevailing wind to blow along the long axis. It is quite evident from Figure 84 that the trajectory of stack effluent from a low stack on a building will be considerably different from that of a tall one, i.e., one whose effluent is above the building's aerodynamic effect. The dispersion of the stack gases will depend on the location of the stack on the roof, such as in the center or at one edge, and, for an off-center location, will also depend on wind direction.

Movies of smoke flow patterns over buildings with small stacks made at the Argonne National Laboratory[30] illustrate "cartwheels" forming on the lee side with a diameter several times the height of the building, thus providing high concentrations of contaminant. Information on return flows is important in locating ventilation intakes to minimize the recirculation of contaminants to the inside of the building.

Another illustration of the effect of the building in reducing the height of the chimney plume may be seen in Figure 85, taken from work at the New York University Wind Tunnel.[31] This figure shows that the

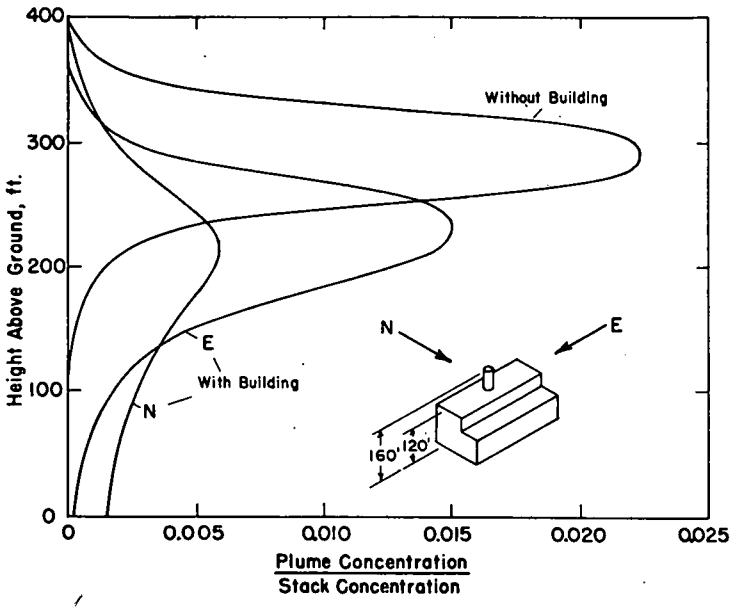

Figure 85

Vertical concentration profiles through center of a gas plume found in a scale-model wind tunnel experiment. These were taken 1440 ft downwind of the stack at a wind speed of 11.2 m/sec. The numerical values are prototype equivalents.[31]

plume from a stack remains narrower (turbulent diffusion is smaller) and at a higher level without a building than with one. It may also be seen that turbulence is greatest when the wind is perpendicular to the long dimension of the building.

The "$2\frac{1}{2}$ Times Rule"

To minimize building interference with a chimney plume, the British Electricity Industry has, since the 1930's, used the well-known $2\frac{1}{2}$ times rule, which states: the height of the stack above ground should be $2\frac{1}{2}$ times the height of the building. Sutton points out[32] that this rule was intended to apply to a stack located near the central point of a rectangular building. He indicates that the rule was probably derived by Sir David Brunt from information gained by W. R. Morgan in a study on the height of disturbances over a long ridge in connection with a British airship disaster investigation. The Beaver Report[23] realizes that $2\frac{1}{2}$ times rule cannot be applied in all cases and suggests that, for low buildings, the chimney should be not less than 120 ft high, although, of course, discretion must be used in specific cases.

According to ter Linden,[33] the Dutch use a $1\frac{1}{2}$ times rule; that is, the stack must be $1\frac{1}{2}$ times the height of the highest building in the neighborhood.

The Working Party on the Dispersion of Gaseous Pollution from Chimneys of the Warren Spring Laboratory, Department of Scientific and Industrial Research, England, in a report to the Ministry of Housing and Local Government as reported by Lucas,[34] discusses a modified $2\frac{1}{2}$ times rule for buildings whose height is smaller than the larger horizontal dimension. This rule states that a stack $2\frac{1}{2}$ times the building height may be considered as if the building were absent, i.e., the effective height is $2\frac{1}{2}$ times the building height; a stack $1\frac{1}{2}$ times the building height does experience interference and has an effective height of only 0.9 times the building height. The Working Party suggests a linear interpolation between $1\frac{1}{2}$ and $2\frac{1}{2}$ times the building height to obtain the effective stack height and then extrapolation to nearly zero. A nearly identical relationship may be obtained by assuming a stack at roof level as at zero effective height, i.e., a ground source, and one at $2\frac{1}{2}$ times the building height as having no interference. Intermediate points may be obtained by linear interpolation.

In assessing the behavior of a plume, one must consider not only the building on which the stack is located, but the effects of adjacent buildings and stacks. In fact, the possibility that a nearby building may act as a heat source because it is poorly insulated must not be overlooked.

The design of a stack is frequently a compromise among many, often contradictory, factors: economics of construction and operation, the nature of the ejected matter the character of the surrounding areas, esthetics, permissible ground-level concentrations, prevailing weather conditions, and economic and health consequences of excessive pollution. It is quite clear that no elementary rule, such as a $1\frac{1}{2}$ or $2\frac{1}{2}$ times rule, can be applied to all situations.

Terrain Shapes

In mountainous areas, the airflow can be quite complicated, as has been shown by Davidson,[35] Crow,[36] and many others. Figure 86 illustrates the airflow over a ridge and the resulting pollution areas which may emanate from a building located on its lee or its windward sides. Bierly and Hewson[39] have shown that forested areas and large bodies of water materially affect plume rise. Surface roughness elements, such as trees, buildings, hills, and even smooth objects with differing albedoes, such as black-top roads and rivers, affect air flow over large distances. Thus, terrain irregularities which are located many stack heights upwind influence plume motions. Whenever a potential pollution problem results from an effluent emitted by a stack located in all but perfectly uniform terrain, wind tunnel studies should be considered.

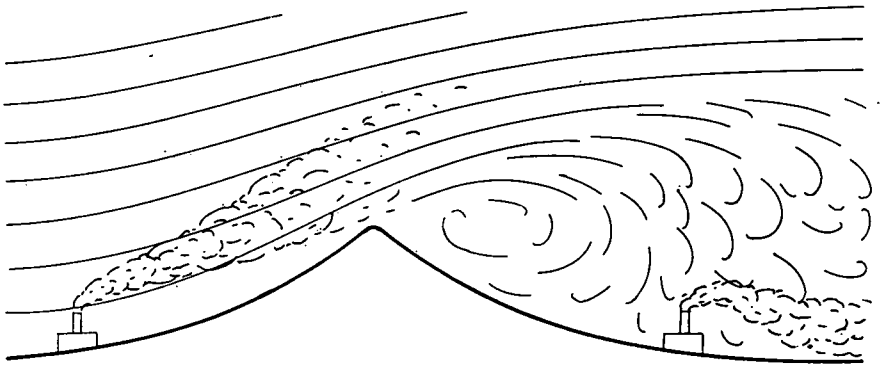

Figure 86

Pattern of air motion over a hill showing effect on gas plumes.[31]

Practical Considerations for Minimizing Ground Level Concentrations

The pollution on the ground due to a chimney effluent may be diminished by increasing the momentum or bouyancy of the emitted gases as well as by increasing the stack height.

Momentum may be increased by raising the effluent's exit velocity through the use of a nozzle or through the use of auxiliary blowers. It should be pointed out that the addition of air at ambient temperature may reduce the effluent temperature sufficiently to destroy the advantage gained by increased momentum because of loss in buoyancy. In some cases with hot plumes an increase in momentum due to an increase in exit velocity, even without the addition of outside air, will increase mixing and thereby reduce the benefit of the existing buoyancy. As a result, the plume rise will be smaller. Mixing the effluent with heated air or heating the effluent itself will increase buoyancy and provide greater plume rise.

Parodoxically, contamination at the ground may be increased when power stacks are operating at partial load, even though the total amount of pollutants emitted is less.[24] The reduction in momentum and/or buoyancy and the consequent lowering of the plume in such cases may result in higher ground concentrations. The stack of the Bankside Power Station in England is divided internally into four sections to minimize this effect. At half load, two of these carry all of the discharge.

In building complexes where several chimneys are used, pollution may be minimized by combining the effluent into a single tall stack. Although the total emission of contaminants would be the same, the concentrations at the ground would be reduced because of the increase in stack height. Further, with a single tall stack the increase in momentum would be beneficial.

At two large London power stations, an attempt to reduce sulphur dioxide contamination was made by removing 90% of the gas through a washing process.[24] Unfortunately, the process also reduced the temperature of the gas and saturated it with water vapor. As a result, the washed plume lost much of its original buoyancy and spread to the ground more quickly. Isopleths of SO_2 concentration at the ground showed that the maximum concentration of the washed plume was comparable to that of the unwashed plume, even though 90% of the sulphur dioxide had been removed. One advantage gained by washing, however, was that the areas bounded by isopleths of relatively high concentration were substantially reduced.

Comparison of Formulas

Adequate and sufficient data to test fully the validity of the above and other proposed formulas do not exist. Nevertheless, a number of investigations have been made in which available data were tested. The earliest studies comparing plume rise formulas with observations were made by Katz,[38] who compared the formula of Sutton[18] with that of Bosanquet, Carey, and Halton;[6] and Best[39] who compared these two and the one by Holland.

More recently, comparisons between observed and calculated plume rises were made by: 1) Moses and Strom using data taken at the Argonne National Laboratory in the United States;[40] 2) Rauch using data taken at Duisburg and at Gernsheim in Germany;[41] and 3) Stümke using data taken at the Argonne National Laboratory, Duisburg, Gernsheim, and at Harwell in England.[17, 42]

Moses and Strom used least square techniques to compare the formulas of Davidson-Bryant, Holland, and Bosanquet, as well as those of Sutton, Scorer, and Bosanquet, Carey, and Halton. The plume-rise data used by Moses and Strom were obtained by means of the Argonne Experimental Meteorology Stack employing photogrammetric techniques.[43] These measurements extended only to 60 m. The buoyancy in these experiments was very low, and it is likely that the plume rises were near their maximum since the angles between the smoke centerline and the horizontal in 27 of the 31 cases studies were 5° or less; nevertheless, one can not be certain of this. A statistical summary of the three formulas considered in this paper is shown in Table 50. Also included are the plume rises obtained by applying Stümke's correction factor, K. These data show that both the Holland and Davidson-Bryant formulas yield values which are too low, and the Bosanquet formula yields values which are too high.

Table 50

Statistical summary of calculated and observed plume heights at 60 m from experimental smoke stack at Argonne National Laboratory, Argonne, Illinois,[40] based on 31 observations.

	Observed	Davidson-Bryant	Holland	Bosanquet C = 0.13
		Without Stümke's K correction factor		
Mean plume rise, m	6.1	3.5	2.6	7.3
Standard deviation, m	3.5	3.6	1.5	6.1
Root-mean-square, observed-minus-calculated height, m		4.2	4.7	5.2
Correlation coefficient (calculated vs observed)		0.52	0.46	0.52
		With Stümke's K correction factor		
Mean plume rise, m	6.1	5.7	4.8	5.5
Standard deviation, m	3.5	5.9	2.8	4.6
Root-mean-square, observed-minus-calculated height, m		4.9	4.3	4.0
Correlation coefficient (calculated vs observed)		0.52	0.46	0.52
Stümke's correction factor		1.63	1.86	0.753

Rauch, using the data from the Gernsheim and Duisberg stacks used by Stümke plus measurements taken later (a total of 428 individual runs were used), compared Holland's formula with a K factor of 3.09 and a formula suggested by Lucas, Moore, and Spurr[11] which states

$$\Delta h = \frac{186.4\ (Q_H')^{1/4}}{U} \tag{33}$$

where Q_H' is given in megawatts and U in m/sec. He concludes that for these two stacks the Lucas formula is superior to that of Holland. It is to be noted that the Lucas, Moore, and Spurr formula does not take into account the contribution due to momentum.

The most extensive tests of observed and calculated plume rise have been made by Stümke.[17, 42] In the first of these two papers, measurements by Stewart, Gale, and Crooks[44] from a stack at Harwell, and by Rauch[41] from stacks at Gernsheim, and Duisburg, as well as the four sets of data presented in the paper by Bosanquet, Carey, and Halton, were used. Stümke compared eight different formulas with these measurements: 1) Bosanquet, Carey, and Halton; 2) Davidson-Bryant; 3) Holland; 4) Scorer; 5) Morton; 6 and 7) two of his own; 8) Hill, Thomas, and Abersold. The Hill, Thomas, and Abersold[20] formula states that a 1°F temperature increase represents $2\frac{1}{2}$ ft of plume rise.

Stümke concluded that the Holland formula (after a 2.92-multiplying factor was applied) gave the best representation for the plume rise, since the quantity $\frac{1}{N}\sum\left(\frac{\Delta h^*_{cal} - \Delta h_{obs}}{\Delta h_{obs}}\right)^2$ was smallest. Also the correlation coefficient between observed and calculated values was largest. Several other statistical parameters were calculated to arrive at this conclusion. The authors of this paper using the data of Stümke have tested the Bosanquet 1957 formula for comparison and the results are summarized in Table 51.

Table 51

Statistical summary of Stümke's 1961 analysis based on stacks of Gernsheim, Harwell, and Duisberg. (The Stümke K correction factor was applied.)

	Observed	Davidson-Bryant	Holland	Bosanquet C = 0.13
Average plume rise height, m	65.4	66.7	65.4	66.1
Standard deviation, m	17.7	44.1	34.0	56.8
Stümke correction factor		6.69	2.92	0.75
Root-mean-square of calculated-minus-observed height, m		37.4	26.5	51.7
Correlation coefficient		0.62	0.64	0.43

Stümke[42] in his second paper used the data of Moses and Strom; of Stewart, Gale, and Crooks; and of Rauch (though Rauch's data appear to have been re-evaluated), and derived a generalized formula of which the Holland and the Lucas, Moore, and Spurr formulas are special cases. This generalized formula may be written as

$$\Delta h = \frac{1}{U}\left\{C_J V_s d + C_\theta d^{-\mu} V_s^{-\lambda}\left[\frac{V_s d^2 \Delta T}{T_s}\right]^{\nu}\right\} \tag{34}$$

where C_J, C_θ, ν, λ, and μ are adjustable parameters. By a combination of techniques involving least squares and graphical optimization he arrives at values of the coefficients and exponents to give a good fit to the data for small stacks, such as those discussed by Moses and Strom, as well as for the larger stacks discussed by Stewart, Gale, and Crooks, and by Rauch. With the added number of adjustable parameters, a better fit is to be expected. After determining his adjustable parameters, the formula may be written as

$$\Delta h = 1.5\frac{V_s d}{U} + \frac{65}{U} d^{3/2}\left(\frac{\Delta T}{T_s}\right)^{1/4}. \tag{35}$$

One is tempted to recommend Stümke's new formula, but a common pitfall is to place high hopes on a regression equation before it has been tested on independent sets of data. Therefore, its usefulness has yet to be proved.

As a result of examining various plume rise formulas, the Beaver Committee has decided to recommend the Holland formula for calculating maximum ground concentrations from stacks.[23] This, however, has been criticized by Hawkins and Nonhebel[24] on the grounds that the Holland formula is empirical and its use, therefore, should be limited to the ranges of the variables used in its derivation. Nonhebel[22] suggests the use of the Bosanquet formula because it has a sounder theoretical basis, but he presents no plume rise measurements to support his preference. It should be pointed out that some of the assumptions made by Bosanquet leave much to be desired. For example, he assumes a constant diffusion coefficient of 0.13 for all meteorological conditions and does not take into account possible differences between horizontal and vertical diffusion rates. He also bases his derivation on the behavior of a solid cylinder. The Holland formula is also widely used in France[45] and Sweden.[46]

Considering the available measurements of plume rise and the calculating techniques at our disposal, it is extremely difficult to recommend any technique with enthusiasm.

Conclusions

It is extremely difficult to measure plume rise in the field. To obtain reliable results photogrammetric or other tedious techniques must be used, and measurements to distances of the order of 1000 meters should be made. In addition, the effect of atmospheric eddies requires that many measurements be taken in succession to arrive at a mean plume position which is statistically stable. For a fuller understanding of the problem, data on short term time variations are essential, also. This is especially true where instantaneous peak concentrations are of concern, such as in odor nuisances. Despite the lack of adequate measurements and satisfactory theory, practical decisions must be made on the selection of a minimum stack height so that threshold values of atmospheric contaminants are not exceeded.

In this paper two of the most widely used empirical formulas, those of Davidson-Bryant and Holland, and the semitheoretical formula of Bosanquet have been discussed in detail. The latter was selected for study because it presumably represents an improvement over the widely-used formula of Bosanquet, Carey, and Halton.

A critical examination of the three formulas indicates that none is as good as one would hope. One is tempted to recommend Stümke's generalized formula, but further tests have to be made with independent data before it becomes accepted. Under the circumstances, it appears that for large stacks with appreciable buoyancy such as those at Gernsheim or Duisburg, one may use Holland's formula with a Stümke correction factor of about 3, i.e.,

$$\Delta h = \frac{3(1.5\, V_s d + 4 \times 10^{-5}\, Q_H)}{U}. \qquad (36)$$

For smaller stacks with little buoyancy such as the Argonne stack, a Stümke K factor of about 2 may be used. The effect of stability on plume rise can be taken into account by adding 10 to 20% of the computed value, under lapse conditions, and subtracting the same amount under stable stratifications.

It is well to caution that terrain effects, such as nearby buildings, hills and valleys or forested areas, must be taken into account. In most cases, this can only be done by wind-tunnel tests. Further, meteorological conditions may materially affect plume rise. For example, under sunny conditions with winds of 2 mph or less, intermittent gusts may bring the effluent to the ground within one or two stack heights. Moderate to heavy rain in association with gusty thunderstorm winds may be expected to produce wide deviations from calculated results. As Scorer points out,[47] no one formula can or should be expected to provide acceptable results under all conditions.

The authors acknowledge the advice and encouragement given by Mr. L. D. Marinelli and Dr. John E. Rose in discussions during the course of the preparation of this paper and the assistance provided by Mr. Frank C. Kulhanek and Mrs. Lee Ryan in the preparation of the charts and calculations.

References

1. C. H. Bosanquet and J. L. Pearson. The Spread of Smoke and Gases from Chimneys, Disperse Systems in Gases. Trans. Faraday Soc. 32, 1249 (1936).

2. O. G. Sutton. The Problem of Diffusion in the Lower Atmosphere. Quart. J. Roy. Meteorol. Soc. 73, 257 (1947).

3. H. E. Cramer, F. A. Record, and H. C. Vaughan. Final Report, Contract #AF 19(604)-1058, ARCRC-TR-58-239, Mass. Institute of Technology, 1958.

4. F. A. Gifford, Jr. Atmospheric Dispersion. Nucl. Safety 1 (3), 56 (1960).

5. F. Wipperman and W. Klug. Eine Method zur Bestimmung von Schornsteinmindesthöhen. Intern. J. Air Water Poll. 6, 27 (1962).

6. C. H. Bosanquet, W. F. Carey, and E. M. Halton. Dust Deposition from Chimney Stacks. Proc. Inst. Mech. Eng. 162, 355 (1950).

7. C. H. Bosanquet. The Rise of a Hot Waste Gas Plume. J. Inst. Fuel 30 (197), 322 (1957).

8. L. W. Bryant and C. F. Cowdrey. Effects of Velocity and Temperature of Discharge on the Shape of Smoke Plumes from a Funnel or Chimney: Experiments in a Wind Tunnel. Proc. Inst. Mech. Engrs. (London) 169, 371 (1955).

9. W. F. Davidson. The Dispersion and Spreading of Gases and Dust from Chimneys. Trans. Conf. on Industrial Wastes, 14th Annual Meeting Ind. Hygiene Foundation America, 1954. pp. 38-55.

10. J. Z. Holland. A Meteorological Survey of the Oak Ridge Area. U. S. Atomic Energy Commission Report, ORO-99, 1953. pp. 554-559.

11. D. H. Lucas, D. J. Moore, and G. Spurr. The Rise of Hot Plumes from Chimneys. Intern. J. Air Water Poll. 7, 473 (1963).

12. B. R. Morton. Forced Plumes. J. Fluid Mech. 5 (1), 378 (1959).

13. C. H. B. Priestley. A Working Theory of the Bent-over Plume of Hot Gas. Quart. J. Roy. Meteorol. Soc. 82, 165 (1956).

14. A. F Rupp, S. E. Beall, L. P. Bornwasser, and D. H. Johnson. Dilution of Stack Gases in Cross Winds. U. S. Atomic Energy Commision Report, AECD-1811, 1948. pp. 1-15.

15. F. H. Schmidt. On the Diffusion of Stack Gases in the Atmosphere. Mededelingen en Verhandelingen, K.N.M.I. Series 102, Nr. 68 (1957).

16. R. S. Scorer. The Behavior of Chimney Plumes. Intern. J. Air Poll. 1 (3), 198 (1959).

17. H. Stümke. Zur Berechnung der Aufstiegshöhe von Rauchfahnen. VDI-Forschungsheft, Ausgabe B, 27 (483) 38-43 (1961).

18. O. G. Sutton. The Dispersion of Hot Gases in the Atmosphere. J. Meteorol. 7 (5), 307 (1950).

19. F. W. Thomas. TVA Air Pollution Studies. Air Repair 4 (2), 59 (1954).

20. G. R. Hill, M. D. Thomas, and J. M. Abersold. High Stacks Overcome Concentrations of Gases. Min. Congr. J. 31, 21 (1945).

21. L. W. Bryant. The Effects of Velocity and Temperature of Discharge on the Shape of Smoke Plumes from a Funnel or Chimney in a Wind Tunnel. National Physical Laboratory, Great Britain, 1949. pp. 1-14.

22. G. Nonhebel. Discussion before Institute of Fuel, February 13, 1953. J. Inst. Fuel 36, 336 (1957).

23. Report of Government Committee on Air Pollution (Sir Hugh Beaver, Chairman). Cmd. 9322, Her Majesty's Stationary Office, London, 1954.

24. J. E. Hawkins and G. Nonhebel. Chimneys and the Dispersal of Smoke. J. Inst. Fuel 28 (178), 530 (1955).

25. U. S. Weather Bureau. Meteorology and Atomic Energy. U. S. Atomic Energy Commission Report AECU-3066 (1955).

26. M. Jensen and N. Franck. Model-Scale Tests in Turbulent Wind. Part 1, Phenomena Dependent on the Wind Speed, Shelter at Houses - Dispersal of Smoke. The Danish Technical Press, Copenhagen, 1963.

27. R. H. Sherlock and E. A. Stalker. A Study of Flow Phenomena in the Wake of Smoke Stacks. Engineering Research Bull. #29, Dept. of Engineering Research, Univ. of Michigan, Ann Arbor, Michigan, 1941.

28. B. H. Evans. Natural Air Flow Around Buildings. Research Report #59, Texas Engineering Experiment Station, Texas A & M College, 1957.

29. J. Halitsky. Diffusion of Vented Gas Around Buildings. J. Air Poll. Control Assoc. 12 (2), 74 (1962).

30. H. Moses. Air Flow Patterns Near Buildings - A Motion Picture Study. 48th Ann. Air Pollution Control Assoc. Mtg., Detroit, 1955. Air Poll. Control Assoc., Pittsburgh, Pa., 1955. pp. 7-1 - 7-5.

31. G. H. Strom. Atmospheric Dispersion of Stack Effluents. Air Pollution, Vol. 1, ed. Arthur C. Stern. Academic Press, Inc., New York, 1962. pp. 118-195.

32. O. G. Sutton. Discussion before Institute of Fuel, May 23, 1960. J. Inst. Fuel 33, 495 (1960).

33. A. J. ter Linden. Air Pollution in Holland - Problems and Control of Air Pollution, ed. F. S. Mallette. Reinhold Publishing Corp., New York, 1955. pp. 236-244.

34. D. H. Lucas. Comment during Symposium on the Dispersion of Chimney Gases held on December 7, 1961, at the Royal Meteorol. Soc. Intern. J. Air Water Poll. 6, 94 (1962).

35. B. Davidson. Some Turbulence and Wind Variability Observations in the Lee of Mountain Ridges. J. Appl. Meteorol. 2 (4), 463 (1963).

36. L. W. Crow. Airflow Related to Denver Air Pollution. J. Air Poll. Control Assoc. 14 (2), 56 (1964).

37. E. W. Bierly and E. W. Hewson. Atmospheric Diffusion Studies Near a Lake Shore. J. Appl. Meteorol. 2 (3), 390 (1963).

38. M. Katz. Application of Diffusion Theory to Dispersion of Stack Gas in the Atmosphere. Defence Research Board of Canada, Defence Research Chemical Laboratories Report No. 110, Ottawa, Canada, 1952.

39. A. C. Best. Maximum Gas Concentration at Ground Level from Industrial Chimneys. J. Inst. Fuel 30 (197), 329 (1957).

40. H. Moses and G. H. Strom. A Comparison of Observed Plume Rises with Values Obtained from Well-known Formulas. J. Air Poll. Control Assoc. 11 (10), 455 (1961).

41. H. Rauch. Zur Schornstein-Überhöhung. Bericht des Meteorologischen Institutes an der Tech. Hochschule, Darmstadt, 1962.

42. H. Stümke. Vorschlag einer empirischen Formel für die Schornsteinüberhöhung im Anschluss und eine Überprüfung bekannter Formeln mit zusätzlichem Beobachtungsmaterial. Dem Ausschuss II der VDI-Kommission "Reinhaltung der Luft" vorgelegt als wissenschaftliches Gutachten, Institut für Gasströmungen der Technischen Hochschule, Stuttgart, 1963.

43. P. E. Wasko and H. Moses. Photogrammetric Technique for Studying Atmospheric Diffusion. Photogrammetric Engineering 27, 92 (1961).

44. N. G. Stewart, H. J. Gale, and R. M. Crooks. The Atmospheric Diffusion of Gases Discharged from the Chimney of the Harwell Reactor, BEPO. Intern. J. Air Poll. 1, 87 (1958).

45. R. Le Quinio. Service Controle Rayonnements and Genie Radioactif. B.P. No. 2, Centre d'Etudes Nucleaires, Saclay, France, personal communication (1964).

46. Ulf Högström. Sveriges Meteorologiska Och Hydrologiska Institute, Stockholm, Sweden, personal communication (1964).

47. R. S. Scorer and C. F. Barrett. Gaseous Pollution from Chimneys. Intern. J. Air Water Poll. 6, 49 (1962).

DETERMINATION OF TURBULENCE DISSIPATION BY EULERIAN VARIANCE ANALYSIS*

Paul Frenzen

Abstract

Using a "variance function" to specify the variance retained by a time series smoothed via running means, it is shown that the rate of turbulence dissipation can be computed from an Eulerian wind record supplied by a single, 3-cup anemometer through the relation

$$\epsilon = \frac{A}{\overline{U}} \left[\frac{u^2_{T_j} - u^2_{T_k}}{T_k^{2/3} - T_j^{2/3}} \right]^{3/2}$$

Here $A \approx 3.3$ derives from the Kolmogoroff law, $\overline{U}$ is the mean flow, and the numerator of the bracketed term represents the additional reduction in variance effected by increasing the averaging interval from T_j to T_k. Preliminary verifications of the relation are presented, and an experimental program designed to use the method is outlined.

Introduction

Rapidly fluctuating, statistically stationary time series data, such as are commonly recorded in micrometeorological measurement, are invariably "smoothed" to some degree by the limited high-frequency response of real measuring devices. Under certain conditions, this fact of experimental life can be overcome, and even turned to advantage; for when the averaging characteristics of the recording instrument and certain statistical properties of the data source are both known, it becomes possible either a) to calculate the amount of variance lost and thus determine the total variance of the undistorted signal, or b) to utilize the observed losses of variance to compute additional information concerning the fluctuating field from which the data came.

In a previous application of these procedures, Ball[1] determined values of the structure function (and, subsequently, the dissipation) from

*Work performed under the auspices of the U. S. Atomic Energy Commission, in part at C.S.I.R.O., Division of Meteorological Physics, Aspendale, Victoria, Australia. Submitted to Quart. J. Roy. Meteorol. Soc.

the records of ordinary anemometers through an analysis that essentially represents a special case of the present more general method. Pasquill,[2] whose Equation 14 is similar in form to Equation 6 below, has determined the eddy diffusivity from the turbulent energy detected by a hot-wire yawmeter and transmitted through certain band-pass filters. Similarly, MacCready[3] has shown that the variance of the fluctuating wind direction can be used to compute the dissipation. Indeed, MacCready's Equation 17 is a directional counterpart to the present Equation 7 in terms of wind speed for the ideal case in which variance reductions are based upon the total variance recorded by a perfect instrument.

The present method uses sequences of running means produced by an ordinary 3-cup anemometer by recording switch pulses during a series of consecutive, identical short intervals of time. By collecting these means in overlapping averages over successively larger multiples of the basic recording interval, this comparatively unsophisticated instrument can be made to supply wind-speed data in the form of time series smoothed over any interval larger than some minimum associated with the speed of response of the equipment. What is more, an inherent restriction of the analysis to fluctuations drawn solely from the inertial subrange is accomplished automatically by the manner in which the variances of the averaged data are combined; neither mechanically-tuned sensors nor electronically-filtered input signals are required.

Theoretical Discussion

The variance of the first integral of any stationary, random time series u(t) can be written in two essentially independent ways:

$$\overline{x^2(T)} = 2\,\overline{u^2}\int_0^T\int_0^t R(\xi)\,d\xi\,dt \qquad (1)$$

$$\overline{x^2(T)} = \overline{u_T^2}\cdot T^2 \qquad (2)$$

The first above is the familiar equation for diffusion by continuous movements (Taylor[4]) in which $R(\xi)$ specifically represents the Lagrangian autocorrelation function. More generally however, this term can be identified simply as that autocorrelation associated with the particular series chosen for analysis. The second expression will be seen to be an abbreviated version of the first in which an integral representation has been replaced by running mean values, thus: $u_{Ti} \equiv (1/T)\int_{t_i}^{t_i-T} u(t)\,dt$. By equating their right hand sides and solving for the ratio of smoothed to unsmoothed series variance, Expressions 1 and 2 combine to define the "variance function":

$$u_T^2/u^2 \equiv \beta(T) = (2/T^2) \int_0^T \int_0^t R(\xi)\, d\xi\, dt \qquad (3)$$

(cf. Ogura;[5] Pasquill,[6] Section 1.4.)

The familiar case of Lagrangian dispersion analysis affords such graphic physical interpretations of the several terms appearing in the foregoing expressions, that this single special application tends to overshadow the more general value of these relations as a set which may be applied to any stationary, random time series. For the present application, we consider u(t) to represent an Eulerian wind record which, for the purposes of the theoretical discussion, has been filtered to eliminate all fluctuations save those of the inertial subrange. In passing, it is of interest to note that neither the first integral of such an Eulerian velocity fluctuation record nor its variance has any obvious physical significance. On the other hand, none is needed; for these Eulerian counterparts of the more familiar Lagrangian measures of particle displacement and mean-square dispersion are eliminated from consideration once the variance function has been defined.

When the form of the correlation function is known, the variance function can be written from Equation 3. This condition obtains in the inertial subrange of the atmospheric turbulence spectrum, a high-frequency regime within which the principal statistical characteristics of turbulence depend solely upon the rate of dissipation. From this property it has been shown that, within the subrange, the Eulerian time correlation has the form

$$R_E(\xi) = 1 - \frac{c}{\overline{u^2}}\, \overline{U}^{2/3}\, \epsilon^{2/3}\, \xi^{2/3} \qquad (4)$$

where c is a universal constant and ϵ represents the rate of turbulence dissipation (MacCready[7]). Substituting this relation in Equation 3 and integrating we obtain

$$\beta(T) = 1 - \frac{9c}{20\, \overline{u^2}}\, \overline{U}^{2/3}\, \epsilon^{2/3}\, T^{2/3} \qquad (5)$$

In short, $(1 - \beta) \propto T^{2/3}$; which is to say, the percentage variance lost by an anemometer that averages over a running interval T increases as $T^{2/3}$ in the inertial subrange, a result that forms the basis of the first procedure outlined in the introduction.

By rearranging terms, Equation 5 can be written for the absolute rather than relative reduction of variance. Specifying this alternate form for two different averaging times T_j and T_k, and subtracting the smaller of the resulting expressions from the larger, we eliminate the total variance to obtain:

$$\overline{u_{T_j}^2} - \overline{u_{T_k}^2} = \frac{9c}{20} \bar{U}^{2/3} \epsilon^{2/3} (T_k^{2/3} - T_j^{2/3}) \tag{6}$$

which represents the additional reduction in variance effected by increasing the averaging time from T_j to T_k. Solving this expression for the rate of dissipation gives our principal result

$$\epsilon = \frac{A}{\bar{U}} \left[\frac{\overline{u_{T_j}^2} - \overline{u_{T_k}^2}}{T_k^{2/3} - T_j^{2/3}} \right]^{3/2} \tag{7}$$

in which $A \equiv (20/9c)^{3/2}$. MacCready[7] notes that, as $\overline{u^2}/\overline{U^2}$ approaches zero, the value of c approaches twice that of the universal constant in the Kolmogoroff law for the turbulence spectrum. Since the magnitude of the latter is very nearly 0.5,[8] and since in the inertial subrange $\overline{u^2}$ must be quite small relative to the energy of the mean flow, it follows that $c \approx 1.0$; consequently $A \approx (20/9)^{3/2} \approx 3.3$.

At this point it can be seen that, because $\overline{u_{T_j}^2}$ and $\overline{u_{T_k}^2}$ are computed from the same basic data, the noninertial subrange fractions of turbulent energy appear equally in both terms, provided the larger averaging interval T_k is not so large that it begins to reduce these lower frequency contributions as well. It, therefore, follows that only contributions from the inertial subrange remain in the difference of smoothed variances in Equation 7. For practical purposes, however, it may be desirable to adopt some form of low-frequency filter in order to keep the magnitude of the recorded variances small. Nevertheless, there remains the distinct advantage that no critical considerations are contingent upon the characteristics of the particular device thus employed.

Some Comparisons with Experiment

The foregoing EVA relation for "Eulerian variance analysis" has been applied to a number of tabulations of consecutive, 2-sec mean wind speeds extracted from chart records supplied by ordinary anemometers. These were Sheppard-type, 3-cup instruments mounted at 12, 64, and 153 m on a radio mast located near Sale in Victoria, Australia.[9] Unfortunately, since it was not appropriate to the original study, these measurements were not associated with independent measures of ϵ, which might have been used to verify the magnitude of A. Since a determination of this kind would constitute a critical test of the validity of the EVA relation, a suitable observation program utilizing an improved anemometer is currently being prepared at this Laboratory.

In order for any one set of anemometer data to determine a unique value of ϵ when substituted in the EVA relation, the terms enclosed by brackets must exhibit a constant ratio over a range of averaging times extending from very small values to some maximum associated with the period of the slowest fluctuations in the inertial subrange. In Figures 87 and 88, values of the numerator of this ratio are plotted against corresponding values of the denominator, the variance reductions having been computed from the data of eight Victorian tower runs (summarized in Table 52) for a number of T_j, T_k combinations. Regions within which constant ratios, and hence unique determinations of ϵ, prevail are thus designated by straight lines which pass through the origin. This last is necessarily the case since very small averaging times result in very small reductions in variance; as T_j and T_k become small, the numerator and the denominator of the bracketed terms both converge upon zero. Obviously, the slope of the line through the origin represents the magnitude of the bracketed terms in the EVA relation.

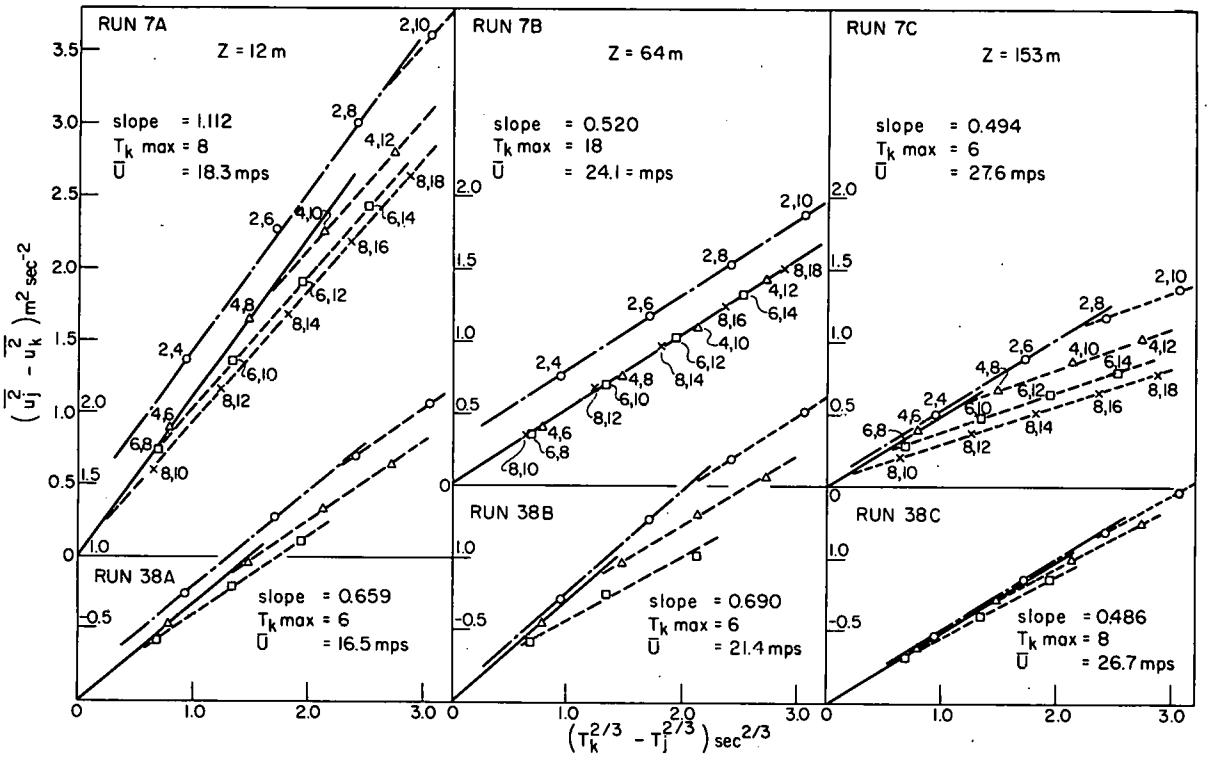

Figure 87

Variance reduction factors computed from Runs 7 and 38, the two runs with highest average wind speeds; slopes of solid lines correspond to magnitude of bracketed terms in Equation 7, and numbers adjacent to points designate T_j, T_k averaging intervals.

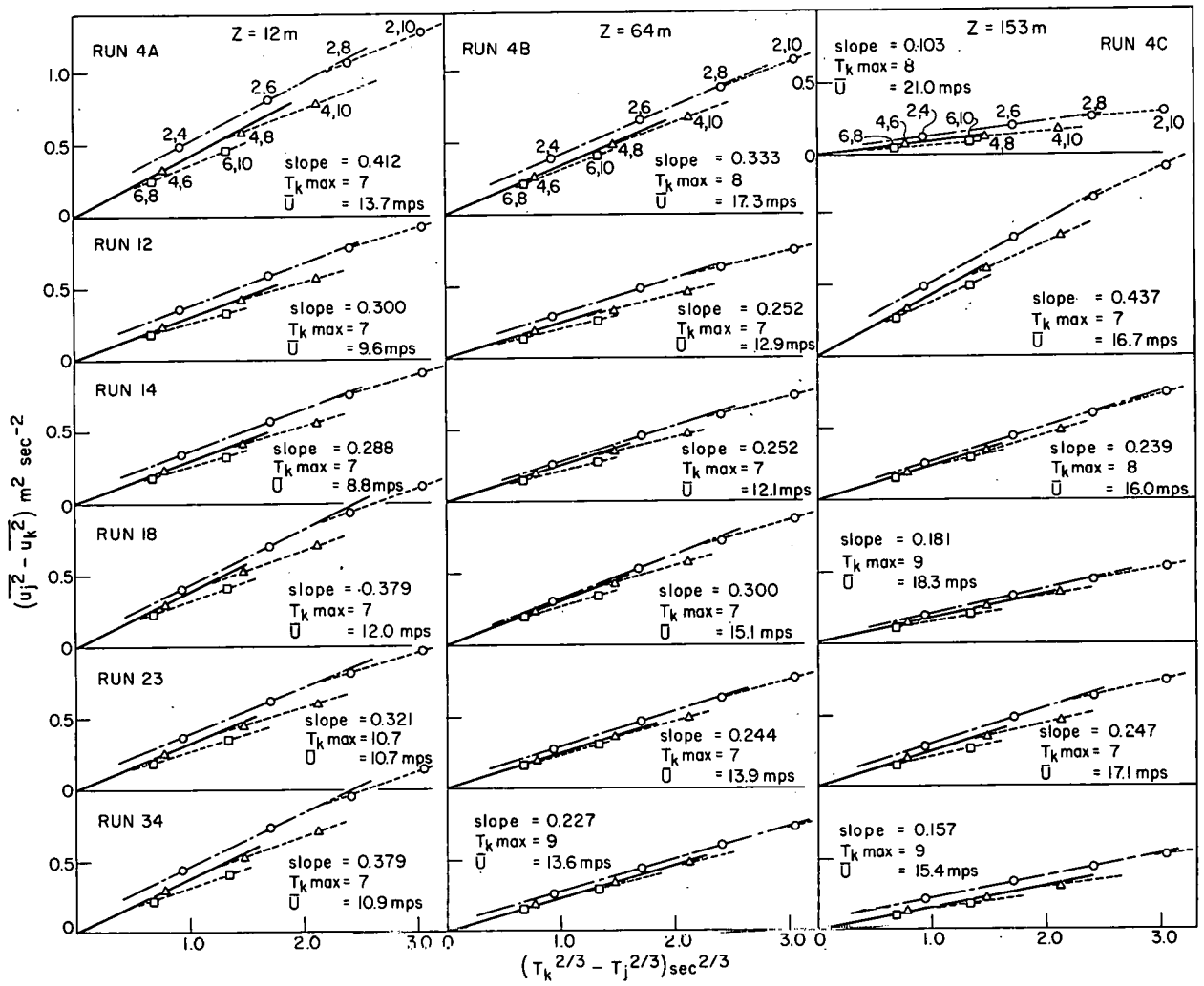

Figure 88

Variance reduction factors computed from Runs 4, 12, 14, 18, 23, and 34; note that, in every case, the slope of the solid line connecting the origin and the point located by the first 4 sec mean (T_j, $T_k = 4,6$) is identical to that of the dash-dot line located by 2-sec means immcdiately above.

Table 52

Summary of wind speed records obtained at three elevations near Sale, Victoria, Australia

Run No.	Date, 1952	Time, LST	Duration, min.	$\bar{U}$, m sec^{-1}			$\overline{u^2}$, m^2 sec^{-2}		
				12 m	64 m	153 m	12 m	64 m	153 m
4	14 Sept.	1634	8.6	13.7	17.3	21.0	4.21	5.02	1.74
7	16 Sept.	1821	4.9	18.3	24.1	27.6	9.25	6.24	4.32
12	17 Sept.	1925	7.9	9.6	12.9	16.7	2.89	3.08	4.08
14	17 Sept.	2155	7.9	8.8	12.1	16.0	2.41	2.02	3.93
18	20 Sept.	1000	8.6	12.0	15.1	18.3	3.89	3.28	3.34
23	15 Oct.	2148	13.2	10.7	13.9	17.1	4.78	3.92	5.08
34	28 Oct.	1450	8.0	10.9	13.6	15.4	4.10	3.03	2.68
38	19 Nov.	1330	6.8	16.5	21.4	26.7	6.67	4.77	6.63

Features typical of the graphical presentation are shown in detail in Figure 87. Note that, both here and in Figure 88, the sloping lines determined by variance reductions computed from 2-sec means ($T_j = 2$) fail to intersect the origin in every case. This deficient behavior upon the part of the least smoothed data can be attributed to the presence of spurious variance contributed by small, random reading errors introduced when the original chart record of switch pulses was reduced to 2-sec means. Since but one contact was made for each 5 m run of wind, errors in the means on the order of ± 0.1 count could contribute sufficient variance to account for the observed displacement. Additional smoothing effected by averaging over 4 sec or more evidently largely eliminates this noise introduced at higher frequency, for the expected intercept at the origin does occur when $T_j = 4$. In the upper left of the figure (Run 7, z = 12 m), points for $T_j \geq 4$ and $T_k \leq 8$ locate a line which does indeed pass through the origin. What is more, the slope of this (solid) line is virtually identical to that of the displaced (dash-dot) line located by $T_j = 2$ points immediately above, this supporting the view that these less-smoothed measures of variance reduction have been translated upward by high-frequency noise. When the data of this case are averaged over 10 sec, however, noninertial subrange contributions begin to be affected; therefore, all points for $T_k \geq 10$ depart from the line of principal interest. Interestingly, they depart in a highly uniform fashion, indicating that the turbulence regime on the low frequency side of the inertial subrange may be nearly as well organized as the subrange itself (cf. Figure 1, Reference 1).

Data taken at 64 m in the same run (upper center, Figure 87) provide a most dramatic illustration of the EVA method. Here a fortuitous combination of high wind speed (significantly improving the high-frequency response of the anemometers) and a turbulence spectrum featuring an unusually broad inertial subrange have combined to furnish data that fall on the principal line through the origin for all variance reductions from $T_j = 4$ to $T_k = 18$. In the same run at 153 m, however (upper right, Figure 87), smoothing over intervals larger than $T_k = 6$ again begins to reduce fluctuations that are not characteristic of the inertial subrange. This suggests that, at this great height, the field of turbulence had not attained a condition in equilibrium with the layers below. Complete adjustment through such a comparatively deep layer of air, it would appear, requires a fetch over a uniform surface significantly longer than that available at Sale.

From the additional runs of Figure 88 (where only the first few, significant T_j, T_k points are shown) as well as from those of Figure 87, it can be seen that, in every case, the first one or two variance reductions based upon 4-sec means locate a line through the origin which closely parallels an essentially independent slope derived from the 2-sec means. Thus, we may adopt a purely objective rule designating the value of the principal slope as that of the line intersecting both the origin and the first 4-sec mean, noting that this choice is invariably supported by the displaced

slope of the first few 2-sec means, and sometimes by both the second 4-sec mean and the first 6-sec mean (cf. Run 34, z = 64 m and 153 m). From slopes evaluated in this way, estimates of the dissipation rate were computed through the EVA relation, using the value A ≈ 3.3. Upon being reduced to a standard wind speed of 5 m/sec, according to the relation $\epsilon \propto \overline{U^3}$ as suggested by Priestley,[10] the results obtained appear to be of entirely reasonable magnitude. This is demonstrated by the plot of dissipation against height in Figure 89, where the average of the normalized values of the dissipation n observed at each level (cf. Table 53) lie quite close to the theoretical surface layer relation[11] for the not unlikely values of surface stress and roughness length of 1.2 dynes/cm^2 and 0.1 m, respectively.

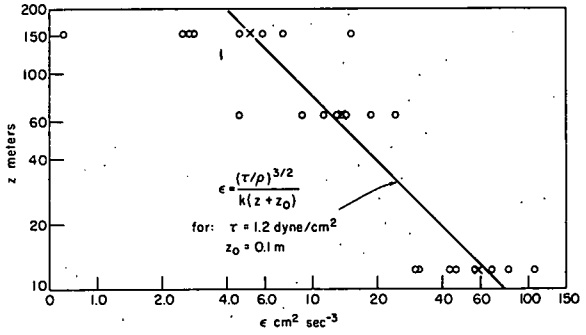

Figure 89

Observed variation of normalized dissipation with height; note close correspondence between average values at each level (X) and the theoretical surface layer relation for values of stress and roughness length indicated.

Table 53

Rates of turbulence dissipation observed at levels indicated; normalized values have been reduced to standard wind of 5 msec^{-1}

Run No.	Observed ε, cm^{2}sec^{-3}			Normalized ε, cm^{2}sec^{-3}		
	12 m	64 m	153 m	12 m	64 m	153 m
4	636.	367.	52.	31.	8.9	0.7
7	2118.	512.	416.	43.	4.6	2.5
12	558.	322.	569.	81.	18.8	15.1
14	583.	344.	240.	107.	24.2	7.3
18	641.	359.	139.	46.	12.9	2.8
23	561.	286.	237.	57.	13.4	5.9
34	705.	285.	133.	68.	14.2	4.6
38	1071.	883.	418.	30.	11.2	2.7
			Average	58.0	13.5	5.2

Conclusions

Application of the variance function to the analysis of smoothed time series has been shown to yield a comparatively simple relation for determining the rate of turbulence dissipation from data supplied by a single, 3-cup anemometer. This latter instrument offers a number of practical advantages, for its output is essentially linear and can be readily collected in true running-mean measures of the wind speed. Further, these sensors are relatively sturdy and free of calibration changes, being distinctly superior to hot-wire anemometers in both these respects. In order to use this simple instrument for EVA measurements at lower elevations and slower wind speeds, however, it will be necessary to improve both its resolution and response. Zubkovskii[12] has found that, at a height z, the lower limit of the inertial subrange is near $0.2\overline{U}/z$ cycles/sec when the atmosphere is neutrally stratified, the multiplying factor ranging from 0.08 in unstable conditions to 1.0 when the atmosphere is stable. Therefore, an anemometer, to be capable of detecting a significant portion of the inertial subrange in average conditions, should respond adequately to fluctuations with periods of the order of a single second or less; in other words, its response length should be less than 1 m. To this end, a low-inertia, high-torque 3-cup anemometer that produces a large number of pulses per unit of wind is now being completed at this laboratory.

Initial tests with this device will check the magnitude of the constant A by comparing EVA estimates of ϵ with those computed from simultaneous profile measurements. Assuming the promise of present results to be sustained by these more critical observations, the system will be applied to the problem of determining the vertical flux of momentum from single point measurements.[13,14] Eventually it is planned to carry out this procedure over water in order to obtain wind stress measurements appropriate to this most extensive and least understood portion of the earth's surface.

The writer would like to express his gratitude to the C.S.I.R.O. for affording him the opportunity to work with their Division of Meteorological Physics, Aspendale, Victoria, during the past year; sincere appreciation is extended to C. H. B. Priestley and W. C. Swinbank, leaders of that group, for many rewarding conversations on this work and similar matters, while special thanks are accorded E. L. Deacon who introduced the problem to the author and generously allowed him to use his wind-observation data.

References

1. F. K. Ball. J. Meteorol. 18, 553 (1961).

2. F. Pasquill. Quart. J. Roy. Meteorol. Soc. 89, 95 (1963).

3. P. B. MacCready and H. R. Jex. Quart. J. Roy. Meteorol. Soc. 90, 198 (1964).

4. G. I. Taylor. Proc. London Math. Soc. 20, 196 (1921).

5. Y. Ogura. J. Meteorol. 14, 176 (1957).

6. F. Pasquill. Atmospheric Diffusion. D. van Nostrand Co., Ltd., London, 1962.

7. P. B. MacCready. J. Meteorol. 10, 434 (1953).

8. H. A. Panofsky and F. Pasquill. Quart. J. Roy. Meteorol. Soc. 89, 550 (1963).

9. E. L. Deacon. Quart J. Roy. Meteorol. Soc. 81, 562 (1955).

10. C. H. B. Priestley. Turbulent Transfer in the Lower Atmosphere. University of Chicago Press, Chicago, 1959.

11. H. Lettau. J. Meteorol. 18, 125 (1961).

12. S. L. Zubkovskii. Izv. A.S. USSR, Geophys. Ser., No. 10, 887 (1962).

13. E. L. Deacon. Advances in Geophysics. 6, 211 (1959).

14. R. J. Taylor. J. Fluid Mech. 10, 449 (1961).

INSTRUMENTATION FOR ATMOSPHERIC TURBULENCE STUDIES

Paul Frenzen

In order to obtain data more suitable to the method of Eulerian variance analysis than those employed for the preliminary computations of the preceding article, an unusual 3-cup anemometer has been constructed. Further, since both the absolute calibration and the step-function response characteristics of this and future wind-measuring devices must be accurately known so that field measurements can be correctly interpreted, a calibration wind tunnel has recently been placed in operation. Suitable equipment for the measurement of flow velocity has also been installed.

The Low-inertia, High-torque (LIHT) Anemometer

Figure 90 shows the unique "LIHT" anemometer designed for the current study. For comparison, it is pictured alongside an instrument of

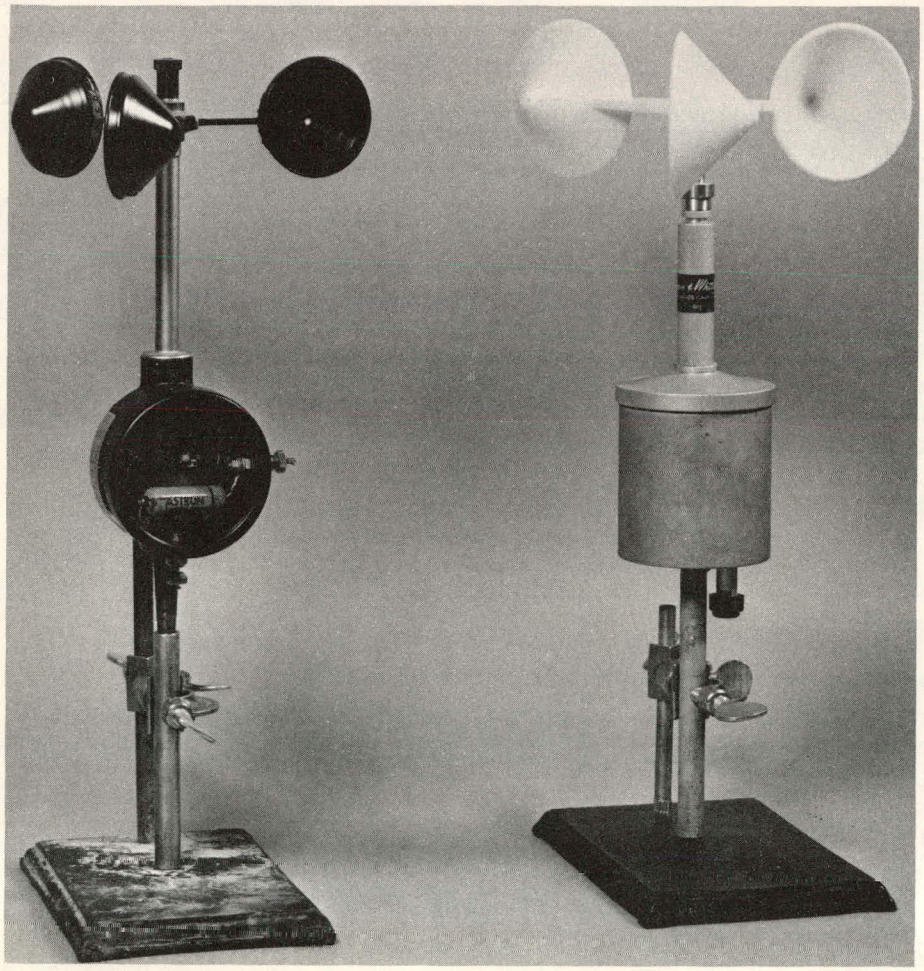

Figure 90

LIHT Anemometer

standard design, a 3-cup anemometer of the Sheppard type (Casella and Co., Ltd., of London) similar to those used to record the data used in the analyses of the preceding article. As may be seen, the cups of the LIHT instrument are nearly 50% greater in diameter than those of the Casella; they present, in fact, very nearly twice the frontal area to the wind stream. Since in both instruments the centers of the cups are mounted approximately the same distance from their respective axes of rotation, the net driving torque of the LIHT anemometer is about twice that of the Casella.

The three cups and the central, triangular support which together constitute the LIHT rotor are made of expanded polystyrene. Initially in the form of small beads pre-expanded to a density of 5 lb/cu ft, this material was sintered into solid components of the desired shape in machined brass molds brought to a temperature of 150°C for a few minutes in an ordinary autoclave. When assembled in a single rotor, the complete 3-cup assembly weighs only 6.4 g, this in marked contrast with the nearly 39-g weight of the aluminum and steel Casella rotor.

Assuming, to a first approximation, that the mass distributions of the two rotors are similar, and (for the purposes of this qualitative comparison) that the inertial contributions of the two different shaft assemblies are negligible, it follows that the ratio of the LIHT anemometer's driving torque to its moment of inertia will exceed that of the Casella in the same windstream by more than a factor of ten. Since this ratio largely determines the speed with which an anemometer can accelerate and decelerate in gusty winds, the relative superiority of the LIHT anemometer as an instrument to record turbulent wind fluctuations is evident. In fact, preliminary wind-tunnel tests of the LIHT anemometer indicate that the rotor accelerates from rest to $(1 - 1/e) \approx 63\%$ of the prevailing wind speed after only 0.5 meter of the wind has passed the rotor; in an average wind of 5 m/sec, this "response length" corresponds to a time constant of 0.1 sec. From the characteristics of exponential response, it follows that, under these conditions, the LIHT rotor will adjust to 95% of a sudden change in wind speed in 0.3 sec; therefore, the anemometer can be expected to be capable of accurately recording turbulent fluctuations to frequencies as high as 1 cycle/sec.

The base assembly of the LIHT anemometer (adapted from an older Beckman and Whitley instrument) includes a photocell, light-chopper arrangement for detecting the rotation of the shaft. The original assembly has been modified by reducing the moments of inertia of rotating components wherever possible, and substituting a six-hole light chopper for the original single-hole unit. This latter change is intended to improve the resolution of the short-duration (2 sec) measurements of the mean wind required for variance reduction analysis in the inertial subrange.

Because the three-cup design inherently results in three positions of maximum torque during each shaft rotation (successive "shading" of each cup by the next also impressing small, secondary minima roughly midway in each period of maximum torque), the angular velocity of the anemometer shaft experiences three major pulses during each complete revolution. This variation is not seen by either a one- or three-hole chopper, but it begins to contribute spurious, high-frequency variance to the anemometer record when choppers with more than three holes are employed. Future experiments with various choppers installed in the LIHT anemometer will determine what price, in the form of increased detection of rotor pulsation, one can afford to pay in order to gain the increased resolution desired for the variance analysis.

Wind-tunnel calibrations of the LIHT anemometer indicate that its output is virtually linear from 2.5 to 11.2 m/sec, the higher value representing the maximum tunnel speed presently available. The anemometer's response falls off gradually at lower wind speeds, the output being down about 3% near 2 m/sec, and down a rather large 12% near 1 m/sec. However, for the Eulerian Variance Analysis (EVA) measurements of turbulence dissipation, departures from linearity in this range are not serious, since other considerations limit the usefulness of the method at low wind speeds anyway.

The Calibration Wind-Tunnel

Figure 91 represents the general configuration of the calibration wind tunnel recently placed in operation at this Laboratory. Measuring about 19 ft in length over-all, the tunnel can supply a steady flow of air at speeds up to 25 mph with the present drive arrangement, but this can be readily increased by a simple change of pulleys. The 8-foot long test section measures 21 in. sq, while the intake of the contraction shown on the right is 55 in. sq, these dimensions giving a contraction ratio of 6.9.

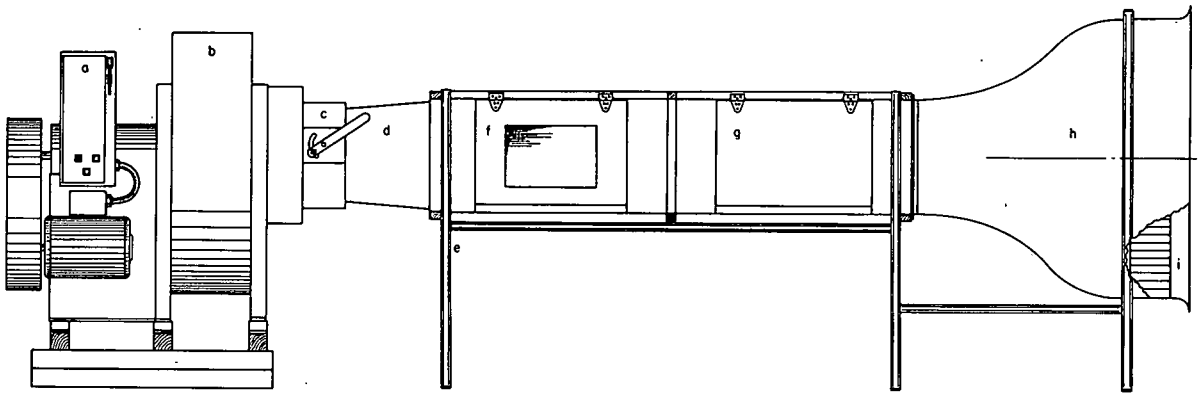

Figure 91

Configuration of calibration wind tunnel

In the figure, the letter (a) designates the location of the electrical control box mounted just above the 10-HP, 440-V, constant-speed motor which drives a large centrifugal blower through V-belts and pulleys located within the safety guard visible on the left. The blower exhausts upward at (b), at present without a special diffuser arrangement although this may become desirable when the tunnel speed is increased. At present maximum velocity, 6500 cu ft/min are exhausted at (b) (only about 6 ft below the room ceiling), the exit velocity approaching 40 mph; when these figures are multiplied by some factor between $1\frac{1}{2}$ and 2, it is clear that a diffusing arrangement will be needed in order to maintain a reasonable exhaust speed. Note that the entire blower unit is mounted on a heavy wooden frame of 4x4's, making it possible to move the assembly by forklift.

The velocity of the flow through the tunnel is controlled by an adjustable damper with four, alternately opposed blades installed at the inlet of the blower near (c) in the drawing. A short converging, sheet-metal adaptor shown at (d) connects the blower assembly to the test section; this component also contains a safety screen to prevent small objects from being drawn into the impeller blades.

Constructed of 1/2 in. exterior plywood, the 8-ft x 21-in. x 21-in. test section is framed with 1 x 2's and 2 x 3's. It is held at the height of the blower axis by a steel frame made of Unistrut, one leg of which is designated (e) in the sketch. Access to the principal working area is through the $2\frac{1}{2}$-ft wide door containing a Lucite window shown at (f), while the forward section can be reached through a similar door without a window as shown at (g).

The convergent entrance section was fabricated from 1/32-inch mild steel. Four identical sides for the assembly were carefully laid out and cut from flat sheets, the desired rectangular horn being obtained when the sheets were clamped and tack-welded along their four edges. In operation, air enters the tunnel at only 3 or 4 mph, first passing through a honeycomb array of some 1500 $1\frac{1}{2}$ x 8-in. close-packed paper tubes [shown at (i)] which smooth the initial flow. From a cross section in the neighborhood of the forward Unistrut leg, the entrance section converges parabolically, this forcing the incoming air to accelerate smoothly from rest, the acceleration increasing until the air reaches a cross section in the vicinity of the letter (h) in the sketch. From here, the cross-sectional area decreases linearly downstream to a point where the walls of the converging-cone are faired into the parallel walls of the test section. Thus, the air accelerates at a constant rate until it smoothly attains a constant, maximum speed as it enters the test section.

For calibration applications, the velocity of flow through the tunnel is measured by an N.P.L. standard pitot-static tube (Casella and Co.).

When used in conjunction with a tilting-tube manometer of the Krell type, measurements with better than 1% reproducibility are obtained for wind velocities in excess of 3 m/sec. Constructed by R. Selman of the RPY Staff Shop, this device affords a relative pressure measuring sensitivity of 4 dyn/cm^2 per millimeter displacement of the meniscus. A more sensitive, Chattock-Fry gauge recently obtained will extend the low-speed application of the pitot tube to about 2 m/sec. In addition, a precision, vane-type air meter (Short and Mason Portable Airmeter, Casella and Co.) has been obtained as a low-speed laboratory standard. Ultimately, its calibration will be verified by checking its performance on a rotating-arm.

PLUME RISE CHARACTERISTICS OF A SCALE MODEL SMOKE PLUME*

Gordon H. Strom** and Edward J. Kaplin†

Introduction

The development of equipment and techniques for conducting scale-model wind-tunnel experiments on the atmospheric diffusion of smoke plumes is a principal objective of the experiments reported here. An important feature of these experiments is the inclusion of temperature gradient as one of the test variables.

Following each of four series of experiments, various modifications and additions were made in wind-tunnel equipment and instrumentation to correct defects found in experimental results. The last two series (identified as Series III and IV) produced results which showed significant agreement with prototype data obtained with the Argonne Experimental Smoke Stack.

Diffusion characteristics found in Series III experiments have been reported.(1) Plume rise is reported here for Series III and IV. Of the meteorological and stack variables measured in these experiments only those significant to plume rise are included in this report. Plume diffusion and the remaining variables for both series will be reported later.

Modeling Criteria

Past experiments have shown that the following test variables are significant to plume rise and diffusion.

z = elevation

L = a reference dimension

*The experiments were conducted in the New York University Air Pollution Wind Tunnel with the sponsorship of the U. S. Atomic Energy Commission through the Argonne National Laboratory under subcontract #31-109-39-743.

**Resident Research Associate, Argonne National Laboratory, during several recent summers. Professor of Aeronautics, New York University, New York.

†Resident Research Associate, Argonne National Laboratory, summer 1959. Research Scientist, New York University, New York.

T = absolute temperature

dT/dz = temperature gradient

Γ = adiabatic lapse rate

u = airspeed at a given elevation

V_s = stack gas ejection speed

ρ = ambient air density

ρ_s = stack gas density

g = acceleration due to gravity assumed to have the same constant value in model and prototype

o = subscript denoting a reference elevation

It can be shown with a dimensional analysis that plume rise and diffusion are functions of the following set of dimensionless factors.

$$\frac{\rho_s}{\rho_o}, \frac{V_s}{u}, \frac{u_o^2}{gL}, \frac{u}{u_o}, \frac{L}{T}\left(\frac{dT}{dz} + \Gamma\right)$$

These factors are used to design the model experiments by giving them the same values in the model as in the prototype.

Plume rise is the elevation of plume centerline above the top of the stack from which it issues. This may be at a given distance downwind of the stack as reported herein or at the maximum elevation. Experimental results show that plume rise is most dependent on the first three of the above factors and also the fourth if the airspeed u at plume elevation is much different from u_o. The third factor u_o^2/gL is commonly known as Froude Number. It determines the airspeed at which the experiment is to be conducted.

Plume diffusion is measured in these experiments by the width of the plume at a given downwind distance. Plume diffusion is most dependent on Froude Number and on the last of the above factors. It is also dependent on mechanical turbulence which is not included in the above group of variables except to the extent that it is related to u/u_o. Mechanical turbulence is strongly dependent on the character of the ground surface upwind of the stack but is difficult to express in terms of a single variable. Convective turbulence is most dependent on the last of the above factors. u/u_o may be considered as a measure of the velocity profile which is determined largely by mechanical and convective turbulence, i.e., total turbulence. u/u_o has, therefore, some dependence on the last factor.

The above variables are used because they are closely related to the test variables measured in these experiments. With improvements in

instrumentation and experimental techniques a better group of variables will probably be developed.

Air viscosity is a variable important to many types of fluid motion. Had it been included in the above set, the dimensional analysis would have shown some form of Reynolds Number as an additional factor. Reynolds Number gives a requirement for airspeed different from that found with Froude Number. Experience has shown that a plume with density different from that of the ambient airstream (ρ_s/ρ_o not equal to one) is inaccurately modeled if it is not in accord with Froude Number. One of the purposes of these experiments is to determine under what conditions a plume can be accurately modeled when Reynolds Number is not followed.

Test Apparatus

The experiments were conducted in the New York University Air Pollution Wind Tunnel. This wind tunnel is uniquely equipped to conduct experiments at the very low wind speeds required for Froude Number modeling. This is accomplished with special equipment for precise control of temperatures at the airstream boundaries which prevents the formation of unwanted convective air motions. The interior of the test section which bounds the airstream is in the form of a horizontal rectangular duct 40 ft long, 7 ft wide, and $3\frac{1}{2}$ ft high. The desired temperature gradient is produced by a set of heating elements located in the airstream at the beginning of the test section. Velocity and turbulence profiles are controlled by a set of roughness elements located close to the heating elements. They are supported by horizontal metal plates which are placed one above the other and span the airstream. Adjustment of the size and number of elements on each plate and spacing of the plates provides the means for varying the velocity and turbulence profiles. The roughness elements decrease in number and increase in size with distance above the floor. Plate spacing is greater at the higher elevations. A tabulation of the above dimensions for Series III experiments is given in Reference 1. The values are similar for Series IV.

A 1/96 linear scale model of the Argonne Experimental Smoke Stack (17.5 in. inside diameter, 110 ft high, prototype dimensions) produces the smoke plume. It is located 25 ft downstream of the roughness plates. The desired effluent density and ejection speed are obtained by metering the flow of air and helium. These are combined and fed to the stack. The plume is made visible for photographic purposes by introducing an oil-fog type of smoke.

Two 4- x 5-in. Crown Graphic cameras located outside of the test section are used to photograph the smoke plume from above and from the side.

Airspeed is measured with a hot-wire anemometer arranged to indicate mean speed (turbulence will be measured in the next series). Temperature is measured with thermocouples. The velocity and temperature probes are mounted on a survey carriage so that the probes can be moved in three dimensions.

Test Procedure

Following the establishment of thermal equilibrium between the air-stream and the various thermal controls, a test run is started. Vertical velocity and temperature profiles are measured at a number of stations in the test section starting 43 in. downstream of the roughness plates and ending 80 in. downstream of the model stack. An overlap of measurements at the beginning, during, and at the end of the test run provides a check on the constancy of test conditions. In addition, smoke plume photographs are taken at the beginning, middle, and end of a run. A test run covers a period of approximately 3 hr.

The multiple-exposure technique is used in photographing the plume to obtain the outline of the plume formed over a period of time. Sixteen exposures were made at 2-sec intervals on each negative.

Test variables were selected, in accordance with the modeling criteria given earlier, to cover a range of conditions (at model scale) similar to that in the prototype data. For the 1/96 linear scale of this model, the following conversion equations were obtained:

$$u_{op} = \sqrt{96}\, u_{om}$$

$$(\rho_s/\rho_o)_p = (\rho_s/\rho_o)_m$$

$$(V_s/u_o)_p = (V_s/u_o)_m$$

$$(dT/dz)_p = 1/96[(dT/dz)_m + \Gamma] - \Gamma$$

where the subscripts "p" and "m" refer to prototype and model respectively. The other symbols have the meanings given earlier.

Results and Analysis

All of the results presented are expressed in terms of numerical values at prototype scale obtained by converting model data with the above conversion equations.

The coordinates of the path or centerline of the plume are obtained as part of the total results found in the analysis of the negatives for plume diffusion. The centerline is taken as the locations midway between the top

and bottom of the plume. Plume rise h is the vertical distance from stack top level to the plume centerline. Results presented here are all for a downwind distance (measured from the stack base) of 60 m. This distance was selected because of the availability of prototype data, but it was also a distance at which the plume rise, in most cases, was nearly complete.

Coordinates of the plume outline were obtained from the negatives with the Telereader by the Argonne Meteorology Group. These were reduced to the desired plume characteristics with an electronic computer program by the Argonne Applied Mathematics Division, which also reduced the velocity and temperature profile data to obtain specific values as required and least square regression lines.

Results for Series III and IV experiments are presented. Series IV was conducted during the summer (June-July, 1961) and Series III had been previously conducted during the winter (Nov.-Dec., 1959). Between these two series, various modifications were made in the wind-tunnel equipment to improve thermal control. An instrument towing chamber was developed to obtain more accurate calibration of the hot-wire anemometer used to measure the air speed. Techniques of data reduction and analysis were improved, and on this basis the data that previously had been obtained and reported for Series III were recomputed.

Plume Rise

Plume rise data are presented in two forms. The observed plume rise h_{obs}, at a downstream distance of 60 m, was analyzed first as a function of the stack effluent-to-air speed ratio V_s/u and then as a function of calculated plume rise h_{calc} found with the Holland formula (see Equation 1 below). It should be noted that the value for the air speed u was measured at an elevation of 36.6 m above ground, which was approximately plume height for most test runs. This speed was taken from velocity profile curves obtained from the Meteorology Tower in the prototype and from the measurements at the stack station in the model. In Series IV where there are one or more sets of data for this station, the values used are averages.

Stack load (or simply load) refers to volume flow and is nearly proportional to V_s except for small variations in temperature between the point of measurement and the stack top. Specific fractions of load are identified and while a particular run may show some deviation, it is close enough for classification. In the model data Δt, which in the prototype data is the difference between the stack effluent temperature and the ambient air temperature, is equivalent to the temperature difference which would give the density of the helium-air mixture which is actually used at the ambient temperature. Prototype density difference is due to heating of the air which enters the stack. Prototype Δt values vary but are in the range of 60°F to 70°F.

Figures 92 through 95 show observed plume rise values h_{obs} at 60 m downwind distance as functions of the speed ratio V_s/u. V_s/u is chosen as the variable because of its physical significance in the ratio of momentum of the emitting plume to that of the ambient airstream. It appears also in various plume rise equations developed by various authors. Least squares regression lines are also plotted. In Figures 92, 94, and 95 the lines are computed as the regression of V_s/u on h_{obs} while in Figure 93 the two forms are shown, i.e., V_s/u on h_{obs} and h_{obs} on V_s/u. Correlation coefficients for model data in Figure 94 are 0.61, 0.98, and 0.97 for 1/2, 3/4, and full load, respectively. Prototype data taken from Reference 2 are shown in Figure 93 for comparison with the corresponding model experiments. Prototype regression lines are also shown in the two forms. Correlation coefficient is 0.46. Separation of prototype data by load did not show a distinct division and cannot, therefore, be so identified. Most of the prototype data are at full load with much of the remainder at 3/4 load, and only a few at 1/2 load. Figure 95 shows regression lines only for all model data.

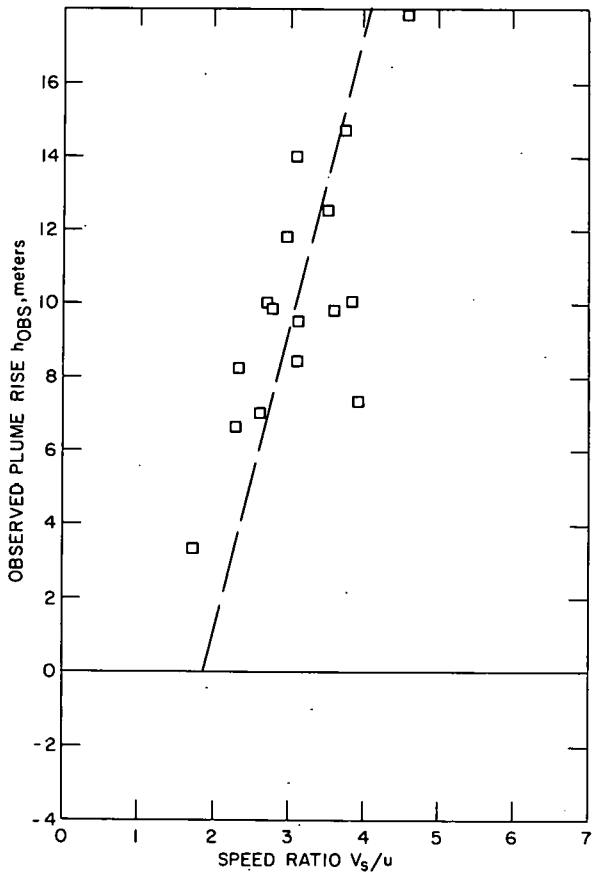

Figure 92

Observed plume rise vs speed ratio for Series III wind tunnel experiments. $\Delta t = 60^{o}F$. Stack is operating at full load (V_s = 12.2 m/sec). Least squares regression line is shown.

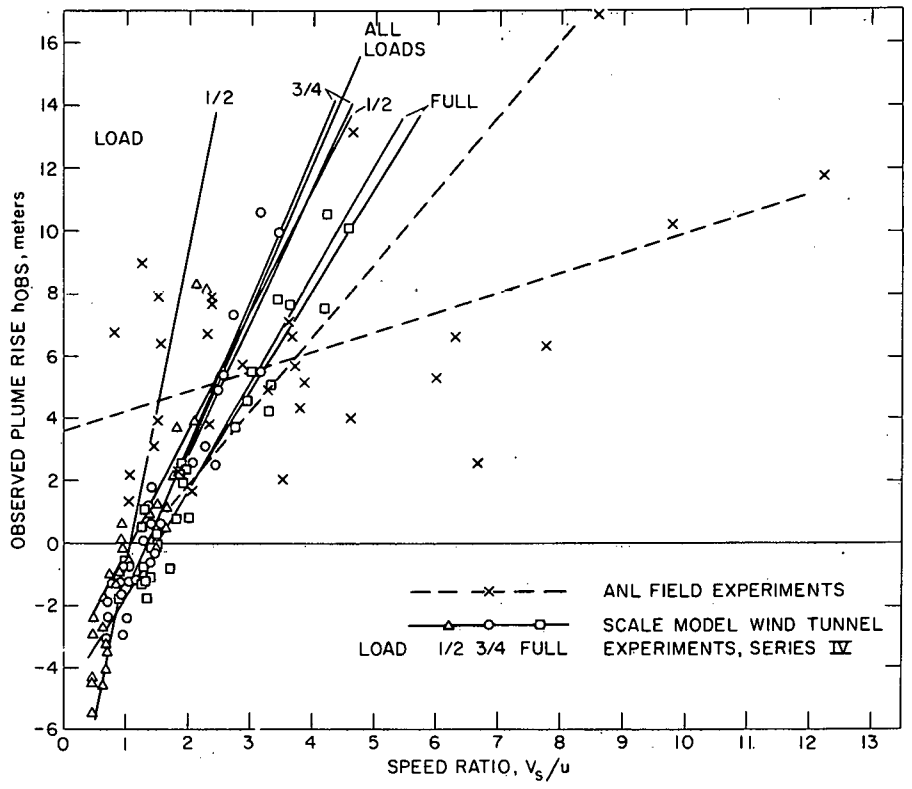

Figure 93

Observed plume rise vs speed ratio for Series IV, $\Delta t = 60^{o}F$, wind tunnel experiments and ANL field experiments. Temperature increment Δt for field experiments varied between 60 and $70^{o}F$. Stack gas ejection speeds V_s are 6.1, 9.14, and 12.2 m/sec for 1/2, 3/4, and full loads, respectively. Regression lines are shown. Curves with smaller slopes are regressions of h_{obs} on V_s/u.

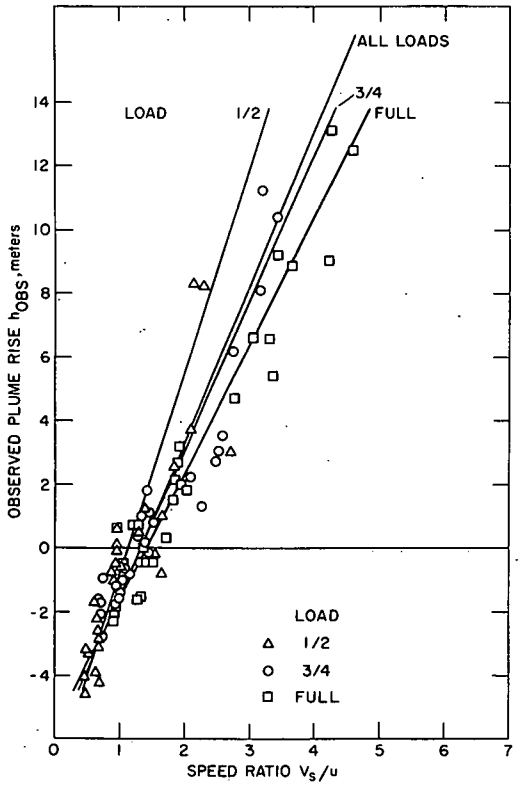

Figure 94

Observed plume rise vs speed ratio for Series IV, $\Delta t = 135^{o}F$, wind tunnel experiments. Regression lines are shown.

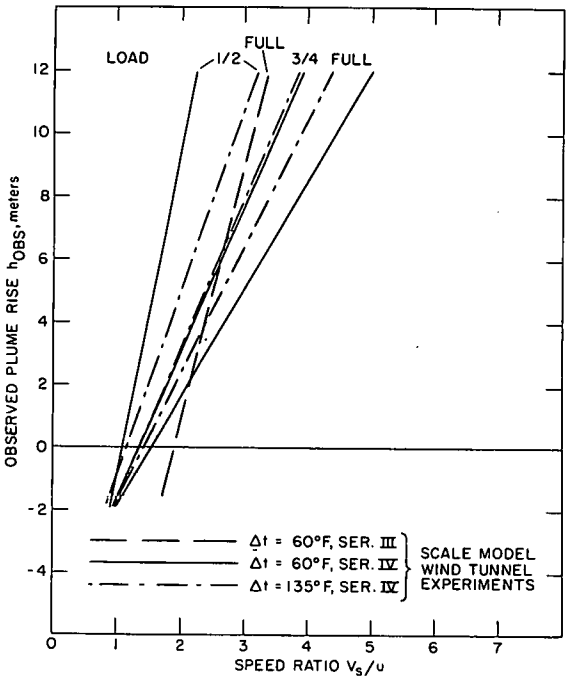

Figure 95

Least squares regression lines of observed plume rise vs speed ratio for all wind tunnel experiments.

Comparison of observed values with those calculated by the Holland formula are shown in Figures 96 and 97. In metric units, Holland's formula has the following form as shown in Reference 2.

$$h_{calc} = \frac{1.5\ V_s d + 4 \times 10^{-5}\ Q_H}{u} \qquad (1)$$

where

d = stack diameter at outlet in meters

V_s = stack effluent ejection speed in m/sec

Q_H = heat emission rate in cal/sec

u = air speed in m/sec

These figures were prepared to provide another form of comparison with the prototype as well as direct comparison with a recognized formula. Least squares regression lines are shown in both forms in Figure 96 and the regression of h_{calc} on h_{obs} in Figure 97. Correlation coefficients for model data in Figure 96 are 0.61, 0.95, and 0.96 for 1/2, 3/4, and full load, respectively. The value for prototype data is 0.46.

Figure 96 shows model data for conditions closest to prototype as in Figure 93, and Figure 97 shows regression lines only.

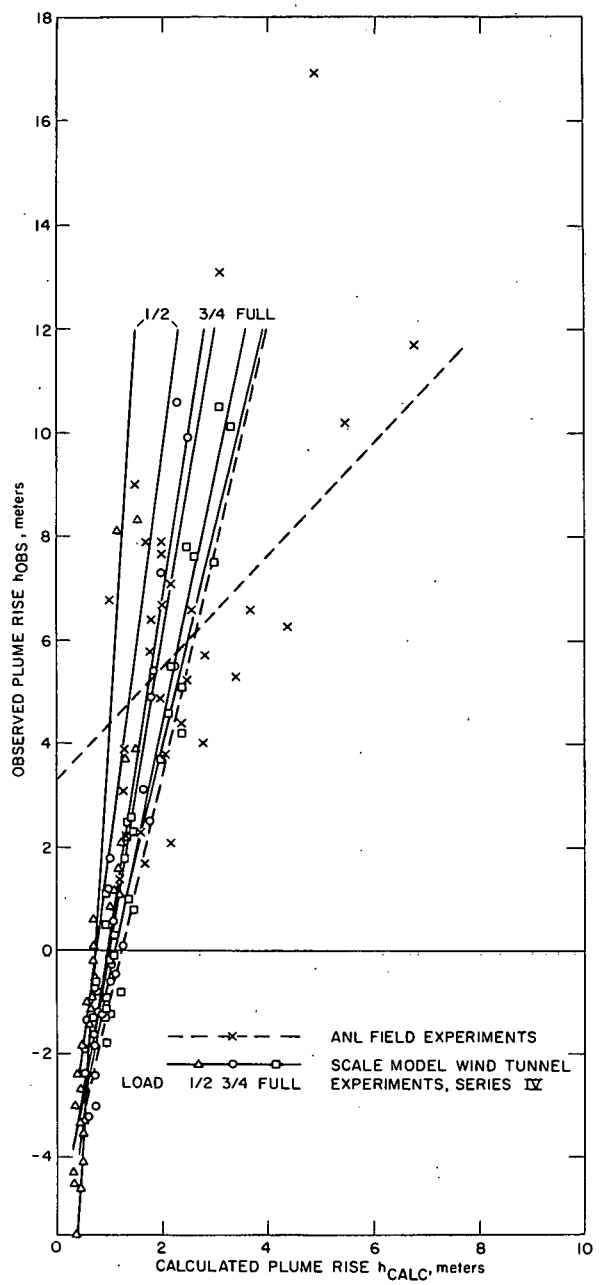

Figure 96

Observed vs calculated plume rise by Holland formula for Series IV, $\Delta t = 60^{o}F$, wind tunnel experiments and ANL field experiments. Regression lines are shown. Curves with smaller slopes represent regressions of h_{obs} on h_{calc}.

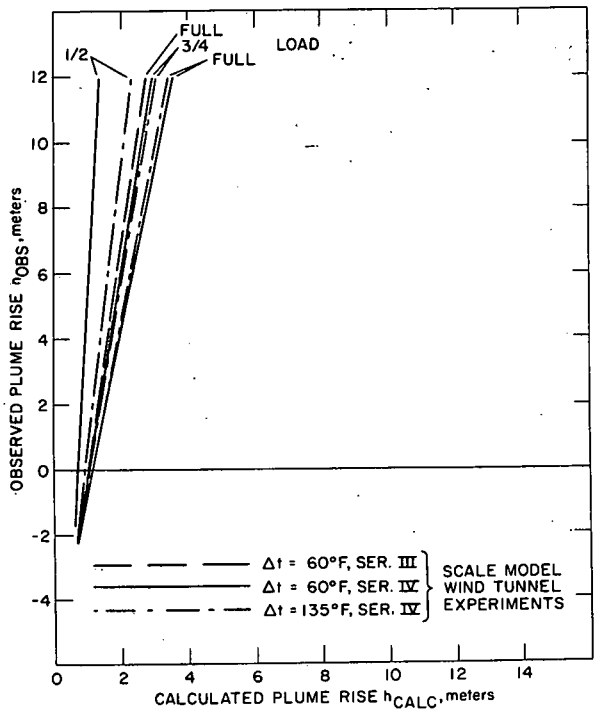

Figure 97

Least squares regression lines of observed vs calculated plume rise by Holland formula for all wind tunnel experiments.

Streamlines

Series III and IV experiments show distinct differences for otherwise identical values of test variables, as is evident when comparing results for full load, $\Delta t = 60°F$. The improvements made in thermal control equipment between these two series were not expected to affect plume rise characteristics. Of the various features in the data which could be checked and offer a possible explanation, the most promising seemed to be the inclination from horizontal of the flow direction in the vicinity of the stack. A relative small change in the inclination of flow could make a significant change in plume rise.

In order to explore this possibility, it was necessary to analyze velocity profile data to determine streamline configuration which, in turn, would show the local direction of air movement. This was necessary

because no attempt had been made during the conduct of the experiments to determine flow direction by direct measurement. It appeared justified to assume two-dimensional flow in the central vertical plane through the stack, because the velocity profiles toward the slides of the test section showed no significant departure from those on the central plane. It was further observed that there was no significant increase in the volume flow along the center plane as would be expected if there had been significant distortion to the propagation of wall effects to the central plane. Since a pair of streamlines (in two-dimensional flow) bounds equal volumes of flow, the analysis was performed by integrating the volume flow vertically at various profile stations starting at the floor, which is assumed to form the lower boundary streamline. From graphs of integrated volume flow versus vertical distance, locations of points which bound equal amounts of flow were found and used for plotting the streamlines. The fields of streamlines for four test runs are shown in Figure 98. The vertical coordinates are expanded to emphasize the deviations from horizontal. Figure 99 and 100 show, for each test run, the one streamline which passes through the top of the stack. Deviations in streamlines showed little

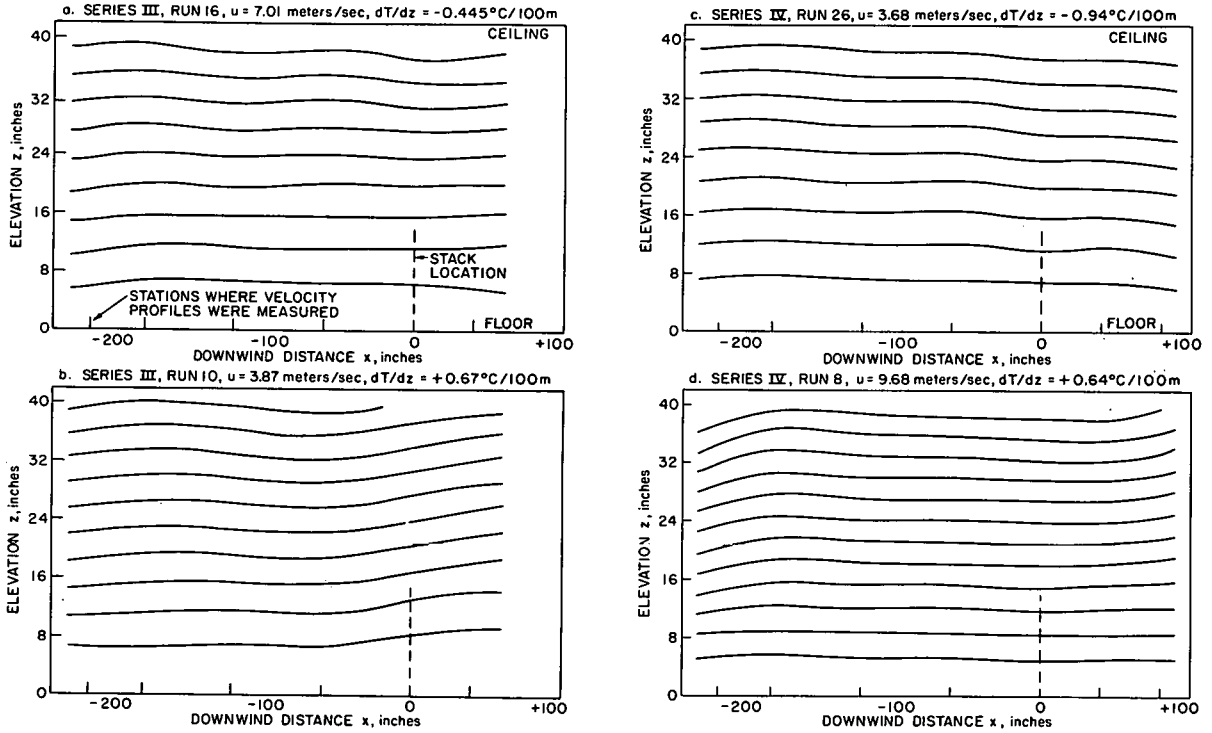

Figure 98

Streamlines of flow in the wind tunnel test section for four test runs. Vertical scale is expanded by a factor of five to magnify deviations in flow. Distances are given in actual wind tunnel units while speed and temperature gradient are in full scale equivalents.

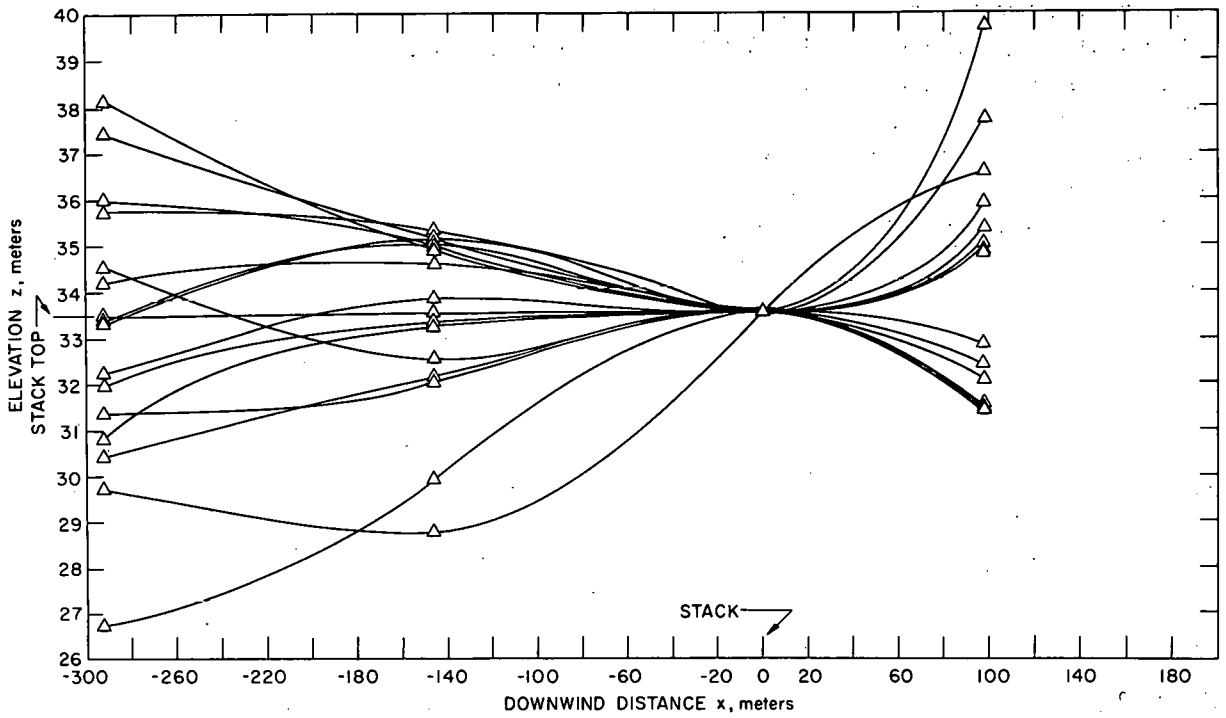

Figure 99

Streamline which passes through top of stack for each of the test runs in Series III. Distances are in full scale equivalents with vertical scale expanded.

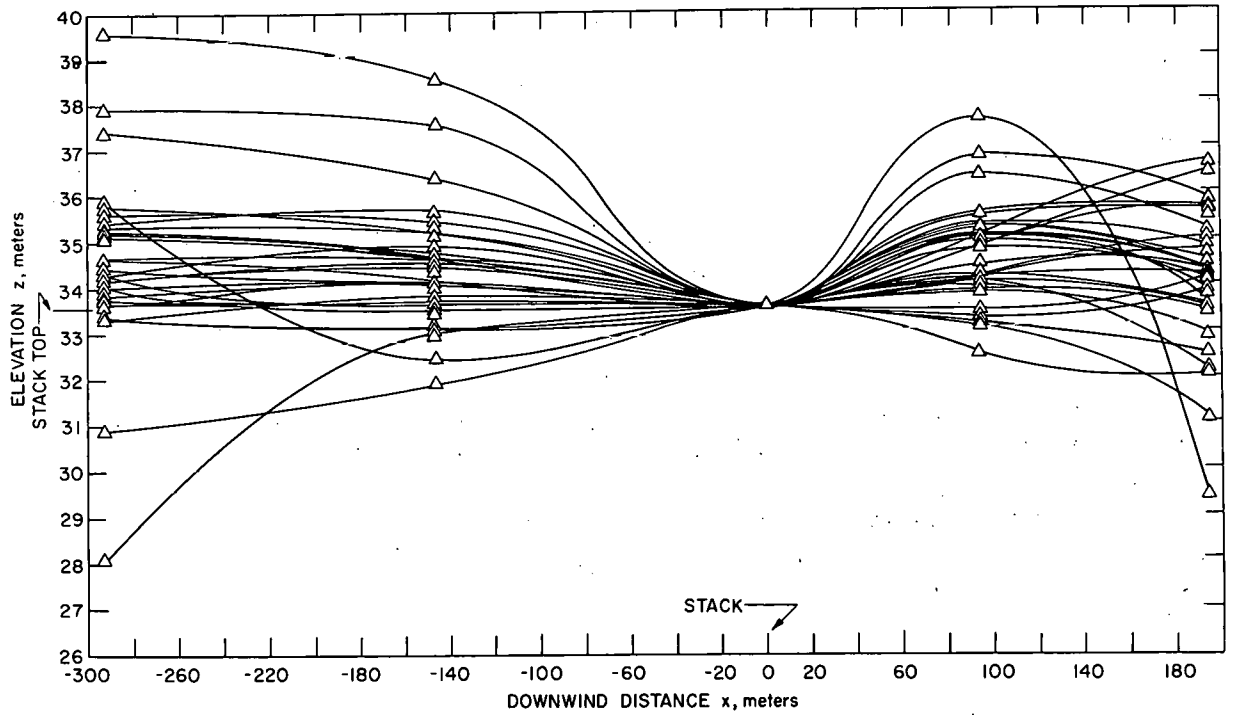

Figure 100

Streamline which passes through top of stack for each of the test runs in Series IV. Distances are in full scale equivalents with vertical scale expanded.

correlation with test variables except airspeed. Airspeed dependence is shown in Figure 101 by the difference in streamline deviation between station 40 (97.6 m downstream of the stack) and station 0 (at the stack). The plume rise values were then corrected by the amount of the changes in elevation of the stack top streamline over the 60 m plume travel distance. Analysis of the resulting values showed that streamline deviation did not account for the differences between Series III and IV experiments.

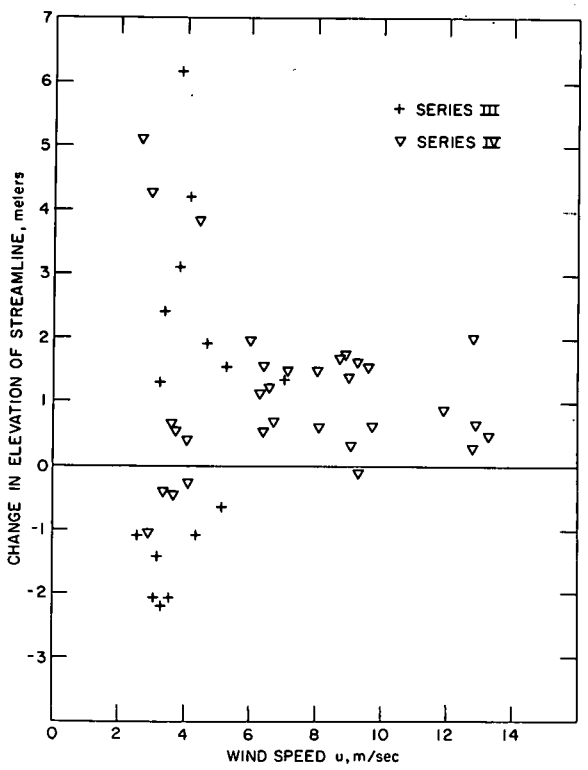

Figure 101

Change in elevation of streamline through stack top when passing from stack to station immediately downstream at x = 97m for all test runs.

Empirical Equations for Plume Rise Test Data

As will be discussed below, the presentation of plume rise data as a function of V_s/u (Figures 92-95) or in terms of calculated rise by the Holland formula (Figures 96 and 97) showed a separation by stack load. Not included herein are results for other plume rise formulas which gave a similar separation by load. In addition, the test results showed a number of cases in which negative values for plume rise were found, which is not predicted by the Holland formula or others for buoyant plumes. Evidently some other formula may give a better fit to these data. For this purpose the empirical equations given below were derived. Since the number of test runs was limited, any empirical relationship is likely to reflect experimental errors peculiar to this set of data and would, therefore, be modified if additional data were acquired.

The following empirical equations are based on Series IV data only. Since only two stack effluent temperatures were tested, the dependence on temperature was not treated in one comprehensive equation; separate equations are given for the two temperatures. The equations are presented in two forms which resulted from various attempts at obtaining a good fit.

Form A

For $\Delta t = 60°F$

$$h_{obs} = 0.423\ V_s + \frac{39.57}{u} - 9.83 \qquad (2)$$

For $\Delta t = 135°F$

$$h_{obs} = 0.523\ V_s + \frac{40.46}{u} - 10.44 \qquad (3)$$

Form B

For $\Delta t = 60°F$

$$h_{obs} = \frac{1}{u}(2.39\ V_s + 17.65) - 5.96 \qquad (4)$$

For $\Delta t = 135°F$

$$h_{obs} = \frac{1}{u}(3.01\ V_s + 12.95) - 5.66 \qquad (5)$$

Figures 102 and 103 show Form A equations plotted as scatter diagrams of observed versus calculated rise. The same diagrams for Form B equations would show a little more scattering of data and thus not quite as good a fit. Form B is included because it includes the speed ratio V_s/u which appears in various published formulas.

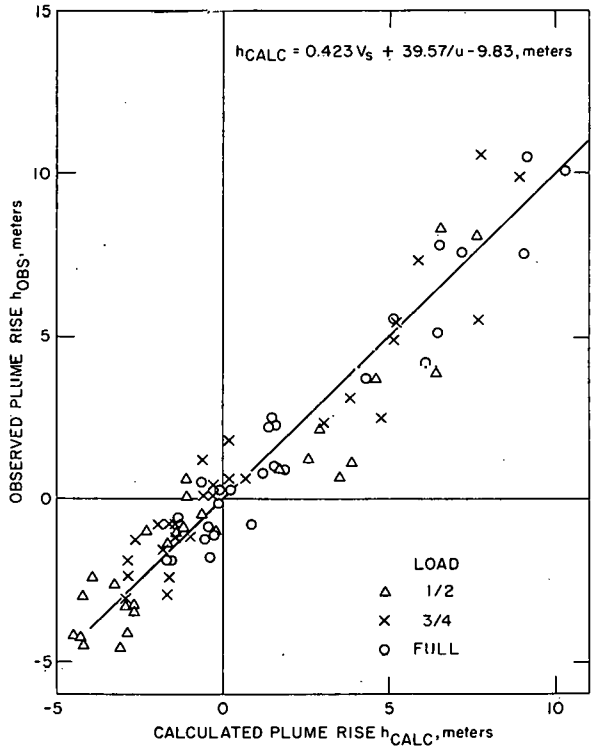

Figure 102

Scatter diagram of observed vs calculated plume rise by empirical equation for Series IV, $\Delta t = 60°F$.

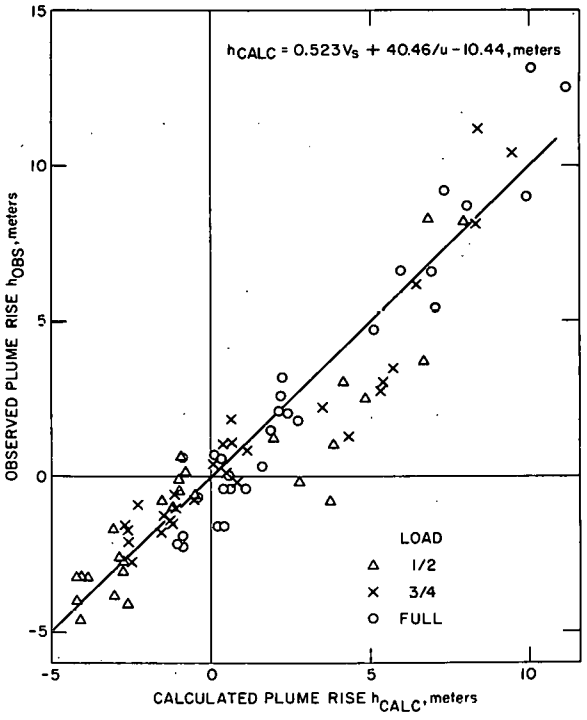

Figure 103

Scatter diagram of observed vs calculated plume rise by empirical equation for Series IV, $\Delta t = 135°F$.

The regression line of V_s/u on h for all loads in Figure 93 is given by the equation

$$h = 4.61\ V_s/u - 6.35 \qquad (6)$$

Figure 104 is the scatter diagram which results from the application of this equation to the Series IV, Δt = 60°F.

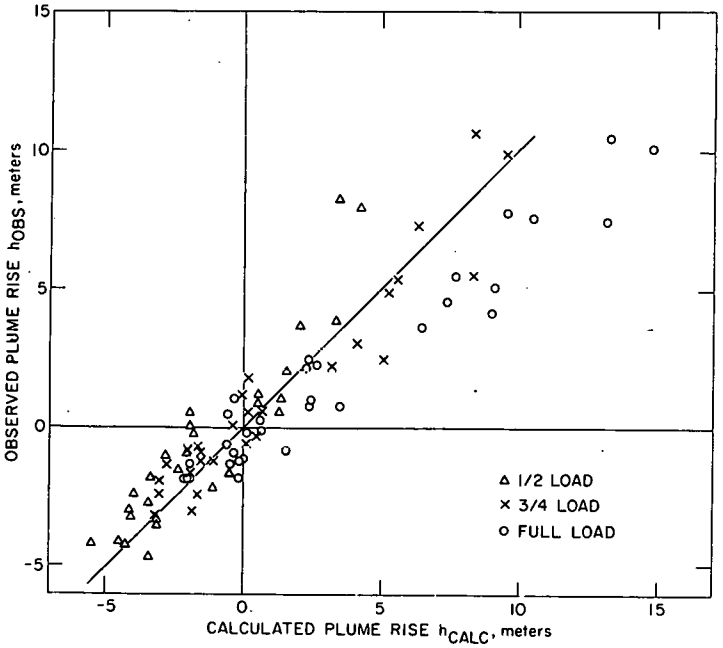

Figure 104

Scatter diagram of observed vs calculated plume rise by regression equation for Series IV, Δt = 60°F.

Discussion of Results

Plume Rise

Series IV experiments (Figures 93-97) show that the plume rise is not adequately represented by a simple linear relationship with V_s. In the empirical Equations 2-5 V_s appears as a linear term, but to this must be added at least a constant. The test results also show that the model predicts rise values which are higher than those found for the prototype. In Reference 1 it is shown that for Series III experiments the scale model plume had less diffusion than the prototype plume and was, therefore, relatively smaller in diameter and less diluted with the ambient airstream. This is expected to result in a greater plume rise as shown in Figure 95. In the next series of experiments it is planned to increase the mechanical turbulence in the airstream. This will increase plume diffusion and probably bring the model plume rise values closer to those of the prototype.

An interesting feature in the test results is the tendency for plume rise to go negative with small values of V_s/u. The crossover occurs between 1.0 and 2.0. A similar result is reported by Jensen and Franck[3] who tested a scale model stack of approximately the same diameter as the Argonne model. None of the well-known plume rise equations,[2] some of which are empirically derived from field data, predicts negative values for small V_s/u. As can be seen in the figure, the Argonne prototype data do not show any negative values. Thus it may appear that the negative

values were peculiar to the model. A possible explanation is the dependence on Reynolds Number which is not accounted for in these experiments since it conflicts with Froude Number as discussed earlier under modeling criteria. Tests of flow around cylinders show that the low pressure turbulent wake is wider at low Reynolds Numbers than at high. If this effect occurred near the top of a stack, there would be a greater tendency for the scale model plume to be drawn into the wake, thus giving lower rise.

The Argonne data do not, however, go to values of V_s/u as low as do the model data. Whether extrapolation of prototype data to low V_s/u will give negative values is difficult to determine because of wide scatter. Since the two regression lines are considerably different, the least squares method does not give a definite result. The best fit may be somewhere between the two lines. If it were midway, it would not yield negative values. If it were closer to the one with the greater slope then negative values would be obtained; the data shown here do not rule out this possibility. Obviously more prototype data are needed for low V_s/u. This is extremely important since substantial agreement with these model results may be interpreted to show that the flow around the stack top is not dependent on Reynolds Number to any significant degree. The stack top is often thought to be a critical location as far as Reynolds Number effects on smoke plume characteristics are concerned.

Streamlines

Series III observed rises were higher than those found in Series IV for the same test conditions. It seemed that the cause must be in the airstream and not in the stack effluent, since control and measurement of effluent characteristics are simple and direct. Also, the turbulence in the airstream does not appear to have changed significantly because plume diffusion characteristics for the two series are approximately the same. Such differences as do occur would suggest an effect on rise opposite to that found. It was expected that the streamline analysis would provide a clue to the reason for the differences in observed rises since airstream inclinations from horizontal would directly affect plume rise. Stack top streamlines in Figures 99 and 100 show a distribution over positive and negative angles of flow inclination with a maximum deviation of 3 deg along the 60 m the plume travels. Inclination of streamlines showed little dependence on test variables except airspeed (see Figure 101). The inclinations are greatest at the lowest speed, indicating that the large inclinations, at least, are caused by thermal influences.

This indication is strengthened by the fact that the two series were conducted during different seasons resulting in differing temperatures of air in the building. This could affect some parts of the wind tunnel which do not have thermal controls, particularly the walls downstream of the test section, and is to be corrected before the next series of tests is run. Thermal stability of the airstream was one of the test variables in both

series. Although a slight trend to higher rise values in both series for unstable conditions could be detected, there was no strong indication that stability affected plume rise. This may be due in part to the fact that there were too few runs of varying stability for any given combination of other variables.

It is believed that Series IV gave a more accurate set of data than Series III because of improvements in techniques, control, and calibration equipment. It is possible that the streamlines in either series are not correct because of change in unmeasured flow conditions over the three-hour period of test measurement. Since the attempt to resolve the difference between the series by applying a correction based on streamline inclination was unsuccessful, the cause remains unknown.

Empirical Equations for Plume Rise Data

Series IV experiments were conducted at two effluent temperatures, (simulated by control of the helium-to-air ratio). Test conditions of the $\Delta t = 60°F$ experiments were close to those for the existing prototype data. $\Delta t = 135°F$ experiments were added in anticipation of future prototype data. The difference in temperature between the two is not large in terms of causing a difference in plume rise. The effect on plume rise is best observed by studying the empirical Equations 2 and 3 or 4 and 5. Using Form A equations 3 minus 2 to find that part of the rise due to temperature results in

$$\Delta h = 0.1\ V_s + 0.89/u - 0.61 \qquad (7)$$

Evidently there are combinations of V_s and u which will give negative Δh. At u = 2.66 m/sec, the lowest tested, Δh will be negative below V_s = 2.75 m/sec. At u = 13.3 m/sec, the highest tested, Δh will go negative below V_s = 5.43 m/sec. It is to be noted that tests were conducted at the three V_s values of 6.1, 9.14, and 12.2 m/sec. Thus there are no experimental data in the range where Equation 7 shows negative values. It should, therefore, not be applied to this range.

The empirical equations are presented to show trends in the results of these experiments including the effect of change in effluent temperature, which was difficult to express directly in terms of test readings. These equations are not intended for application to other situations but may suggest forms to be looked for in empirical formulations. Form A does not appear physically sound because of separation of the effects of V_s and u, but it does give a slightly better fit than Form B. Both forms have a constant term which seems unavoidable because of negative values of rise at low V_s/u.

Figure 104 shows the result of applying the regression Equation 6. The fit is not as good as that obtained with the empirical equations, in

that there is greater scatter. There is some separation by stack load as was found for the Holland formula and when taken as a function of V_s/u in Figures 93-95.

References

1. G. H. Strom and E. J. Kaplin. Convective Turbulence Wind Tunnel Project. Argonne National Laboratory, Radiological Physics Division Semiannual Report January through June 1960. ANL-6199, p. 119.

2. H. Moses and G. H. Strom. A Comparison of Observed Plume Rises with Values Obtained from Well-Known Formulas. J. Air Poll. Control Assoc. 11(10), 455 (1961).

3. M. Jensen and N. Franck. Model Scale Tests in Turbulent Wind, Part 1. Danish Technical Press, Copenhagen, 1963.

PUBLICATIONS

June 1963 - July 1964

Berlman, I. B., R. Grismore, and B. G. Oltman. A Study of α/β Ratios of Organic Scintillation Solutions. Trans. Faraday Soc. 59, 2010-2015 (September 1963).

Berlman, I. B., and O. J. Steingraber. Improved Fluorescence Decay-Time Measuring Apparatus. IEEE Trans. NS-11(3), 27-28 (June 1964).

Bowe, J. C. Electron Velocity Distributions in Gases. Am. J. Phys. 31, 905-912 (December 1963).

Bowe, J. C. Mobility of Electrons in the Noble Gases. Phys. Rev. 135, A355-A361 (April 20, 1964).

DiFerrante, E. R. The Natural Concentration of Ra^{226} in Bovine Bones and Teeth. Health Phys. 10, 259-264 (April 1964).

Frenzen, P. Meteorological Model Experiments. The Australian Meteorological Magazine No. 42, 58-61 (September 1963).

Frenzen, P. A Laboratory Investigation of the Lagrangian Autocorrelation Function in a Stratified Fluid. Argonne National Laboratory Report ANL-6794 (November 1963).

Holtzman, R. B. Lead-210(RaD) and Polonium-210(RaF) in Potable Waters in Illinois. The Natural Radiation Environment. University of Chicago Press, Chicago, 1964. pp. 227-238.

Ilcewicz, F. H., R. B. Holtzman, and H. F. Lucas, Jr. A Rapid Spectrophotometric Method for the Determination of Lead in Bone Ash. Anal. Chem. 36, 1132-1135 (May 1964).

Frost, A. A., M. Inokuti, and J. P. Lowe. Approximate Series Solutions of Non-Separable Schroedinger Equations. II. General Three-Particle System with Coulomb Interaction. J. Chem. Phys. 41, 482 (July 15, 1964).

Inokuti, M. Gel Formation in Polymers Resulting from Simultaneous Cross-linking and Scission. J. Chem. Phys. 38, 2999-3005 (June 15, 1963).

Inokuti, M., and M. Dole. Analysis of Molecular Weight Changes and Gel Data of Some Irradiated Vinyl Polymers. J. Chem. Phys. 38, 3006-3009 (June 15, 1963).

Dole, M., and M. Inokuti. Conditions for the First and Second Order Kinetics During Multiple Zone Reactions. J. Chem. Phys. 39, 310-314 (July 15, 1963).

Inokuti, M., and M. Matsuzawa. Effect of Impurity on Excitation Migration in a Linear Chain of Molecules. J. Chem. Phys. 41, 732-736 (August 1, 1964).

Katsuura, K., and M. Inokuti. Exciton Impurity Level and Its Implications to Radiation Chemistry. J. Chem. Phys. 41, 989-993 (August 1964).

Inokuti, M., and M. Dole. Interpretation of the Intrinsic Viscosity of Polymers Undergoing Simultaneous Degradation and Cross Linking. J. Polymer Sci., Part A. 1, 3289-3302 (October 1963).

Katsuura, K., and M. Inokuti. Excited States of a Linear Molecular Chain Containing an Impurity. J. Phys. Soc., Japan 18, 1486-1494 (October 1963).

Kastner, J., J. E. Rose, and F. R. Shonka. Muscle-Equivalent Environmental Radiation Meter of Extreme Sensitivity. Science 140, 1100-1101 (June 7, 1963).

Ter-Pogossian, M., J. Kastner, and T. B. Vest. Autofluorography of the Thyroid Gland by Means of Image Amplification. Radiology 81, 984-988 (December 1963).

Kastner, J., F. R. Shonka, and J. E. Rose. Natural Environmental Radiation Measurements Utilizing Muscle-Equivalent Ion Chambers. The Natural Radiation Environment. University of Chicago Press, Chicago, 1964. pp. 655-660.

Kastner, J., B. G. Oltman, and L. D. Marinelli. Progress Report on Flux and Spectrum Measurements of the Cosmic-Ray Neutron Background. The Natural Radiation Environment. University of Chicago Press, Chicago, 1964. pp. 441-448.

Gustafson, P. F., J. Kastner, and J. Luetzelschwab. Environmental Radiation Measurements of Dose Rates. Science 145, 44-46 (July 3, 1964).

Lucas, H. F., Jr., R. E. Rowland, C. E. Miller, R. B. Holtzman, R. Hasterlik, and A. J. Finkel. An Unusual Case of Radium Toxicity. Am. J. Roentgenol. 90, 1042-1051 (November 1963).

Emrich, G. H., and H. F. Lucas, Jr. Geologic Occurrence of Natural Radium-226 in Ground Water in Illinois. Bull. Intern. Assoc. Scientific Hydrology (Holland) 8, 5-19, 1963.

Lucas, H. F., Jr., and D. A. Woodward. Effect of Long Decay Chains on the Counting Statistics in the Analysis of Radium-224 and Radon-222. J. Appl. Phys. 35 452-456 (February 1964).

Lucas, H. F., Jr. A Fast and Accurate Survey Technique for Both Radon-222 and Radium-226. The Natural Radiation Environment. University of Chicago Press, Chicago, 1964. pp. 315-330.

Lucas, H. F., Jr., R. B. Holtzman, and D. C. Dahlin. Radium-226, Radium-228, Lead-210 and Fluorine in Persons with Osteogenic Sarcoma. Science 144, 1573-1575 (June 26, 1964).

Marshall, J. H., R. J. Lari, and J. Kastner. Diffusion and Absorption of Gases in Plastic-Walled Ionization Chambers. Health Phys. 10, 331-336 (May 1964).

Marshall, J. H. Theory of Alkaline Earth Metabolism. The power function makes possible a simple but comprehensive model of skeletal systems. J. Theoret. Biol. 6, 386-412 (1964).

May, H. A., and L. D. Marinelli. Cosmic Ray Contribution to the Background of Low Level Scintillation Spectrometers. The Natural Radiation Environment. University of Chicago Press, Chicago, 1964. pp. 463-480.

Mahan, B. H., and J. C. Person. Gaseous Ion Recombination Rates. J. Chem. Phys. 40, 392-401 (January 15, 1964).

Mahan, B. H., and J. C. Person. Gaseous Ion Recombination Rates. II. J. Chem. Phys. 40, 2851-2859 (May 15, 1964).

Parr, R. M., and H. F. Lucas, Jr. A Rigorous Least-Squares Analysis of Complex Gamma-Ray Spectra with Partial Compensation for Instrumental Instability. Trans. IEEE NS-11(3), 349-357 (June 1964).

Platzman, R. L. Some Remarks on the Nature of Ionization, Ionization Yields, and Isotope Effects in the Ionization of Molecules by Various Agencies. J. Chem. Phys. 38, 2775-2776 (June 1, 1963).

Brugger, J. E., F. F. Rieke, and R. A. Semmler. Engine-Wear Studies with Radioisotopes. Isotopes and Radiation Technology 1, 256-264 (Spring 1964).

Rose, J. E. Simple Test for Leaking Radium Sources. Am. J. Roentgenol. 90, 403 (August 1963).

Shonka, F. R., G. Failla, and J. E. Rose. New Electrometer of High Sensitivity. Rev. Sci. Instr. 35, 1046-1049 (August 1964).

Simmons, D. J. Periodicity of S^{35} Uptake in Rat Femurs. Experientia 20, 137-138 (1964).

Simmons, D. J., and A. M. Pankovich. Bone Development in Japanese Quail. Anat. Record 147(3), 325-326 (November 1963).

Simmons, D. J., and A. M. Pankovich. Estrogen-Induced Intramedullary Bone Formation in Japanese Quail. Endocrinology 74, 646-648 (April 1964).

Simmons, D. J. Circadian Mitotic Rhythm in Epiphyseal Cartilage. Nature 202, 906-907 (May 30, 1964).

ABSTRACTS

Berlman, I. B., and O. J. Steingraber. Fluorescence Decay-Time Measurements of Several Deuterated Compounds. Bull. Am. Phys. Soc. 9, 76, (1964).

Bowe, J. C. Effect of Inelastic Collisions on the Drift Velocity of Electrons in Noble Gases. Bull. Am. Phys. Soc. 9, 186 (1964).

Frenzen, P. Determination of the Rate of Turbulence Dissipation by Eulerian Variance Analysis. Bull. Am. Meteorol. Soc. 45, 61 (March 1964).

Holtzman, R. B. The Kinetics of Alkaline Earth and Tracer Metabolism. Radiation Res. 22, 34 (May 1964).

Kastner, J., and L. D. Marinelli. Flux and Spectrum Measurements of the Cosmic Ray Neutron Background. Bull. Am. Phys. Soc. 8, 526 (1963).

Kastner, J., D. R. Roberts, and W. Prepejchal. Internal Sr^{90} Beta-Ray Dosimetry with Fluorods. Radiation Res. 22, 38 (May 1964).

Moses, H., R. L. Martin, and J. Kastner. Man-Made Ionized Columns in the Atmosphere - A New Tool for Meteorological Research. Bull. Am. Meteorol. Soc. 44, 715 (November 1963).

Crutcher, H. L., and H. Moses. Three-Dimensional Patterns Describing Wind Behavior. Bull. Am. Meteorol. Soc. 45, 41 (January 1964).

Simmons, D. J. Periodicity of Mitosis, S^{35} Sulphate and C^{14} Glycine Uptake in Rat Bone. Abstracts of the Communications to the Second European Symposium on Calcified Tissues, Liege, March 31 - April 1964.

ACCEPTED FOR PUBLICATION

Holtzman, R. B. Letter to the Editor: The Source of Unsupported Po^{210} (RaF) in Tissue. Health Phys.

Kastner, J., and R. K. Hukkoo. The Radium Gamma-Ray Calibration of Muscle-Equivalent Ionization Chambers. Health Phys.

Marinelli, L. D. Dosimetrie. Handbook of Medical Radiology. Springer-Verlag, Heidelberg. Vol. II, Chapter III-1.

Marinelli, L. D. General Technical Problems in Radiological Physics. Proceedings of the Symposium on Relations Between Physics and Medicine, Levico-Roncegno, Italy, September 14-20, 1964.

Marshall, J. H. Theory of Alkaline Earth Metabolism II. The Bauer-Carlsson-Lindquist Equation Provides a Unifying Basis for Kinetic Analysis. International Atomic Energy Agency Technical Report Series No. 10, Research Applications of Ca^{47} Vienna, 1964.

Moses, H., G. H. Strom, and J. E. Carson. Stack Plume Rise Determinations Affected by Meteorological and Engineering Factors. Nuclear Safety.

Gill, G. C., N. Islitzer, T. Lemmons, D. Mazzarella, H. Moses, and J. E. Pearson. Meteorological Instruments for Air Pollution Surveys. Informative Report No. 1, TA-8 Meteorological Committee. J. Air Poll. Control Assoc.

Moses, H., R. L. Martin, J. Kastner, and A. J. Ulrich. Man-Made Ionized Columns in the Atmosphere - A New Tool for Meteorological Research. J. Atmospheric Sciences.

Rowland, R. E. Resorption and Bone Physiology. Bone Biodynamics, Proc. Symposium held in Detroit, 1963.